A FRAMEWORK FOR LARGE EDDY SIMULATION OF INCOMPRESSIBLE FLOWS WITH ERROR CONTROL

A Dissertation

Presented to the Faculty of the Graduate School

of Cornell University

in Partial Fulfillment of the Requirements for the Degree of

Doctor of Philosophy

by

Giridhar Jothiprasad

August 2005

A FRAMEWORK FOR LARGE EDDY SIMULATION OF INCOMPRESSIBLE FLOWS WITH ERROR CONTROL

Giridhar Jothiprasad, Ph.D.

Cornell University 2005

This work developed tools to make Large Eddy Simulation (LES) more easily applicable to engineering problems.

An iterative fractional step method was developed for LES. A block-matrix-based analysis procedure proved that two iterations are sufficient to achieve desired second-order temporal accuracy. Stretched Cartesian grids are mapped onto a uniform computational grid. The stencil of the pressure Poisson equation was reduced from seven to five points in each coordinate direction, while still requiring the volume fluxes to satisfy a fourth-order spatially discretized continuity equation to machine precision. The algorithm was implemented in parallel.

Improved criteria for comparing sub-grid models was obtained by comparing the statistics from the LES with those from the unfiltered Navier-Stokes equations. This allowed us to clearly define the convergence of an LES approach with resolution length scale, Δ. The difficulty in assessing the accuracy of the statistics obtained from an LES is solved by modeling the statistics of unresolved, or residual, motions. We then combine the ideas of convergence and modeling the statistics of residual motions to give a rationale for the choice of better values for sub-grid model parameters. The performance of these ideas is studied in the context of forced isotropic turbulence and temporal mixing layer.

In isotropic turbulence, extrapolation techniques were developed to determine the DNS statistics in the limit of infinite Re. The resolved kinetic energy (KE) converged to the same asymptote for the three eddy-viscosity models studied. Addition of modeled residual KE to resolved KE improved estimate for turbulent KE. Improved values for the sub-grid model parameters were obtained by removing the leading order $\Delta^{2/3}$ term in the total KE.

In mixing layer, Δ convergence of the volume-averaged total turbulent KE degraded with time. Eddy-viscosity models were poor models for residual shear stress because the modeled residual shear stress is aligned with the resolved strain rate. Improved model parameters, which minimized the Δ variation of the volume-averaged turbulent KE, strongly depended on the time. Hence, for the above low Re mixing layer LES, it is not possible to remove the Δ variation *at all times*, by choosing a single set of values.

BIOGRAPHICAL SKETCH

Giridhar Jothiprasad was born on June 11, 1978, in Madras, a large city on the east coast of South India. He received his high school education from Padma Seshadri Bala Bhavan. In 1995, he joined the undergraduate program in Aerospace engineering at the prestigious Indian Institute of Technology, Madras. His undergraduate thesis studied the evolution of a shock in a viscous heat conducting gas using perturbation methods. He obtained his Bachelor of Technology degree with the highest academic honor - Gold Medal for outstanding academic performance in Aerospace engineering. He then went to Cornell to pursue a doctoral program in Aerospace engineering with the Sage Graduate Fellowship. At Cornell, he developed techniques to make Large Eddy Simulation, a turbulence modeling methodology, more accessible to practitioners under the guidance of Professor David A. Caughey. His discussions with Professor Stephen B. Pope also helped him formulate his problem statement. He received the Olin Fellowship, awarded to two students in the College of Engineering, for outstanding academic performance. His summer internships at Institute for Computer Applications in Science and Engineering, NASA Langley, with Professor Mavriplis during the years of 2001 and 2002, allowed him to study implicit time-stepping schemes and preconditioning techniques to solve non-linear implicit systems. He received his special Masters in the year of 2002. Upon obtaining his doctorate, he will be working in the Fluid Mechanics Lab at General Electric Corporate Research and Development, Schenectady, NY.

To my grandfather, Alagarswamy, who inspired me to do my best.

ACKNOWLEDGEMENTS

I would like to thank everyone who have made my education possible. My thesis advisor, Professor Caughey has always been a source of inspiration and support. His attention to detail and willingness to help, including debugging lines of my code, have helped me overcome many problems in my graduate studies. He also gave me sufficient freedom to experiment with my ideas.

Professor Pope was instrumental in kindling my interest in turbulent flows and provided valuable suggestions all through my work. I have spent two enjoyable summers with Professor Dimitri Mavriplis working on implicit time-stepping and preconditioning techniques. This work led to my first publication. Professor van Loan taught me matrix computations and gave me advice on efficiently solving linear systems which arise in numerical analysis.

During my graduate career, I have been financially supported my numerous teaching assistantships and prestigious fellowship. Professor Williamson, for whom I have been a teaching assistant, has always taken a special interest in my progress.

I must also thank my system administrators, Andrey Klochko and John Gibson. They have patiently solved my many problems with the Linux cluster and installed the required software promptly. My undergraduate advisor, Rajan, also played an important role in providing a strong foundation in fluid mechanics.

I have had the good fortune of having a number of interesting and entertaining friends who made my stay at Cornell pleasant. My family has sacrificed a lot for me to be here. Lastly, my wife, Lakshmi, has given me much support during our time at Cornell.

TABLE OF CONTENTS

LIST OF TABLES

LIST OF FIGURES

LIST OF ABBREVIATIONS

ADI	Alternating Direction Implicit, 81,**82**
BC	Boundary condition, 45
CFL	Courant-Friedrichs-Lewy, 43
DM	Distributed memory, 66
DNS	Direct Numerical Simulation, **3**
FEM	Finite element method, 223
FFT	Fast Fourier Transform, 71,**75**
KE	Kinetic Energy, 30
LES	Large Eddy Simulation, 1,**5**
MIMD	Multiple Instruction Multiple Data, 66
MPI	Message Passing Interface, 67
NS	Navier-Stokes, 3
PVM	Parallel Virtual Machine, 67
RANS	Reynolds-averaged Navier-Stokes, 5
RHS	Right-hand side, 45
SGS	Sub-grid scale, 109
SSFEM	Spectral Stochastic Finite Element Method, 233
VMS	Variational Multiscale, 222

NOTATION

$\overline{\bullet}$	Spatial filtering operation, Pg **31**
$\mathcal{F}_\kappa\{\bullet\}$	Fourier transform in a periodic, finite domain, Pg **97**
$\langle\bullet\rangle_{12}$	Plane average over the x_1x_2 plane, Pg **163**
$\langle\bullet\rangle_{123}$	Volume average over the computational domain, Pg **97**,163
$\langle\bullet\rangle_{123,t}$	Volume- and time-averaging, Pg 113
$B_i\{\mathbf{W}\}$	Operator used to obtain the volume fluxes, F_i from the velocity, $\mathbf{W}$, Pg 58
$C\{\mathbf{W}\}$	Spatially fourth-order accurate discretization of the continuity/ divergence operator, Pg 42
$C^F\{\mathbf{F}\}$	Spatially fourth order accurate discrete continuity operator based on the volume fluxes F_i, Pg 58
$D_2\{W_i;\nu,\nu_r^{n+1}\}$	Spatial discretization of the viscous and linear eddy-viscosity sub-grid model terms $\frac{\partial}{\partial x_j}\left[2\left(\nu+\nu_r\right)S_{ij}^W\right]$, Pg 42
$G_i\{p\}$	Spatially fourth-order accurate discretization of the pressure gradient, Pg 42
$G_i^F\{p\}$	Spatially fourth-order accurate discretization of the pressure gradient multiplied by the surface area of cell face normal to x_i. It is used to correct the volume fluxes, F_i, Pg 58
$G_i^W\{p\}$	Spatially fourth-order accurate discretization of the pressure gradient used to correct the velocity, W_i, Pg 58
$H_i\{\mathbf{W},\mathbf{F}\}$	Spatially fourth-order accurate discretization of the convective term, Pg 42
$L_{cross}\{;\}$	Spatially second-order discretization of all the cross derivative terms in the viscous and sub-grid stress terms, Pg 82
$L_{x_1}\{;\}$	Spatially fourth-order discretization of the normal derivative term, $\frac{\partial}{\partial x_1}\left(\cdot\frac{\partial(\bullet)}{\partial x_1}\right)$, Pg 82
A_i	Surface area of the cell face perpendicular to ξ_i., Pg 58,**63**
C_0	Kolmogorov constant, Pg **108**
C_E	LES Model parameter appearing in the model for the viscous dissipation of residual KE, ϵ_R, Pg 33
C_ν	LES Model parameter appearing in the sub-grid scale model based on residual KE, k_R, Pg 31

Δ	Resolution length scale which specifies the length scale of the smallest eddies to be numerically resolved in the LES, Pg **17**
δ_m	Momentum thickness of the temporal mixing layer, Pg **163**
δ_w^0	Half the initial vorticity thickness of the temporal mixing layer, used as a reference length, Pg **150**
Δx	Uniform grid spacing used for LES of isotropic turbulence, Pg 96
E_f	Kinetic energy in the Fourier modes being forced in isotropic turbulence, Pg **100**
ϵ	Rate at which energy is extracted from the mean flow = Rate at which energy cascades down the energy cascade = Rate at which energy is dissipated, Pg **16**
ϵ_R	Local viscous dissipation of residual KE k_R, Pg 32
$E(\kappa)$	Instantaneous energy spectrum function , Pg 99
$E_{13}(\kappa)$	Shear stress spectrum, Pg **185**
$\hat{E}^W(\boldsymbol{\kappa})$	Kinetic energy of a Fourier mode defined in a periodic, finite domain, Pg **98**
$E^R(\kappa)$	Energy spectrum of residual motions, Pg **113**,135
$E_{13}^R(\kappa)$	Contribution of residual motions to the shear stress spectrum, Pg **186**
η	Kolmogorov length scale which represents the length scale of the smallest eddies in the turbulent flow, Pg 17
F_m	Volume flux per unit area crossing the surface of constant ξ_m in the computational space, Pg 51,**55**
κ_1	Wave number in the x_1 direction, Pg **77**
κ_2	Wave number in the x_2 direction, Pg **77**
κ_d	Dissipation wave number signifying the wave number for the smallest resolved scales in the LES, Pg **108**
κ_f	Maximum wave number forced in isotropic turbulence simulations, Pg **100**
$\boldsymbol{\kappa}$	Wave number of a Fourier mode, Pg 95
k_W	Resolved KE in the LES of isotropic turbulence, Pg **113**
k_R	Residual KE defined as half the trace of the residual stress tensor τ_{ij}^R, Pg **31**
L	Side-length of the periodic cube used for LES of isotropic turbulence, Pg 95

L_1	Box length in the x_1 direction, Pg **77**
L_2	Box length in the x_2 direction, Pg **77**
λ_{x_1}	The stream-wise wavelength of the most unstable eigenfunction from linear stability analysis of the temporal mixing layer, Pg **151**
$\mathcal{L}$	Characteristic length scale, Pg **3**
M_{11}	A specific combination of geometric metrics appearing in the pressure Poisson equation, Pg **76**
N_1	Number of grid points in the x_1 direction., Pg **70**
N_2	Number of grid points in the x_2 direction., Pg **70**
N_3	Number of grid points in the x_3 direction., Pg **70**
N_p	Number of processes running in parallel, Pg **68**
ν	Kinematic viscosity of fluid, Pg **3**
ν_r	Eddy viscosity appearing in the LES sub-grid model, Pg **19**
$\mathcal{P}$	Rate of energy addition by forcing in isotropic turbulence, Pg **100**
$\Phi_{ij}^W(\boldsymbol{\kappa})$	Two-point velocity spectrum tensor, Pg 98
$\Phi_{ij}^R(\boldsymbol{\kappa})$	Contribution of the residual or unresolved motions in an LES to the two-point velocity spectrum tensor, Pg 134
$\mathcal{P}_R$	Local production of residual KE k_R, Pg 32
Q	Statistic obtained from the unfiltered DNS field, Pg 23
Q'	Statistic obtained from the filtered DNS field, Pg 22
Q^R	Model for the contribution to the statistic Q from the unresolved small eddies, Pg 28
Q^W	Statistic obtained from the LES field W_i, Pg 22
Re	Reynolds number, Pg **3**,89
Re^0	Initial Reynolds number of the temporal mixing layer, Pg **154**
$\hat{R}_{ij}^W(\boldsymbol{\kappa})$	Fourier coefficients of the two-point velocity correlation defined in a periodic, finite domain, Pg **98**
$R_{ij}^R(\mathbf{r})$	Contribution of the residual or unresolved motions in an LES to the two-point velocity correlation, Pg **134**
σ_k	LES model parameter which serves as a turbulent Prandtl number for the residual KE, Pg 33
S_{ij}^W	Strain rate of the computed LES field, Pg 18
τ	Artificial time used in the artificial compressibility approach for incompressible NS, Pg **38**

τ_{ij}^R	Residual stresses denoting the dynamic effect of the unresolved small eddies on the evolution of the large resolved eddies. It needs to be modeled in LES using the sub-grid model., Pg **18**
τ_{ij}^r	Anisotropic part of the residual stress τ_{ij}^R, Pg **19**
θ_i	Non-dimensional wave number appearing in Fourier transforms of discretizations, Pg **77**
$\tilde{a}_{j_1,j_2}$	Amplitude of the eigenfunction disturbances superimposed on the mean velocity profile in the temporal mixing layer, Pg **154**
ϕ_{j_1,j_2}	Phase of the eigenfunction disturbances superimposed on the mean velocity profile in the temporal mixing layer, Pg **154**
$T_k^{(\nu)}$	Viscous transport of residual KE k_R, Pg 32
$T_k^{(p')}$	Pressure transport of residual KE k_R, Pg 32
$T_k^{(u)}$	Turbulent transport of residual KE k_R, Pg 32
E_m	Generic flux per unit area crossing the surface of constant ξ_m in the computational space, Pg **54**
e_j	Generic flux in the physical coordinate system, Pg **54**
J	Jacobian of the coordinate transformation, determinant of the transformation tensor, $\frac{\partial \xi_i}{\partial x_j}$, to go from physical to computational space, Pg **54**
x_i	Coordinates in physical space, Pg **53**,149
ξ_i	Coordinates in computational space, Pg **53**,149
U_i	Underlying Turbulent Velocity field, Pg **4**,17
U_0	Free-stream speed of the temporally evolving mixing layer, Pg **148**
$\mathcal{U}$	Characteristic velocity scale, Pg **3**
u_i	Turbulent velocity fluctuations in the temporal mixing layer, Pg **171**
u_i^R	Residual velocity field, Pg **133**
W_i	Resolved LES Field, Pg **18**
w_i	Resolved turbulent velocity fluctuations in the temporal mixing layer, Pg **176**

Chapter 1

Introduction

Turbulent flows are ubiquitous in geophysical and engineering flows. The presence of chaotic, unsteady fluid motions in a wide range of length and time scales make these flows intractable to numerical resolution of all the length scales and to analytical treatments. The practical significance, as well as the purely intellectual challenge, of this problem has compelled researchers to develop a wide range of turbulence modeling techniques. Large Eddy Simulation (LES) is one such modeling technique which has gained popularity over the last decade on account of its potential to become a robust, predictive tool [Langford & Moser (1999)]. LES is essentially an under-resolved turbulence simulation that uses a model to account for the lack of small-scale resolution [Rogallo & Moin (1984)]. Over the last decade LES has been extended to model a wide variety of complex engineering flows. Despite these advances, LES has largely been used only in the research community. There are two basic reasons for this. Firstly, the effective use of LES to get meaningful results is still an art which requires experts to fine tune a whole host of model parameters. Secondly, LES requires computationally efficient and accurate algorithms for its implementation.

In this chapter, we start with a short perspective on turbulence modeling and show where LES lies in the context of current turbulence modeling techniques. We then present the issues in the current LES methodology which make it hard to use LES in practical engineering problems. The LES framework being developed to address these issues is also briefly alluded to. Finally, we give the organization of the rest of the thesis.

1.1 Turbulence modeling and Large Eddy Simulation

Many flows in nature and engineering are turbulent. Figure 1.1 shows the eruption of the Mount St. Helens volcano in 1980. Being the largest volcanic eruption in

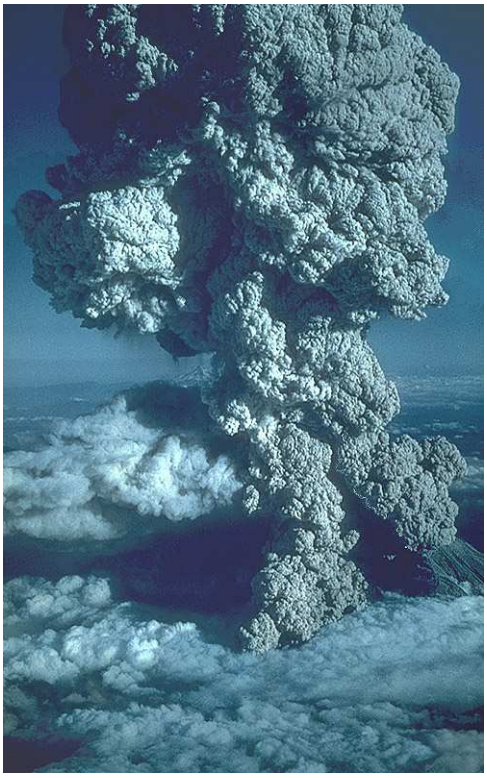

Figure 1.1: Eruption of Mount St. Helens volcano in 1980. Picture by J.W. Vallance.

America, it is a fine illustration of the characteristics of turbulent flow. The most striking characteristic is the presence of turbulent motions in a wide range of length and time scales. The largest motions or eddies in this flow have sizes in the order of a few kilometers while the smallest eddies have sizes in the order of a few millimeters. It is this wide range of length and time scales which makes turbulent flows hard to simulate on the computer even though the Navier-Stokes (NS) equations which govern these fluid motions have been well known for almost

2 centuries. Any numerical simulation begins with a discretization of the governing equations on a numerical grid which captures all the required flow features. To resolve all the motions in a turbulent flow computationally, we have to choose the simulation domain size based on the size of the largest eddies in the problem while the grid spacing is determined based on the size of the smallest eddies. This requires a numerical grid with a prohibitively large number of grid points when the flow is turbulent. Since the computational cost of the numerical simulation is approximately proportional to the 4/3 power of the number of grid points, turbulent flows are computationally expensive to simulate on a computer.

The range of length scales occurring in a turbulent flow is characterized by a single non-dimensional number called the Reynolds number, Re. The Reynolds number is a measure of the ratio of inertial to viscous forces in the fluid flow and is defined to be,

$$Re = \frac{\mathcal{U}\mathcal{L}}{\nu} \tag{1.1}$$

where

$\mathcal{U}$ - Characteristic velocity scale

$\mathcal{L}$ - Characteristic length scale

ν - Kinematic viscosity of fluid

Larger Re corresponds to a wider range of length and time scales of the eddies in the turbulent flow.

A turbulence simulation which numerically resolves the eddies in *all* the length and time scales is called a Direct Numerical Simulation (DNS). DNS does not introduce any turbulence modeling assumptions. However it is limited to simulations of low to medium Re flows as the computational cost of DNS goes up as Re^3

[Pope (2000*a*)]. So DNS mainly finds use as a research tool to provide insights into turbulence physics and to aid the development of other turbulence models [Moin & Mahesh (1998)].

Another characteristic of turbulent flows is their extreme sensitivity to initial and boundary conditions. This has led researchers to attempt *statistical descriptions of turbulent flow* as opposed to trying to describe the flow by specifying the instantaneous velocity and pressure fields at every point in space and time. In statistical descriptions we specify only the statistics such as means of the velocity and pressure fields. In fact, for many engineering applications, the mean and a few second-order statistical moments would be a sufficient description of the turbulent flow. Hence the goal of any turbulence simulation is to describe the underlying turbulent velocity field, U_i, through its statistics.

There have been conceptually many different approaches to turbulence simulation [Pope (1999)]. One such approach is to develop techniques which directly compute *only* the required flow statistics such as the mean velocity fields without computing the turbulent velocity field, U_i. The starting point for many of these techniques is the exact evolution equations for the set of required flow statistics which can be derived directly from the NS equations. However, all these techniques face the *turbulence closure problem*. This means that the evolution equations for the required statistics depends on additional statistics not in the set considered [Pope (2000*b*)]. Hence the evolution equations for the required statistics are said to be *not closed*. For example, the evolution of the mean velocity field depends on the second-order statistical moments of the velocity field. Hence, to advance the evolution equations one needs to develop models for these additional statistics and it is this closure problem which much of the turbulence modeling community

addresses.

The simplest level of description would be to compute only the mean velocity fields. Such methods are called Reynolds-Averaged Navier-Stokes (RANS) models and require the second-order statistical moments of the velocity field to be modeled. The computational advantage of RANS models over DNS is that the mean velocity fields are usually confined to motions only in the largest length scales making it much easier to numerically resolve the mean velocity field as compared to the underlying turbulent velocity field. With the current computational capabilities it is even possible to do design optimizations, requiring thousands of flow calculations, using RANS models.

Over the last three decades a whole range of RANS models with widely differing computational requirements and a broad range of applications have been developed. More complete descriptions of these models can be found in Wilcox (1998); Pope (2000*c*). But the biggest drawback of RANS models is the sensitivity of the flow statistics to the RANS model and the model parameters used. Different RANS models work well for different applications and there is no universal model which works well for all. Hence these calculations are performed by highly qualified personnel, even in an industrial setting.

Large Eddy Simulation (LES) uses a slightly different approach to turbulence modeling. Since in many applications the statistics of interest such as the mean velocity field depend primarily on the large eddies, we resolve only the large eddies of the turbulent velocity field. But the time evolution of the large resolved eddies is affected by the unresolved small eddies. This effect of the small eddies on the large eddies is modeled in LES using a *sub-grid model*. Again, many sub-grid models have been proposed for LES [Smagorinsky (1963); Bardina *et al.* (1983); Germano

et al. (1991); Zang *et al.* (1993); Pope (2000*d*)].

LES lies between RANS models and DNS in computational expense and is motivated by the limitations of these approaches [Pope (2000*d*)]. In many high Re flows such as free shear flows, the rate-controlling processes and the quantities of interest are determined mainly by the resolved, large-scale motions, which are represented explicitly in an LES. Hence there is reason to expect LES to be more reliable and accurate than RANS models for such flows. For the same reason we also expect LES to be less sensitive to the sub-grid model used. On the other hand, when compared with DNS, the huge computational effort involved in resolving the small eddies in DNS has been avoided in LES.

It should be noted that there are many important applications in which the arguments in favor of LES break down [Pope (1999)]. For example in turbulent combustion the rate controlling processes of molecular mixing and chemical reaction occur at the smallest scales. This places a first order dependence of the statistics computed on the LES sub-grid model used. There are other situations such as high Re near-wall flows where there are no large eddies. Despite these concerns, LES has been successful in many flows including some flows for which the arguments in its favor break down. To illustrate the complexity of the flow fields simulated using LES, we end this section with three interesting applications of LES.

1. **Solid Rocket Booster:** This 3d simulation of the Space Shuttle solid rocket booster [Wasistho & Moser (2005)] was carried out in the Center for Simulation of Advanced Rockets, University of Illinois at Urbana-Champaign. The hot gas from the igniter flows down the combustion chamber and heats the propellant over a period of about 125 ms. When the surface temperature

at some locations reaches the ignition temperature (850 K) burning begins. Figure 1.2 shows the velocity and temperature contours of the gas in the booster. This is an extremely hard flow to simulate because it is a two-phase turbulent flow involving complex ignition and reaction mechanisms. The turbulence was modeled using LES.

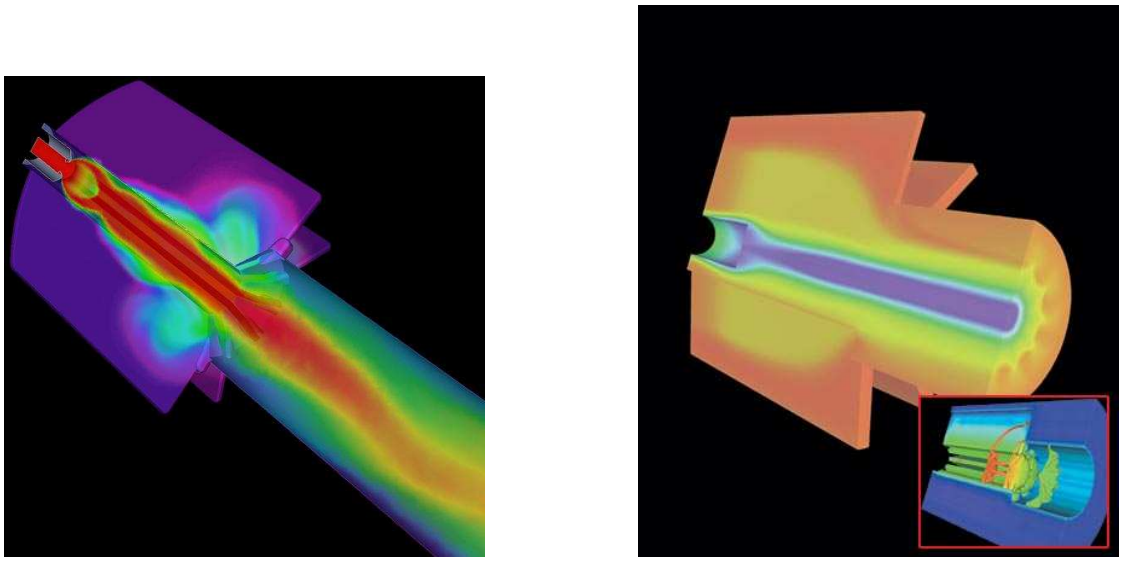

(a) Temperature contours (b) Velocity contours

Figure 1.2: Numerical simulation of ignition and two-phase turbulent flow in the Space Shuttle solid rocket booster

2. **Gas-turbine combustor:** Incompressible simulations in the exceedingly complex geometry of the Pratt and Whitney gas-turbine combustor [Mahesh *et al.* (2004)] were performed at the Center for Integrated Turbulence Simulations, Stanford University. The use of a complex unstructured mesh for the LES simulation of a reacting flow makes this a landmark application of LES. Figure 1.3 illustrates the geometric complexity of the combustor and the unstructured mesh used.

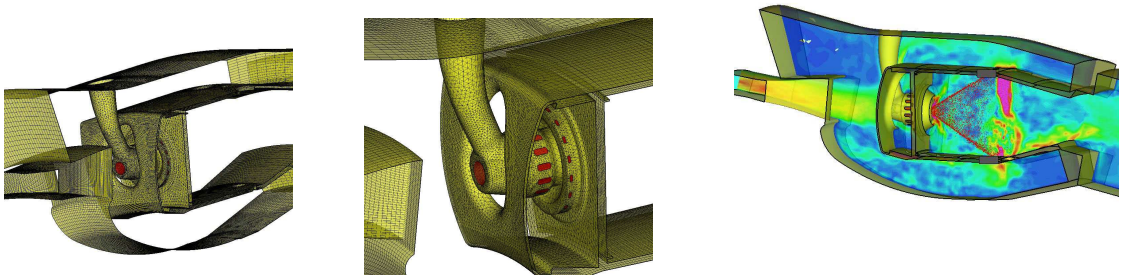

(a) Geometry (b) Surface Mesh (c) Velocity contours

Figure 1.3: Incompressible simulations in the complex geometry of the Pratt and Whitney gas-turbine combustor.

3. **Temporal Mixing Layer** - These large eddy simulations of temporally evolving turbulent mixing layers [Balaras *et al.* (2001)] were carried out at University of Maryland at College Park. Although these simulations do not involve complex geometries or flow physics, it is an important example of how LES has been used to study flow structures observed in mixing layers. This illustrates the confidence placed by researchers on LES to faithfully reproduce these turbulent flow structures. Figure 1.4 shows the flow structures observed in this LES.

1.2 Issues with LES methodology

Despite the application of LES to complicated flows and geometries, there remain certain basic shortcomings in the LES methodology. As mentioned earlier, one of the greatest attractions of LES was that it would provide a robust turbulence simulation procedure capable of being used by *all*. However, LES has primarily been used in the research community and is only slowly making its presence felt

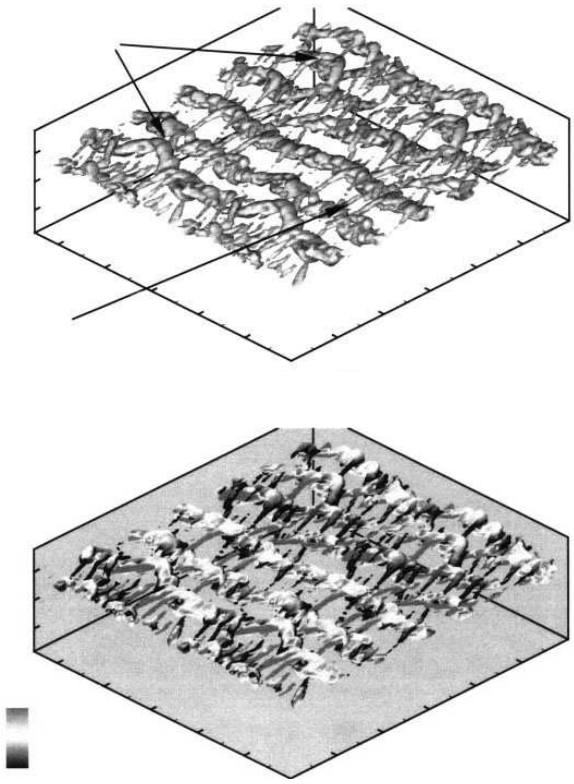

Figure 1.4: Flow structures such as span-wise rollers observed in LES of temporally evolving turbulent mixing layers

in the engineering community. This is mostly because the effective use of LES to get meaningful results is still an art which requires the intervention of an expert. This difficulty in the use of LES can be attributed to the following 3 issues:

- **Current criteria for comparing sub-grid models are inadequate.** A number of sub-grid models have been developed for LES but criteria used to compare the performance of these sub-grid models are still an active area of research [Clark *et al.* (1979); Langford & Moser (1999)]. Existing criteria are inadequate because they give misleading judgments on the performance of sub-grid models. In this work we define a new notion of convergence for LES of very high Re flow and use this notion of convergence to develop better comparison criteria for sub-grid models.

- **Difficulty in choosing the length scale of the smallest eddies that needs to be resolved to achieve a given error tolerance.** Many a time, the poor performance of LES can be attributed to insufficient resolution of the eddies in the given LES. This problem can be avoided if the estimation of error in the statistic computed from LES becomes an inherent part of the LES methodology. Such error estimates can indicate whether the length scale of the smallest eddies resolved is sufficiently small or not. In this thesis, we developed estimates for the error in commonly computed statistics such as the turbulent kinetic energy. Such error estimates could then be incorporated into a framework which automatically determines the length scale of the smallest eddies that needs to be resolved based on a given error tolerance.

- **Difficulty in choosing model parameters.** Sub-grid models used in LES require certain model parameters to be chosen based on the flow, length scale

of the smallest eddies being resolved, and other numerical factors governing the particular LES implementation. The dynamic procedure [Germano *et al.* (1991)] has proven to be an effective procedure to choose these model parameters automatically. Here, we provide an alternative procedure for choosing these model parameters by combining the notion of convergence of LES and error estimates developed to address the earlier issues.

Addressing these issues is an important step towards making LES less of an art, thereby allowing it to be more easily used in industry. Equally important for the widespread use of LES is to develop efficient and accurate numerical algorithms for use in an LES implementation. The fractional step method [Chorin (1968); Kim & Moin (1985)] commonly used in unsteady, incompressible flow simulations becomes first-order accurate in time when boundaries are present. We develop an iterative fractional step method which maintains second-order temporal accuracy even with boundaries. Energy-conserving discretizations [Morinishi *et al.* (1998)] are used for the convective terms to improve robustness. Stretched Cartesian grids allow us to solve flow problems which have confined regions of large flow gradients, such as the temporal mixing layer, more efficiently. Finally, care was taken to implement these algorithms in parallel so that a good speedup was achieved.

1.3 Organization

The rest of the thesis is organized as follows. In chapter 2 we present the governing equations for LES, expand on the issues with the current LES methodology and how we addressed these issues. In chapter 3 we develop the numerically efficient algorithms used for performing LES. In chapter 4 we discuss some of the implementation aspects of the code in particular those required to achieve good parallel

speedup. In chapter 5 we study the issues with the LES methodology in the case of forced, homogeneous, isotropic turbulence. This flow is one of the simplest turbulent flows in which these issues can be addressed. In chapter 6 we extend our ideas to the temporally evolving mixing layer. This is a free shear flow with a single direction of inhomogeneity making this flow problem more complicated than isotropic turbulence. Finally, in chapter 7 we summarize how we addressed the problems in the LES methodology and give directions for future research in LES.

Chapter 2

Large Eddy Simulation

In this chapter, we first explain the rationale behind why LES works for turbulent flows based on the energy cascade hypothesis of turbulent flows. This leads us to the current LES methodology and the concept of resolution length scale, which specifies the size of the smallest eddies which are resolved in the LES. The governing equations for LES and the class of linear eddy-viscosity based sub-grid models used in all the simulations in this work are also introduced simultaneously. The pros and cons of the most prevalent filtering approach to LES are discussed. The resolution length scale is an important parameter in LES which largely determines the error introduced in the statistics computed from the LES. The notion of convergence of the required statistic when the resolution length scale tends toward zero is introduced in the context of LES of a very high Re flow. This notion of convergence is then used to develop better criteria for comparing sub-grid models. The advantage of modeling the statistics of the unresolved small scale motions, both to estimate the error in the statistic computed from the LES and to develop better sub-grid models, is then explained. We also present two sub-grid models which, apart from modeling the effect of the unresolved small scales on the resolved large scales, also include models for the statistics of the unresolved small scales. A new LES methodology which utilizes these modeled statistics of the unresolved eddies for error-control is also described. Finally, we develop a procedure for determining the model parameters appearing in the LES sub-grid models by combining the notions of convergence of LES and the modeled statistics of the unresolved eddies.

2.1 Why does LES work?

Before we proceed to describe the LES methodology we give a short explanation as to why LES works for high Re turbulent flows. The energy cascade hypothesis [Richardson (1922)], originally proposed by Richardson, forms the basis of this explanation. According to Richardson's view, turbulence is composed of motions or eddies of different sizes. The eddies of size, l, are characterized by a velocity scale, $u(l)$ and a timescale, $l/u(l)$.

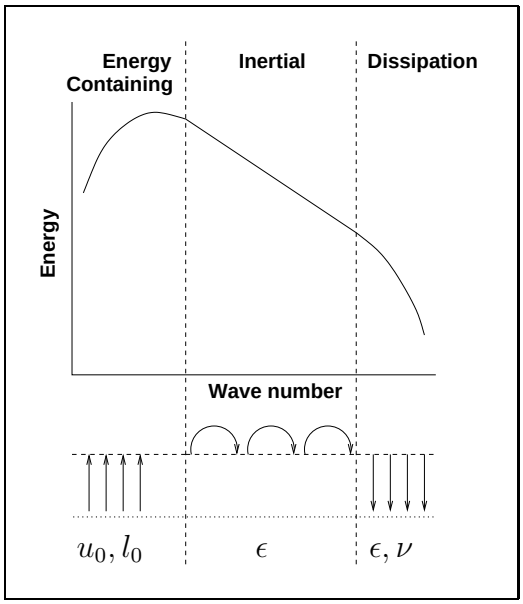

Figure 2.1: Energy spectrum function for a high Re turbulent flow in a log-log plot along with a schematic explanation of the energy cascade

Figure 2.1 shows the typical energy spectrum function for a high Re turbulent flow along with a schematic explanation of the energy cascade. The energy spectrum function can be thought of as giving the distribution of the energy contained in eddies of a particular length scale with wave number, which is inversely proportional to the length scale of the eddies. So smaller wave numbers correspond to the larger eddies while the largest wave numbers correspond to the smallest eddies

in the turbulent flow. Figure 2.1 also shows the classification of the eddies in a high Re turbulent flow into 3 ranges. These 3 ranges of eddies are described below with a view to justifying LES as a turbulence modeling procedure.

1. **Energy-Containing Range:** These are the largest eddies in the turbulent flow and, as the name suggests, contain most of the energy. The size of these eddies is comparable to the flow length scale, and these eddies are affected by the geometry and boundary conditions imposed on the flow. Hence, these large eddies differ from one flow to another, and a turbulence modeling procedure which explicitly resolves these eddies is likely to perform better.

   Further, it is believed that these are the eddies which extract energy from the mean flow thereby determining the energy available for sustaining the turbulent motions. If it were not for this energy input, the turbulent eddies would simply decay under the action of viscosity. According to Richardson, these large eddies are unstable and break up, transferring their energy to slightly smaller eddies. These slightly smaller eddies undergo a similar break-up process transferring their energy to smaller and smaller eddies. This transfer of energy to smaller and smaller eddies is referred to as the *energy cascade*.

   The length scale l_0 and velocity scale u_0 characterizing the energy-containing eddies are comparable to the characteristic flow length scale $\mathcal{L}$ and velocity scale $\mathcal{U}$ respectively. Simple arguments can be used to show that these eddies extract energy at the rate $\epsilon = u_0^3/l_0$ from the mean flow.

2. **Inertial Sub-range:** The eddies in this range of length scales undergo a similar break-up process transferring their energy to smaller and smaller eddies.

However, an important difference between these and the energy-containing eddies is that eddies in the inertial sub-range are believed to be *independent* of the flow geometry and boundary conditions. This is justified based on Kolmogorov's hypothesis [Kolmogorov (1991)] that any directional biases imposed by the geometry and boundary conditions are lost in the chaotic eddy-break-up process. He also hypothesized that the statistics of these eddies are universal, independent of the turbulent flow under consideration. This universal nature opens up the possibility of modeling the dynamic effect of these motions using a universal model which works for all turbulent flows. Such a turbulence modeling approach is also aided by the fact that the rate ϵ at which energy cascades down the energy cascade is simply the rate at which eddies in the energy-containing range extract energy from the mean flow. Since we have hinted at explicitly resolving these energy-containing eddies, the rate-controlling processes are explicitly resolved.

3. **Dissipation Range:** These are the smallest eddies in the turbulent flow. The eddy-break-up process occurring in the energy-containing and inertial range is essentially an inertial process not affected by the viscosity. But viscosity plays an important role in the dynamic evolution of eddies in the dissipation range. These eddies simply dissipate the energy cascading down the energy cascade into heat. Again, due to the chaotic break-up processes, we expect the eddies in the dissipation range to have universal statistics independent of the specific turbulent flow. Because of this universal nature, there is again the possibility of modeling the dynamic effect of these eddies with a universal model.

   The eddies in the dissipation range are characterized by the Kolmogorov

length scale η which can be related to the energy dissipation rate ϵ and the viscosity ν.

Although the validity of the Kolmogorov hypotheses has been a subject of much debate [Saddoughi & Veeravalli (1994); Shen & Warhaft (2000)] much of turbulence modeling and theory is based on these hypotheses. Similarly, Large Eddy Simulation is also founded based on the ideas given above.

2.2 Current LES methodology

The goal of an LES is to describe the underlying turbulent velocity field, U_i, through required statistics such as means and second-order velocity moments. In LES, this is achieved by partially resolving the turbulent flow. So, we choose a resolution length scale Δ which specifies the length scale of the smallest eddies to be numerically resolved in the LES. The resolution length scale is chosen to be in the inertial sub-range because it is hoped that one can develop a universal sub-grid model which models the dynamic effect that the unresolved eddies have on the evolution of the larger, resolved eddies. There is hope for such a universal sub-grid model because eddies in the inertial and dissipation range are believed to have universal statistics independent of the turbulent flow being simulated. Figure 2.2 schematically illustrates the choice of the resolution length scale in the inertial sub-range and the resolved and unresolved eddies.

Our goal in this work is to address the shortcomings of current LES methodology by studying relatively simple incompressible flows, such as isotropic turbulence

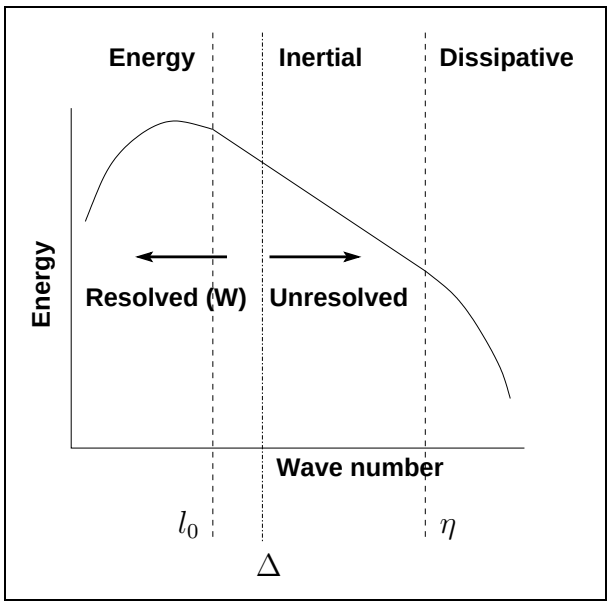

Figure 2.2: Schematic illustration of the resolved and unresolved eddies in LES

and mixing layers. The governing equations for LES of incompressible flows are

$$\frac{\partial W_i}{\partial t} + \underbrace{\frac{\partial \left(W_i W_j\right)}{\partial x_j}}_{\text{Convective}} = - \underbrace{\frac{\partial p}{\partial x_i}}_{\text{Pressure}} + \underbrace{\frac{\partial}{\partial x_j}\left(2\nu S_{ij}^W\right)}_{\text{Viscous}} - \underbrace{\frac{\partial}{\partial x_j}\left(\tau_{ij}^R\right)}_{\text{Sub-grid}} \tag{2.1}$$

$$\underbrace{\frac{\partial W_i}{\partial x_i}}_{\text{Continuity}} = 0 \tag{2.2}$$

where

W_i - Resolved or computed LES field

τ_{ij}^R - Residual stresses representing the dynamic effect of the unresolved small eddies on the evolution of the large resolved eddies. This needs to be modeled using the sub-grid model.

S_{ij}^W - Strain rate of the computed LES field, $\frac{1}{2}\left(\frac{\partial W_i}{\partial x_j} + \frac{\partial W_j}{\partial x_i}\right)$

It should be noted that:

- We clearly distinguish between the LES field W_i computed by solving the governing LES equations, Eqs. (2.1)-(2.2), and the underlying turbulent velocity field U_i which are governed by the Navier-Stokes equations.

- The governing LES equations, Eqs. (2.1)-(2.2), are equivalent to the incompressible NS equations plus an added sub-grid model term.

As mentioned earlier, a number of sub-grid models have been developed in the past. Very good descriptions of these can be found in textbooks [Geurts (2004); Sagaut (2002); Pope ($2000d$)] and reviews [Lesieur & Metais (1996); Rogallo & Moin (1984)]. Our goal was not to develop new sub-grid models but to highlight the shortcomings of the current LES methodology using the sub-grid models available in literature.

The simplest, and probably the earliest, sub-grid models developed for LES fall under the class of eddy-viscosity based sub-grid models where an eddy-viscosity is used to linearly relate the anisotropic part of the residual stress, τ_{ij}^r, to the strain rate of the LES field, S_{ij}^W,

$$\tau_{ij}^r = \tau_{ij}^R - \frac{1}{3}\delta_{ij}\tau_{kk}^R \stackrel{M}{=} -2\nu_r S_{ij}^W \tag{2.3}$$

This model is based on the reasoning that the most important dynamic effect of the unresolved eddies is to take the energy coming down the energy cascade and transfer it to smaller and smaller eddies until the energy is dissipated by the eddies in the dissipation range. The simplest way to model this is to choose the sub-grid model to be similar to the viscous dissipation term but use an eddy-viscosity, ν_r, instead of the physical viscosity, ν. Different specifications of ν_r correspond to different sub-grid models. The eddy viscosity ν_r, unlike the physical viscosity ν, is

- generally a function of space and time

- not a property of the fluid.

All the sub-grid models used in this work are in this class of eddy-viscosity based sub-grid models. The simplest specification for the eddy viscosity is to take ν_r to be a constant in both space and time. We refer to this model later in the thesis as the Constant eddy-viscosity model. Other sub-grid models used are described later in this chapter. We now proceed to discuss the issues with the LES methodology and how we have addressed these issues.

2.3 Issue 1: Good Criteria for comparing sub-grid models

It is important to develop good criteria for comparing the various sub-grid models. Although, many such criteria have been developed, they are inadequate and could provide misleading results. In order to understand the failings of the current criteria, we need to understand the filtering approach, which is the most prevalent approach to developing LES equations. After this, we describe the inadequacies of the current criteria used for comparing sub-grid models.

2.3.1 Filtering Approach to LES

Although we have discussed that LES requires the turbulent velocity field U_i to be decomposed into a resolved velocity or LES field W_i and an unresolved velocity field, we have not mathematically defined the resolved velocity or LES field. The most prevalent approach for defining the LES field is the filtering approach [Germano (1992); Pope ($2000d$)]. In the filtering approach, the turbulent velocity field, U_i, is decomposed as,

$$\text{Turbulent velocity} = \text{Filtered velocity} + \text{Residual velocity}$$

where,

Filtered velocity - Obtained by filtering the turbulent velocity field using a spatial filter with filter width Δ.

Residual velocity - Difference between the underlying turbulent velocity field and the filtered velocity.

The filtered velocity field is then thought of as the LES or resolved velocity field, W_i, determined using the governing LES equations (2.1)-(2.2). In the filtering approach, the resolution length scale is replaced by the filter width used for the spatial filter. Being the prevalent approach, the terms filter width and resolution length scale are frequently used interchangeably in LES literature.

The filtering approach also provides a mathematical basis for deriving the governing equations for LES. The evolution equation for the filtered velocity field can be obtained by filtering the Navier-Stokes (NS) equations. These equations include terms which represent the effect of the residual velocity field on the evolution of the filtered velocity field. Since the residual velocity field is not computed in LES, all such terms must be modeled using the sub-grid model.

2.3.2 Inadequacies in current comparison criteria

Although the filtering approach provides a mathematical foundation for decomposing the turbulent velocity field, taking this approach literally has led to misleading comparison criteria for sub-grid models. In this section, we introduce the conventional approach to *a posteriori* testing, why it leads to misleading comparisons, and how this can be corrected. We also briefly touch upon the inadequacies of other comparison criteria at the end of this section.

A posteriori testing is widely used in the literature to compare LES sub-grid models [Vreman *et al.* (1997)]. In *a posteriori* testing one performs both the DNS and the LES using different sub-grid models for the same turbulent flow. A statistic is chosen for comparing the sub-grid models. Conventionally, in *a posteriori* testing, we compare the statistic obtained from the LES (Q^W) performed using a specified sub-grid model and resolution length scale with that obtained from the *filtered* DNS velocity field (Q').

The LES field W_i, hence its statistic Q^W, the filtered DNS velocity field, and hence it statistic Q' all depend strongly on the resolution length scale Δ (or filter width) used. So, the biggest drawback of the conventional approach to *a posteriori* testing is that the yardstick used for comparison, Q', strongly depends on the resolution length scale or filter width, Δ. Further, the goal of any LES or in fact any turbulence modeling procedure, is to obtain the statistics of the unfiltered velocity field, Q. So Q' is not even the relevant statistic to be used for comparing sub-grid models.

Figure 2.3 schematically illustrates the drawbacks of the conventional approach to *a posteriori* testing. Let Q_A^W and Q_B^W denote some statistic for a given turbulent flow obtained from different LES fields computed using two different sub-grid models, A and B, respectively. Q' denotes the statistic from the filtered DNS field. The variation of these statistics with some power p of the resolution length scale is shown in Fig. 2.3. It can be seen that Q_A^W is closer to Q' than Q_B^W at all resolution length scales, Δ larger than l^*. Based on the conventional approach to *a posteriori* testing, we would wrongly conclude that sub-grid model A is better than sub-grid model B for the coarse resolutions for which LES usually is feasible. However in reality, sub-grid model B is better, even at these coarse resolutions,

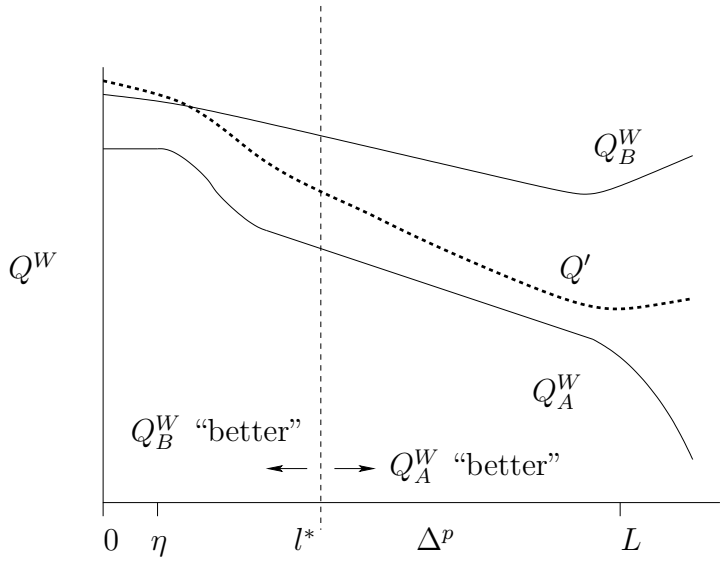

Figure 2.3: Schematic illustration of the conventional approach to *a posteriori* testing. The statistic computed from LES field, Q^W is compared with the statistic obtained from the filtered DNS field, Q'.

because its statistics are closer to those obtained from the unfiltered DNS velocity field Q (given by the value of Q' at $\Delta = 0$).

The drawbacks in *a posteriori* testing can be corrected by comparing the statistics obtained from the LES field, Q^W, with the statistics obtained from the *unfiltered* DNS field, Q. The yardstick for now comparing sub-grid models, Q, is independent of the filter width as the filter width does not enter the definition of Q. The additional advantage is that Q is the relevant statistic which an LES attempts to determine. Figure 2.4 schematically illustrates this alternative approach to *a posteriori* modeling. Clearly, sub-grid model B emerges as the superior sub-grid model when comparing with the statistic from the unfiltered DNS field, Q.

The other commonly used procedure for comparing the performance of sub-grid

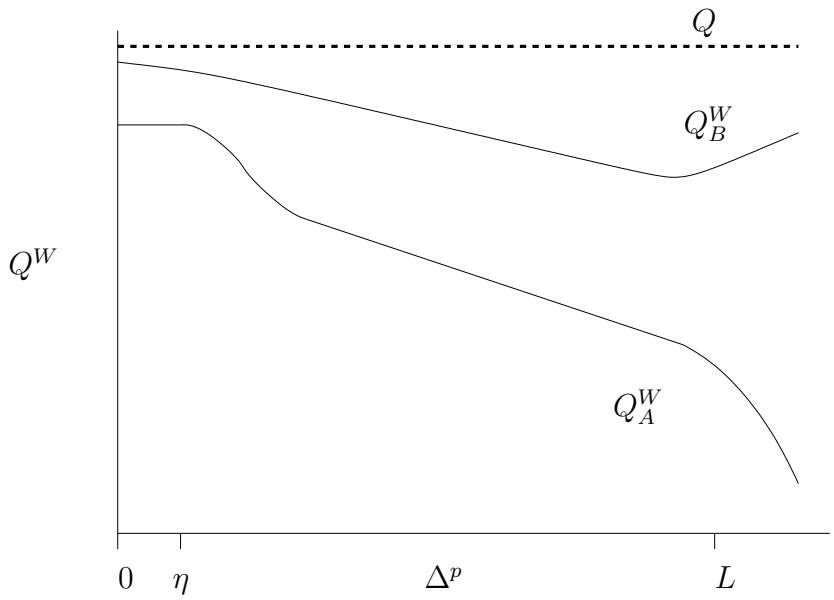

Figure 2.4: Schematic illustration of the proposed approach to *a posteriori* testing. The statistic computed from LES field, Q^W is compared with the statistic obtained from the unfiltered DNS field, Q.

models is *a priori* testing [McMillan & Ferziger (1979); Clark *et al.* (1979)]. An *a priori* test uses experimental or DNS data to directly measure the accuracy of a modeling assumption used in the sub-grid models. Pope ($2000d$) argues that such tests are inherently flawed because a given filtered velocity field can correspond to infinitely many unfiltered turbulent velocity fields. Further, researchers have noted that *a priori* tests are inadequate because most sub-grid models perform poorly on such tests [Langford & Moser (1999); Liu *et al.* (1994)]. The optimal LES formulation of Langford & Moser (1999) clarifies some of these issues, but again proposes a test in which most sub-grid models perform poorly.

2.4 The convergence of LES for very high Re flows

Comparison with statistics from the unfiltered DNS fields allows us to develop a notion of convergence with resolution length scale for LES of very high Re flow which is independent of the filter width. This convergence notion reinforces the criteria suggested in the earlier section for comparing the various sub-grid models.

As mentioned earlier, taking the filtering approach too literally leads to unnecessary expectations from the LES sub-grid model. One such expectation is to require the statistics obtained from an LES performed at a specified, finite resolution length scale to match with the statistics of the filtered DNS fields. Such an expectation is unnecessary because the only relevant statistics are those from the unfiltered DNS fields. This expectation further confuses the definition of convergence of LES as the resolution length scale is decreased because it requires the LES to converge to a different statistic at each resolution length scale.

We can develop a clear notion of convergence of LES with resolution length scale by recognizing that the only relevant statistics are those from the unfiltered DNS fields, and we want the statistics obtained from LES to converge to these statistics as the resolution length scale, Δ, is reduced to zero. Different sub-grid models would have different convergence characteristics. So, in order to determine the convergence of an LES approach performed using a specified sub-grid model, we need to answer the following questions:

- Does the statistic obtained from the LES field, Q^W, converge as $\Delta/l_0 \to 0$ while $\Delta \gg \eta$?
- Does Q^W converge to the statistic from the unfiltered DNS fields, Q?

where,

Δ - Resolution length scale or filter width used in LES

l_0 - Length scale representing the size of the largest eddies in the turbulent flow.

η - Kolmogorov length scale representing the size of the smallest eddies in the turbulent flow.

The above questions provide a notion of convergence for LES of very high Re flows. At high Re, the length scales of the largest eddies l_0 and smallest eddies η differ by a wide range. One is interested in how the statistics obtained from the LES field vary when more and more of the motions in the turbulent flow are numerically resolved in the LES. This is expressed by the limit, $\Delta/l_0 \to 0$. However this limit needs to be attained while there are significant unresolved motions as resolving all the turbulent motions, i.e. when $\Delta \approx \eta$, removes the computational advantage of LES over DNS. So we include the condition, $\Delta \gg \eta$. Strictly speaking, both these conditions can be satisfied only when $\eta/l_0 \to 0$ which occurs only when $Re \to \infty$. However, it is easy to extend these ideas to high Re turbulent flows by relaxing the mathematical rigor of the limiting process and simply requiring $l_0 \gg \Delta \gg \eta$. Finally, by requiring the statistic to converge to the statistics from the unfiltered DNS fields Q, we have a notion of convergence which is independent of the filter width or resolution length scale Δ.

The convergence behaviour depends on the sub-grid model used in the LES approach and is likely to vary from one turbulent flow to another. In this thesis, we investigate the convergence of three eddy-viscosity based sub-grid models for isotropic turbulence and for the temporal mixing layer. The convergence of averaged turbulent kinetic energy with resolution length scale is investigated. Figure 2.4 schematically illustrates this concept of convergence for LES using two

different sub-grid models A and B.

This notion of convergence also allows us to compare two different LES approaches which differ in the sub-grid model being used. So if there is a set of convergent LES approaches differing in the sub-grid model being used,

- Do the statistics obtained from the two different LES approaches converge to the same value?
- If they converge to the same value, how rapidly do they converge to this value?

Answers to these questions allows us to compare sub-grid models and choose the better one for a class of turbulent flows. Figure 2.4 clearly illustrates that sub-grid model B is better than A when subject to the above questions.

Currently, such studies of convergence with resolution length scale are rarely presented in papers comparing sub-grid models. Most comparisons of sub-grid model performance are made at a specified resolution length scale. Comparisons made at a specified resolution length scale cannot provide useful information on how the sub-grid model behaves when the resolution length scale is modified. In this work, we compare sub-grid models for isotropic turbulence and the temporal mixing layer by studying the variation of statistics with resolution length scale. Again, the average turbulent kinetic energy was the statistic used for comparing sub-grid models.

2.5 Issue 2: Accuracy of LES

The second issue with the current LES methodology is that there are no procedures to assess the accuracy of the LES solution. Such assessments of accuracy must be

an inherent part of the LES framework and should not require comparisons with DNS. Many times the poor performance of a given sub-grid model in a particular turbulent flow can be attributed to not resolving the required large eddies. The resolution length scale needs to be in the inertial sub-range, and sufficiently small, for LES to provide good estimates of the required statistics. But to determine whether the resolution length scale Δ is small enough to achieve a given error tolerance is hard to answer under the current LES framework.

This assessment is difficult because current LES methods carry little or no information on the unresolved eddies. As illustrated in Fig. 2.5, with no information about the kinetic energy in the unresolved motions it is hard to determine whether the resolution length scale is small enough to be in the inertial sub-range. A large resolution length scale Δ' leads to poor estimates of statistics from the LES field. On the other hand, the resolution length scale Δ'' may be smaller than necessary for required accuracy, leading to increased computational cost.

One solution to this problem is to model the statistics of the unresolved eddies. Any statistic Q of the underlying turbulent motions $\mathbf{U}(\mathbf{x}, t)$ can be modeled as consisting of 2 parts,

$$Q \stackrel{M}{=} \text{Resolved } (Q^W) + \text{Modeled Residual } (Q^R) \tag{2.4}$$

where

Q^W - Same statistic computed using the LES field, $\mathbf{W}(\mathbf{x}, t)$

Q^R - Model for the contribution to the statistic Q from the unresolved small eddies.

Figure 2.6 illustrates the advantages of modeling Q as the sum of two parts. The advantages of such modeling is two-fold:

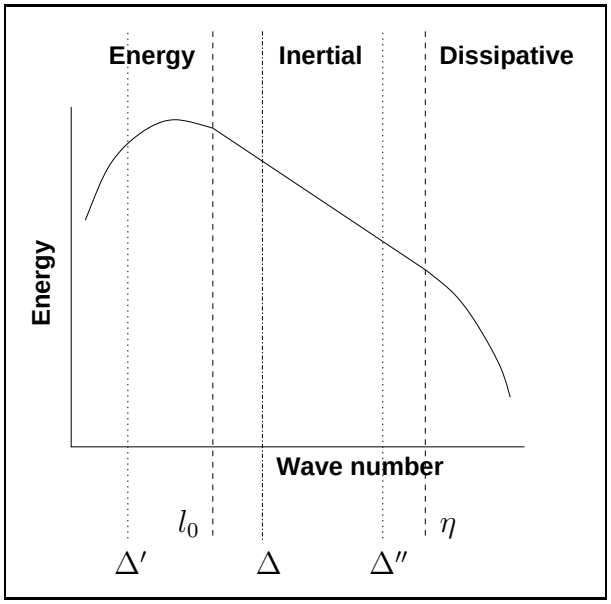

Figure 2.5: Choice of resolution length scale based on required error tolerance. Large resolution length scale Δ' leads to poor estimates of statistics from the LES field. Small resolution length scale Δ'' leads to increased computational cost.

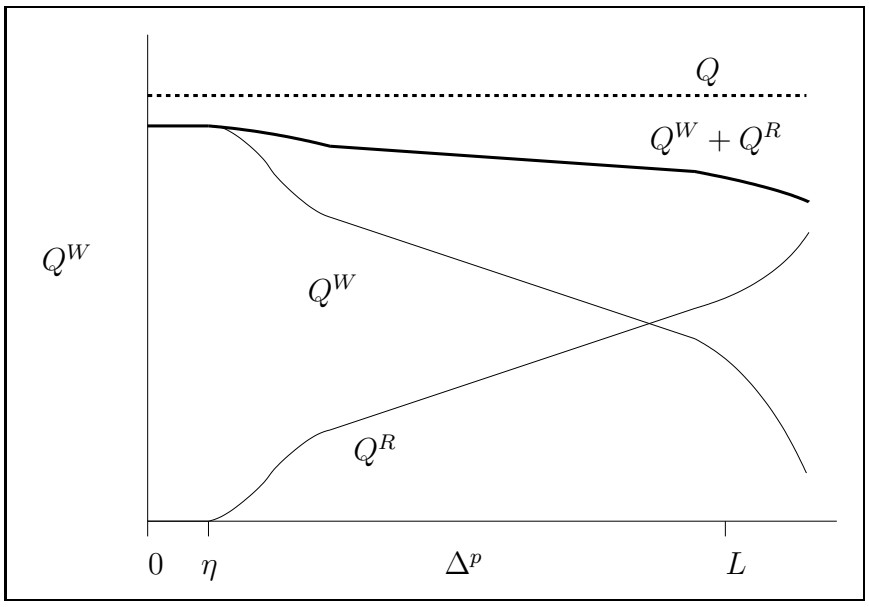

Figure 2.6: Statistic Q of the turbulent flow is modeled as the sum of the same statistic computed from the LES field Q^W and a model for the contribution from the unresolved small eddies Q^R.

- We have a better estimate for the statistic, Q, at lower computational cost because $Q^W + Q^R$ should be closer to Q than Q^W at any given resolution length scale Δ.

- Since we model Q^R we have a measure of the fraction of motions resolved in the LES without comparison to DNS. This can be used in estimating error in the computed statistic and for determining whether the resolution length scale is sufficiently small.

These ideas were implemented for the flow problems of isotropic turbulence and the temporal mixing layer. Since kinetic energy was the main statistic studied, we required models for the kinetic energy in the unresolved eddies. We describe in the next section two sub-grid models which include a specification for the kinetic energy in the unresolved eddies.

2.5.1 Sub-grid models with specifications for kinetic energy in the unresolved eddies

Residual kinetic energy k_R represents the kinetic energy (KE) in the residual, or unresolved, eddies. Eddy-viscosity models using the resolution length scale Δ to provide a length scale and the residual KE k_R to provide a velocity scale have been developed in the literature [Deardorff (1980); Ghosal *et al.* (1995)]. The above specification is complete when we specify a model for the residual KE, k_R. Again, different models for k_R correspond to different sub-grid models. In this section we first describe the sub-grid models using the residual KE and then describe the development of model equations for the residual KE starting from its exact evolution equation. We end the section with details on how such models for k_R

can further be used in LES to provide better estimates of the turbulent KE.

The filtering approach allows us to provide mathematical definitions for the quantities of interest and to derive the exact evolution equations for them. So we use the filtering approach to define and develop models for the residual k_R. In the filtering approach, the residual stress is given by

$$\tau_{ij}^R \equiv \overline{U_i U_j} - \overline{U}_i \overline{U}_j \tag{2.5}$$

where $\overline{\bullet}$ denotes the spatial filtering operation. The residual kinetic energy k_R is defined [Pope $(2000d)$] to be half the trace of the residual stress tensor τ_{ij}^R

$$k_R \equiv \frac{1}{2}\tau_{ii}^R \tag{2.6}$$

We decompose the residual stress tensor, τ_{ij}^R, into an isotropic part given by the residual KE, k_R, and an anisotropic part which is modeled using the eddy-viscosity hypothesis

$$\tau_{ij}^R \overset{M}{=} \frac{2}{3}k_R\delta_{ij} - 2\nu_r\overline{S}_{ij} \tag{2.7}$$

where $\overline{S}_{ij}$ is the filtered rate of strain,

$$\overline{S}_{ij} \equiv \frac{1}{2}\left(\frac{\partial \overline{U}_i}{\partial x_j} + \frac{\partial \overline{U}_j}{\partial x_i}\right) \tag{2.8}$$

Next, the eddy viscosity is modeled using the resolution length scale Δ to provide a length scale and the residual KE k_R to provide a velocity scale,

$$\nu_r = C_\nu \Delta k_R^{\frac{1}{2}} \tag{2.9}$$

where C_ν is a dimensionless model parameter which needs to be specified.

Finally, we specify a model for k_R to close the set of equations. The starting point for deriving such models is the evolution equation for the residual KE

[Germano (1992)] given by,

$$\begin{aligned}\frac{\overline{D}k_R}{\overline{D}t} &\equiv \frac{\partial k_R}{\partial t} + \overline{U}_k \frac{\partial k_R}{\partial x_k} \\ &= -\frac{\partial}{\partial x_k}\left\{T_k^{(u)} + T_k^{(p')} + T_k^{(\nu)}\right\} + \mathcal{P}_R - \epsilon_R\end{aligned} \tag{2.10}$$

where

$T_k^{(u)}$ - Turbulent transport of k_R, $\frac{1}{2}\tau\left(U_i, U_i, U_k\right)$

$T_k^{(p')}$ - Pressure transport of k_R, $\tau\left(p, U_k\right)$

$T_k^{(\nu)}$ - Viscous transport of k_R, $-\nu\frac{\partial k_R}{\partial x_k}$

$\mathcal{P}_R$ - Local production of k_R, $-\tau\left(U_i, U_k\right)\overline{S}_{ik}$

ϵ_R - Local viscous dissipation of k_R, $\nu\tau\left(\frac{\partial U_i}{\partial x_k}, \frac{\partial U_i}{\partial x_k}\right)$

In the above equations, we have used Germano's notation [Germano (1992)] for the generalized central moments,

$$\tau\left(f, g\right) \equiv \overline{fg} - \overline{f}\,\overline{g} \tag{2.11}$$

$$\tau\left(f, g, h\right) \equiv \overline{fgh} - \overline{f}\tau\left(g, h\right) - \overline{g}\tau\left(h, f\right) - \overline{h}\tau\left(f, g\right) - \overline{f}\,\overline{g}\,\overline{h} \tag{2.12}$$

The convective term and the viscous transport term in the above evolution equation are fully determined or in closed form. Given the sub-grid model for the residual stress Eq. (2.7), the production term $\mathcal{P}_R$ is also in closed form. The remaining transport terms and the viscous dissipation term are not in closed form and need to be modeled. The following two model equations were used for k_R,

1. **Smagorinsky Model:** We obtain an algebraic equation for k_R by assuming a local balance of production and dissipation of k_R,

$$\mathcal{P}_R = \epsilon_R \tag{2.13}$$

The production, using the sub-grid model for the residual stress Eq. (2.7), is given by

$$\mathcal{P}_R = \nu_r \left(2\overline{S}_{ij}\overline{S}_{ij}\right) \tag{2.14}$$

Since the dissipation is not in closed form, it is modeled using

$$\epsilon_R \stackrel{M}{=} \frac{C_E k_R^{3/2}}{\Delta} \tag{2.15}$$

where C_E is another dimensionless model parameter which needs to be specified. Substituting Eqs. (2.14), (2.9), and (2.15) into Eq. (2.13) and simplifying for residual KE k_R, we have

$$k_R = \frac{C_\nu}{C_E}\Delta^2 \left(2\overline{S}_{ij}\overline{S}_{ij}\right) \tag{2.16}$$

Substituting the above algebraic model for k_R into Eq. (2.9), we have

$$\nu_r = \frac{C_\nu^{3/2}}{C_E^{1/2}}\Delta^2 \left(2\overline{S}_{ij}\overline{S}_{ij}\right)^{1/2} \tag{2.17}$$

Equation (2.17) is equivalent to the Smagorinsky model [Lilly (1967)] for the sub-grid stresses, but here we also have a model for the residual KE, Eq. (2.16).

2. **Model k_R equation:** Here, we solve a modeled transport equation for k_R by modeling the transport terms in Eq. (2.10) as,

$$\left\{T_k^{(u)} + T_k^{(p')} + T_k^{(\nu)}\right\} \stackrel{M}{=} -\frac{\nu_r}{\sigma_k}\frac{\partial k_R}{\partial x_k} \tag{2.18}$$

where σ_k is a model parameter which serves as a turbulent Prandtl number for the residual KE.

The local production and dissipation of k_R are the same as that given in Eqs. (2.14) and (2.15), respectively. This results in the following differential

equation for k_R,

$$\frac{\partial k_R}{\partial t} + \overline{U}_k \frac{\partial k_R}{\partial x_k} = \frac{\partial}{\partial x_k}\left\{\nu_r \frac{\partial k_R}{\partial x_k}\right\} + \mathcal{P}_R - \epsilon_R \tag{2.19}$$

The residual KE k_R is positive for positive filters [Vreman *et al.* (1994)]. So the numerical scheme used to advance the model k_R equation (2.19) ensures that k_R remains positive at all points in space and time.

We end this section with a small note on interpreting the filtering approach. Since the filtered velocity field $\overline{U}_i$ represents the resolved LES field W_i, we make the following substitutions,

$$\overline{U}_i \rightarrow W_i \tag{2.20}$$

$$\overline{S}_{ij} \rightarrow S^W_{ij} \tag{2.21}$$

The above two model equations for k_R results in two different sub-grid models for LES that are used to study the ideas of convergence and error estimation were studied.

2.6 Issue 3: Choice of LES Model Parameters

The final issue with the LES methodology is the appropriate choice of values for the various model parameters such as C_ν (Eq. (2.9)) and C_E (Eq. (2.15)) which occur in the sub-grid models based on k_R. In this section, we explain the procedure developed for choosing these model parameters using the statistic of averaged turbulent kinetic energy as an example.

The total kinetic energy has contributions from both the resolved motions W_i and the unresolved motions. The KE computed from the LES field or resolved motions is called the resolved KE. The residual KE $\langle k_R \rangle$ represents the contribution

from the unresolved motions and is computed using one of the models described in the earlier section. It can be argued [Lilly (1967); Pope (2000d)] that the residual KE and resolved KE vary as $\Delta^{2/3}$ to leading order in Δ. Hence a good model for the residual KE varies to leading order as $\Delta^{2/3}$ and converges to zero at $\Delta = 0$ as there are no unresolved motions. Similarly, the resolved KE also varies to leading order as $\Delta^{2/3}$ and converges to some value k^0 which represents the kinetic energy of the underlying turbulent flow. Since the total kinetic energy is modeled as the sum of the resolved and residual KE, it has a similar leading order variation and converges to the same asymptote, k^0 at $\Delta = 0$. Thus, we can write

$$\text{Resolved KE} = k^0 - \qquad a(\Delta)^{2/3} + \ldots \tag{2.22}$$

$$\text{Residual KE} = \qquad\qquad c(\Delta)^{2/3} + \ldots \tag{2.23}$$

$$\text{Total KE} = k^0 + (c-a)(\Delta)^{2/3} + \ldots \tag{2.24}$$

Values of a and c depend on the values chosen for the model parameters C_ν and C_E. These slopes, a and c, can be determined from numerical simulations carried out at different resolution length scales Δ using the specified values for the model parameters.

The goal of an LES is to estimate a value as close as possible to k^0 for the total KE while performing the LES at a finite resolution length scale, Δ. We can achieve this goal by choosing C_ν and C_E such that *the leading order Δ term in the total KE vanishes*, i.e., $(c-a) = 0$. This is a good choice for the model parameters because the estimate for the total KE should be close to k^0 even while performing the LES at a finite Δ.

It must be mentioned here that the dynamic procedure [Germano *et al.* (1991)] has widely been used in LES to choose such model parameters. It was argued in

Pope (2004) that the above argument to remove the leading order variation with resolution length scale Δ in the estimate for the statistic of interest is probably the same reason as to why the dynamic procedure works well in practice. In Pope's argument, the statistic of interest was the turbulent stresses.

In this chapter we have described in detail the issues with the current LES methodology and how we addressed these issues. In chapters 3 and 4 we will address the problem of developing and implementing an efficient numerical algorithm for carrying out LES.

Chapter 3

Numerical Algorithm

The governing equations for LES using linear eddy-viscosity based sub-grid models are similar in form to the incompressible NS equations. In this chapter, we will start with a brief discussion of the solution methods for incompressible NS equations and indicate why the fractional step method is superior for time-accurate calculations. The problem of poor time accuracy with fractional step methods is overcome by developing an iterative fractional step scheme. Stretched Cartesian grid formulation needed to efficiently solve problems such as the mixing layer are then developed. Energy conserving discretization for the convective terms which are believed to improve the robustness of the solver have also been incorporated. The pressure Poisson equation to be solved at each time-step to satisfy continuity is derived and the approximation carried out to reduce the stencil size is described lastly.

3.1 Solution Techniques for incompressible NS

The governing equations for LES of incompressible flows using linear eddy-viscosity based sub-grid models, Eqs. (3.1)-(3.2), are similar in form to the incompressible NS equations.

$$\frac{\partial W_i}{\partial t} + \frac{\partial \left(W_i W_j\right)}{\partial x_j} = -\frac{\partial p}{\partial x_i} + \frac{\partial}{\partial x_j}\left(2\nu S_{ij}^W\right) + \frac{\partial}{\partial x_j}\left(2\nu_r S_{ij}^W\right) \tag{3.1}$$

$$\frac{\partial W_i}{\partial x_i} = 0 \tag{3.2}$$

So the vast literature on numerical algorithms for incompressible flows provides a good starting point for the development of an efficient LES solver. We start with

a brief overview of algorithms used to solve the incompressible NS. Although, a large number of approaches have been developed in the past few decades, we focus here on those approaches which solve for the primitive flow variables, namely the velocity, W_i and pressure, p. More complete reviews can be found in Tannehill *et al.* (1997*a*); Langtangen *et al.* (2002); Gresho (1991).

Physically, incompressible NS equations and the LES equations are characterized by the elliptic behavior of the pressure waves, the speed of which is infinite. This gives rise to a mixed system of elliptic-parabolic equations for the unknowns, velocity W_i and pressure p. The approaches which solve directly for these unknowns are called primitive-variable approaches and can be grouped into two broad categories.

1. **Artificial compressibility approach:** In this approach, artificial-time derivatives are introduced into the governing equations to make them a hyperbolic-parabolic system of equations in artificial-time. The speed of the pressure waves in artificial-time is made finite by introducing an artificial-time derivative of the pressure in the continuity equation.

$$\frac{1}{\beta}\frac{\partial p}{\partial \tau} + \frac{\partial W_i}{\partial x_i} = 0 \tag{3.3}$$

where β is an artificial compressibility parameter and τ is the artificial-time. The speed of propagation of the pressure waves in artificial-time depends on the magnitude of the artificial compressibility parameter, β. The momentum equations are also modified by introducing an artificial-time derivative term as shown below,

$$\frac{\partial W_i}{\partial \tau} + \frac{\partial W_i}{\partial t} + \frac{\partial \left(W_i W_j\right)}{\partial x_j} = -\frac{\partial p}{\partial x_i} + \frac{\partial}{\partial x_j}\left(2\nu S_{ij}^W\right) + \frac{\partial}{\partial x_j}\left(2\nu_r S_{ij}^W\right) \tag{3.4}$$

Please note that in order to obtain the solutions at each physical time t, we have to advance the equations in artificial-time, τ until we reach a steady-state in τ.

This method was originally developed by Chorin (1967) and since then a number of variants [Steger & Kutler (1976); Choi & Merkle (1985); Kwak *et al.* (1986)] have been developed for many impressive applications.

2. **Pressure Projection Approach:** In this approach, the pressure is simply considered as a Lagrange multiplier used to make the velocity field satisfy the divergence-free constraint. The general formulation consists of a sequence of steps for the solution of velocity and pressure at each time-level. In the first step, the momentum equations are solved for the velocity components using the best available estimate for the pressure distribution. Such a procedure will not yield a divergence-free velocity field unless the correct pressure distribution is employed. So in the second step the pressure distribution is improved, usually by solving a pressure Poisson equation, such that the computed pressure field will cause the velocity field to become divergence-free. Since a change in pressure would affect the solution of the momentum equations, the above sequence of steps is repeated until a divergence-free velocity field is obtained.

   The first primitive variable method using this approach was the marker-and-cell (MAC) method of Harlow & Welch (1965). Since then a number of variants of this approach, differing primarily in the algorithms used to solve the momentum equations, the strategies employed to develop an improved pressure field and how this pressure field could be used to update the velocity

field, have been developed. Some of the commonly used variants are the SIMPLE and SIMPLER methods [Patankar (1980, 1975)], the fractional-step method [Chorin (1968); Yanenko (1971); Kim & Moin (1985)] and the primitive-variable implicit split operator method [Issa *et al.* (1986)].

Many authors have compared the relative efficiency and advantages of the different approaches. The general conclusion is that for time-accurate solutions the pressure projection approach using the fractional-step method is around 3 times faster than the artificial compressibility approach [Kwak *et al.* (1998)]. This is because in the artificial compressibility approach, at each time-step, we need to advance the equations in artificial-time until the steady-state between the pressure and velocity fields is reached. But in the fractional step method the sub-iteration in artificial-time is replaced by the solution of a single pressure Poisson equation. This significantly reduces the computational expense of fractional step method for unsteady problems but degrades the temporal accuracy of the method to first-order. Also, for problems in which one is interested only in the steady-state, the artificial-compressibility approach could be advantageous. Preliminary investigations by us, comparing the two methods for two-dimensional incompressible flows, also resulted in similar conclusions.

Since we are interested in time-accurate solutions we decided to use the the fractional step method for our LES solver. In the next section, I will discuss in more detail the iterative fractional step method developed to achieve second-order temporal accuracy.

3.2 Iterative fractional-step method

The iterative fractional-step method developed here is an improvement of the fractional-step method used by Kim & Moin (1985). We start with a temporally second-order discretization of the governing LES equations and highlight the numerical difficulty posed in solving these equations such that the divergence-free velocity constraint is satisfied. A block-matrix-based analysis procedure, similar to that developed by Perot (1993), is used to develop an iterative scheme to solve these discretized equations. The temporal order of accuracy is determined by the number of iterations carried out in the iterative fractional step procedure. If we perform only a single iteration then the method becomes first-order accurate. However if we perform more than 1 iteration we can achieve second-order temporal accuracy. We present a proof of the above statements. It must be mentioned that there have been other attempts to develop higher-order fractional step methods by either modifying the boundary conditions used [Kim & Moin (1985); Orszag *et al.* (1986)] or by modifying the discretized equations being solved [Perot (1993)] or by developing higher-order splitting schemes [Dukowicz & Dvinsky (1992); Karniadakis (1991)].

3.2.1 Temporally second-order discretization

A temporally second-order accurate discretization of the governing LES equations (Eqs. (3.1)-(3.2)) is shown below in Eqs. (3.5)-(3.6).

$$\frac{W_i^{n+1} - W_i^n}{\Delta t} = \underbrace{\left[\frac{3}{2} H_i\left\{\mathbf{W^n}, \mathbf{F^n}\right\} - \frac{1}{2} H_i\left\{\mathbf{W^{n-1}}, \mathbf{F^{n-1}}\right\}\right]}_{\text{Convective, Adams-Bashforth}} - \underbrace{G_i\left\{p^{n+1}\right\}}_{\text{Pressure gradient}} + \underbrace{\frac{1}{2}\left[D_2\left\{W_i^{n+1}; \nu, \nu_r^{n+1}\right\} + D_2\left\{W_i^n; \nu, \nu_r^n\right\}\right]}_{\text{Sub-grid + Viscous Dissipation, Crank-Nicolson}} \tag{3.5}$$

$$\underbrace{C\left\{\mathbf{W^{n+1}}\right\} = 0}_{\text{Continuity}} \tag{3.6}$$

where,

$\bullet^n$ - Superscripts denote the time-level

$\mathbf{W^n}$ - Velocity field at time-level n

p^n - Pressure field at time-level n

$\mathbf{F^n}$ - Volume flux through the appropriate cell faces at time-level n

$H_i\left\{\mathbf{W}, \mathbf{F}\right\}$ - Spatial discretization of the convective term, $\frac{\partial(W_i W_j)}{\partial x_i}$ computed using the given velocity field $\mathbf{W}$ and volume flux $\mathbf{F}$

$G_i\left\{p\right\}$ - Spatial discretization of the pressure gradient, $\frac{\partial p}{\partial x_i}$

$D_2\left\{W_i; \nu, \nu_r^{n+1}\right\}$ - Spatial discretization of the viscous and the linear eddy-viscosity sub-grid model terms $\frac{\partial}{\partial x_j}\left[2\left(\nu + \nu_r\right) S_{ij}^W\right]$

$C\left\{\mathbf{W^{n+1}}\right\}$ - Spatial discretization of the continuity/ divergence operator, $\frac{\partial W_i}{\partial x_i}$

The convective terms are discretized explicitly in time using the Adams-Bashforth scheme. Although this imposes a Courant-Friedrichs-Lewy (CFL) condition on the time-step based on stability considerations, such a condition is not restrictive because time-accurate evolution requires us to take a time-step with CFL of order one. Also, the numerical scheme used for the convective terms in the modeled residual kinetic energy equation imposes a more stringent CFL criterion on the time-step. The viscous terms and sub-grid stresses are treated implicitly using the Crank-Nicholson scheme which makes them unconditionally stable. We make the following comments on this discretization.

1. We have not specified the spatial discretization used making the analysis valid for all spatial discretization.

2. The choice of Adams-Bashforth for the convective terms and Crank-Nicholson for the viscous terms is very common [Kim & Moin (1985); Zang *et al.* (1994)]. The time-step constraint due to the CFL condition is proportional to Δx while that due to the Fourier condition is proportional to $(\Delta x)^2$. Hence in regions of grid refinement the Fourier condition introduced by an explicit treatment of the viscous terms becomes more restrictive than the CFL constraint introduced by the convective terms.

3. Since the nonlinear convective terms are treated explicitly and the linear viscous and sub-grid stress terms are treated implicitly, at each time-step, we need to solve an implicit system of equations subject to linear constraints arising from the discretization of the continuity equation. It is these constraints imposed by the discrete continuity equation which makes this system of equations hard to solve. Without these linear constraints, it should

be fairly easy to develop a numerical scheme to solve this implicit system.

4. The dependence of the eddy-viscosity on the velocity fields introduces a slight non-linearity into the implicit equations apart from which these equations are essentially linear.

The iterative fractional-step method solves this implicit system without loss of numerical accuracy and efficiency. We first rewrite the discretized equations in block-matrix form. This allows us to develop an iterative solution scheme for solving these equations and to study the effect of boundaries and boundary conditions. Use of an iterative scheme gets rid of the need to apply artificial boundary conditions on the provisional velocities to achieve second-order temporal accuracy. Once the iterative scheme is developed we show that 2 iterations are sufficient to reduce the iterative error introduced by carrying out finite number of iterations to the same order as the discretization error.

3.2.2 Iterative procedure and Block-Matrix Analysis

The use of the block-matrix form to analyze the discretized equations was first introduced by Perot [Perot (1993)]. He used this analysis to bring out the analogy between the fractional step method and the block-LU factorization of a temporally first-order accurate discretization of the governing equations. This allowed him to not only prove that the fractional step method was first-order accurate but also develop a second-order accurate fractional step method.

Here, we start with the block-matrix representation of the temporally second-order accurate discretization, Eqs. (3.5)-(3.6), and note that it is hard to invert this system. We then replace this block-matrix with another which is easy to invert.

In order to converge to the solution of the original set of discretized equations we design an iterative scheme in which at each iteration we need only to invert this new block-matrix. Finally we show that the iteration error introduced by carrying out greater than 2 but finite number of iterations is lower than the numerical discretization error.

In order to bring out the fact that we are solving for the unknowns, $\mathbf{W^{n+1}}$ and p^{n+1}, Eqs. (3.5)-(3.6) can be written as,

$$\left\{\frac{I}{\Delta t} - \frac{1}{2}D2\left\{;\nu^{n+1},\nu_r^{n+1}\right\}\right\}W_i^{n+1} + G_i\left\{p^{n+1}\right\} = \left[\frac{3}{2}H_i\left\{\mathbf{W^n},\mathbf{F^n}\right\} - \frac{1}{2}H_i\left\{\mathbf{W^{n-1}},\mathbf{F^{n-1}}\right\}\right] + \left\{\frac{I}{\Delta t} + \frac{1}{2}D2\left\{;\nu^{n},\nu_r^{n}\right\}\right\}W_i^{n} + \text{BCs} \tag{3.7}$$

$$C\left\{\mathbf{W^{n+1}}\right\} = 0 \tag{3.8}$$

Please note the following:

- None of the terms which appear on the right hand side (RHS) depend on the unknowns, $\mathbf{W^{n+1}}$ and p^{n+1}. Hence they are source terms for the equations which can be determined at the start of the time-step.

- The boundary conditions (BCs) are based on $\mathbf{W^{n+1}}$ and not on the provisional velocities which appear in the middle of the fractional step. The BCs are an implicit part of the spatial discretization operators and also appear partly as source terms in the RHS. As mentioned earlier, researchers have developed schemes which modify the velocity boundary conditions so as to apply them on the provisional velocities and achieve second-order temporal accuracy. Our scheme does not require these modifications.

Eqs. (3.7)-(3.8) can now be written in block-matrix form, Eq. (3.9), to develop the

iterative scheme.

$$\begin{bmatrix} A & G \\ C & 0 \end{bmatrix} \begin{bmatrix} \mathbf{W^{n+1}} \\ p^{n+1} \end{bmatrix} = \begin{bmatrix} s + \text{BCs} \\ 0 + \text{BCs} \end{bmatrix} \tag{3.9}$$

where,

$$\begin{aligned} \mathbf{W} &\equiv \begin{bmatrix} W_1 \\ W_2 \\ W_3 \end{bmatrix} \\ G &\equiv \begin{bmatrix} G_1 \\ G_2 \\ G_3 \end{bmatrix} \\ A &\equiv \left(\frac{I}{\Delta t} - \frac{1}{2} L\left\{ ; \nu^{n+1}, \nu_r^{n+1} \right\} \right) \\ L\left\{ ; \nu, \nu_r \right\} &\equiv \begin{bmatrix} D2\{;\nu,\nu_r\} & 0 & 0 \\ 0 & D2\{;\nu,\nu_r\} & 0 \\ 0 & 0 & D2\{;\nu,\nu_r\} \end{bmatrix} \\ s &\equiv \text{Source Terms} \end{aligned}$$

Eq. (3.9) is easily seen to be of the form,

$$Px = b$$

Since P is hard to invert directly we developed an iterative procedure where P is replaced by a matrix M which is easier to invert. At the m^{th} iteration we solve,

$$M\delta x^{[m]} = b - Px^{[m-1]} \tag{3.10}$$

where we obtain a better estimate for the solution, $x^{[m]} = x^{[m-1]} + \delta x^{[m]}$, by using the residual of the earlier estimate, $b - Px^{[m-1]}$. More details on the convergence and stability of such iterative schemes can found in Golub & Loan (1996).

We require M to have the following properties,

- M should be *easy to invert*.
- M should be *close to* P so that the iterative procedure converges in a few (2 or 3) iterations.

M is obtained by making the following 2 approximations to P.

$$P = \begin{bmatrix} A & G \\ C & 0 \end{bmatrix} \xrightarrow[\text{approx.}]{} M \equiv \begin{bmatrix} \mathbf{\hat{A}} & \mathbf{\Delta t \hat{A} } G \\ C & 0 \end{bmatrix} \tag{3.11}$$

- A **is replaced by** $\hat{A}$:

  The inversion of M requires the inversion of A as will be seen later. Since it is hard to invert A directly we invert A using a *finite* number of iterations of an *iterative scheme*. So we have sub-iterations to invert A within each iteration of the iterative fractional step method. Since we carry out only a finite number of sub-iterations we introduce another iterative error which can be viewed as exactly inverting a nearby matrix, $\hat{A}$. The exact form of $\hat{A}$ depends on the sub-iterations used and the number of sub-iterations. Details on the sub-iteration to invert A are given later.

  Note that A is dominated by $\frac{I}{\Delta t}$ for small Δt. Hence A is of order, $O\left(\frac{1}{\Delta t}\right)$ and the sub-iteration is chosen such that $A - \hat{A}$ is of order, $O\left(1\right)$.

- G **is replaced by** $\Delta t \hat{A} G$:

  This is a clever move motivated by the fact that M now has an easy block-LU decomposition. This makes it easier to invert M as compared to P, since it is hard to find a block-LU decomposition for P in closed form.

$$M \equiv \begin{bmatrix} \hat{A} & \Delta t \hat{A} G \\ C & 0 \end{bmatrix} = \begin{bmatrix} \hat{A} & 0 \\ C & -\Delta t C G \end{bmatrix} \begin{bmatrix} I & \Delta t G \\ 0 & I \end{bmatrix} \tag{3.12}$$

  Again note that $\hat{A}$ is dominated by $\frac{I}{\Delta t}$ for small Δt and so $G - \Delta t \hat{A} G$ is of order, $O\left(\Delta t\right)$.

Finally we show that M is close to P. Because P is dominated by the $\frac{I}{\Delta t}$ for

small Δt, it is of order, $O\left(\frac{1}{\Delta t}\right)$.

$$P = \begin{bmatrix} \frac{I}{\Delta t} + \cdots & \cdots \\ \cdots & 0 \end{bmatrix} = O\left(\frac{1}{\Delta t}\right) \tag{3.13}$$

The 2 changes introduced to approximate P with M introduces only an $O(1)$ difference between the 2 matrices.

$$M - P = \begin{bmatrix} \hat{A} - A & \left(\Delta t \hat{A} - I\right) G \\ 0 & 0 \end{bmatrix} = \begin{bmatrix} O(1) & O(\Delta t) \\ 0 & 0 \end{bmatrix} \tag{3.14}$$

Hence, M is not only close to P but also much easier to invert than P. In practice, we carry out only 2-3 iterations to converge to the right solution. Next, we show that the iteration error introduced by carrying out more than 2 but finite number of iterations is smaller than the numerical discretization error of $O(\Delta t^2)$.

We first define the iteration error in the m^{th} iteration to be the residual, $r^{[m]}$, computed using the m^{th} estimate for the solution, $x^{[m]}$.

$$r^{[m]} \equiv b - P x^{[m]} \tag{3.15}$$

Eq. (3.10) can be easily reduced to show that,

$$r^{[m]} = (NM^{-1}) r^{[m-1]} \tag{3.16}$$

where $N \equiv M - P$. Applying the above equation recursively we have,

$$r^{[m]} = (NM^{-1})^m r^{[0]} \tag{3.17}$$

Next, we make order estimates of N, M and $r^{[0]}$ to show that $r^{[m]} = O(\Delta t^m)$. From Eqs. (3.13) and (3.14), we have that $M = O\left(\frac{1}{\Delta t}\right)$ and $N = O(1)$. So (NM^{-1}) is of $O(\Delta t)$. In order to make an estimate of $r^{[0]}$ we need to know $x^{[0]}$. In our implementation we have taken $x^{[0]}$ to be the field values at the previous time-level.

$$x^{[0]} = \begin{bmatrix} \mathbf{W^n} \\ p^n \end{bmatrix} \tag{3.18}$$

So $r^{[0]}$ is of order, $O(1)$. Using the above order estimates and Eq. (3.16), it can be seen that $r^{[m]}$ is of order, $O(\Delta t^m)$. So if we carry out two iterations the iteration error becomes the same order as the numerical discretization error which is $O(\Delta t^2)$. Further, if we perform three iterations the iterative error becomes $O(\Delta t^3)$, but, because the discretization error is $O(\Delta t^2)$, the overall scheme continues to be second-order accurate in time.

3.2.3 Similarity with normal fractional step method

In this subsection, we show that the normal fractional step method is equivalent to carrying out a single iteration of the iterative fractional step. However the iteration error introduced by carrying out a single iteration makes the normal fractional step scheme first-order time accurate.

To see the similarity between the normal and iterative fractional step method we need to see that the sequence of steps used to invert M using its block-LU factorization, Eq. (3.12), is the same as that carried out in the normal fractional step method. The inversion of M carried out at each iteration of the iterative fractional step method is equivalent to the following 3 steps:

1. Solve for a provisional velocity, $\hat{\mathbf{W}}$, using the latest approximation to the pressure, $p^{[m-1]}$.

$$\hat{A}\left(\delta\hat{\mathbf{W}}\right) = s + \text{BCs} - AW^{[m-1]} - Gp^{[m-1]} \tag{3.19}$$

   where the provisional velocity, $\hat{\mathbf{W}} = \mathbf{W}^{[\mathbf{m-1}]} + \delta\hat{\mathbf{W}}$

2. Solve a pressure Poisson equation which computes a pressure correction, $\delta p^{[m]}$, that projects the provisional velocity on to a divergence-free space.

$$CG\left\{\delta p^{[m]}\right\} = \frac{C\left\{\hat{\mathbf{W}}\right\}}{\Delta t} \tag{3.20}$$

3. Correct the provisional velocity using the pressure gradient so that it becomes divergence-free.

$$\mathbf{W}^{[\mathbf{m}]} = \hat{\mathbf{W}} - (\Delta t)\, G\left\{\delta p^{[m]}\right\} \tag{3.21}$$

Since the above 3 steps are the same as that carried out in a normal fractional step method, carrying out 1 iteration of the iterative fractional step and the normal fractional step are equivalent. However, as shown in the earlier subsection, carrying out 1 iteration introduces an iterative error of $O(\Delta t)$ making the normal fractional step only temporally first-order accurate.

3.3 Spatial Discretization

The iterative fractional step method can be coupled with different choices of dependent variables and grid layouts. In this section, I will describe in detail the choice of spatial discretization used in our numerical algorithm. The collocated grid layout which has superior performance on curvilinear grids [Rhie & Chow (1983); Zang *et al.* (1994)] is first described. In order to efficiently solve problems which have concentrated regions of high flow gradients, such as temporal mixing layers, we included the capability of solving on stretched Cartesian grids by mapping the grid onto a uniform computational grid. Next, we discuss the energy-conserving discretization [Morinishi *et al.* (1998)] used for the convective terms. This discretization has been preferred for simulating turbulent flows on account of its stability and accuracy properties. The convective terms in the momentum equation and the divergence operator appearing in the continuity equation were discretized to fourth-order spatial accuracy. The use of such high-order schemes results in a very large stencil for the pressure Poisson equation. A clever method

to reduce the size of the stencil while satisfying the discretized continuity equation to machine precision is presented.

3.3.1 Collocated grid layout

There are a number of different grid layouts which can used for incompressible flows. The more popular ones fall under the framework of either uniform, staggered or collocated grid layouts. Zang *et al.* (1994) has a very nice discussion of the relative advantages and disadvantages of the different formulations along with references to literature using these different methods.

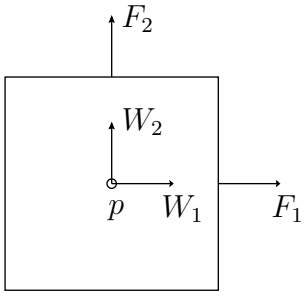

Figure 3.1: Dependent variables and their locations in a collocated grid layout

We used a collocated grid scheme in which one solves for both the Cartesian velocities, W_i and the volume fluxes, F_i. In the collocated grid layout Cartesian velocity components, W_i, are defined at the center while the volume fluxes, F_i, are defined at the mid-point of the corresponding faces of the control volume (/cell) in computational space. This layout is advantageous for curvilinear grids [Zang *et al.* (1994)] because the governing equations remain in a relatively simple form and can be cast in strong conservation form. Further, staggered grid layouts and some non-staggered layouts may require storage of many geometric metrics per cell or complicated interpolation schemes as compared to the collocated grid. While non-staggered grids may require storage of fewer geometric quantities, they have

long had the reputation of producing spurious oscillations in the pressure field [Patankar (1980)]. The collocated grid overcomes this problem by defining volume fluxes at the cell faces to avoid pressure-velocity decoupling. This problem is related to the fact that a straightforward discretization of the continuity equation does not enforce mass conservation in the cell and causes decoupling of the velocity field.Rhie & Chow (1983) were the first to prevent this decoupling by developing the collocated grid layout.

It should be noted that the numerical algorithm was implemented for a special case of curvilinear grids namely stretched Cartesian grids. For such grids a staggered grid layout also works well [Vasilyev (2000)]. However we decided to use the collocated grid layout with the intention of making the code extensible to more complicated curvilinear grids. More details on stretched Cartesian grids and the governing equations are given in the next subsection. Other scalars such as the pressure, p, viscosity, ν, and eddy-viscosity, ν_r, are also stored at the cell-centers.

3.3.2 Stretched Cartesian grids

We were interested in solving problems such as the temporal mixing layer where large flow gradients occur in the region between the 2 streams. Such problems can be efficiently solved using grids which are refined only in the regions of high flow gradients and are widely spaced elsewhere. So we included the capability of solving on stretched Cartesian grids by mapping the stretched physical grid onto a uniform computational grid. Such a method is preferred because it is relatively easy to transform the governing equations to a new coordinate system. In this subsection we present the governing equations for the mapped computational grid in strong conservation form and details on the computation of geometric metrics.

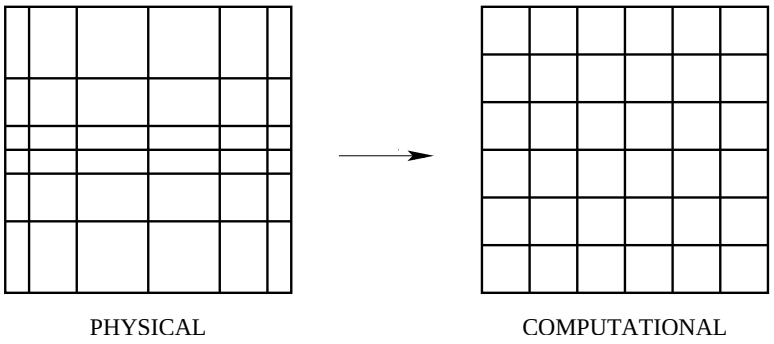

Figure 3.2: Mapping of stretched physical grid to uniform computational grid

Stretched Cartesian grids are grids whose mappings can be written in the form,

$$\xi_i = \xi_i (x_i) \tag{3.22}$$

where,

ξ_i - Coordinates in computational space

x_i - Coordinates in physical space

In other words, the physical grid can be constructed as a product of uni-directional mappings. Fig. (3.2) shows such a mapping of a stretched Cartesian grid onto an uniform computational grid.

The properties of a general curvilinear transformation at any point are contained in the transformation tensor, $\frac{\partial \xi_i}{\partial x_j}$. The determinant of the transformation tensor,

$$J \equiv \det \left(\frac{\partial \xi_i}{\partial x_j} \right) \tag{3.23}$$

is proportional to the ratio of the volumes in the computational and physical space. In the special case of stretched Cartesian grids, the transformation tensor becomes

a diagonal matrix as shown below,

$$\frac{\partial \xi_i}{\partial x_j} = \begin{bmatrix} \frac{\partial \xi_1}{\partial x_1} & 0 & 0 \\ 0 & \frac{\partial \xi_2}{\partial x_2} & 0 \\ 0 & 0 & \frac{\partial \xi_3}{\partial x_3} \end{bmatrix} \tag{3.24}$$

Vinokur [Vinokur (1974)] and Viviand [Viviand (1974)] have shown that the governing equations in the transformed space can be put in strong conservation form. This form is particularly well-suited for coming up with numerical discretizations which are momentum and mass conserving because all the terms in this form appear as divergences of some flux. We give a brief outline of the derivation of the transformed governing equations. More detailed treatments can be found in CFD textbooks [Tannehill *et al.* (1997*b*); Shih & Caughey (1994)]. Much of the derivation is based on the following 2 rules.

1. **Transformation of the divergence of a flux, e_j:** All the terms in the governing equations, Eqs. (3.1)-(3.2)), appear as the divergence of some flux, e_j. For example, velocity flux, $e_j = W_j$ appears in the continuity equation, momentum flux, $e_j = W_j W_i$ and viscous flux, $e_j = 2\nu S_{ij}^W$ appear in the momentum equations and so on. It can be proved that the divergence of a generic flux, $\frac{\partial e_j}{\partial x_j}$ when multiplied by the inverse of the Jacobian, J^{-1} can be rewritten in the conservative form given below.

$$J^{-1}\frac{\partial e_j}{\partial x_j} = \frac{\partial E_m}{\partial \xi_m} = \frac{\partial}{\partial \xi_m}\left(J^{-1}\frac{\partial \xi_m}{\partial x_j} e_j\right) \tag{3.25}$$

   where $E_m = J^{-1}\frac{\partial \xi_m}{\partial x_j} e_j$ can be interpreted as the fluid flux per unit area crossing the surface of constant ξ_m in the computational space.

2. **Chain rule of differentiation:** The other commonly used rule in the

derivation is the chain rule,

$$\frac{\partial(\bullet)}{\partial x_j} = \frac{\partial(\bullet)}{\partial \xi_m}\frac{\partial \xi_m}{\partial x_j} \tag{3.26}$$

The governing equations in the transformed computational space are derived by multiplying Eqs. (3.1)-(3.2)) with J^{-1} and manipulating using the above rules. The divergence term in the continuity equation (3.2) transforms as,

$$J^{-1}\frac{\partial W_j}{\partial x_j} = \frac{\partial F_m}{\partial \xi_m} = \frac{\partial}{\partial \xi_m}\left(J^{-1}\frac{\partial \xi_m}{\partial x_j}W_j\right) \tag{3.27}$$

where $F_m = J^{-1}\frac{\partial \xi_m}{\partial x_j}W_j$ is the volume flux per unit area crossing the surface of constant ξ_m in the transformed space. Similarly, the terms in the momentum equations transform as,

$$J^{-1}\frac{\partial\left(W_j W_i\right)}{\partial x_j} = \frac{\partial\left(F_m W_i\right)}{\partial \xi_m} \tag{3.28}$$

$$J^{-1}\frac{\partial p}{\partial x_i} = \frac{\partial}{\partial \xi_m}\left(J^{-1}\frac{\partial \xi_m}{\partial x_i}p\right) \tag{3.29}$$

$$J^{-1}\frac{\partial}{\partial x_j}\left(2\nu S_{ij}^W\right) = \frac{\partial}{\partial \xi_m}\left[J^{-1}\frac{\partial \xi_m}{\partial x_i}\nu\left\{\frac{\partial W_i}{\partial \xi_l}\frac{\partial \xi_l}{\partial x_j} + \frac{\partial W_j}{\partial \xi_n}\frac{\partial \xi_n}{\partial x_i}\right\}\right] \tag{3.30}$$

Hence, the conservation equations to be solved in the transformed computational space are given in strong conservation form below.

$$\begin{aligned}\frac{\partial\left(J^{-1}W_i\right)}{\partial t} + \frac{\partial\left(F_m W_i\right)}{\partial \xi_m} =& -\frac{\partial}{\partial \xi_m}\left(J^{-1}\frac{\partial \xi_m}{\partial x_i}p\right) \\ &+ \frac{\partial}{\partial \xi_m}\left[J^{-1}\frac{\partial \xi_m}{\partial x_i}\left(\nu+\nu_r\right)\left\{\frac{\partial W_i}{\partial \xi_l}\frac{\partial \xi_l}{\partial x_j} + \frac{\partial W_j}{\partial \xi_n}\frac{\partial \xi_n}{\partial x_i}\right\}\right]\end{aligned} \tag{3.31}$$

$$\frac{\partial F_m}{\partial x_m} = 0 \tag{3.32}$$

The number of terms in the transformed conservation equations reduces a lot in the special case of stretched Cartesian grids because the transformation tensor, $\frac{\partial \xi_i}{\partial x_j}$ is diagonal.

Now we give a description of how the geometric metrics are computed. The computed metrics need to satisfy the following geometric constraints.

- Volume of the various cells add up to the volume of the domain.

$$\iiint_{\text{domain}} J^{-1} \partial\xi_1 \, \partial\xi_2 \, \partial\xi_3 = \text{Volume of domain in physical space}$$

  A discrete version of the above constraint is given by,

$$\sum_{\text{all cells}} J^{-1} \Delta\xi_1 \, \Delta\xi_2 \, \Delta\xi_3 = \text{Volume of domain in physical space}$$

- Surface area of a closed volume adds up to zero.

$$\frac{\partial}{\partial \xi_i} \left(J^{-1} \frac{\partial \xi_i}{\partial x_j} \right) = 0$$

  This condition is trivially satisfied because the transformation is a product of unidirectional mappings.

- For time-varying meshes, the *geometric conservation law* [Thomas & Lombard (1978)] must also be satisfied in order to prevent additional errors from being introduced into the solution.

$$\frac{\partial J^{-1}}{\partial t} + \frac{\partial}{\partial \xi_i} \left(J^{-1} \frac{\partial \xi_i}{\partial t} \right) = 0$$

  This law is simply a statement of the conservation of volume and is not of importance to us because our meshes were not time-varying.

Care was taken to satisfy the above constraints while determining the numerical discretization of the geometric metrics. We used a spatially second-order discretization because we felt that the stretching introduced by the mapping was small enough to be treated accurately by a second-order discretization and to avoid complex formulae for the discretization of the geometric metrics.

Storage of these metrics is not a problem because the metrics in each direction can be stored independently using one-dimensional arrays. This is possible because the transformation is a product of uni-directional mappings.

3.3.3 Extension of iterative fractional-step to collocated grids

In the previous subsections, we have described the collocated grid layout and the use of coordinate transformation to solve on stretched Cartesian grids. We now extend the iterative fractional step method to the collocated grid layout. The main difference is the fact that we solve for the volume fluxes, F_i, defined on the cell faces as well as for the cartesian velocity components, W_i. This introduces aditional equations for defining the volume fluxes at the cell faces in terms of the velocity components at the cell center and the geometric metrics.

So the temporally second-order discretization presented in Eqs. (3.5)-(3.6) is modified to include an interpolation equation for the volume fluxes and to discretize the continuity equation based on the volume fluxes defined at the cell faces instead of on the velocities defined at the cell centers.

$$\frac{W_i^{n+1} - W_i^n}{\Delta t} = \underbrace{\left[\frac{3}{2} H_i\left\{\mathbf{W^n}, \mathbf{F^n}\right\} - \frac{1}{2} H_i\left\{\mathbf{W^{n-1}}, \mathbf{F^{n-1}}\right\}\right]}_{\text{Convective, Adams-Bashforth}} - \underbrace{G_i^W\left\{p^{n+1}\right\}}_{\text{Pressure gradient}} + \underbrace{\frac{1}{2}\left[D_2\left\{W_i^{n+1}; \nu, \nu_r^{n+1}\right\} + D_2\left\{W_i^n; \nu, \nu_r^n\right\}\right]}_{\text{Sub-grid + Viscous Dissipation, Crank-Nicolson}} \tag{3.33}$$

$$B_i\left\{\mathbf{W^{n+1}}\right\} = F_i^{n+1} \tag{3.34}$$

$$\underbrace{C^F\left\{\mathbf{F^{n+1}}\right\} = 0}_{\text{Continuity}} \tag{3.35}$$

where the new notation introduced is,

$G_i^W\{p\}$ - Spatial discretization of the pressure gradient, $\frac{\partial p}{\partial x_i}$ appearing in the momentum equations. The superscript W denotes the fact that this discretization is used to advance the velocities, W_i and not the volume fluxes, F_i

$G_i^F\{p\}$ - Spatial discretization of the pressure gradient multiplied by the surface area of cell face normal to x_i, $\frac{\partial p}{\partial x_i} * A_i$. This operator is used to correct the volume fluxes, F_i. Again, the superscript F denotes the fact that this discretization is used to correct the volume fluxes, F_i, and not the velocities, W_i. Although this operator has not been used in the above equations it is introduced for completeness.

$B_i\{\mathbf{W}\}$ - Operator used to obtain the volume fluxes, F_i, by interpolating the velocity, $\mathbf{W}$ to the cell faces and multiplying by the area of the appropriate cell face.

$C^F\{\mathbf{F}\}$ - Spatially fourth order accurate discrete continuity operator based on the volume fluxes F_i instead of on the velocity, W_i.

As described earlier, the discretized equations, Eqs. (3.33)-(3.35) can be written in block-matrix form to develop an iterative scheme.

$$\begin{bmatrix} A & 0 & G^W \\ -B & I & 0 \\ 0 & C^F & 0 \end{bmatrix} \begin{bmatrix} \mathbf{W^{n+1}} \\ \mathbf{F^{n+1}} \\ p^{n+1} \end{bmatrix} = \begin{bmatrix} s \\ 0 \\ 0 \end{bmatrix} + \text{BCs} \tag{3.36}$$

where,

$\mathbf{F} \equiv \begin{bmatrix} F_1 \\ F_2 \\ F_3 \end{bmatrix}$

$B \equiv$ Interpolation operator to obtain $\mathbf{F}$ from $\mathbf{W}$

The iterative scheme is developed by replacing the above block-matrix with one which has an easy block-LU factorization. At the m^{th} iteration, we solve,

$$\begin{bmatrix} \hat{A} & 0 & \Delta t\hat{A}G^W \\ -B & I & -\Delta tBG^W + \Delta tG^F \\ 0 & C^F & 0 \end{bmatrix} \begin{bmatrix} \delta\mathbf{W}^{[\mathbf{m}]} \\ \delta\mathbf{F}^{[\mathbf{m}]} \\ \delta p^{[m]} \end{bmatrix} = r^{[m-1]} = \begin{bmatrix} s \\ 0 \\ 0 \end{bmatrix} + \text{BCs} - \begin{bmatrix} A & 0 & G^W \\ -B & I & 0 \\ 0 & C^F & 0 \end{bmatrix} \begin{bmatrix} \mathbf{W}^{[\mathbf{m-1}]} \\ \mathbf{F}^{[\mathbf{m-1}]} \\ p^{[m-1]} \end{bmatrix} \tag{3.37}$$

This matrix is much easier to invert because of its block-LU decomposition.

$$\begin{bmatrix} \hat{A} & 0 & \Delta t\hat{A}G^W \\ -B & I & -\Delta tBG^W + \Delta tG^F \\ 0 & C^F & 0 \end{bmatrix} = \begin{bmatrix} \hat{A} & 0 & 0 \\ -B & I & 0 \\ 0 & C^F & -\Delta tC^FG^F \end{bmatrix} \begin{bmatrix} I & 0 & \Delta tG^W \\ 0 & I & \Delta tG^F \\ 0 & 0 & I \end{bmatrix} \tag{3.38}$$

As detailed earlier, the steps involved in the block-LU decomposition are exactly those used in the normal fractional step method. So carrying out 1 iteration is equivalent to performing the fractional-step on a collocated grid. We end this subsection showing the steps involved in the m^{th} iteration of the iterative fractional-step method used on collocated grids.

1. Solve for a provisional velocity, $\hat{\mathbf{W}}$, using the latest approximation to the pressure, $p^{[m-1]}$.

$$\hat{A}\left(\delta\hat{\mathbf{W}}\right) = s + \text{BCs} - AW^{[m-1]} - G^W p^{[m-1]} \tag{3.39}$$

where the provisional velocity, $\hat{\mathbf{W}} = \mathbf{W}^{[\mathbf{m-1}]} + \delta\hat{\mathbf{W}}$

2. Compute the provisional volume flux, $\hat{\mathbf{F}}$ by interpolating the velocity, $\hat{\mathbf{W}}$, to the cell faces.

$$\hat{\mathbf{F}} = B\hat{\mathbf{W}} \tag{3.40}$$

3. Solve a pressure Poisson equation which computes a pressure correction, $\delta p^{[m]}$, that projects the *provisional volume flux* on to a divergence-free space.

$$C^F G^F \left\{\delta p^{[m]}\right\} = \frac{C^F \left\{\hat{\mathbf{F}}\right\}}{\Delta t} \tag{3.41}$$

4. Correct the provisional volume flux using the pressure correction, $\delta p^{[m]}$ so that it becomes divergence-free.

$$\mathbf{F}^{[\mathbf{m}]} = \hat{\mathbf{F}} - (\Delta t)\, G^F \left\{\delta p^{[m]}\right\} \tag{3.42}$$

5. Correct the provisional velocity using the pressure correction, $\delta p^{[m]}$.

$$\mathbf{W}^{[\mathbf{m}]} = \hat{\mathbf{W}} - (\Delta t)\, G^W \left\{\delta p^{[m]}\right\} \tag{3.43}$$

6. Update the pressure, $p^{[m]} = p^{[m-1]} + \delta p^{[m]}$

3.3.4 Energy-conserving discretization for convective terms

In the differential equations (not discretized) the convective and pressure terms do not dissipate energy. They simply rearrange energy within the domain. It has been observed that the stability and accuracy of the numerical scheme improves [Morinishi *et al.* (1998); Vasilyev (2000)] if the discrete version satisfies these energy-conservation properties as well. In this subsection, we will describe the energy-conservation properties of the convective terms and the discretization used to satisfy these conservation properties.

In the discretized equations, Eqs. (3.33)-(3.35)), mass and momentum conservation is ensured because we used the strong conservation form of the equations. However the convective terms in the governing equations for incompressible LES, Eqs. (3.1)-(3.2)), satisfy other conservation properties as well. These properties are listed below.

1. **Conservation of $\frac{W_1 W_1}{2}$:** The evolution equation for $\frac{W_1 W_1}{2}$ is obtained by multiplying the W_1 momentum equation, Eq. (3.1) with W_1. On doing so, the convective term becomes,

$$W_1 \frac{\partial (W_j W_1)}{\partial x_j} = \frac{\partial (W_j W_1^2/2)}{\partial x_j} - \frac{W_1^2}{2} \frac{\partial (W_j)}{\partial x_j} \tag{3.44}$$

   Because the continuity equation is satisfied, Eq. (3.2), the second term in the RHS of the above equation drops out. Thus the convective term conserves $\frac{W_1 W_1}{2}$ because the first term in the RHS is the divergence of a flux. Similar conservation properties hold for $\frac{W_2 W_2}{2}$ and $\frac{W_3 W_3}{2}$ as well.

2. **Conservation of resolved kinetic energy, $\frac{W_i W_i}{2}$:** The individual components of the resolved kinetic energy namely $\frac{W_1 W_1}{2}$, $\frac{W_2 W_2}{2}$ and $\frac{W_3 W_3}{2}$ are individually conserved if continuity is satisfied. Hence the sum of these components which is the resolved kinetic energy is also conserved if continuity is satisfied.

Our goal is to ensure that these conservation properties are satisfied in the semi-discrete form of the governing equations which are obtained by discretizing Eqs. (3.33)-(3.35)) in space only. Since any central difference discretization for the convective term does not satisfy these conservation properties care must be taken in the choice of numerical discretization. All the discretizations are computed in the computational space which has a uniform grid. The presence of a uniform grid

in computational space also simplifies the presentation. We use the notation of Morinishi *et al.* (1998) shown below to represent the numerical discretizations.

$$\left.\frac{\delta_n \phi}{\delta_n \xi_1}\right|_{\xi_1,\xi_2,\xi_3} \equiv \frac{\phi\left(\xi_1 + (n/2)\Delta\xi_1, \xi_2, \xi_3\right) - \phi\left(\xi_1 - (n/2)\Delta\xi_1, \xi_2, \xi_3\right)}{n\Delta\xi_1} \tag{3.45}$$

$$\left.\overline{\phi}^{n\xi_1}\right|_{\xi_1,\xi_2,\xi_3} \equiv \frac{\phi\left(\xi_1 + (n/2)\Delta\xi_1, \xi_2, \xi_3\right) + \phi\left(\xi_1 - (n/2)\Delta\xi_1, \xi_2, \xi_3\right)}{2} \tag{3.46}$$

Combinations of these discrete operators can be used to make higher order approximations to function values and derivatives. The convective term is approximated by a spatially fourth-order approximation given by,

$$\frac{\partial\left(F_m W_i\right)}{\partial \xi_m} \overset{C}{=} H_i\left\{\mathbf{W^n}, \mathbf{F^n}\right\} = \frac{9}{8}\frac{\delta_1\left[F_m \overline{W_i}^{1\xi_i}\right]}{\delta_1 \xi_m} - \frac{1}{8}\frac{\delta_3\left[F_m \overline{W_i}^{3\xi_i}\right]}{\delta_3 \xi_m} \tag{3.47}$$

It can be proved [Morinishi *et al.* (1998)] that the above approximation for the convective terms conserves energy if,

$$\frac{9}{8}\frac{\delta_1 F_m}{\delta_1 \xi_m} - \frac{1}{8}\frac{\delta_3 F_m}{\delta_3 \xi_m} = 0 \tag{3.48}$$

The above is clearly a fourth order approximation to the continuity equation and so for energy conservation the discrete continuity operator is chosen to be,

$$\frac{\partial\left(F_m\right)}{\partial \xi_m} \overset{C}{=} C^F\left\{\mathbf{F}\right\} = \frac{9}{8}\frac{\delta_1 F_m}{\delta_1 \xi_m} - \frac{1}{8}\frac{\delta_3 F_m}{\delta_3 \xi_m} \tag{3.49}$$

The volume fluxes at the cell faces is determined from the velocity at the cell centers using a fourth-order interpolation and the geometric metrics as shown below,

$$F_i \equiv \left[\frac{9}{8}\overline{W_i}^{1\xi_i} - \frac{1}{8}\overline{W_i}^{3\xi_i}\right] * A_i \tag{3.50}$$

where A_i is the surface area of the cell face perpendicular to ξ_i. In the simple case of stretched Cartesian grids A_1 is given by,

$$A_1 = J^{-1}\frac{\partial \xi_1}{\partial x_1} = \frac{\partial x_2}{\partial \xi_2} \times \frac{\partial x_3}{\partial \xi_3} \tag{3.51}$$

and so on.

Thus a specific discretization needs to be used for the continuity operator in order to make the convective terms energy-conserving. We have chosen a particular spatially fourth order accurate discretization for both the convective terms and the continuity operator which conserves energy on a collocated grid layout.

3.3.5 Pressure Poisson equation

In the earlier subsection we have shown how to discretize the convective terms and continuity operator so that the convective terms are energy-conserving. The pressure gradient term in the differential equation also conserves kinetic energy but not the individual components such as $\frac{W_1 W_1}{2}$. So it would be desirable to choose its discretization such that this property holds. However, it is not possible to do this in a collocated grid layout. In this subsection, I will discuss the discretization used for the pressure gradient operator, the reasons for the choice and the order of the error it introduces in the energy-conservation property.

There are 2 pressure gradient operators which need to be determined.

1. **Pressure gradient correcting the velocity, $G_i^W\{p\}$:** This is the pressure gradient which appears in the discretized momentum equation, Eq. (3.33). Since we are trying to develop a spatially fourth-order scheme, this pressure gradient, G_i^W, needs to be fourth order accurate and was taken to be,

$$G_i^W\{p\} \equiv \left[\frac{4}{3}\frac{\delta_2 p}{\delta_2 \xi_i} - \frac{1}{3}\frac{\delta_4 p}{\delta_4 \xi_i}\right]\left(\frac{\partial \xi_i}{\partial x_i}\right) \tag{3.52}$$

2. **Pressure gradient correcting the volume flux, $G_i^F\{p\}$:** This is the pressure gradient operator which is used to correct the volume fluxes so that it becomes divergence-free, Eq. (3.42). In this sense, the pressure correction,

$\delta p^{[m]}$ can be thought of as a Lagrange multiplier which constrains the volume flux, $\mathbf{F}^{[\mathbf{m}]}$ to be divergence free. There is no spatial accuracy requirement on the choice of G_i^F but the choice of G_i^F affects the pressure Poisson equation because the Poisson operator is given by $C^F\left\{\mathbf{G}^{\mathbf{F}}\left\{\bullet\right\}\right\}$ (see Eq. (3.41)). Hence, G_i^F was chosen to minimize the stencil size of the Poisson operator.

Since the continuity operator, $C^F\left\{\bullet\right\}$, needs to be spatially fourth order accurate we have to use a 4-point stencil in each direction. If we were to choose a fourth order accurate discretization for G_i^F as well then this would also have a 4-point stencil in each direction. The combination of these 2 operators would result in a 7-point stencil in each direction for the pressure Poisson equation. Since it would be costly to invert this system with a large stencil we tried to minimize the stencil size. This is possible because there is no accuracy requirement on G_i^F. Also when the iterations in the iterative fractional step scheme converge, they would converge to the solution of Eqs. (3.33)-(3.35) which is discretized to be spatially fourth-order accurate. So we choose G_i^F to be a spatially second-order accurate discretization of the pressure gradient multiplied by the surface area of the cell face normal to ξ_i.

$$G_i^F\left\{p\right\} \equiv \left[\frac{\delta_1 p}{\delta_1 \xi_i}\right]\left(\frac{\partial \xi_i}{\partial x_i}\right) A_i \tag{3.53}$$

The above has a 2-point stencil in each direction. So the arising pressure Poisson equation only has a 5-point stencil in each direction.

Different choices for the 2 pressure gradient operators were experimented with. The above mentioned combination was found to work the best in terms of maintaining fourth-order spatial accuracy and in designing a computationally efficient scheme.

Chapter 4

Parallel code implementation and validation

In this chapter we will discuss some of the implementation aspects of the numerical algorithm, in particular those required to develop a good parallel code. We start with a brief description of high performance computing and the cluster configuration on which the code is designed to be executed. Next we describe the block data structure used for storing the velocity and scalar fields. The block data structure was chosen because it provided a natural way to store either the x_1x_2 planes or x_2x_3 planes of data in the same array and it required the minimum amount of data rearrangement when we transfered between the 2 configurations. The solution procedure for the pressure Poisson equation is described next. We use Fourier transforms for 2 directions and solve a linear system in the 3^{rd} direction. The singular matrix which arises at zero wavenumber is inverted using a special procedure which removes this singularity by identifying the null space of the matrix. Periodic boundary conditions introduce additional complexity in the inversion of matrices which arise in the pressure Poisson equation and ADI sub-iterations. The Sherman-Morrison-Woodbury formula forms the basis of an algorithm which exploits the band structure of such matrices to invert them in linear time. Next we focus on the ADI sub-iterations in which an important fraction of the computational time is spent. The efficiency and parallel speedup of the various schemes implemented for this purpose are compared, showing that the best one minimizes the data transfer between the processes. Finally, we verify the order of accuracy of the code in time and space for 2 test problems, the 2d periodic

vortex and the Taylor-Green vortex. We also make comparisons with simulations using the commercial code, Fluent, to validate our code.

4.1 Cluster Configuration

High performance computing has increasingly been used to simulate fluid flows both in industry and academia. These high performance systems are usually classified based on the way they manipulate instructions and data streams [van der Steen & Dongarra (2004); Flynn (1972)]. There are four main architectural classes out of which we focus on Multiple Instruction Multiple Data (MIMD) machines. These machines execute several instruction streams in parallel on different data. The instructions and data are usually related because they represent different parts of the same task to be executed. So, MIMD systems may run many sub-tasks in parallel in order to shorten the time-to-solution for the main task to be executed. MIMD systems can be broadly subdivided into 2 classes of systems:

1. **Shared Memory systems:** These systems have multiple CPUs, all of which share the same memory. This means that the knowledge of where data is stored is of no concern to the user as there is only one memory accessed by all CPUs on an equal basis.

2. **Distributed Memory (DM) systems:** In this case each CPU has its own associated memory. The CPUs are connected by a network and may exchange data between their respective memories when required. In contrast to shared memory machines, the user must be aware of the location of the data in the local memories and will have to move or distribute these data explicitly when needed.

> Distributed processing takes the Distributed Memory-MIMD concept one step further: instead of many integrated processors in one or several boxes, a number of workstations, mainframes, etc., are connected by (Gigabit) Ethernet, or otherwise, and set to work concurrently on tasks in the same program. Conceptually, this is not different from DM-MIMD computing, but the communication between processors is often orders of magnitude slower. Many packages to realize distributed computing are available. Examples of these are Parallel Virtual Machine (PVM), and Message Passing Interface (MPI). This style of programming, called the 'message passing' model, has become so much accepted that PVM and MPI have been adopted by virtually all major vendors of distributed-memory MIMD systems and are available even on shared-memory MIMD systems for compatibility reasons.

The high performance system on which we carried out most of our calculations was a Linux cluster named JIT. The adoption of clusters, collections of workstations/PCs connected by a local network, has virtually exploded since the introduction of the first Beowulf cluster in 1994. The attraction lies in the (potentially) low cost of both hardware and software and the control that builders and users have over their system. Also books on how to build and maintain clusters have greatly added to their popularity [Sterling *et al.* (1999); Spector (2000)]. Many companies such as Dell also offer more or less ready out-of-the-box cluster solutions for those groups that do not want to build their cluster from scratch.

The JIT cluster is a 32 node cluster assembled by Dell. Each node has two 2.4 GHz Intel Xeon processors and are connected using a 1 Gigabit network switch. As mentioned earlier, the Linux operating system is used. Most of the program was written in Fortran 90 using MPI for the communication between processes.

In particular, we primarily used the MPI-LAM implementation. Since communication is usually slower than computations in these clusters, care was taken in the distribution of data to minimize communication between processes. Some of these details and algorithm performance are given in this chapter

4.2 Block data structure

Flow problems, such as the temporal mixing layer and forced isotropic turbulence, can be simulated on fairly simple Cartesian grids. The natural choice for the data structure to hold velocity, pressure and other fields on a single processor is a 3D array where each array dimension represents a coordinate direction. However, on a distributed memory parallel machine the data needs to be divided or *domain decomposed* among the various processes. The most important criterion for the choice of domain-decomposition is to minimize communication between the processes.

Figures 4.1-4.3 depict three conceptually different domain-decompositions on N_p processes. Each red cuboid is representative of the array section stored in a particular process. The sum of the array sections stored in all processes add up to the entire data array. Among the three, the one which minimizes the communication between the processes is the preferred domain-decomposition. Typical finite-volume codes use information from the nearest neighbors for the differencing. For the elements stored at the boundaries of the red array sections this information is not available in the same process and needs to be obtained from the process containing the neighboring array section. So the surface area of the red array section is a rough, but a good, measure of the amount of communication required in a finite-volume code. This is summarized in Table 4.1 for the three different domain-decompositions. We have used the following notation,

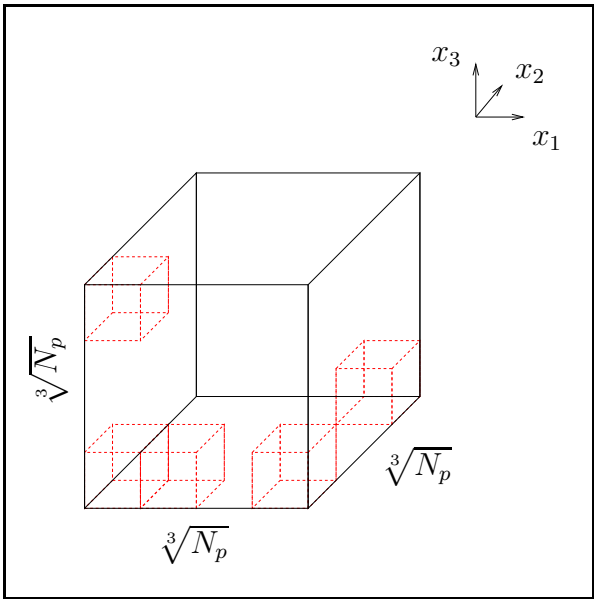

Figure 4.1: Data divided among processes for parallel implementation along x_1, x_2, and x_3 directions.

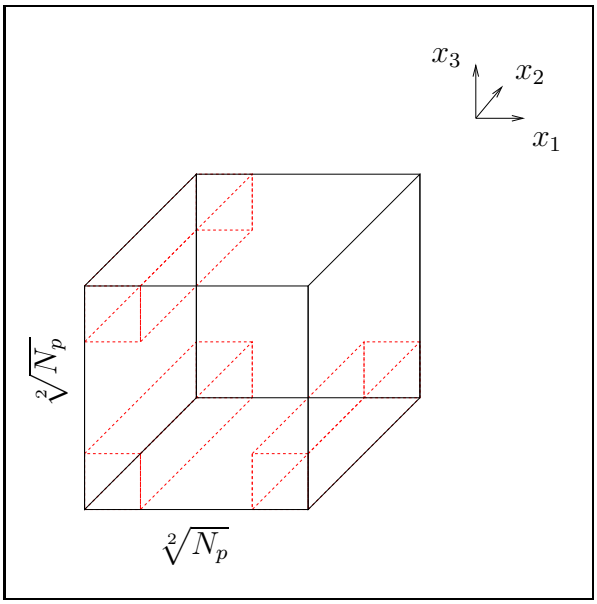

Figure 4.2: Data divided among processes for parallel implementation along x_1 and x_3 directions only.

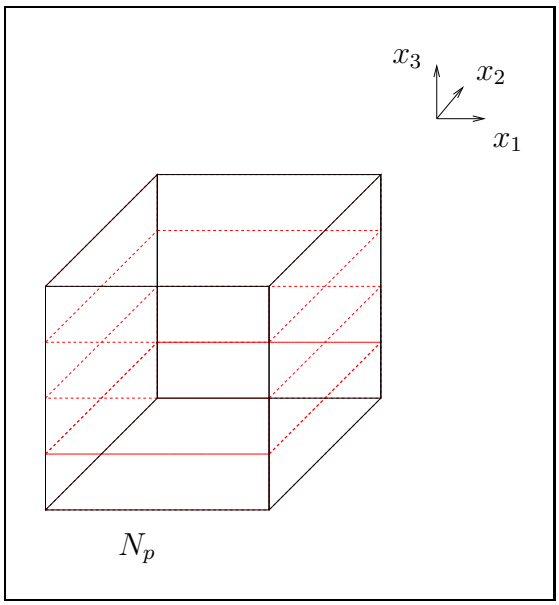

Figure 4.3: Data divided among processes for parallel implementation along x_3 direction only.

N_1 - Number of grid points in the x_1 direction.

N_2 - Number of grid points in the x_2 direction.

N_3 - Number of grid points in the x_3 direction.

Table 4.1: Surface area of the array sections in each process. This represents the communication overhead in a finite-volume code using a nearest neighbor stencil.

Domain-Decomposition	Surface Area
Division along x_1, x_2, and x_3	$\frac{2}{N_p^{2/3}}\left[N_1N_2 + N_2N_3 + N_3N_1\right]$
Division along x_1, and x_3	$\frac{2}{N_p^{1/2}}\left[N_1N_2 + N_2N_3\right]$
Division along x_3	$2\left[N_2N_3\right]$

From Table 4.1 it is clear that the communication overhead reduces as $O\left(N_p^{-2/3}\right)$,

$O\left(N_p^{-1/2}\right)$, and $O\left(N_p^0\right)$ respectively for the three different domain-decompositions strategies considered. This means that for a finite-volume code dividing the data along all 3 directions would minimize the communication overhead.

The current code also uses Fast Fourier Transforms (FFTs) to solve a Poisson equation for the pressure, and the communication requirements of this step must also be considered. We need to carry out Fourier transforms only in the x_1 and x_2 directions because in all the flow problems we consider, only periodic boundary conditions are imposed in the x_1 and x_2 directions. So it is computationally easier to solve in these directions using Fourier transforms. Domain-decomposition shown in Fig. 4.3 is the only one among the three which requires no communication between the processes for carrying out a Fast Fourier Transform (FFT) in the x_1 and x_2 directions. For this reason, we divided the data along x_3 direction only (Fig. 4.3), in spite of the communication penalty incurred in the finite volume portion of the code.

Further the data is stored using a 4d array instead of a 3d array. The first 3 array dimensions represent the 3 coordinate directions while the last dimension represents what we call the block. The red array section stored in each process is further subdivided into blocks of size $N_1/N_p \times N_2 \times N_3/N_p$. These blocks are denoted in Fig. (4.4) using blue color. The solution procedure for the pressure Poisson equation required us to shift between configurations which stored either x_1x_2 planes or x_2x_3 planes. This justified the use of this block data structure because it allows us to:

- Use the same array for storing either x_1x_2 planes or x_2x_3 planes.
- Shift between the 2 configurations with a simple MPI_ALLTOALL command and without data rearrangement.

We also included pseudo array locations on the sides of the block to make the differencing routines simpler to code. Another point to note is that the number of blocks into which the array section is divided is equal to the number of processes, N_p.

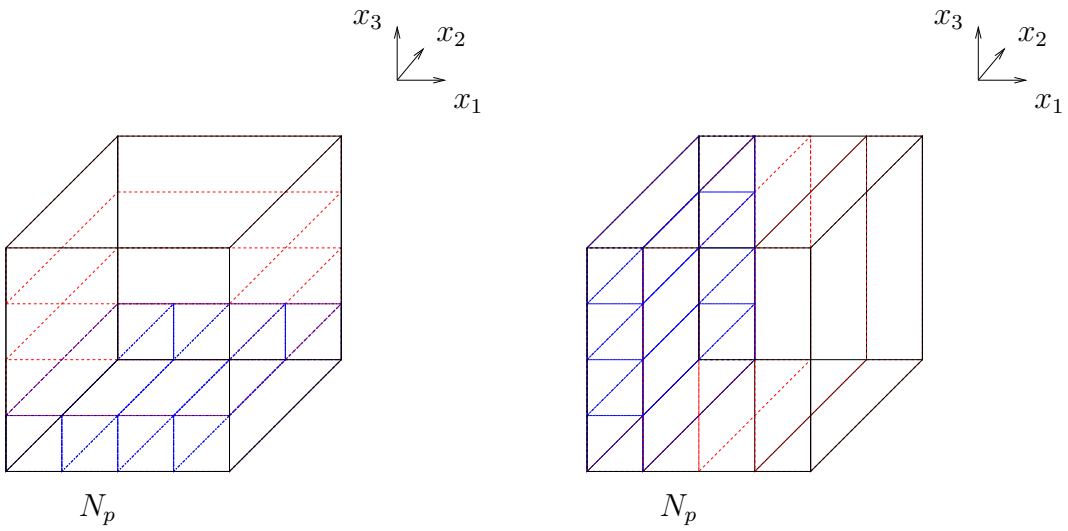

(a) Configuration with x_1x_2 planes in each process

(b) Configuration with x_2x_3 planes in each process

Figure 4.4: Block data structure, red denotes the array section stored in a given process and blue denotes the blocks in that array section.

It should be mentioned that, although breaking up the data along x_3 direction was a good choice, the use of the block data structure (4d array) was not the best. Later tests showed that simply storing the data as a 3d array (henceforth called the slab data structure) gave the best performance in terms of parallel speedup and minimum computational time. The block data structure has poorer performance because even while carrying out simple differencing operations we do not access contiguous memory locations, as the use of blocks introduces more discontinuities

or jumps in the memory locations accessed. This problem becomes worse as the number of processes N_p increases because we subdivide the array section into a larger number of smaller size blocks.

In order to illustrate this point, we compared the two data structures. One is the block data structure described above and the other is a slab data structure where the array section is simply stored as a 3d array without further subdivision into blocks. We compare their performance by looking at their computational time required for the following simple, but representative, subroutines:

1. **diffx1:** which computes a first difference in the x_1 direction.

2. **diffx2:** which computes a first difference in the x_2 direction.

3. **diffx3:** which computes a first difference in the x_3 direction.

There is little or no communication in these subroutines and the CPU timings are indicative of the time required for computing differences in parallel using the different data structures. In Fig. 4.5 we show the variation of SPEC number with number of processes, N_p for the different subroutines using the 2 data structures. The SPEC number is basically the number of times the given subroutine can be executed in a unit of time (say a day). By looking at the variation of SPEC number with N_p we also have an idea on how the data structure performs in parallel.

From Fig. 4.5 it is clear that the slab data structure is superior to the block data structure. Future improvements could include modifying the code to use the slab data structure. The way the code is written allows us to implement this relatively easily. I have rewritten major portions of the code but much needs to be done in terms of checking this code. So all the results presented in the following sections will be based on the block data structure code which has been validated

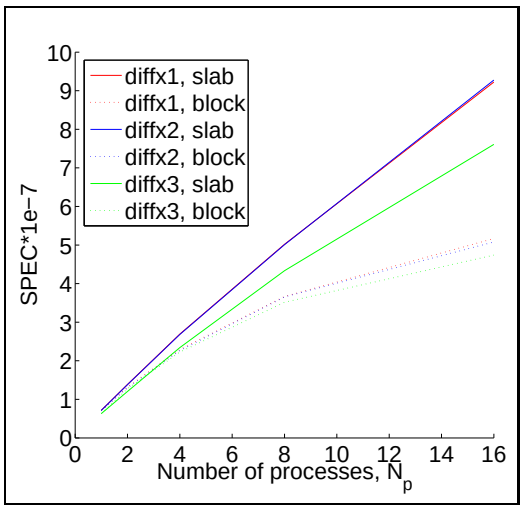

Figure 4.5: Comparison of the block and slab data structure by plotting the SPEC number against the number of processes for 3 representative differencing subroutines.

more thoroughly.

4.3 Pressure Poisson equation

In order to project the provisional volume fluxes onto a divergence-free space we need to solve a pressure Poisson equation (Eq. (3.41)). Details on how to choose the continuity and pressure gradient operators were given in section 3.3.5. In this section we will discuss how Fourier transforms can be used to efficiently solve the pressure Poisson equation. The pressure Poisson equation is singular allowing it to have infinitely many solutions. Details on how this singularity is handled are also given. Finally we give results on the parallel performance of the pressure Poisson equation solver. The less than ideal speedup is attributed to the large communication requirement between processes.

When we have periodic boundary conditions, it is computationally efficient to

solve the Poisson equation in Fourier space. This is true for 2 reasons:

1. The pressure Poisson equation reduces to a simple algebraic equation in Fourier space; and

2. The Fourier transform of N data points can be computed in $O(N \log_2 N)$ operations using the *Fast Fourier Transform* [Press *et al.* (1992)] instead of $O(N^2)$ operations. The discovery of the Fast Fourier Transform (FFT) has made computationally tractable the use of Fourier transforms in this and other applications as well.

Since all the flow problems considered had at least 2 periodic directions we solved in Fourier space in the x_1 and x_2 directions. For the x_3 direction, we solved a linear system arising from discretizing the Poisson operator in this direction. The advantage of this approach is that instead of solving 1 linear system for $N_1 N_2 N_3$ unknowns we solve $N_1 N_2$ linear systems for N_3 unknowns each.

Here we derive the linear systems needed to solve the Poisson equation. We start with an expression for the Poisson operator in each direction using the discretizations given in section 3.3.5. Taking Fourier transforms in the x_1 and x_2 directions we obtain the linear systems to be solved. The Poisson operator at an interior grid point in the x_1 direction (say) is given by,

$$\begin{aligned} C^F\left\{G^F\{p\}\right\}\Big|_{\xi_1,\xi_2,\xi_3} &= \frac{9}{8\Delta\xi_1}\left[G^F\{p\}\Big|_{\xi_1+\frac{1}{2}\Delta\xi_1} - G^F\{p\}\Big|_{\xi_1-\frac{1}{2}\Delta\xi_1}\right] \\ &\quad - \frac{1}{8\times 3\Delta\xi_1}\left[G^F\{p\}\Big|_{\xi_1+\frac{3}{2}\Delta\xi_1} - G^F\{p\}\Big|_{\xi_1-\frac{3}{2}\Delta\xi_1}\right] \end{aligned} \tag{4.1}$$

where,

$$G^F\{p\}\Big|_{\xi_1} = \left[\frac{\left(\frac{\partial x_2}{\partial \xi_2}\right)\left(\frac{\partial x_3}{\partial \xi_3}\right)}{\left(\frac{\partial x_1}{\partial \xi_1}\right)}\Bigg|_{\xi_1}\right] \frac{p\big|_{\xi_1+\frac{1}{2}\Delta\xi_1} - p\big|_{\xi_1-\frac{1}{2}\Delta\xi_1}}{\Delta\xi_1} \tag{4.2}$$

For simplicity of notation we define,

$$\begin{aligned} M_{11}\Big|_{\xi_1} &\equiv J^{-1}\left(\frac{\partial \xi_1}{\partial x_1}\right)\left(\frac{\partial \xi_1}{\partial x_1}\right)\Bigg|_{\xi_1} \\ &= \frac{\left(\frac{\partial x_2}{\partial \xi_2}\right)\left(\frac{\partial x_3}{\partial \xi_3}\right)}{\left(\frac{\partial x_1}{\partial \xi_1}\right)}\Bigg|_{\xi_1} \end{aligned} \tag{4.3}$$

and so on.

Substituting Eq. (4.2) into Eq. (4.1) we have,

$$\begin{aligned} C^F\left\{G^F\left\{p\right\}\right\}\Big|_{\xi_1,\xi_2,\xi_3} = &\left[-\frac{M_{11}\Big|_{\xi_1+\frac{3}{2}\Delta\xi_1}}{24\left(\Delta\xi_1\right)^2}\right] p\Big|_{\xi_1+2\Delta\xi_1} + \\ &\left[\frac{M_{11}\Big|_{\xi_1+\frac{3}{2}\Delta\xi_1}}{24\left(\Delta\xi_1\right)^2} + \frac{9M_{11}\Big|_{\xi_1+\frac{1}{2}\Delta\xi_1}}{8\left(\Delta\xi_1\right)^2}\right] p\Big|_{\xi_1+\Delta\xi_1} + \\ &\left[-\frac{9M_{11}\Big|_{\xi_1+\frac{1}{2}\Delta\xi_1}}{8\left(\Delta\xi_1\right)^2} - \frac{9M_{11}\Big|_{\xi_1-\frac{1}{2}\Delta\xi_1}}{8\left(\Delta\xi_1\right)^2}\right] p\Big|_{\xi_1} + \\ &\left[\frac{M_{11}\Big|_{\xi_1-\frac{3}{2}\Delta\xi_1}}{24\left(\Delta\xi_1\right)^2} + \frac{9M_{11}\Big|_{\xi_1-\frac{1}{2}\Delta\xi_1}}{8\left(\Delta\xi_1\right)^2}\right] p\Big|_{\xi_1-\Delta\xi_1} + \\ &\left[-\frac{M_{11}\Big|_{\xi_1-\frac{3}{2}\Delta\xi_1}}{24\left(\Delta\xi_1\right)^2}\right] p\Big|_{\xi_1-2\Delta\xi_1} \end{aligned} \tag{4.4}$$

In the case of a uniform physical grid in the x_1 direction, M_{11} is independent of ξ_1 and the above expression, Eq. (4.4), simplifies to,

$$\begin{aligned} &C^F\left\{G^F\left\{p\right\}\right\}\Big|_{\xi_1,\xi_2,\xi_3} = \\ &\frac{M_{11}\left(\xi_2,\xi_3\right)}{24\left(\Delta\xi_1\right)^2}\left[-p\Big|_{\xi_1+2\Delta\xi_1} + 28p\Big|_{\xi_1+\Delta\xi_1} - 54p\Big|_{\xi_1} + 28p\Big|_{\xi_1-\Delta\xi_1} - p\Big|_{\xi_1-2\Delta\xi_1}\right] \end{aligned} \tag{4.5}$$

The above expression holds for the periodic directions, x_1 and x_2, which have a uniform physical grid. Since we have a uniform physical grid we can take the

computational and physical grid to be the same. Finally, we search for solutions of the form,

$$p\left(\xi_1,\xi_2,\xi_3\right) = \hat{p}\left(\kappa_1,\kappa_2,\xi_3\right) e^{i\kappa_1\xi_1} e^{i\kappa_2\xi_2} \tag{4.6}$$

where,

$$\kappa_1 = b_1 * \left(\frac{2\pi}{L_1}\right) \qquad 0 < b_1 < N_1 - 1 \tag{4.7}$$

$$L_1 \equiv \text{Box length in the } x_1 \text{ direction} \tag{4.8}$$

$$\kappa_2 = b_2 * \left(\frac{2\pi}{L_2}\right) \qquad 0 < b_2 < N_2 - 1 \tag{4.9}$$

$$L_2 \equiv \text{Box length in the } x_2 \text{ direction} \tag{4.10}$$

Eq. (4.5) reduces to,

$$C^F\left\{G^F\left\{p\right\}\right\}\Big|_{\xi_1,\xi_2,\xi_3} = \frac{M_{11}\left(\xi_2,\xi_3\right)}{3\left(\Delta\xi_1\right)^2}\left[\sin^2\left(\frac{\theta_1}{2}\right)\right]\left[12 + 2\sin^2\left(\frac{\theta_1}{2}\right)\right]\hat{p}\left(\kappa_1,\kappa_2,\xi_3\right) e^{i\kappa_1\xi_1} e^{i\kappa_2\xi_2} \tag{4.11}$$

where $\theta_i \equiv \kappa_i \Delta\xi_i$ is a non-dimensional number. .

Hence the pressure Poisson equation (Eq. (3.41)) including all directional derivatives, in the special case of a uniform and periodic grid in the x_1 and x_2 directions,

reduces to,

$$\frac{M_{11}(\xi_3)}{3(\Delta\xi_1)^2}\left[\sin^2\left(\frac{\theta_1}{2}\right)\right]\left[12+2\sin^2\left(\frac{\theta_1}{2}\right)\right]\hat{p}(\kappa_1,\kappa_2,\xi_3)\,e^{i\kappa_1\xi_1}e^{i\kappa_2\xi_2}+$$
$$\frac{M_{22}(\xi_3)}{3(\Delta\xi_2)^2}\left[\sin^2\left(\frac{\theta_2}{2}\right)\right]\left[12+2\sin^2\left(\frac{\theta_2}{2}\right)\right]\hat{p}(\kappa_1,\kappa_2,\xi_3)\,e^{i\kappa_1\xi_1}e^{i\kappa_2\xi_2}+$$
$$\left[-\frac{M_{33}\Big|_{\xi_3+\frac{3}{2}\Delta\xi_3}}{24(\Delta\xi_3)^2}\right]\hat{p}(\kappa_1,\kappa_2,\xi_3+2\Delta\xi_3)\,e^{i\kappa_1\xi_1}e^{i\kappa_2\xi_2}+$$
$$\left[\frac{M_{33}\Big|_{\xi_3+\frac{3}{2}\Delta\xi_3}}{24(\Delta\xi_3)^2}+\frac{9M_{33}\Big|_{\xi_3+\frac{1}{2}\Delta\xi_3}}{8(\Delta\xi_3)^2}\right]\hat{p}(\kappa_1,\kappa_2,\xi_3+\Delta\xi_3)\,e^{i\kappa_1\xi_1}e^{i\kappa_2\xi_2}+$$
$$\left[-\frac{9M_{33}\Big|_{\xi_3+\frac{1}{2}\Delta\xi_3}}{8(\Delta\xi_3)^2}-\frac{9M_{33}\Big|_{\xi_3-\frac{1}{2}\Delta\xi_3}}{8(\Delta\xi_3)^2}\right]\hat{p}(\kappa_1,\kappa_2,\xi_3)\,e^{i\kappa_1\xi_1}e^{i\kappa_2\xi_2}+$$
$$\left[\frac{M_{33}\Big|_{\xi_3-\frac{3}{2}\Delta\xi_3}}{24(\Delta\xi_3)^2}+\frac{9M_{33}\Big|_{\xi_3-\frac{1}{2}\Delta\xi_3}}{8(\Delta\xi_3)^2}\right]\hat{p}(\kappa_1,\kappa_2,\xi_3-\Delta\xi_3)\,e^{i\kappa_1\xi_1}e^{i\kappa_2\xi_2}+$$
$$\left[-\frac{M_{33}\Big|_{\xi_3-\frac{3}{2}\Delta\xi_3}}{24(\Delta\xi_3)^2}\right]\hat{p}(\kappa_1,\kappa_2,\xi_3-2\Delta\xi_3)\,e^{i\kappa_1\xi_1}e^{i\kappa_2\xi_2}=\frac{C^F\left\{\hat{\mathbf{F}}\right\}}{\Delta t} \tag{4.12}$$

The above represents N_1N_2 banded linear systems, each for the N_3 unknowns, $\hat{p}(\kappa_1,\kappa_2,\xi_3)$ occurring at each value of (κ_1,κ_2). Each of these linear systems can be solved in $O(N_3)$ time which gives a complexity of $O(N_1N_2N_3)$ for solving the entire Poisson equation. We perform the FFT in the x_1 and x_2 directions, resulting in a linear system of equations for unknowns in the x_3 direction. So we need to exchange the data arrays such that each process contains x_2x_3 planes instead of x_1x_2 planes. This was found to be more efficient than using a parallel matrix solver but still has a large communication overhead.

It should be noted that Eq. (4.12) becomes singular at $\kappa_1 = \kappa_2 = 0$. It is easy to understand this physically because there are infinitely many solutions to

the pressure Poisson equation subject to either periodic boundary conditions or boundary conditions based on pressure gradients. Each of these solutions differs only by an additive constant. So when we discretize the pressure Poisson equation, the resulting system has rank N_3-1 at $\kappa_1 = \kappa_2 = 0$. If we add up all the equations at $\kappa_1 = \kappa_2 = 0$, we end up with the trivial equation $0 = 0$. So one of the equations can be written as a linear combination of the other $N_3 - 1$ equations. We use a very simple procedure to solve this singular system arising at at $\kappa_1 = \kappa_2 = 0$. We assume one of the unknowns to be zero and solve for the remaining $N_3 - 1$ unknowns by using only the first N_3-1 equations. Finally, we modify the pressure solution by adding a constant such that the volume average of the pressure is zero.

We end this section with results on the parallel performance of the pressure Poisson solver. In order to determine the parallel performance we used the 2d periodic vortex problem computed using a 96^3 grid as a test problem. This problem is described in detail later. Here we look at the computational times spent in the pressure Poisson solver and interpret the less than ideal speedup performance of this subroutine based on the large communication required between the processes.

Fig. 4.6 shows the variation of the SPEC number with number of processes. This is the number of times the pressure Poisson equation can be solved in a day utilizing the given number of processes.

It is clear from Fig. 4.6 that the pressure Poisson equation solver does not parallelize well. In fact when we go from 8 to 16 processes there is actually an increase in computational time. This is because of the large communication, of $O(N_1N_2N_3)$, required between the processes. Typically the communication of a float between processes on a cluster takes about 10 times as much time as a floating point operation. So a good parallel algorithm requires the number of floats to be

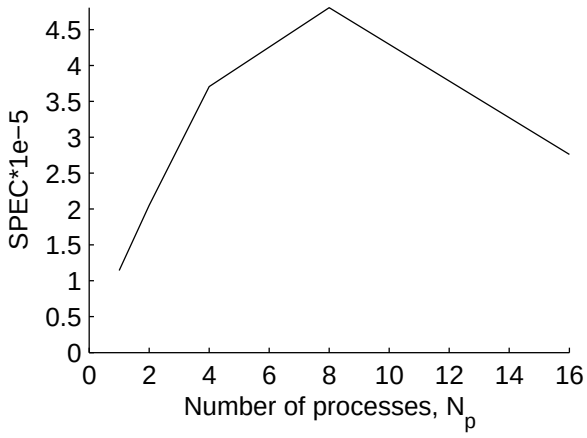

Figure 4.6: Variation of the SPEC number for the pressure Poisson equation with number of processes on the JIT cluster.

communicated between processes to be at least one order of magnitude smaller than the number of floating point operations. However in the solution of the pressure Poisson equation both communication and computation are of the same order, $O(N_1 N_2 N_3)$. This is because in order to solve the linear system in the x_3 direction we need to shift from $x_1 x_2$ planes to $x_2 x_3$ planes. This requires the exchange of $O(N_1 N_2 N_3)$ data. Fig. 4.7 further highlights this point by showing that the fraction of the time spent in communication in the subroutine which solves the pressure Poisson equation increases with the number of processes.

4.4 Choice of $\hat{A}$

In section 3.2 the need to replace the matrix A, occurring in the iterative fractional step, with $\hat{A}$ was justified on the basis of ease of inversion of $\hat{A}$. It was also hinted that a finite number of sub-iterations of some iterative scheme used to invert A would result in the definition of $\hat{A}$. In this section we will describe the

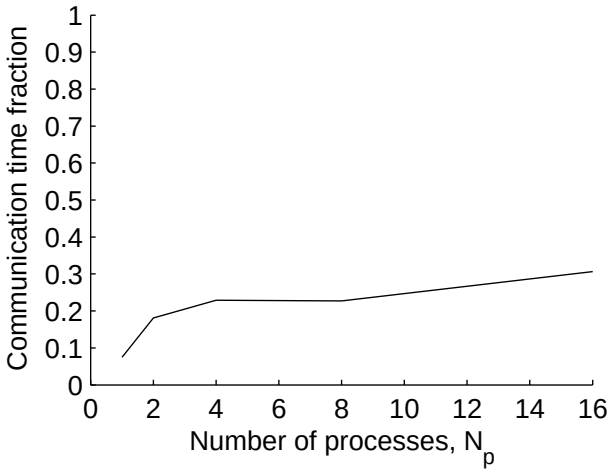

Figure 4.7: Fraction of the time spent in communication in the subroutine which solves the pressure Poisson equation.

sub-iteration used in our parallel code. It is an iterative version of the commonly used Alternating Direction Implicit (ADI) algorithm. In ADI, finite differences occurring in each direction are factored out separately resulting in linear systems which are computationally easier to invert on account of their smaller bandwidth. For the sake of good parallel speedup these linear systems need to be further modified to those which require minimum communication between the processes for their solution.

The first step in the iterative fractional step procedure Eq. (3.39), where we compute a provisional velocity, requires us to solve,

$$\hat{A}y = b \tag{4.13}$$

The matrix $\hat{A}$ must be chosen such that:

1. $\hat{A}$ is a close approximation to A, and

2. $\hat{A}$ is easily invertible.

So we start with the matrix A and introduce successive approximations to obtain a matrix A' which needs to be inverted at each sub-iteration of an iterative scheme. Depending on the number of sub-iterations carried out we have the definition of $\hat{A}$. At the q^{th} sub-iteration we correct the earlier estimate for y using

$$A'\delta y^{\{q\}} = b - Ay^{\{q-1\}} \tag{4.14}$$

The above matrix A defined in Eq. (3.9) consists of discretizations of normal second order derivatives such as $\frac{\partial}{\partial x_1}\left(.\frac{\partial(\bullet)}{\partial x_1}\right)$ and cross derivatives such as $\frac{\partial}{\partial x_1}\left(.\frac{\partial(\bullet)}{\partial x_2}\right)$. For ease of explanation we rewrite A as

$$\begin{aligned} A &\equiv \frac{I}{\Delta t} - \frac{1}{2}L\left\{;\nu^{n+1},\nu_r^{n+1}\right\} \\ &= \frac{I}{\Delta t} - \frac{1}{2}\left(L_{x_1}\{;\} + L_{x_2}\{;\} + L_{x_3}\{;\} + L_{cross}\{;\}\right) \end{aligned} \tag{4.15}$$

where

$L_{x_1}\{;\}$ - Spatially fourth-order discretization of the normal derivative term, $\frac{\partial}{\partial x_1}\left(.\frac{\partial(\bullet)}{\partial x_1}\right)$.

$L_{cross}\{;\}$ - Spatially second-order discretization of all the cross derivative terms.

The starting approximation used to define A' was,

$$A' = \frac{1}{\Delta t}\left(I + \frac{\Delta t}{2}L_{x_1}\right)\left(I + \frac{\Delta t}{2}L_{x_2}\right)\left(I + \frac{\Delta t}{2}L_{x_3}\right) \tag{4.16}$$

Here we have introduced the following 2 simplifications to approximate A:

1. The cross derivative terms are treated explicitly; and

2. The normal derivative terms in the different directions have been factored out separately just as one does in an ADI factorization. Each of these factors involves the inversion of linear systems for unknowns along lines in a single direction, say x_1. These are much easier to invert than the original matrix A.

Although the above definition of A' works well for a serial algorithm, the inversion along lines in the x_3 direction (due to the factor $\left(I + \frac{\Delta t}{2} L_{x_3}\right)$) makes it a a poor choice for a parallel algorithm. Just as in the pressure Poisson solver, inversion along lines in the x_3 direction requires swapping from $x_1 x_2$ planes in a process to $x_2 x_3$ planes. Since this requires communication of the order $O(N_1 N_2 N_3)$, computation and communication requirements are of the same order for this algorithm. The fact that we need to swap the planes in each sub-iteration further exacerbates the problem. Fig. 4.8 shows the fraction of time spent in swapping the planes in the subroutine which performs a single inversion of A'. It can be seen that communication is a significant fraction of the time for inverting A' in the case of large number of processes.

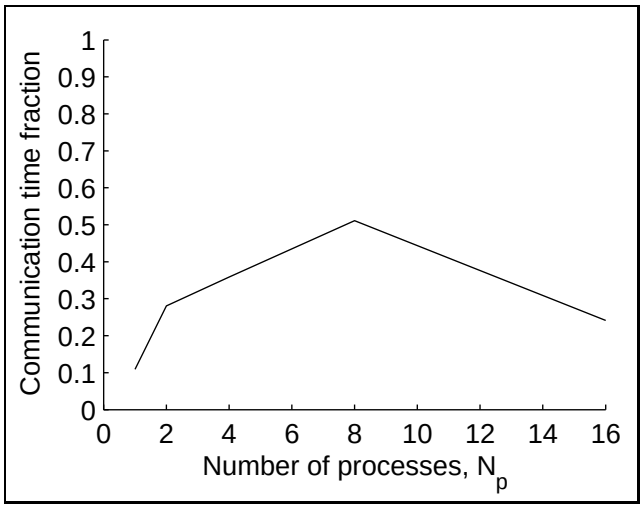

Figure 4.8: Fraction of time spent in swapping the planes in the subroutine which performs a single inversion of A'

In order to address the problem of poor parallel speedup, we modified the linear system arising in the x_3 direction such that we require no communication between processes. Typically we would need to solve a banded linear system along lines in the x_3 direction. Fig. 4.9 is a schematic representation of a tridiagonal

matrix in which the non-zero elements are denoted by either crosses or asterisks. The division of data among 4 (say) processes is denoted by dashed boxes. If the elements denoted by asterisks are zero then we would essentially have 4 smaller linear systems which can be solved without exchange of data between the processes.

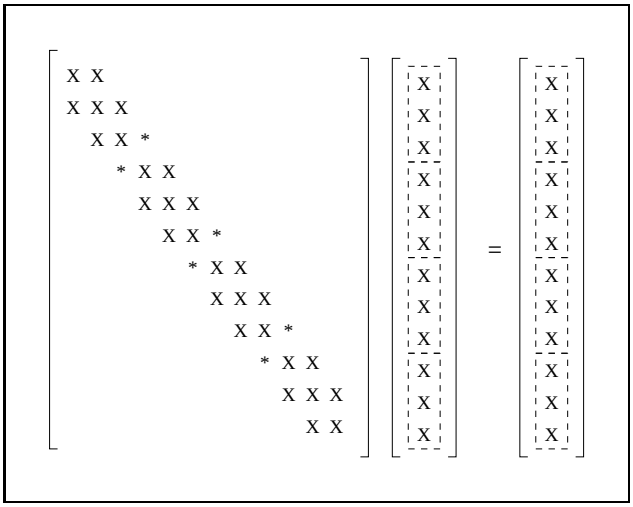

Figure 4.9: Schematic Representation of a tri-diagonal matrix in which non-zero elements are denoted by crosses and asterisks. Dashed box denotes the division of data between 4 (say) processes. Elements denoted by asterisks necessitate communication between process for solving the linear system.

So in order to solve a linear system which has minimum communication requirements we approximate the original matrix system arising along lines in the x_3 direction by taking the elements denoted by asterisks to be zero. We refer to this as using *broken lines in the x_3 direction*. So in the definition for the matrix A', Eq. (4.16), $\left(I + \frac{\Delta t}{2} L_{x_3}\right)$ has been replaced by broken lines in the x_3 direction. The inversion of A' now requires *no communication* between the processes. An algorithm very similar to the above can be found in Pierce (2001).

Figure 4.10 compares the parallel speedup of using broken lines in the x_3 direc-

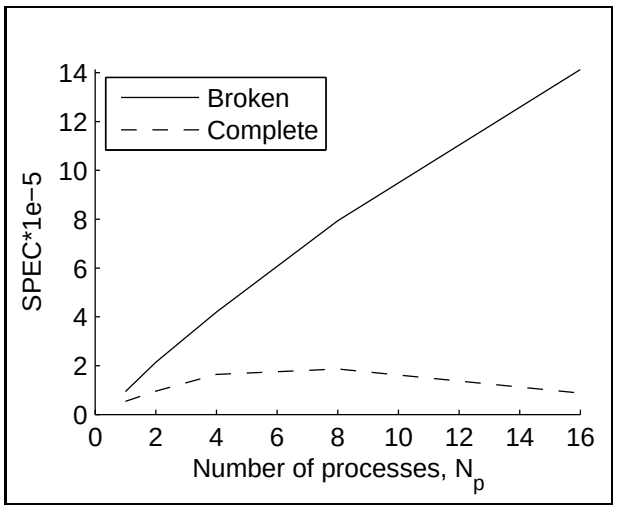

Figure 4.10: Comparison of the parallel performance of broken and complete lines in the x_3 direction for the ADI sub-iterations.

tion against the original ADI factorization, Eq. (4.16). We again look at the SPEC number for the subroutine which performs the matrix inversion of A' in each sub-iteration. The comparison was again made using the 2d periodic vortex problem on a 96^3 grid as a test problem. It is clear that the broken lines modification in the x_3 direction results in near linear speedup. The difference between the two methods becomes more pronounced when using larger number of processes because more elements in the banded linear system along lines in the x_3 direction are neglected. This degrades the convergence rate of the sub-iterations when using larger number of processes. However, typically we used only 4 processes and 2 sub-iterations were sufficient to make the residual error sufficiently small in all numerical simulations.

4.5 Code Validation

The code developed was extensively validated using both known analytical solutions for certain simple test problems and numerical solutions obtained from codes

developed outside Cornell. In this section we will present some of these code validation results. Checks of the order of accuracy of the code using the 2d periodic vortex problem as a test problem are first presented. We then compare the flow evolution obtained for the Taylor-Green vortex problem with a numerical simulation of the same flow carried out in Fluent. These tests give sufficient confidence on the working of the code.

4.5.1 2d periodic vortex

The 2d periodic vortex problem was extensively used to validate the spatial order of accuracy of the code. This is one of the few flow problems for which there is a known analytical solution. This allows us to compute errors in the computed numerical solution and study how these errors vary with grid spacing and time-step. The initial conditions for a periodic vorticial flow in the x_1x_3 plane are given by,

$$\begin{aligned} W_1(0) &= -\cos(x_1)\sin(x_3) \\ W_2(0) &= 0 \\ W_3(0) &= \cos(x_3)\sin(x_1) \end{aligned} \tag{4.17}$$

Since the sub-grid stress terms are of the same form as the viscous terms, the sub-grid viscosity, ν_r was set to 0 for code validation. The viscous evolution of the flow is such that the amplitude of the vortex decays exponentially in time. The time evolution of the flow is given by,

$$\begin{aligned} W_1(t) &= e^{-2\nu t}\left(-\cos(x_1)\sin(x_3)\right) \\ W_2(t) &= 0 \\ W_3(t) &= e^{-2\nu t}\left(\cos(x_3)\sin(x_1)\right) \end{aligned} \tag{4.18}$$

The numerical solutions are compared with the above analytical solution. In order to completely validate the difference coding for all 3 directions, solutions for a periodic vortex in the x_2x_3 plane were also computed. Although the test problem has some symmetries, any serious error in the code would have been detected using this test case.

A mesh refinement study used to verify the spatial order of accuracy is shown in Fig. 4.11. This 2d problem was simulated as a 3d problem with periodic boundary conditions in the x_2 direction. Periodic boundary conditions were also applied in the x_1 direction. Since the code had the capability to apply non-periodic boundary conditions in the x_3 direction, the implementation of these boundary conditions was verified as well using this test problem.

The problem was simulated in a box with edge length 2π. The time-step, Δt was fixed at 0.01 and the viscosity, ν was set to 0.01. To determine the spatial order of accuracy we used a sequence of uniform grids, 8^3, 16^3, 32^3, and 64^3 grids. The boundary conditions applied in the x_3 direction are given below,

- For the case, bc=per, Periodic boundary conditions in the x_3 direction for all 3 velocity components.

- For the case, bc=nper1

$$\begin{aligned} \frac{\partial W_1}{\partial x_3} = \frac{\partial^3 W_1}{\partial x_3^3} = 0 \quad \text{at } x_3 = \frac{\pi}{2}, \frac{5\pi}{2} \\ \frac{\partial W_2}{\partial x_3} = \frac{\partial^3 W_2}{\partial x_3^3} = 0 \quad \text{at } x_3 = \frac{\pi}{2}, \frac{5\pi}{2} \\ W_3 = \frac{\partial^3 W_3}{\partial x_3^3} = 0 \quad \text{at } x_3 = \frac{\pi}{2}, \frac{5\pi}{2} \end{aligned} \tag{4.19}$$

- For the case, bc=nper3

$$\begin{aligned} \frac{\partial W_1}{\partial x_3} = \frac{\partial^3 W_1}{\partial x_3^3} = 0 \quad \text{at } x_3 = \frac{\pi}{2}, \frac{5\pi}{2} \\ \frac{\partial W_2}{\partial x_3} = \frac{\partial^3 W_2}{\partial x_3^3} = 0 \quad \text{at } x_3 = \frac{\pi}{2}, \frac{5\pi}{2} \\ W_3 = \frac{\partial^2 W_3}{\partial x_3^2} = 0 \quad \text{at } x_3 = \frac{\pi}{2}, \frac{5\pi}{2} \end{aligned} \tag{4.20}$$

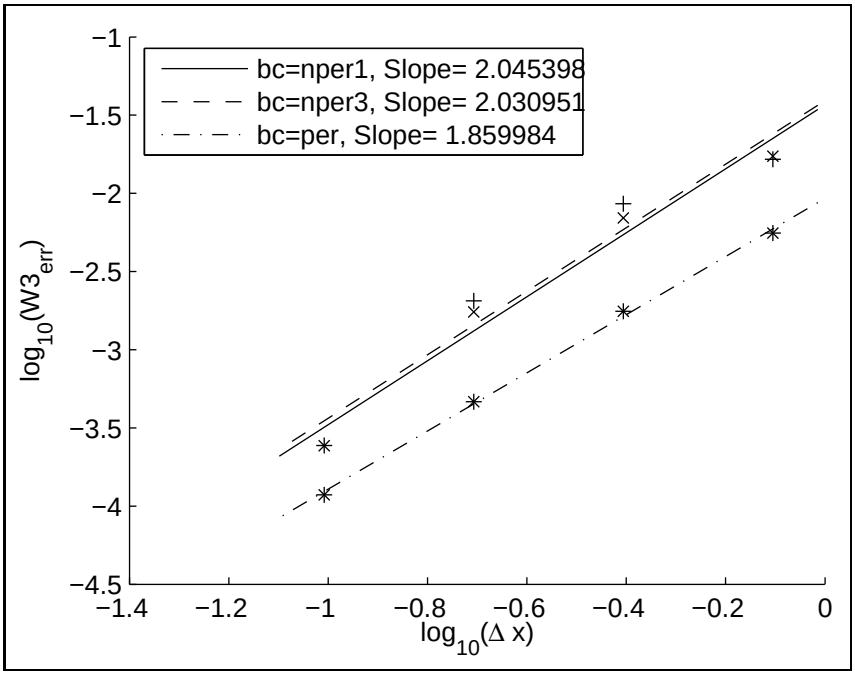

Figure 4.11: Variation of the rms error in W_3 with grid spacing, Δx on a log-log plot. Slope of the curve gives the spatial order of accuracy. Test problem was the 2d periodic vortex problem using different BCs in the x_3 direction.

Figure 4.11 shows the variation of the rms error in W_3 with grid spacing, Δx on a log-log plot. Slope of the curve gives the spatial order of accuracy and is around 2 for all three BCs. Since the cross derivative terms were the only terms which were discretized to second order spatial accuracy, we verified that the remaining terms were fourth order accurate by simply setting the cross derivative terms to zero. We also verified that the temporal order of accuracy was 2.

4.5.2 Taylor-Green vortex

Next, the code was used to carry out a DNS of the Taylor-Green vortex flow [Brachet *et al.* (1983)], and we compared our results with those from a Fluent simulation. This flow is one of the simplest systems in which one can study the generation of small scales and the turbulence resulting from the three-dimensional vortex stretching. The initial conditions for the Taylor-Green vortex flow are

$$\begin{aligned} u_1 &= \frac{2}{\sqrt{3}} \sin\left(\frac{2\pi}{3}\right) \sin(x_1)\cos(x_2)\cos(x_3) \\ u_2 &= \frac{2}{\sqrt{3}} \sin\left(-\frac{2\pi}{3}\right) \cos(x_1)\sin(x_2)\cos(x_3) \\ u_3 &= 0 \end{aligned} \tag{4.21}$$

Although the streamlines lie in the x_1x_2 plane at time $t = 0$, the flow soon becomes three-dimensional due to the variation in the x_3 direction introduced by the $\cos(x_3)$ term in the initial conditions.

The Reynolds number for this flow is defined as $Re = 1/\nu$. The DNS of the Taylor-Green flow was carried out for $Re = 50$ and 200. The simulations were carried out in a 3d box of edge length, 2π. A sequence of uniform grids, 24^3, 32^3, 48^3, 64^3, and 96^3, was used to study the variation of the flow evolution with grid spacing. In these simulations the cross derivative viscous terms were neglected and we expected fourth order spatial accuracy. The neglect of the cross derivative terms is justified in this case because the physical viscosity is constant in space; therefore the continuity equation forces their combined contribution to the evolution of momentum to be zero. All simulations were carried out at a constant time-step, $\Delta t = 0.00625$. Periodic boundary conditions were used in all directions. The Fluent simulations were carried out with the same parameter values. The Fluent simulations were carried out on Cartesian cubic grids with

the same number of grid points even though Fluent has the capability to use unstructured grids. Fluent also uses a spatially second order scheme.

Figures 4.12 and 4.13 compare the evolution of the volume-averaged dissipation at $Re = 50$ and 200, respectively. The figures show that the time histories of the dissipation are well predicted by our code. In Fig. 4.13 it can be seen that the peak of the dissipation rate was not determined correctly when the grid spacing was not small enough to resolve the small scale flow structures. Comparisons of the kinetic energy and the rate of change of kinetic energy were also made but are not presented here.

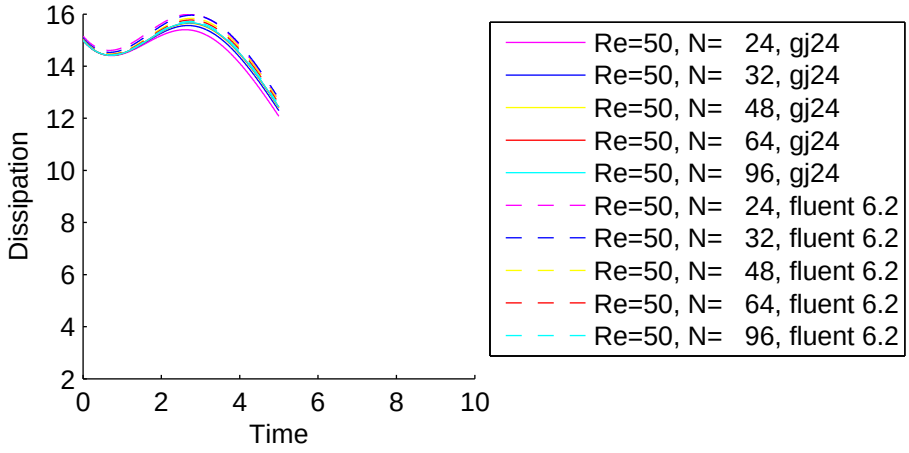

Figure 4.12: History of the volume-averaged dissipation rate for the Taylor-Green flow at $Re = 50$. Comparison with results from Fluent are shown in dashed lines.

Figure 4.14 shows the variation of volume-averaged dissipation rate at time $t = 2$ with N_{grid}^{-2} for $Re = 50$. Since we used a uniform grid, the number of grid points in each direction N_{grid} is inversely proportional to the grid spacing. The power of 2 was chosen because a spatially second-order scheme (such as the Fluent code) should produce a linear variation of the dissipation while a spatially fourth-order scheme (such as our code) would produce a quadratic variation at sufficiently

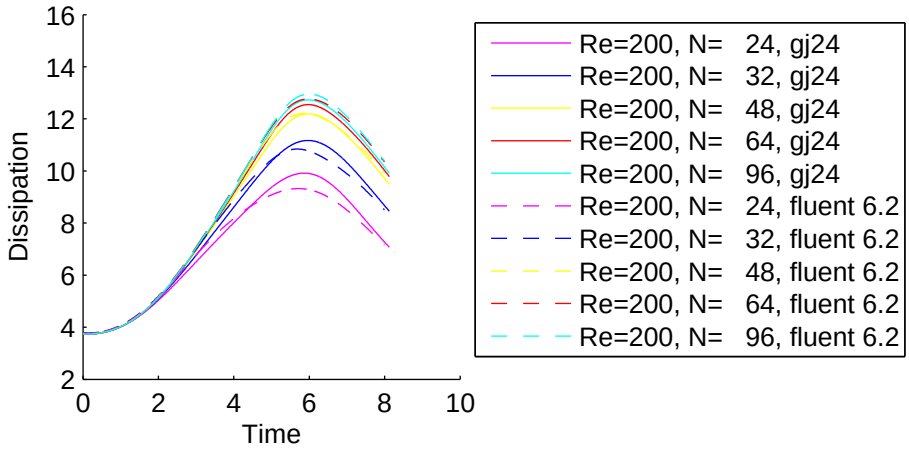

Figure 4.13: History of the volume-averaged dissipation rate for the Taylor-Green flow at $Re = 200$. Comparison with results from Fluent are shown in dashed lines.

small grid spacings. The curve fits in Fig. 4.14 was drawn using the data points at the smallest 2 grid spacings. Since the other data points, at least those at small grid spacings, lie very close to these curves, this is another verification that the spatial order of accuracy of our code is 4 and that of Fluent is 2. This figure further allows us to compare the asymptotic value of the volume-averaged dissipation obtained at zero grid spacing by determining the y-intercept. It can be seen that the asymptotic values for the 2 codes are virtually identical, further increasing the confidence in our code. Fig. 4.15 gives similar results for $Re = 200$ at time $t = 6$. At both Re, the time for comparison was chosen to be close to the peak of the dissipation rate so that the flow has sufficient small-scale structures. In Fig. 4.15, the curve was fitted only through the 48^3, 64^3 and 96^3 grids because the 24^3 and 32^3 grids do not resolve all the small-scale flow features.

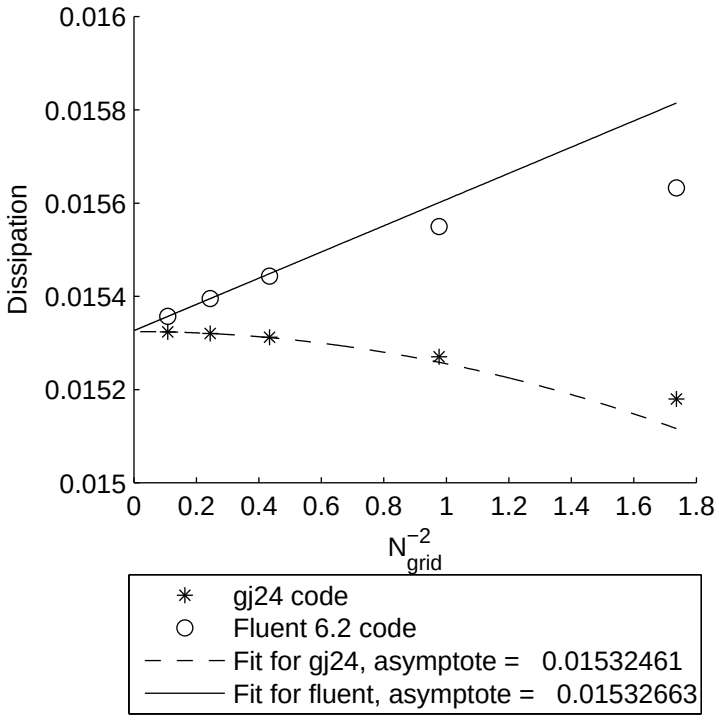

Figure 4.14: Variation of volume-averaged dissipation rate at time $t = 2$ with N_{grid}^{-2} for $Re = 50$. N_{grid} is the number of grid points in each coordinate direction.

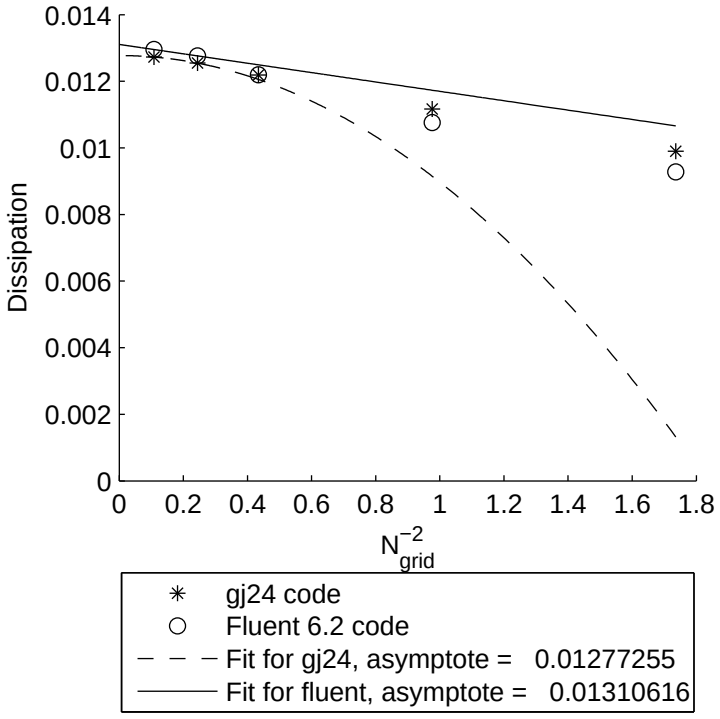

Figure 4.15: Variation of volume-averaged dissipation rate at time $t = 6$ with N_{grid}^{-2} for $Re = 200$. N_{grid} is the number of grid points in each coordinate direction.

Chapter 5

Forced isotropic turbulence

The issues with the LES methodology and their proposed solutions need to be studied in a wide range of turbulent flows to demonstrate their feasibility and importance. The simplest turbulent flow in which these issues can be addressed is forced, isotropic turbulence in which the statistics are independent of spatial location and time.

We start this chapter with a description of isotropic turbulence and its numerical simulation. An important difference between the two is that the use of a periodic box in the numerical simulation causes interaction between *discrete* Fourier modes as opposed to the *continuous* spectrum of Fourier modes present in the actual turbulent flow. The small wave number Fourier modes were artificially forced to sustain the turbulent motions as there was no mean flow for the eddies to extract energy. The Wray forcing used for this purpose is described. The generation of initial conditions to be used on the various grids starting from a turbulent flow with a specified model energy spectrum is then described.

We then proceed to study the convergence properties of the constant eddy-viscosity model by looking at the resolved KE. Comparisons were then made between the different sub-grid models to contrast their convergence properties and to determine the better sub-grid model. Next we illustrate the importance of modeling the statistics of the residual motions for improving the estimate of the required flow statistic. This is followed by a discussion of the choice of better values for the model parameters. In all the above studies, total KE of the turbulent flow was the statistic of interest. We end the chapter with the development of a model for the

1d velocity correlation.

5.1 Numerical simulation domain

Homogeneous, isotropic turbulence is a flow which is statistically invariant under translations, reflections and rotations of the coordinate system [Pope (2000*e*)]. Many wind-tunnel experiments [Comte-Bellot & Corrsin (1971); Mydlarski & Warhaft (1996)] and numerical simulations [Rogallo (1981); Yeung & Pope (1989)] of approximately isotropic turbulence have been performed to understand the nature of turbulent flows. Much of turbulence theory centers on homogeneous, isotropic turbulence because of the simplifications it affords.

Usually pseudo-spectral methods [Orszag & Patterson (1972); Rogallo (1981)] are preferred for numerical simulations of isotropic turbulence because of their accuracy. But here we carry out finite-volume simulations of isotropic turbulence in order to illustrate our ideas on LES methodology using a numerical procedure more commonly used in engineering applications. The solution domain is a periodic box with equal sides of length, L. The imposition of periodic boundary conditions restricts the wave numbers of allowed Fourier modes to integer multiples of the fundamental frequency,

$$\boldsymbol{\kappa} = \left(p_1 \left[\frac{2\pi}{L}\right], p_2 \left[\frac{2\pi}{L}\right], p_3 \left[\frac{2\pi}{L}\right] \right) \quad p_1, p_2, \text{ and } p_3 \text{ are integers} \tag{5.1}$$

This must be contrasted with the fact that in actual turbulent flow we have an infinite domain resulting in a continuous spectrum of Fourier modes interacting with each other. Also the use of a finite domain size in the numerical simulations places restrictions on the length scale of the largest motions which can be resolved.

The other restriction emerges from the use of a grid with uniform grid spacing

Δx in all directions. This places a restriction on the length scale of the smallest motions which can be resolved. So the wave numbers of the allowed Fourier modes are,

$$\kappa_i = p_i \left[\frac{2\pi}{L}\right] \quad 0 \leq p_i \leq N-1, p_i \text{ an integer} \tag{5.2}$$

where $N = L/(\Delta x)$ = number of grid points in each direction. So care must be taken to ensure that the grid chosen for the LES resolves all the features of the LES field, W_i.

All simulations were carried out in a periodic cube with each side having length $L = 2\pi$.

5.2 Limit of infinite Re

LES is a simulation methodology designed for high Re flows. So, all our simulations of isotropic turbulence were carried out in the limit of infinite Re by simply setting the physical viscosity to zero. The length scale of the smallest eddies which need to be resolved in the LES is determined by the eddy viscosity. Based on this length scale, the grid spacing for the LES was chosen.

Although modeling a turbulent flow in the limit of infinite Re is the correct Re range for LES comparisons and verifications, it leads us to the interesting question of how to obtain the statistics of a turbulent flow in the limit of infinite Re. We would be required to perform a DNS with infinite resolution which is clearly not feasible. So we achieve this limit of infinite Re by extrapolating the statistics obtained from DNS simulations carried out at as high a Re as possible. More details on this extrapolation procedure for the statistic of KE are given in section 5.6.4 where we study the convergence properties of the constant eddy-viscosity sub-grid model.

It must be mentioned that such extrapolation procedures were not exhaustively investigated in this work, although such procedures could also play an important role in testing and verifying sub-grid models. Most sub-grid model comparisons are currently carried out at low to moderate Re because of the computational requirements of the DNS with which the LES is compared.

5.3 Definitions of Fourier transforms

In the following sub-sections we discuss the Fourier transforms in a finite periodic domain. We relate the energy spectrum function defined in this domain to that defined on an infinite domain. These definitions are also required to interpret the results of the isotropic flow simulations. More details can be found in Pope ($2000c$).

5.3.1 Fourier modes in a periodic, finite domain

In a periodic 3d box, the Fourier transform $\mathcal{F}_\kappa\{\bullet\}$ is given by,

$$\begin{aligned}\hat{W}_j(\boldsymbol{\kappa},t) &\equiv \mathcal{F}_\kappa\{W_j(\mathbf{x},t)\}\\ &\equiv \left\langle W_j(\mathbf{x},t)\, e^{-i\boldsymbol{\kappa}\cdot\mathbf{x}}\right\rangle_{123}\\ &\equiv \frac{1}{L^3}\int_0^L\!\!\int\!\!\int W_j(\mathbf{x},t)\, e^{-i\boldsymbol{\kappa}\cdot\mathbf{x}}\mathbf{dx}\end{aligned} \tag{5.3}$$

where L denotes the length of each side of the periodic box and $\langle\bullet\rangle_{123}$ denotes the volume average over the periodic box. The Fourier coefficients, which are represented by $\hat{\bullet}$ in Eq. (5.3), are defined for discrete values of $\boldsymbol{\kappa}$ which are integer multiples of $2\pi/L$.

The Fourier coefficients of the two-point velocity correlation, $R_{ij}^W(\mathbf{r})$, are denoted by $\hat{R}_{ij}^W(\boldsymbol{\kappa})$ and are related to the Fourier coefficients of the velocity field (for

more details see Pope (2000c), Pg 215) as follows,

$$\begin{aligned}\hat{R}_{ij}^{W}(\boldsymbol{\kappa}) &\equiv \left\langle \hat{W}_i^{*}(\boldsymbol{\kappa},t)\,\hat{W}_j(\boldsymbol{\kappa},t)\right\rangle \\ &= \left\langle \hat{W}_i(-\boldsymbol{\kappa},t)\,\hat{W}_j(\boldsymbol{\kappa},t)\right\rangle \\ &= \mathcal{F}_{\kappa}\left\{R_{ij}^{W}(\mathbf{x},t)\right\}\end{aligned} \tag{5.4}$$

$\hat{R}_{ij}^{W}(\boldsymbol{\kappa})$ is defined at discrete values of $\boldsymbol{\kappa}$ while the velocity-spectrum tensor $\Phi_{ij}^{W}(\boldsymbol{\kappa})$ is a continuous function of $\boldsymbol{\kappa}$. Hence the two are related using Delta functions by,

$$\Phi_{ij}^{W}(\overline{\boldsymbol{\kappa}}) = \sum_{\boldsymbol{\kappa}} \delta(\overline{\boldsymbol{\kappa}} - \boldsymbol{\kappa})\,\hat{R}_{ij}^{W}(\boldsymbol{\kappa}) \tag{5.5}$$

We end this sub-section with the definition of kinetic energy of a Fourier mode $\hat{E}(\boldsymbol{\kappa},t)$ which is used in the next sub-section to relate the energy spectra in the finite and infinite domain cases. As earlier, the kinetic energy of a Fourier mode $\hat{E}(\boldsymbol{\kappa},t)$ is obtained by removing all directional information as follows,

$$\begin{aligned}\hat{E}^{W}(\boldsymbol{\kappa},t) &\equiv \frac{1}{2}\hat{W}_i^{*}(\boldsymbol{\kappa},t)\,\hat{W}_i(\boldsymbol{\kappa},t) \\ &= \frac{1}{2}\hat{R}_{ii}^{W}(\boldsymbol{\kappa},t)\end{aligned} \tag{5.6}$$

5.3.2 Relation between energy spectra defined in the infinite and finite domains

The energy spectrum for a function defined on an infinite domain is a continuous function of κ while for a function defined on a finite, periodic box the energy is concentrated in Delta functions located at discrete locations in wave number space. So we define the instantaneous energy spectrum function in a finite, periodic box

by equating the kinetic energy in a spherical shell of wave numbers centered around κ and finite thickness $\Delta\kappa$,

$$\begin{aligned}\int_{\kappa-\frac{\Delta\kappa}{2}}^{\kappa+\frac{\Delta\kappa}{2}} E^W(\kappa,t)d\kappa &= \sum_{\boldsymbol{\kappa} \text{ in shell}} \hat{E}^W(\boldsymbol{\kappa},t) \\ &= \sum_{\boldsymbol{\kappa} \text{ in shell}} \frac{1}{2}\left\langle \hat{W}_i^*(\boldsymbol{\kappa},t)\,\hat{W}_i(\boldsymbol{\kappa},t)\right\rangle\end{aligned} \tag{5.7}$$

The number of wave numbers M_κ, in the shell centered around κ, approximately scales as the surface area of the spherical shell

$$M_\kappa \approx \frac{4\pi\kappa^2\Delta\kappa}{\Delta\kappa^3} = \frac{4\pi\kappa^2}{\Delta\kappa^2} \tag{5.8}$$

Thus, Eq. (5.7) allows us to obtain the energy spectrum from the kinetic energy of the discrete Fourier modes.

5.4 Wray Forcing

Isotropic turbulence has no mean flow, which implies that the large eddies cannot extract any energy from the mean flow to sustain the turbulent motions. So isotropic turbulence, left to itself, decays under the action of viscosity. It is decaying, isotropic turbulence which is studied in the various experiments [Mydlarski & Warhaft (1996); Comte-Bellot & Corrsin (1971)]. Further, in decaying isotropic turbulence, the smallest motions in the flow decay faster than the large motions, thereby reducing the range of length scales in the flow. So even if we start with a high Re turbulent flow with a wide range of length and time scales, as time progresses the range of scales become smaller and smaller, making the turbulence modeling using LES less applicable. So we artificially force the largest eddies in the flow to sustain the turbulent motions. Forced, isotropic turbulence has the added

benefit that the flow becomes statistically stationary in time. Hence, a statistic such as resolved KE can be obtained by not only volume-averaging (because isotropic turbulence is statistically homogeneous) but also through time-averaging.

Many forcing schemes have been used in literature [Yeung & Brasseur (1991); Eswaran & Pope (1988); Overholt & Pope (1998)]. We chose to use the Wray forcing scheme primarily because of its simplicity and because it is known to have performed reasonably in earlier simulations [Lamorgese *et al.* (2005)]. The Wray forcing scheme is best explained in Fourier space. We force the Fourier modes with wavenumber magnitude less than κ_f by including a production term in the evolution equation for these modes. The production term is chosen to be proportional to the Fourier coefficients of the forced velocity modes and to add energy to the flow at a specified rate, $\mathcal{P}$. So the evolution equation of the forced modes is modified as follows,

$$\frac{\partial \hat{W}_i(\boldsymbol{\kappa}, t)}{\partial t} = \ldots + \frac{\mathcal{P}}{2E_f^W(t)} \hat{W}_i(\boldsymbol{\kappa}, t) \tag{5.9}$$

where E_f denotes the kinetic energy in the Fourier modes being forced, and is given by,

$$E_f^W(t) \equiv \sum_{|\boldsymbol{\kappa}|<\kappa_f} \hat{E}^W(\boldsymbol{\kappa}, t) = \sum_{|\boldsymbol{\kappa}|\geq\kappa_f} \frac{1}{2} \hat{W}_i^*(\boldsymbol{\kappa}, t) \hat{W}_i(\boldsymbol{\kappa}, t) \tag{5.10}$$

In our numerical implementation, the production term was first computed in Fourier space and then transformed to physical space using inverse FFTs. Also, in all our simulations, $\kappa_f = 3$ and $\mathcal{P} = 1$.

5.5 Initial Conditions

The flow must reach a statistically stationary state in time before we can collect statistics such as volume- and time-averaged KE. This statistically stationary state

is reached by starting from an artificial turbulent flow chosen to match a given model energy spectrum. It is expected that the final statistically stationary state reached is independent of the initial conditions used. However, the use of an initial condition matching the expected energy spectrum reduces the time required to reach this statistically stationary state. Once this statistically stationary state is reached, we can measure the required statistics of the flow. In this section we describe the model energy spectrum chosen and the procedure used to determine the artificial flow from the model energy spectrum. Again, this procedure is best explained in Fourier space.

Figure 5.1 shows the chosen model energy spectrum in a log-log plot. It is

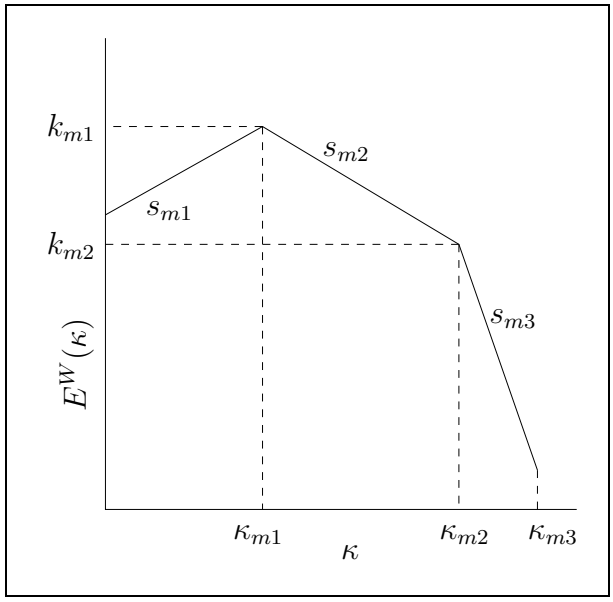

Figure 5.1: Given model energy spectrum in a log-log plot.

a simple energy spectrum with power-law variations of the energy density in all the wavenumber ranges. The parameters defining the model energy spectrum are chosen as follows,

- The peak of the model energy spectrum κ_{m1} was assumed to occur at the

maximum forcing wavenumber, κ_f. So $\kappa_{m1} = \kappa_f = 3$.

- The initial slope s_{m1} was chosen to be 2 corresponding to equal energy in all the Fourier modes with $|\boldsymbol{\kappa}| \leq \kappa_{m1}$.

- The peak of the energy spectrum k_{m1} was arbitrarily taken to be 0.2403 simply to set the initial kinetic energy to be approximately unity.

- The slope s_{m2} was chosen to be $-5/3$ based on the expected slope in the inertial sub-range.

- The cutoff wavenumber κ_{m3} was taken to be $N\left(\frac{2\pi}{L}\right) = N$ where N is the number of grid points in each direction.

- κ_{m2} which signifies the end of the inertial sub-range was arbitrarily taken to be $10\left(\frac{2\pi}{L}\right) = 10$

- The slope s_{m3} was assumed to be equal to s_{m2}. This makes the value of κ_{m2} irrelevant.

Again, too much importance need not be given to the values defining the model energy spectrum because we expect the final statistically stationary state to be independent of the choice of initial conditions.

Equation (5.7) allows us to compute the energy spectrum given the Fourier coefficients of the velocity. But now we are faced with the inverse problem where we need to compute the Fourier coefficients given the energy spectrum. Clearly, the energy spectrum does not uniquely specify the Fourier coefficients of the velocity field and additional assumptions need to be made to obtain the Fourier coefficients. These assumptions are mentioned when needed.

In the following three sub-sections, we describe the procedure used to determine the Fourier coefficients $\hat{W}_j(\boldsymbol{\kappa}, 0)$ of the velocity field. First, we describe how the magnitude of the Fourier modes, $|\hat{\mathbf{W}}(\boldsymbol{\kappa}, 0)|$, can be determined using the given model energy spectrum. Next, the Fourier coefficients, $\hat{W}_j(\boldsymbol{\kappa}, 0)$, are fully determined such that the continuity equation is satisfied. Finally, certain symmetry conditions, imposed by the fact that the velocity field is real are described. We conclude with a brief description of the volume fluxes and pressure field chosen for the initial conditions.

5.5.1 Magnitude of the Fourier modes

First, we determine the magnitude of the Fourier coefficients of the velocity. Eq. (5.7) relates the energy in a given wavenumber shell to the magnitude of the Fourier coefficients. Further, assuming that all Fourier modes in the given shell have the same kinetic energy, and approximating the integral in the LHS, we have,

$$\begin{aligned}\int_{\kappa-\frac{\Delta\kappa}{2}}^{\kappa+\frac{\Delta\kappa}{2}} E^W(\kappa,t)d\kappa &\approx E^W(\kappa,t) * (\Delta\kappa) \\ &= M_\kappa \left\{ \frac{1}{2} \left\langle \hat{W}_i^*(\boldsymbol{\kappa},t)\, \hat{W}_i(\boldsymbol{\kappa},t) \right\rangle \right\}\end{aligned} \tag{5.11}$$

Hence, the magnitude of the Fourier mode in a given shell is given by,

$$|\hat{\mathbf{W}}(\boldsymbol{\kappa},t)| = \sqrt{\frac{E^W(\kappa,t)\,(\Delta\kappa)}{M_\kappa}} \tag{5.12}$$

We chose the spherical shells to be centered at $\kappa = \left(\frac{2\pi}{L}\right) p = p$ with $\Delta\kappa = \frac{2\pi}{L} = 1$ and p a positive integer.

5.5.2 Individual components of the Fourier modes

The continuity equation, Eq. (2.2), in Fourier space is given by,

$$W_i \kappa_i = 0 \tag{5.13}$$

Geometrically, this means that $\hat{\mathbf{W}}$ must lie in a plane perpendicular to $\boldsymbol{\kappa}$. This is illustrated graphically in Fig. 5.2. We first find 2 orthonormal vectors in the

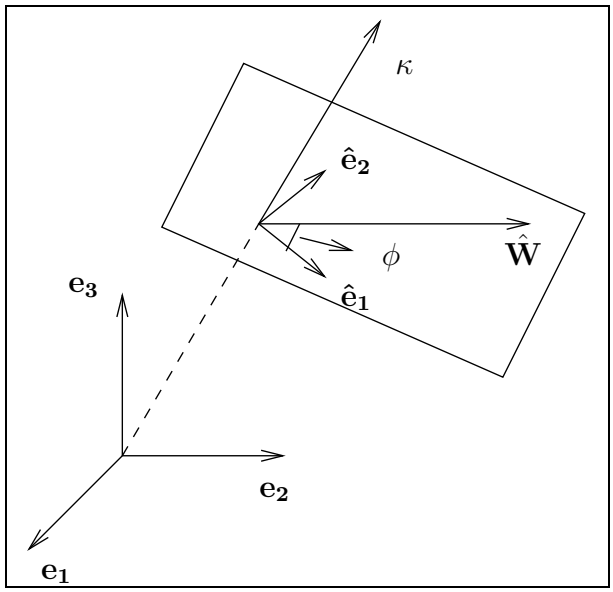

Figure 5.2: Determination of the individual components of the Fourier modes such that continuity is satisfied.

plane perpendicular to $\boldsymbol{\kappa}$. These are given by,

$$\hat{\mathbf{e}}_\mathbf{1} \equiv \frac{\boldsymbol{\kappa} \times \mathbf{e_1}}{|\boldsymbol{\kappa} \times \mathbf{e_1}|} \tag{5.14}$$

$$\hat{\mathbf{e}}_\mathbf{2} \equiv \frac{\boldsymbol{\kappa} \times \mathbf{e_2}}{|\boldsymbol{\kappa} \times \mathbf{e_2}|} \tag{5.15}$$

Let ϕ be the angle that $\hat{\mathbf{W}}$ makes with $\hat{\mathbf{e}}_\mathbf{1}$ and let the complex components of $\hat{\mathbf{e}}_\mathbf{1}$ and $\hat{\mathbf{e}}_\mathbf{2}$ be $e^{-i\theta_1}$ and $e^{-i\theta_2}$ respectively, then we determine,

$$\hat{\mathbf{W}} = \sqrt{\frac{E^W(\kappa,t)}{2\pi\kappa^2}\left(\Delta\kappa\right)^3}\left\{\left(e^{-i\theta_1}\cos\phi\right)\hat{\mathbf{e}}_\mathbf{1} + \left(e^{-i\theta_2}\sin\phi\right)\hat{\mathbf{e}}_\mathbf{2}\right\} \tag{5.16}$$

The angles ϕ, θ_1, θ_2 are chosen randomly from independent uniform distributions.

5.5.3 Symmetry conditions

The fact that the velocity field is real imposes certain symmetry conditions on the generated Fourier coefficients. These symmetry conditions require that only half the Fourier coefficients of the velocity field are independent and hence only half the Fourier coefficients are generated. This allows the complex Fourier coefficients of the velocity to be stored in the same array space used to store the real velocity field. Also, for some Fourier coefficients, the simplest way to satisfy these symmetry conditions along with the divergence restriction is to simply set these coefficients to zero. This was done at the following locations in Fourier space,

- $(0, 0, 0)$,
- Plane of wave numbers, $\boldsymbol{\kappa} = (N_1/2, i_2, i_3)$, $i_2 = 0, N_2$, $i_3 = 0, N_3$.
- Plane of wave numbers, $\boldsymbol{\kappa} = (i_1, i_2, N_3/2)$, $i_1 = 0, N_1$, $i_2 = 0, N_2$.
- Plane of wave numbers, $\boldsymbol{\kappa} = (i_1, N_2/2, i_3)$, $i_1 = 0, N_1$, $i_3 = 0, N_3$.

where N_i refers to the number of grid points in the i direction.

Now the velocity field is fully determined to match the given model energy spectrum function. Figure 5.3 shows the energy spectrum of the generated velocity fields on various grids, along with the model energy spectrum specified. The deviation at the high wave numbers is due to enforcing the symmetry conditions as described above.

The above procedure determines the velocity field at the cell centers. For a collocated grid layout, the volume fluxes at the cell faces also need to be specified as part of the initial conditions. These volume fluxes must satisfy the discrete continuity equation, Eq. (3.35), so that the convective terms are energy conserving.

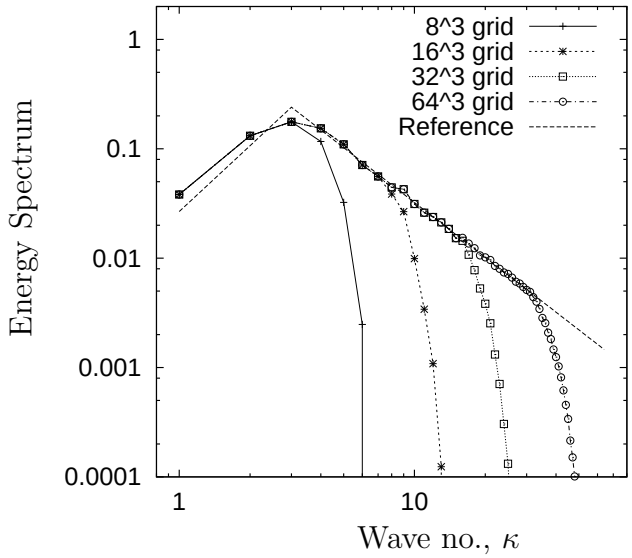

Figure 5.3: Energy spectrum of the generated velocity field on different grids to match a specified model energy spectrum.

In general, the volume fluxes, obtained by interpolating the velocity field, will not satisfy the discrete continuity equation. However, these volume fluxes can be easily projected onto a divergence-free space by carrying out a single pressure step, as described in section 3.3.3. Finally, the pressure field, which is also part of the initial conditions, can be set to zero everywhere. The very first time step is first-order accurate in time because the convective terms are discretized using an explicit Euler scheme instead of the Adams-Bashforth scheme.

Once the above initial conditions have been generated, the flow is evolved until a statistically stationary or steady state is reached. We ensured that a statistically stationary state is reached by ensuring that the volume-averaged dissipation and energy spectrum became stationary in time. Figure 5.4 shows the initial time evolution of the volume-averaged resolved KE and SGS production for the LES on a 32^3 grid using the constant eddy-viscosity sub-grid model with $\nu_r = 0.0413$. The

statistics were averaged in time only after time $t = 129$. Figure 5.4 shows that the flow has evolved well beyond the initial transient even at time $t = 100$.

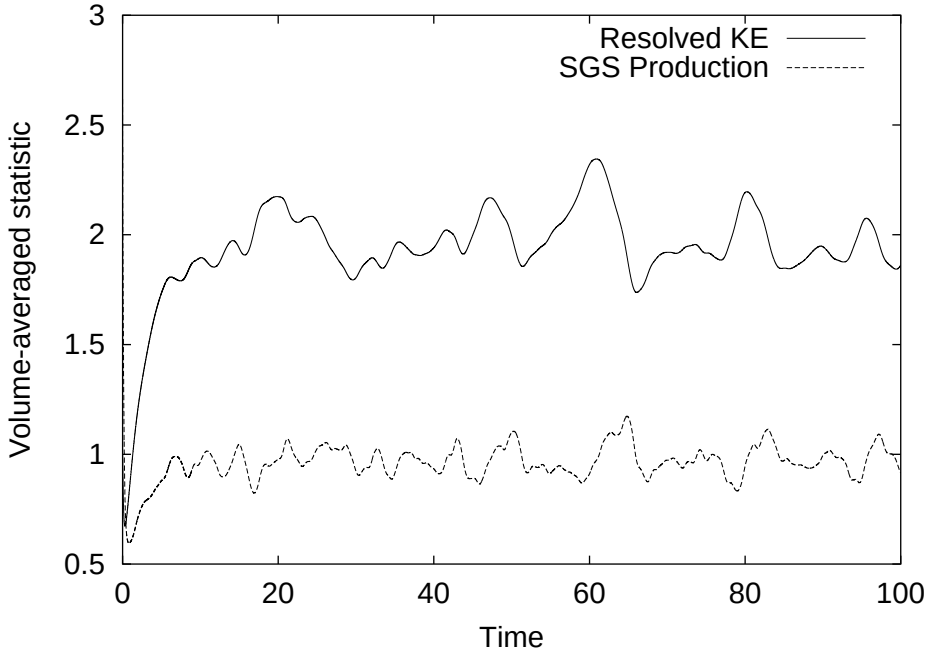

Figure 5.4: Initial time evolution of the volume-averaged resolved KE and SGS production for the LES on a 32^3 grid using the constant eddy-viscosity sub-grid model with $\nu_r = 0.0413$.

5.6 Convergence properties of constant eddy viscosity model

We now proceed to answer the questions on convergence with resolution length scale of an LES approach. These questions are first answered in the context of isotropic turbulence using the simplest LES sub-grid model: the constant eddy viscosity model. In this and following sections, the primary statistic whose convergence is studied is the kinetic energy of the turbulence motions. In this section, we first relate the resolution length scale Δ to the eddy viscosity ν_r. A sequence of

simulations at varying resolution length scales is needed to study the convergence properties of the constant eddy viscosity model. So we describe the numerical simulation parameters chosen to resolve the LES fields, followed by a discussion on the convergence of the resolved KE. The parallel between carrying out a LES in the limit of infinite Re using the constant eddy viscosity model and a DNS at finite Re is used to reinterpret the convergence results.

5.6.1 Choice of numerical parameter values

In the constant eddy viscosity model the eddy viscosity ν_r is chosen to be constant in both space and time. The value of ν_r determines the length scale of the smallest eddies in the LES. So we first describe how ν_r was chosen such that the smallest eddies in the LES field are of the order of the resolution length scale Δ.

The resolution length scale Δ defines a dissipation wave number, $\kappa_d = \frac{\pi}{\Delta}$, which signifies the wave number for the smallest resolved scales in the LES. Based on Kolmogorov's hypotheses [Kolmogorov (1991); Pope (2000f)], the energy spectrum in the inertial sub-range of a fully developed turbulent flow is given by

$$E(\kappa) = C_0 \epsilon^{\frac{2}{3}} \kappa^{-\frac{5}{3}} \tag{5.17}$$

where C_0 is the Kolmogorov constant. Experimental data [Saddoughi & Veeravalli (1994)] suggests a value of 1.5 for C_0. At steady state, the dissipation ϵ in the turbulent flow is balanced by the production $\mathcal{P}$ due to Wray forcing. So ϵ can be replaced by $\mathcal{P}$ in Eq. (5.17)

A simple model for the energy spectrum of the resolved LES field would be to extend the above form for the energy spectrum, Eq. (5.17), into the energy

containing range, and to place a sharp spectral cutoff at $\kappa = p_1\kappa_d$.

$$E^W(\kappa) \stackrel{M}{=} \begin{cases} C_0\mathcal{P}^{\frac{2}{3}}\kappa^{-\frac{5}{3}} & \text{for } \kappa \leq p_1\kappa_d \\ 0 & \text{for } \kappa > p_1\kappa_d \end{cases} \tag{5.18}$$

where p_1 is a non-dimensional parameter of $O(1)$, as the smallest eddies which are resolved in the LES are $O(\kappa_d)$.

At steady state, the production due to Wray forcing $\mathcal{P}$ is in balance with the rate at which the viscous and sub-grid terms remove energy from the LES field W_i. The energy removed by the viscous term from the LES field is negligible because it is dominant only in the dissipation range which is not resolved in an LES. Further, since we are simulating the limit of infinite Re, the contribution from the viscous term is identically zero. The sub-grid model term transfers energy from the resolved LES field to the residual or unresolved fields. So the energy transfer due to the sub-grid model term is called sub-grid scale (SGS) production, $\mathcal{P}_\mathcal{R}$

The mean SGS production, $\langle\mathcal{P}_R\rangle$, can be estimated using the model for the energy spectrum as shown below,

$$\begin{aligned} \langle\mathcal{P}_R\rangle &= \int_0^\infty \nu_r\kappa^2 E^W(\kappa)\,d\kappa \\ &= \int_0^{p_1\kappa_d} \nu_r\kappa^2 E^W(\kappa)\,d\kappa \\ &= \frac{3}{4}\nu_r C_0\mathcal{P}^{\frac{2}{3}}(p_1\kappa_d)^{\frac{4}{3}} \end{aligned} \tag{5.19}$$

We now solve for ν_r using the fact that the mean SGS production $\langle\mathcal{P}_R\rangle$ is in balance with the production $\mathcal{P}$,

$$\begin{aligned} \nu_r &= \frac{4}{3C_0}\mathcal{P}^{\frac{1}{3}}(p_1\kappa_d)^{-\frac{4}{3}} \\ &= \frac{4}{3C_0}\mathcal{P}^{\frac{1}{3}}\left(p_1\frac{\pi}{\Delta}\right)^{-\frac{4}{3}} \\ &\approx \frac{4}{3C_0}\mathcal{P}^{\frac{1}{3}}\left(\frac{\pi}{\Delta}\right)^{-\frac{4}{3}} \end{aligned} \tag{5.20}$$

Equation (5.20) provides a specification of ν_r so that the smallest eddies in the LES field are of the order of the resolution length scale. Also in the very last step of Eq. (5.20), assuming p_1 to be one provides a good enough approximation for ν_r.

Care was taken to numerically resolve all the features of the LES field by choosing the uniform grid spacing, Δx to be around 2Δ. In all simulations we set $\mathcal{P} = 1$. The integral time scale of the flow was estimated to be around 7 time units using a test simulation. In order to reduce the statistical error introduced by time averaging, the flow was simulated for a time period of 140 time units after steady state was reached. Table 5.1 summarizes the values of other numerical parameters in the LES carried out to study the convergence with Δ for the constant eddy-viscosity model. To provide a perspective on the times required to carry out these LES simulations, rough measurements of the wall-clock times are given in Table 5.2. Since a queuing system was not in place in the JIT cluster, other jobs may have been executed at the same time and in the same processes used for these LES. The broken lines modification (see section 4.4), to obtain improved parallel speedup, was not implemented at the time of these simulations.

5.6.2 Lilly's analysis for resolved KE variation

The statistic whose convergence is studied is the resolved KE. The kinetic energy is the simplest statistic which can be studied in isotropic turbulence. Since statistics in forced isotropic turbulence are independent of spatial location and time, the KE can be computed by volume- and time-averaging. As mentioned earlier, performing an LES of isotropic turbulence decomposes the total KE into a part which is resolved by the LES and that which is unresolved. So the resolved KE, $\langle k_W \rangle$, refers to the KE contained in the motions resolved by the LES and is computed

Table 5.1: Summary of numerical parameters in the LES carried out to study the convergence with Δ of the constant eddy-viscosity model. Notation used: resolution length scale Δ, dissipation Wave no. κ_d, number of grid points in each direction N, eddy viscosity ν_r, and time step Δt.

Δ	κ_d	N	ν_r	Δt
0.785	4	16	0.1400	0.020
0.628	5	16	0.1040	0.020
0.524	6	24	0.0815	0.015
0.393	8	32	0.0556	0.010
0.314	10	32	0.0413	0.010
0.224	14	48	0.0263	0.0075
0.175	18	64	0.0188	0.005
0.121	26	96	0.0115	0.004
0.092	34	128	0.0081	0.003

Table 5.2: Rough measurements of the wall-clock times for the LES simulations carried out to study the convergence with Δ of the constant eddy-viscosity model. Notation used: resolution length scale Δ, number of grid points in each direction N, time step Δt, number of time-steps, N_{TS}, wall-clock time per time-step, $T_{\Delta t}$, wall-clock time, T_W, and number of processes, N_p.

Δ	N	Δt	N_{TS}	$T_{\Delta t}$ (secs)	T_W (secs)	T_W (days)	N_p
0.785	16	0.020	7000	0.143	999.0	0.012	1
0.628	16	0.020	7000	0.105	731.7	0.008	1
0.524	24	0.015	9334	0.378	3529.7	0.041	2
0.393	32	0.010	14000	1.080	15122.4	0.175	4
0.314	32	0.010	14000	0.752	10527.7	0.122	2
0.224	48	0.0075	18667	2.240	41891.7	0.485	4
0.175	64	0.005	28000	4.560	127662.8	1.480	4
0.121	96	0.004	35000	11.440	400519.8	4.640	4
0.092	128	0.003	46667	27.860	1300145.0	15.050	4

as,

$$\langle k_W \rangle \equiv \left\langle \frac{1}{2} W_i W_i \right\rangle_{L,t} \tag{5.21}$$

where $\langle \rangle_{123,t}$ denotes volume- and time-averaging.

Before we look at the convergence of the resolved KE, we determine the power-law variation of resolved KE at small values of Δ. This was done primarily to plot the various convergence graphs against the right power of Δ. The rate at which KE in the unresolved motions decreases would be the same rate at which the resolved KE increases as we reduce Δ toward zero. So by estimating the power-law variation of the residual KE, which is the energy in the eddies not resolved in the LES, we can determine the power-law variation of resolved KE.

A simple model for the energy spectrum $E^R(\kappa)$ of the residual motions is,

$$E^R(\kappa) \stackrel{M}{=} \begin{cases} 0 & \text{for } \kappa < p_1 \kappa_d \\ C_0 \mathcal{P}^{\frac{2}{3}} \kappa^{-\frac{5}{3}} & \text{for } \kappa \geq p_1 \kappa_d \end{cases} \tag{5.22}$$

where p_1 is some non-dimensional constant. The above model simply extends the behavior expected in the inertial sub-range of fully developed turbulent flows to $\kappa = \infty$. This is a reasonable assumption because we are trying to simulate isotropic turbulence in the limit of infinite Re where we expect the dissipation range to tend towards ∞. The other modeling assumption is that we have a sharp spectral cutoff at $\kappa = p_1 \kappa_d$ which simply signifies that the LES resolves all the motions with wave number less than $p_1 \kappa_d$.

The above model for the energy spectrum $E^R(\kappa)$ allows us to determine the

variation of $\langle k_R \rangle$ with κ_d and hence Δ. The mean residual KE $\langle k_R \rangle$ is given by

$$\begin{aligned} \langle k_R \rangle &= \int_0^\infty E^R(\kappa) d\kappa \\ &= \int_{p_1 \kappa_d}^\infty C_0 \mathcal{P}^{\frac{2}{3}} \kappa^{-\frac{5}{3}} d\kappa \\ &= C_0 \mathcal{P}^{\frac{2}{3}} \left(p_1 \kappa_d\right)^{-\frac{2}{3}} \\ &= C_0 \mathcal{P}^{\frac{2}{3}} \left(p_1 \pi\right)^{-\frac{2}{3}} \Delta^{\frac{2}{3}} \end{aligned} \tag{5.23}$$

So we expect the residual KE $\langle k_R \rangle$ and the resolved KE $\langle k_W \rangle$ to vary as $\Delta^{\frac{2}{3}}$ at sufficiently small values of Δ. Such analysis, where we assume simple models for the energy spectrum to determine the power-law variation with Δ of required statistics, originated with Lilly [Lilly (1967); Pope ($2000d$)]. We refer to similar analysis as Lilly's analysis in the rest of thesis.

5.6.3 Statistical error due to time-averaging

In this sub-section, we briefly indicate how we estimated the statistical error in the *finite* time-average of the volume-averaged resolved KE. Basically, we are given a time-series d_1, d_2, d_3, ... d_N with N samples and where successive samples are separated by a time Δt. The average computed from this finite series is

$$\langle d \rangle_N \equiv \frac{1}{N} \sum_{n=1}^{N} d_n \tag{5.24}$$

If successive samples were statistically independent, a good estimate for the variance in $\langle d \rangle_N$ is

$$\text{var}\left(\langle d \rangle_N\right) = N \, \text{var}\left(d\right) \tag{5.25}$$

where $\text{var}\left(d\right)$, the variance of the given time-series, can be computed using

$$\text{var}\left(d\right) \stackrel{C}{=} \frac{1}{N-1} \sum_{n=1}^{N} \left(d_N - \langle d \rangle_N\right)^2 \tag{5.26}$$

However, the samples are not statistically independent but correlated over an integral time scale T_i. We obtained an estimate for the integral time scale T_i from the auto-correlation of the given time series. Using this integral time scale we can improve the above estimate for $\mathrm{var}\left(\langle d \rangle_N\right)$ to

$$\frac{\mathrm{var}\left(\langle d \rangle_N\right)}{\mathrm{var}\left(d\right)} = \frac{1}{N}\left[\frac{1+r}{1-r}\right] - \frac{1}{N^2}\left[\frac{2r\left(1-r^N\right)}{1-r^2}\right] \tag{5.27}$$

where $r = e^{-\frac{\Delta t}{T_i}}$. The above expression assumes that $\langle d(t)d(t+s)\rangle = e^{-\frac{s}{T_i}}$. More details can be found in Papoulis (1991).

5.6.4 Convergence of resolved KE

Figure 5.5 shows the observed variation of resolved KE with $\Delta^{\frac{2}{3}}$ for the constant eddy-viscosity model. A straight line fit through the first four points is also shown.

The most important observation is that the resolved KE converges at $\Delta = 0$. Although it is widely expected that the statistics obtained from LES would converge as $\Delta \to 0$, this is the first time it has been demonstrated. Another observation is that the resolved KE does vary as $\Delta^{\frac{2}{3}}$ at small Δ, but deviates from this behavior at larger Δ.

Next, to answer the question whether the asymptote to which the resolved KE converges is the same as the KE of the underlying turbulent velocity field, we reinterpret the LES we have carried out as a DNS at finite Re. The constant eddy-viscosity sub-grid model has exactly the same form as the physical viscous terms because the eddy-viscosity is taken to be constant in space and time. Hence, the above numerical simulations can be interpreted as

- LES of isotropic turbulence in the limit of infinite Re; or

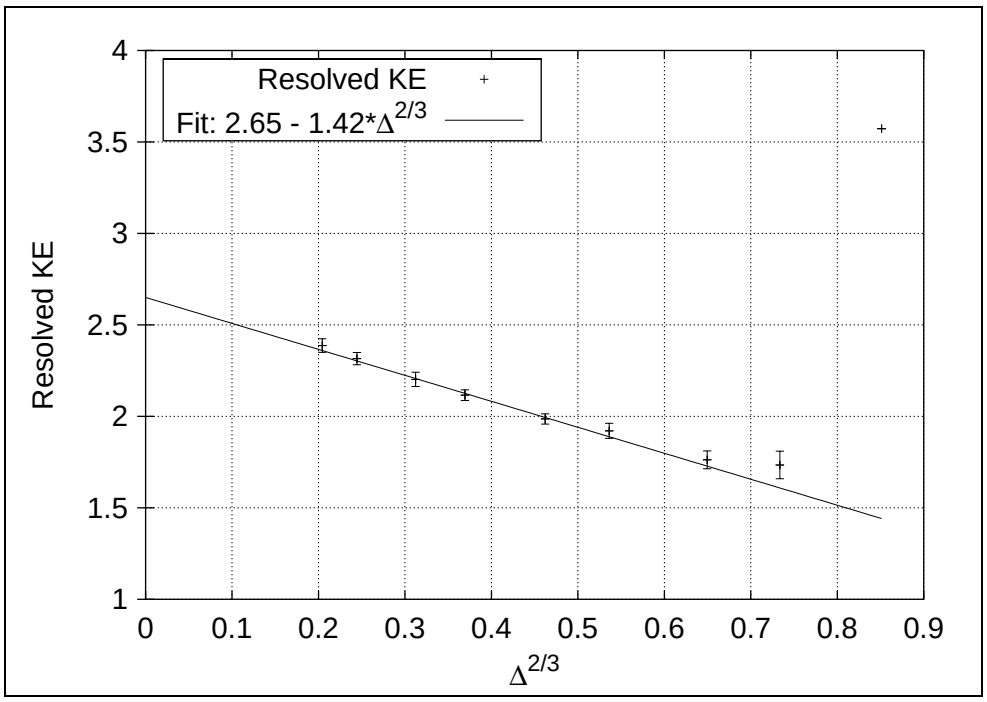

Figure 5.5: Variation of resolved KE with $\Delta^{\frac{2}{3}}$ for the Constant eddy-viscosity model.

- DNS of isotropic turbulence at a finite Re, where the Re is based on the eddy-viscosity ν_r instead of the physical viscosity ν.

The second interpretation, as a DNS, allows us to interpret the asymptote as the value of total KE of isotropic turbulence in the limit of infinite Re. Since it is not possible to carry out a DNS in the limit of infinite Re we need to resort to such indirect techniques to determine the statistics in the limit of infinite Re. Further, the above interpretation of the simulation trivially shows that the resolved KE from the LES using the constant eddy-viscosity model converges to the KE of the underlying turbulent velocity field.

LES is a turbulence modeling procedure designed for high Re flows. However most comparisons and verifications of LES are carried out for small to moderate Re flows because of the computational limitations placed by the DNS required to

compare the LES statistics. Hence, extrapolation techniques (similar to the one above) to determine the statistics of a high Re flow using the statistics computed from the DNS at a lower Re need to be investigated further. The development of this idea would allow comparisons of LES to be made at the high Re for which the technique was designed.

5.7 Comparison of sub-grid models

In the previous section, we have shown that the LES approach using the constant eddy viscosity sub-grid model is a convergent approach. We now study convergent LES approaches using other sub-grid models and determine whether they converge to the same asymptote. We also compare the performance of various sub-grid models. In this section we compare the constant eddy-viscosity, the Smagorinsky, and Model k_R equation models in the context of forced isotropic turbulence. We first describe the numerical simulations carried out, and then give results on the convergence of resolved KE used for comparing the various sub-grid models.

5.7.1 Choice of numerical parameter values

Since the parameter values used in the LES using the constant eddy viscosity model have already been described, we describe here only the parameter values chosen for the LES using the Smagorinsky and Model k_R equation sub-grid models. The two model parameters which need to be specified in both these models are C_ν and C_E (see Eqs. (2.9), (2.16), and (2.19)). In this sub-section, we start with the estimates for C_ν and C_E based on Lilly's analysis, followed by our choice of values for these parameters. Finally, we give details on the grid spacings chosen for the various resolution length scales.

Estimates of C_ν and C_E based on Lilly's analysis can be found in Schmidt & Schumann (1989). Here we present a sketch of the analysis. The basis of this analysis is the assumption for the energy spectrum $E^W(\kappa)$ of the resolved LES field, Eq. (5.18), and the energy spectrum $E^R(\kappa)$ of the residual velocity field, Eq. (5.22). Throughout this sub-section, we assume $p_1 = 1$, as we are again interested in only rough estimates.

The following two estimates are used frequently in the derivations to follow.

- Estimate for the mean residual KE $\langle k_R \rangle$:

$$\begin{aligned} \langle k_R \rangle &= \int_0^\infty E^R(\kappa) d\kappa \\ &= \int_{\pi/\Delta}^\infty E^R(\kappa) d\kappa \\ &= \int_{\pi/\Delta}^\infty C_0 \mathcal{P}^{2/3} \kappa^{-5/3} d\kappa \\ &= \frac{3}{2} C_0 \mathcal{P}^{2/3} \left(\frac{\pi}{\Delta}\right)^{-2/3} \end{aligned} \tag{5.28}$$

- Estimate for the mean square of characteristic strain rate $\mathcal{S}^W$ of the resolved LES field:

$$\begin{aligned} \left\langle \mathcal{S}^W \mathcal{S}^W \right\rangle &= 2 \left\langle S_{ij}^W S_{ij}^W \right\rangle \\ &= \int_0^\infty 2\kappa^2 E^W(\kappa) d\kappa \\ &= \int_0^{\pi/\Delta} 2\kappa^2 E^W(\kappa) d\kappa \\ &= \int_0^{\pi/\Delta} 2 C_0 \mathcal{P}^{2/3} \kappa^{1/3} d\kappa \\ &= \frac{3}{2} C_0 \mathcal{P}^{2/3} \left(\frac{\pi}{\Delta}\right)^{4/3} \end{aligned} \tag{5.29}$$

In LES of high Re isotropic turbulence, there is a balance in the mean between production due to forcing $\mathcal{P}$ and the SGS production $\mathcal{P}_R$. Further, using the

sub-grid model for determining $\mathcal{P}_R$, we can estimate C_ν.

$$\begin{aligned}
\mathcal{P} &\approx \langle \mathcal{P}_R \rangle \\
&\stackrel{M}{=} \left\langle 2\nu_r S_{ij}^W S_{ij}^W \right\rangle \\
&= \left\langle 2C_\nu \Delta k_R^{1/2} S_{ij}^W S_{ij}^W \right\rangle \\
&\approx C_\nu \Delta \left\langle k_R^{1/2} \right\rangle \left\langle 2S_{ij}^W S_{ij}^W \right\rangle \\
&= C_\nu \left(\frac{3}{2} C_0 \right)^{3/2} \pi \mathcal{P}
\end{aligned} \tag{5.30}$$

The above implies,

$$C_\nu = \left(\frac{3}{2} C_0 \right)^{-3/2} \frac{1}{\pi} \approx 0.094 \tag{5.31}$$

when $C_0 = 1.5$

In an LES of high Re isotropic turbulence, most of the viscous dissipation occurs in the unresolved eddies and so there is also a balance in the mean between production due to forcing $\mathcal{P}$ and SGS dissipation ϵ_R. Again using the model for SGS dissipation ϵ_R we can estimate C_E:

$$\begin{aligned}
\mathcal{P} &\approx \langle \epsilon_R \rangle \\
&\stackrel{M}{=} \left\langle \frac{C_E k_R^{3/2}}{\Delta} \right\rangle \\
&= \frac{C_E \left\langle k_R^{3/2} \right\rangle}{\Delta} \\
&= C_E \left(\frac{3}{2} C_0 \right)^{3/2} \frac{\mathcal{P}}{\pi}
\end{aligned} \tag{5.32}$$

The above implies,

$$C_E = \left(\frac{3}{2} C_0 \right)^{-3/2} \pi \approx 0.93 \tag{5.33}$$

Finally, the Model k_R equation also requires a turbulent Prandtl number σ_k to be chosen for the residual KE equation. The parameter σ_k is usually chosen

arbitrarily [Schmidt & Schumann (1989); Deardorff (1980)] or through a dynamic procedure [Ghosal *et al.* (1995)] .

The above estimates, parameter values used in literature [Schmidt & Schumann (1989); Deardorff (1980, 1974); Mason (1989)], and the values chosen for our LES are summarized below.

1. C_ν

   - $C_\nu = 0.094$ is obtained using Lilly's analysis for a sharp spectral cutoff energy spectrum along with the Kolmogorov constant, $C_0 = 1.5$.
   - Values used in the literature cited above range from 0.0646 to 0.1.
   - Value used in our LES, $C_\nu = 0.094$.

2. C_E

   - $C_E = 0.93$ is obtained using Lilly's analysis for a sharp spectral cutoff energy spectrum along with the Kolmogorov constant, $C_0 = 1.5$.
   - Values used in the literature cited above range from 0.0634 to 0.845.
   - Value given by Deardorff (1980), $C_E = 0.7$, is most commonly used in the meteorological community.
   - Value used in our LES, $C_E = 0.7$.

3. σ_k

   - σ_k cannot be determined from Lilly's analysis.
   - Values used in the literature cited above range from 0.2 to 1.0.
   - Value used in our LES, $\sigma_k = 1.0$.

Again, the numerical grid resolution and the time step were chosen to resolve all the flow features of the LES field. The production due to forcing is set at $\mathcal{P} = 1$ and the flow was simulated for a time period of 140 time units after a statistically stationary state was reached. Table 5.3 summarizes the values of other numerical parameters in the LES carried out to compare the three sub-grid models.

Table 5.3: Summary of numerical parameters in the LES carried out to study the convergence with Δ of the Smagorinsky and Model k_R equation models. Notation used: resolution length scale Δ, dissipation wave number κ_d, number of grid points in each direction N, time step used in the Smagorinsky model Δt_{Smag}, and time step used in the Model k_R equation model Δt_{Modkr}.

Δ	κ_d	N	Δt_{Smag}	Δt_{Modkr}
0.785	4	16	0.020	0.005
0.628	5	16	0.020	0.005
0.524	6	24	0.015	0.003
0.393	8	32	0.010	0.0025
0.314	10	32	0.010	0.0025
0.224	14	48	0.0075	0.00165
0.175	18	64	0.005	0.00125
0.121	26	96	0.004	0.000825

The Model k_R equation sub-grid model requires the evolution of the modeled transport equation for the residual KE, Eq. (2.19), along with that of the governing LES equations, Eqs. (2.1)-(2.2). The numerical algorithm [Kurganov & Tadmor (2000)] used to advance the modeled transport equation for k_R ensured that k_R

remains positive at all locations and times. However, this algorithm imposed a CFL restriction which caused the time step for the Model k_R equation model to be much smaller than that for the Smagorinsky model. It should be noted that Δt_{Smag} was sufficiently small to achieve the required accuracy in the LES with the Smagorinsky model.

Again, to provide a perspective on the times required to carry out these LES simulations, rough measurements of the wall-clock times are given in Tables 5.4 and 5.5. Since a queuing system was not in place in the JIT cluster, other jobs may have been executed at the same time and in the same processes used for these LES. The broken lines modification (see section 4.4), to obtain improved parallel speedup, was implemented at the time of these simulations. This accounts for the improvement in the wall-clock timings per time-step as compared with the LES using constant eddy-viscosity model (see Tables 5.2). The increased computational cost of the Model k_R equation as compared with the Smagorinsky model is largely from the increase in the number of time-steps required for the Model k_R equation.

5.7.2 Sub-grid model comparison based on resolved KE

Figure 5.6 shows the variation of resolved KE with $\Delta^{\frac{2}{3}}$ for all three sub-grid models. There are two important observations:

- All three sub-grid models, to within statistical error, converge to the same asymptote. By within statistical error, we mean that it is possible to draw the fit lines from a single asymptote for all three sub-grid models but such that they lie within the statistical error bars for the resolved KE at small values of Δ. Further, this asymptote is also the expected value for the KE of the underlying turbulent velocity field in the limit of infinite Re. Again,

Table 5.4: Rough measurements of the wall-clock times for the LES simulations carried out to study the convergence with Δ of the Smagorinsky model. Notation used: resolution length scale Δ, number of grid points in each direction N, time step Δt, number of time-steps, N_{TS}, wall-clock time per time-step, $T_{\Delta t}$, wall-clock time, T_W, and number of processes, N_p.

Δ	N	Δt	N_{TS}	$T_{\Delta t}$ (secs)	T_W (secs)	T_W (days)	N_p
0.785	16	0.020	7000	0.059	416.1	0.005	1
0.628	16	0.020	7000	0.059	410.3	0.005	1
0.524	24	0.015	9334	0.407	3804.5	0.044	2
0.393	32	0.010	14000	0.338	4736.6	0.055	4
0.314	32	0.010	14000	0.381	5338.8	0.062	4
0.224	48	0.0075	18667	0.884	16507.1	0.191	4
0.175	64	0.005	28000	1.785	49966.2	0.578	4
0.121	96	0.004	35000	6.055	211924.5	2.453	4

Table 5.5: Rough measurements of the wall-clock times for the LES simulations carried out to study the convergence with Δ of the Model k_R equation model. Notation used: resolution length scale Δ, number of grid points in each direction N, time step Δt, number of time-steps, N_{TS}, wall-clock time per time-step, $T_{\Delta t}$, wall-clock time, T_W, and number of processes, N_p.

Δ	N	Δt	N_{TS}	$T_{\Delta t}$ (secs)	T_W (secs)	T_W (days)	N_p
0.785	16	0.005	28000	0.138	3859.9	0.045	1
0.628	16	0.005	28000	0.138	3868.5	0.045	1
0.524	24	0.003	46667	0.316	14765.4	0.171	2
0.393	32	0.0025	56000	0.445	24943.1	0.289	4
0.314	32	0.0025	56000	0.414	23192.8	0.268	4
0.224	48	0.00165	84848	1.554	131831.5	1.526	4
0.175	64	0.00125	112000	3.259	365012.4	4.225	4
0.121	96	0.000825	169697	6.709	1138437.7	13.176	4

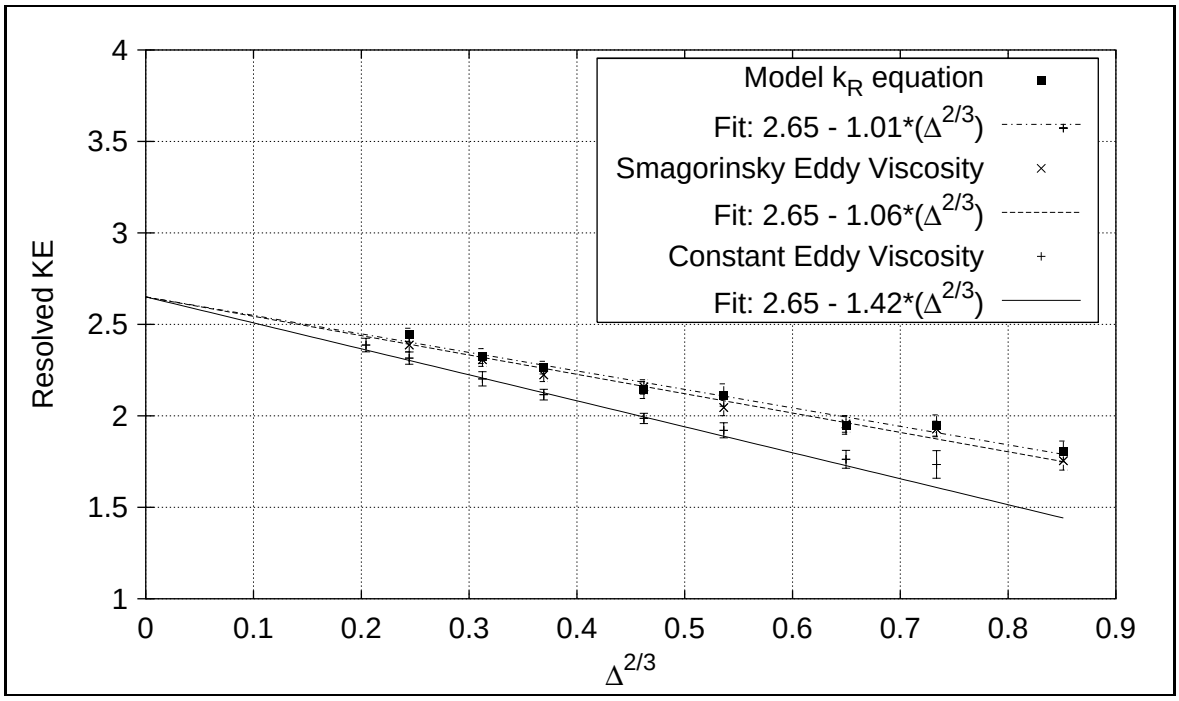

Figure 5.6: Variation of resolved KE with $\Delta^{\frac{2}{3}}$ for the Constant eddy-viscosity, Smagorinsky, and Model k_R equation sub-grid models.

for the first time, it has been demonstrated that statistics obtained using different sub-grid models converge to the same asymptote at $\Delta = 0$.

- We can now compare the performance of the three sub-grid models. The model k_R equation performs the best because, for a given value of Δ, it estimates a resolved KE which is closer to the asymptote at $\Delta = 0$ than other sub-grid models. The Smagorinsky model is a close second, while the performance of the Constant eddy-viscosity model is the worst. Since simulations at a given value of Δ are carried out on similar numerical grids they have similar computational costs. So Fig. 5.6 determines the best model in terms of computational cost as well.

5.8 Improvement of convergence using modeled residual statistics

The Smagorinsky and Model k_R equation sub-grid models also include models for the energy in the unresolved motions. Currently, most LES do not use the information in k_r beyond the model for the sub-grid stresses. However, k_r can be used to improve the estimate of KE of the underlying turbulent motions. In all earlier sections, the resolved KE was considered to be the LES estimate for the KE. However, we can now estimate the KE of the underlying turbulent motions as the sum of the resolved and residual KE. In isotropic turbulence, the mean residual KE is computed by volume- and time-averaging k_R.

$$\langle k_R \rangle \equiv \langle k_R(\mathbf{x}, t) \rangle_{L,t} \tag{5.34}$$

The new LES estimate for the KE is the Total KE defined as,

$$\text{Total KE} \equiv \text{Resolved KE} + \text{Residual KE} = \langle k_W \rangle + \langle k_R \rangle \tag{5.35}$$

Figure 5.7 illustrates the advantage of using the model for the residual KE present in the Smagorinsky model to improve the estimate for the KE. It can be

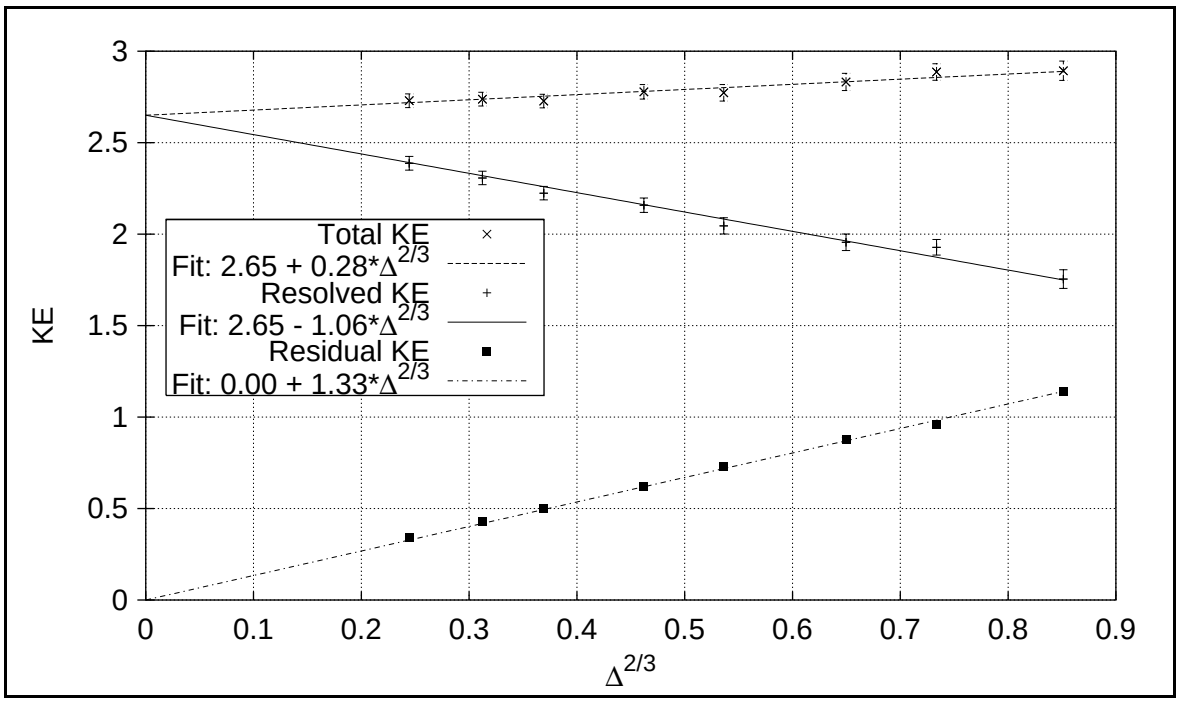

Figure 5.7: Total KE, defined to be the sum of resolved KE and modeled residual KE, is closer to the asymptote at $\Delta = 0$ than the resolved KE. Results from LES using Smagorinsky model.

seen that the Total KE is closer to the asymptote at $\Delta = 0$ than the resolved KE at all values of Δ. This means that the convergence property of the Smagorinsky model was improved by including the model for the residual KE. The model for the residual KE can also be used to estimate the fraction of the energy resolved in an LES carried out at a specified Δ. Figure 5.8 shows that the same observations hold for the Model k_R equation sub-grid model as well.

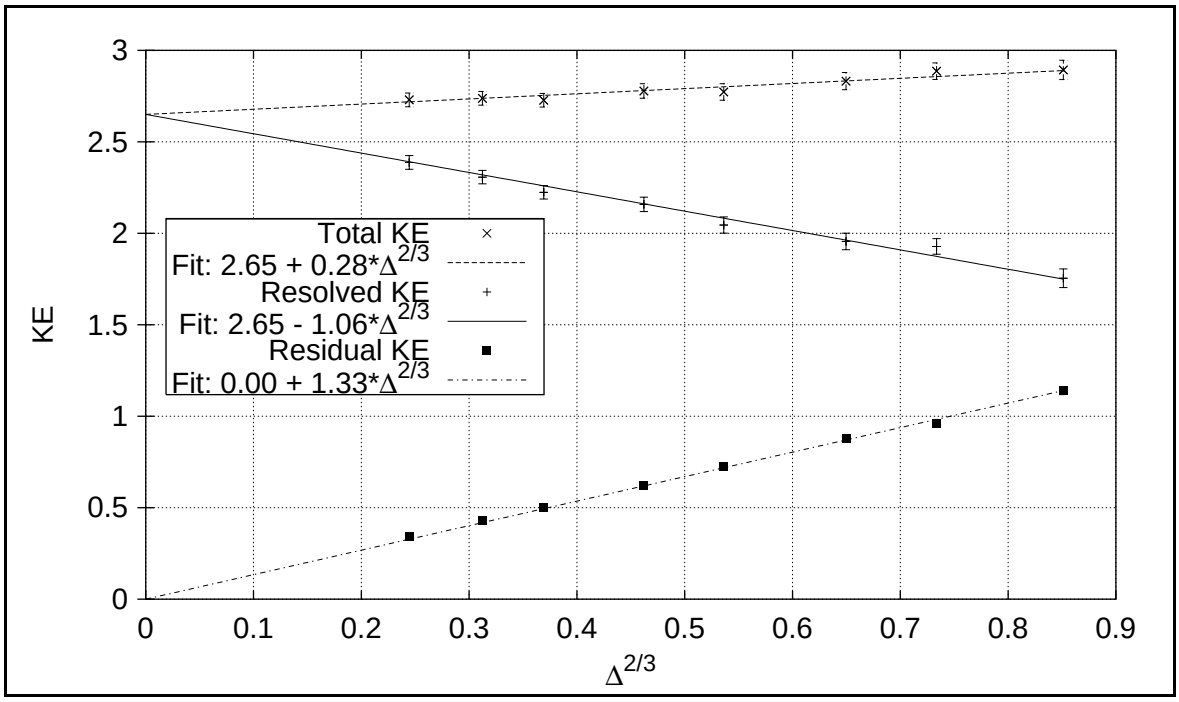

Figure 5.8: Total KE, defined to be the sum of resolved KE and modeled residual KE, is closer to the asymptote at $\Delta = 0$ than the resolved KE. Results from LES using Model k_R equation model.

5.9 Better choice of model parameter values

It can be argued that better choice of model parameter values would correspond to those values which improve the convergence properties of a desired statistic (here KE). In fact, it was suggested earlier (see section 2.6) that the best values for the model parameters are those which remove the leading order Δ dependence of the total KE. In this section we show how the values of the model parameters, C_ν and C_E were improved for the Smagorinsky sub-grid model. These ideas are then extended for the model k_R equation model.

5.9.1 Smagorinsky model

The total, resolved, and residual KE all vary as $\Delta^{2/3}$ to leading order in Δ. The goal is to choose values for the model parameters, C_ν and C_E, in such a way that the leading order $\Delta^{2/3}$ term in the total KE is eliminated. We have already performed LES simulations using the Smagorinsky model with one set of model parameter values, $C_\nu = 0.094$ and $C_E = 0.7$. The brute force search for better model parameter values is to choose another set of values, re-run all the LES simulations at various Δ using this new set and see if the leading order term in total KE has vanished. If not, repeat the above steps until we find the required set of values. Interestingly, in the case of Smagorinsky model, there is a clever way to search for better model parameter values without repeating the LES simulations.

Equation (2.17) shows that C_ν and C_E enter the evolution equation for the resolved velocity field W_i only in the ratio $\frac{C_\nu^{3/2}}{C_E^{1/2}}$. So if the values for C_ν and C_E are changed such that $\frac{C_\nu^{3/2}}{C_E^{1/2}}$ remains unchanged, then the LES velocity field remains unchanged. This means that we do not need to repeat the simulations to find the

optimal values of the model parameters. If we change the model parameters such that,

$$\begin{aligned} C_\nu &\rightarrow a^{-1/2} C_\nu \\ C_E &\rightarrow a^{-3/2} C_E \end{aligned} \tag{5.36}$$

where a is some constant, then the LES velocity field W_i remains unaffected, but $k_R(\mathbf{x}, t)$ changes to,

$$k_R(\mathbf{x}, t) \rightarrow a k_R(\mathbf{x}, t) \tag{5.37}$$

because k_R is proportional to $C_\nu^{3/2}/C_E^{1/2}$ (see Eq. (2.16)). Since the only change is that the residual KE field is multiplied by the same constant a at every location in space and time, the mean residual KE is also multiplied by the same constant a while the resolved KE remains unchanged. This property can be used to modify the model parameter values to those which remove the leading order Δ term in the total KE without performing new LES simulations.

Figure 5.9 compares the total KE variation with Δ for two different sets of model parameter values. It can be seen that for the second set, the leading order Δ term in the total KE drops out. This is a great improvement, because irrespective of the resolution length scale Δ used in the LES, we obtain the same estimate for the total KE.

5.9.2 Model k_R equation model

In this sub-section, we determine the values of C_ν and C_E which remove the leading order term in the total KE using the Model k_R equation sub-grid model. While the special property available in the case of Smagorinsky model was no longer available for the Model k_R equation model, meaning that we had to repeat the LES simulations for different sets of values, some of the arguments in the earlier

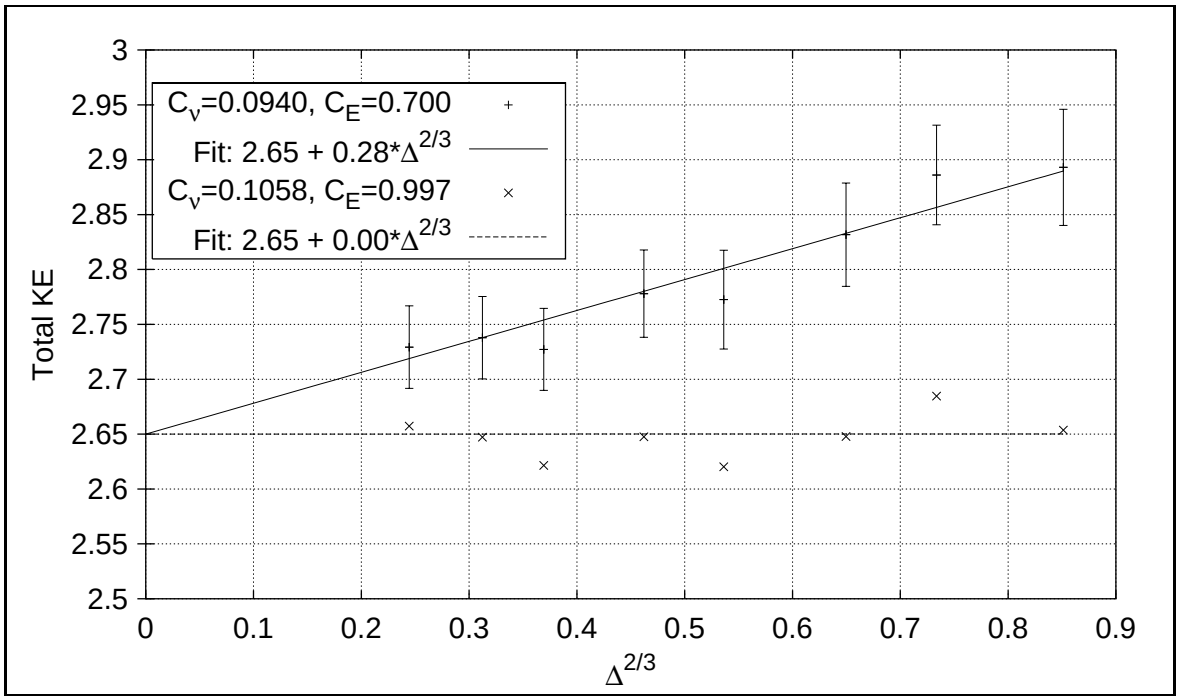

Figure 5.9: Total KE variation with Δ for two different sets of model parameter values using the Smagorinsky sub-grid model.

sub-section were used to determine a good choice for the parameter values instead of simply guessing. Figure 5.10 compares the total KE variation with Δ for two different sets of model parameter values. Although the leading order Δ term was not completely removed, the second set of parameter values clearly performs better than the first, and also suggests that the optimal values have been bracketed.

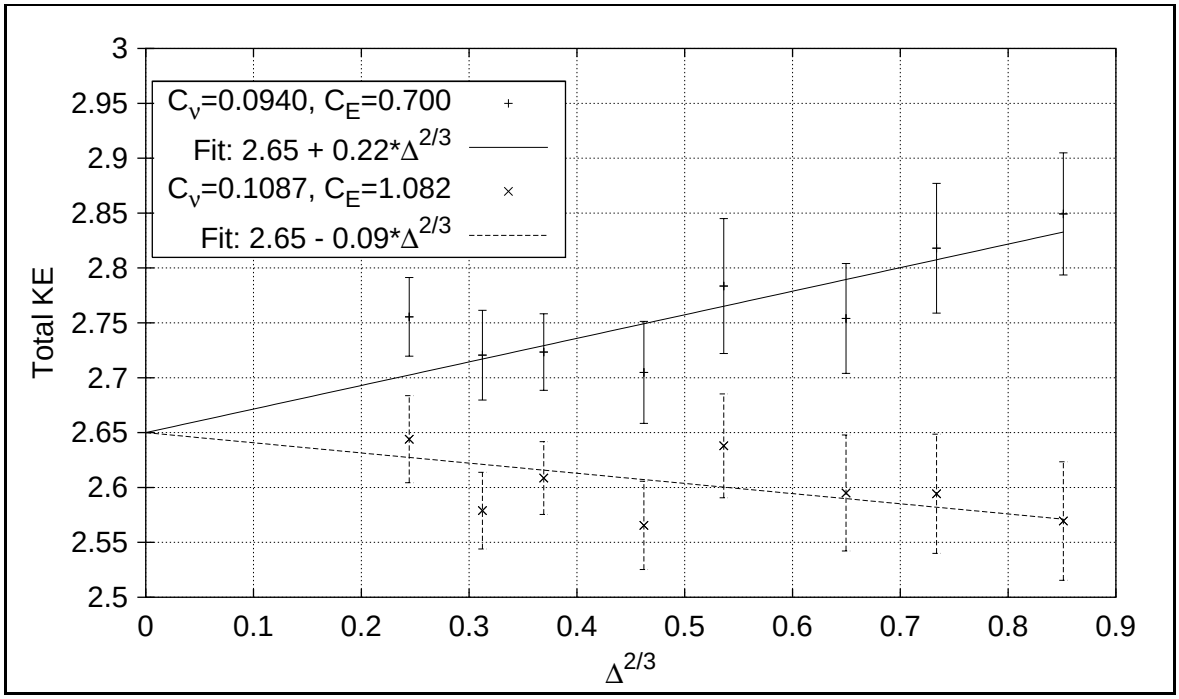

Figure 5.10: Total KE variation with Δ for two different sets of model parameter values using the Model k_R equation sub-grid model.

5.10 Two-point velocity statistics

Up to now the statistic of interest was the KE of the turbulent velocity field. So we studied the convergence of resolved KE with Δ and developed models for the residual KE. In this section, the statistic of interest is the two-point velocity

correlation

$$R_{ij}\left(\mathbf{r};\mathbf{x},t\right) \equiv \left\langle U_i\left(\mathbf{x}+\mathbf{r},t\right) U_j\left(\mathbf{x},t\right)\right\rangle \tag{5.38}$$

In particular, we studied the 1d velocity correlation given by,

$$R_{11}\left(r_1\mathbf{e_1};\mathbf{x},t\right) \equiv \left\langle U_1\left(\mathbf{x}+r_1\mathbf{e_1},t\right) U_1\left(\mathbf{x},t\right)\right\rangle \tag{5.39}$$

We first develop a simple model for the contribution of the residual motions to the 1d velocity correlation by modeling the energy spectrum function of the residual velocity field and assuming local isotropy. This is followed by some preliminary results on the performance of this model in LES simulations carried out using the Smagorinsky sub-grid model.

5.10.1 Model for residual contributions

The turbulent velocity field U_i can be decomposed into a resolved LES field W_i and a residual field u_i^R.

$$U_i = W_i + u_i^R \tag{5.40}$$

Using the above decomposition, the two-point velocity correlation $R_{ij}\left(\mathbf{r};\mathbf{x},t\right)$ can be split into,

$$\begin{aligned} R_{ij}\left(\mathbf{r};\mathbf{x},t\right) &= \left\langle \left[W_i\left(\mathbf{x}+\mathbf{r},t\right)+u_i^R\left(\mathbf{x}+\mathbf{r},t\right)\right]\left[W_j\left(\mathbf{x},t\right)+u_j^R\left(\mathbf{x},t\right)\right]\right\rangle \\ &= \left\langle W_i\left(\mathbf{x}+\mathbf{r},t\right) W_j\left(\mathbf{x},t\right)\right\rangle + \left\langle u_i^R\left(\mathbf{x}+\mathbf{r},t\right) u_j^R\left(\mathbf{x},t\right)\right\rangle \\ &+ \left\langle W_i\left(\mathbf{x}+\mathbf{r},t\right) u_j^R\left(\mathbf{x},t\right)\right\rangle + \left\langle u_i^R\left(\mathbf{x}+\mathbf{r},t\right) W_j\left(\mathbf{x},t\right)\right\rangle \end{aligned} \tag{5.41}$$

The first term in the RHS can be computed from the resolved velocity field while the remaining three need to modeled. This was done using the following three key assumptions:

1. Assume that the LES field W_i and the residual velocity field u_i^R are uncorrelated. This is a reasonable assumption because W_i essentially contains turbulent motions whose length scales are greater than Δ while u_i^R contains motions whose length scales are smaller than Δ. The above assumption implies that the terms involving correlation between the two fields in Eq. (5.41) are zero. So Eq. (5.41) reduces to,

$$\begin{aligned} R_{ij}\left(\mathbf{r};\mathbf{x},t\right) &\stackrel{M}{=} \left\langle W_i\left(\mathbf{x}+\mathbf{r},t\right) W_j\left(\mathbf{x},t\right)\right\rangle + \left\langle u_i^R\left(\mathbf{x}+\mathbf{r},t\right) u_j^R\left(\mathbf{x},t\right)\right\rangle \\ &= R_{ij}^W\left(\mathbf{r};\mathbf{x},t\right) + R_{ij}^R\left(\mathbf{r};\mathbf{x},t\right) \end{aligned} \tag{5.42}$$

Just as for the KE, the two-point velocity correlation is modeled as consisting of two parts: R_{ij}^W which can be determined from the computed LES field W_i and R_{ij}^R which is the residual contribution and needs to be modeled. R_{ij}^R is modeled by developing a model for its Fourier transform ϕ_{ij}^R.

$$\phi_{ij}^R\left(\boldsymbol{\kappa};\mathbf{x},t\right) \equiv \iiint_{-\infty}^{\infty} R_{ij}^R\left(\mathbf{r};\mathbf{x},t\right) e^{-i\boldsymbol{\kappa}\cdot\mathbf{r}} \mathbf{dr} \tag{5.43}$$

2. Assume that the residual velocity field u_i^R is locally isotropic. This allows all the components ϕ_{ij}^R to be related to the 1d scalar function, the residual energy spectrum function $E^R(\kappa)$, according to

$$\phi_{ij}^R\left(\boldsymbol{\kappa};\mathbf{x},t\right) \stackrel{M}{=} \frac{E^R\left(\kappa;\mathbf{x},t\right)}{4\pi\kappa^2}\left[\delta_{ij} - \frac{\kappa_i\kappa_j}{\kappa^2}\right] \tag{5.44}$$

3. Finally, we assume a form for the local residual energy spectrum $E^R(\kappa)$. This is basically the inertial sub-range behavior of fully developed turbulent flows with a sharp spectral cutoff at $\kappa = p_1\kappa_d$

$$E^R\left(\kappa;\mathbf{x},t\right) \stackrel{M}{=} \begin{cases} 0 & \text{for } \kappa < p_1\kappa_d \\ C_0\epsilon^{\frac{2}{3}}\kappa^{-\frac{5}{3}} & \text{for } \kappa \geq p_1\kappa_d \end{cases} \tag{5.45}$$

where

ϵ - Local energy dissipation rate.

C_0 - Kolmogorov constant, $= 1.5$.

p_1 - Non dimensional parameter determined such that the energy in the residual motions equals the local residual KE $k_R(\mathbf{x}, t)$ specified as part of the Smagorinsky model. Thus, we require

$$k_R(\mathbf{x}, t) = \int_{p_1\kappa_d}^{\infty} C_0 \epsilon^{\frac{2}{3}} \kappa^{-\frac{5}{3}} d\kappa \tag{5.46}$$

which, gives

$$p_1 = \left(\frac{3}{2}C_0\right)^{3/2} \frac{1}{\kappa_d} \frac{\epsilon}{k_R^{3/2}} \tag{5.47}$$

Now that we have a model for $\phi_{ij}^R(\boldsymbol{\kappa}; \mathbf{x}, t)$, other quantities such as the 1d velocity spectrum function $E_{ij}^R(\kappa_1; \mathbf{x}, t)$ in the x_1 direction can be easily derived.

$$E_{ij}^R(\kappa_1; \mathbf{x}, t) \equiv 2 \int_{\kappa_2=-\infty}^{\infty} \int_{\kappa_3=-\infty}^{\infty} \phi_{ij}^R(\boldsymbol{\kappa}; \mathbf{x}, t)\, d\kappa_2 d\kappa_3 \tag{5.48}$$

The 1d velocity correlation in the x_1 direction is simply the Fourier transform of the 1d velocity spectrum function $E_{ij}^R(\kappa_1)$.

$$\begin{aligned} R_{ij}^R(r_1\mathbf{e_1}; \mathbf{x}, t) &\equiv \left\langle u_i^R(\mathbf{x} + r_1\mathbf{e_1}, t)\, u_j^R(\mathbf{x}, t) \right\rangle \\ &= \int_{-\infty}^{\infty} \frac{1}{2} E_{ij}^R(\kappa_1; \mathbf{x}, t)\, e^{i\kappa_1 r_1} d\kappa_1 \end{aligned} \tag{5.49}$$

The rest of the derivation to obtain expressions for the 1d velocity correlation and spectrum involves tedious calculations sometimes requiring simplifications in Mathematica. These calculations are omitted here and we give only the final expressions for the 1d velocity spectrum $E_{11}^R(\kappa_1)$ and correlation $R_{11}^R(r_1\mathbf{e_1})$.

- **Model for residual 1d velocity spectrum**

$$E_{11}^{R}\left(\kappa_1;\mathbf{x},t\right) \overset{M}{=} \begin{cases} \frac{3}{5}C_0\epsilon^{\frac{2}{3}}\left(p_1\kappa_d\right)^{-\frac{5}{3}}\left[1-\frac{5}{11}\left(\frac{\kappa_1}{p_1\kappa_d}\right)^2\right] & \text{for } 0<\kappa_1<p_1\kappa_d \\ \frac{18}{55}C_0\epsilon^{\frac{2}{3}}\left(\kappa_1\right)^{-\frac{5}{3}} & \text{for } \kappa_1 \geq p_1\kappa_d \end{cases} \tag{5.50}$$

- **Model for residual 1d velocity correlation**

$$R_{11}^{R}\left(r_1\mathbf{e_1};\mathbf{x},t\right) \overset{M}{=} k_R\left[\frac{6}{55}f_1\left(p_1\kappa_d r_1\right)+\frac{4}{55}f_2\left(p_1\kappa_d r_1\right)\right] \tag{5.51}$$

where

$$f_1\left(x\right) = \Gamma\left(-\frac{2}{3}\right)x^{\frac{2}{3}} + 3\,\text{HypergeometricPFQ}\left[\left\{-\frac{1}{3}\right\},\left\{\frac{1}{2},\frac{2}{3}\right\},-\frac{1}{4}x^2\right]$$

$$f_2\left(x\right) = \left[\frac{-5x\cos x+\left(5+3x^2\right)\sin x}{x^3}\right]$$

5.10.2 One-dimensional velocity spectrum convergence results

Figure 5.11 shows the shape of the volume- and time-averaged residual 1d velocity spectrum given by Eq. (5.50) for $\kappa_d = 10$. The volume- and time-averaged resolved and total velocity spectrum are also shown. Details on this LES using Smagorinsky model are given in Table 5.3. The 1d velocity spectrum function at low wave numbers is well resolved by the LES while at high wave numbers the LES field has no energy. So at these high wave numbers, the residual 1d velocity spectrum contributes most of the energy to the total 1d velocity spectrum while the resolved 1d velocity spectrum has negligible contribution. As we keep moving towards lower wave numbers, more and more of the energy is resolved by the LES field until we are at low enough wave numbers that the resolved 1d velocity spectrum contributes more than the residual 1d velocity spectrum. A small kink in the

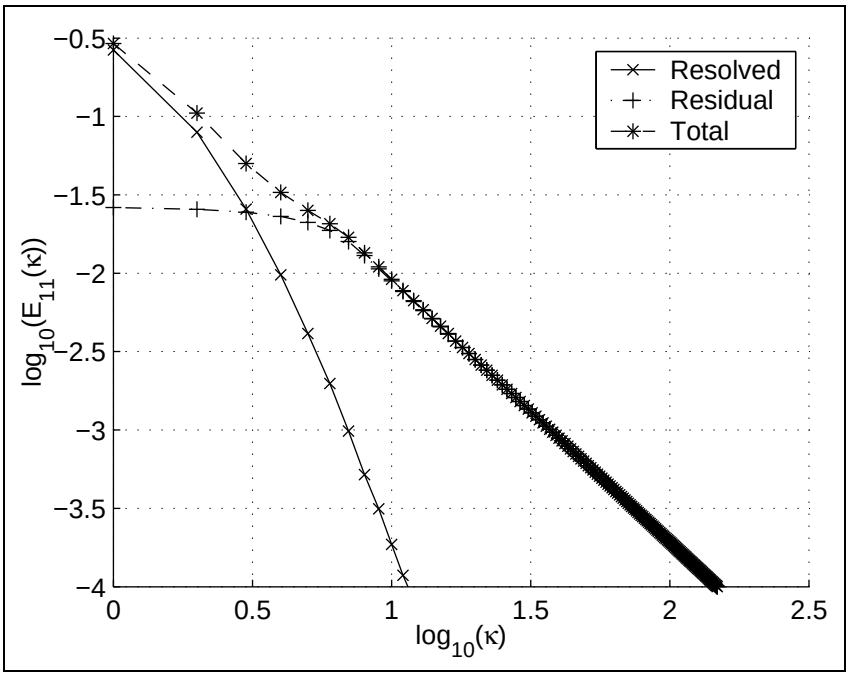

Figure 5.11: Volume- and time-averaged resolved 1d velocity spectrum $E_{11}^{W}(\kappa_1)$ along with models for the residual 1d velocity spectrum $E_{11}^{R}(\kappa_1)$ and total 1d velocity spectrum $E_{11}(\kappa_1)$. Simulation carried out at $\Delta = \pi/\kappa_d = \pi/10$ using Smagorinsky model with $C_\nu = 0.094$ and $C_E = 0.7$.

total 1d velocity spectrum occurring at wave numbers comparable to κ_d indicates this shift in contribution. Also, in the limit of infinite Re, the inertial sub-range extends to $\kappa \to \infty$. This is clearly indicated by the $\kappa^{-5/3}$ behavior shown by the total 1d velocity spectrum over a wide range of wave numbers.

Next we studied the convergence properties of the volume- and time-averaged 1d velocity spectrum function with resolution length scale Δ. For this study, we chose a wave number $\kappa_1 = \kappa_p$ (say) and studied how the resolved and residual contributions to the total 1d velocity spectrum varied with Δ. We expect the convergence behavior to depend on the choice of κ_p. Here we present convergence results for three different values of κ_p which correspond to different convergence behaviors.

The first wave number at which convergence was studied was $\kappa_1 = \kappa_p = 1$. This is a very low wave number and most LES simulations would resolve the energy at this wave number. Eq. (5.50) suggests that at sufficiently small values of Δ the 1d velocity spectrum function varies as $\Delta^{5/3}$. So the convergence behavior of the 1d velocity spectrum at $\kappa = \kappa_p = 1$ is plotted against $\Delta^{5/3}$. Figure 5.12 shows that much of the energy at this wave number has been resolved for all resolution length scales Δ used in the LES. Also, the nearly linear behavior of the residual and resolved 1d velocity spectra indicates that the leading order term is $\Delta^{5/3}$. However, in Fig. 5.12 we have not extrapolated the data to determine the asymptote at $\Delta = 0$. We have simply joined the data points by straight lines. Despite this, it is pretty clear that the total 1d velocity spectrum is closer to the asymptote at $\Delta = 0$ than the resolved 1d velocity spectrum for a given value of Δ.

The next wave number at which we studied convergence was $\kappa_1 = \kappa_p = 4$. At this wave number, some of the LES simulations sufficiently resolved the energy,

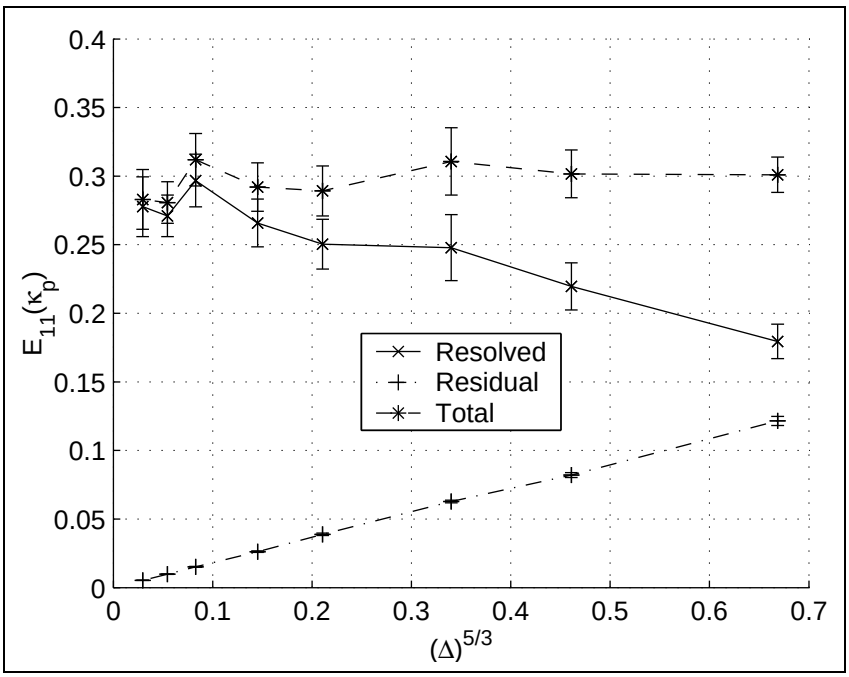

Figure 5.12: Convergence behaviour of the 1d velocity spectrum at $\kappa = \kappa_p = 1$ against $\Delta^{5/3}$.

while other LES simulations at larger values of Δ did not. Figure 5.13 illustrates this point because at larger values the residual 1d velocity spectrum contributes most of the energy while at lower Δ the contributions are reversed. Again, the total 1d velocity spectrum is closer to the asymptote at $\Delta = 0$ than the resolved 1d velocity spectrum for a given value of Δ. Finally, the $\Delta^{5/3}$ behaviour is evident only at the smallest values of Δ if at all!

Lastly, we studied the convergence at $\kappa_1 = \kappa_p = 32$. None of the LES simulations resolved the energy at this wave number. The almost negligible contribution of the resolved 1d velocity spectrum in Fig. 5.14 illustrates this point. Almost all the contribution to the total 1d velocity spectrum is from the model for the residual 1d velocity spectrum.

Figure 5.15 shows that the convergence behaviour at intermediate wave num-

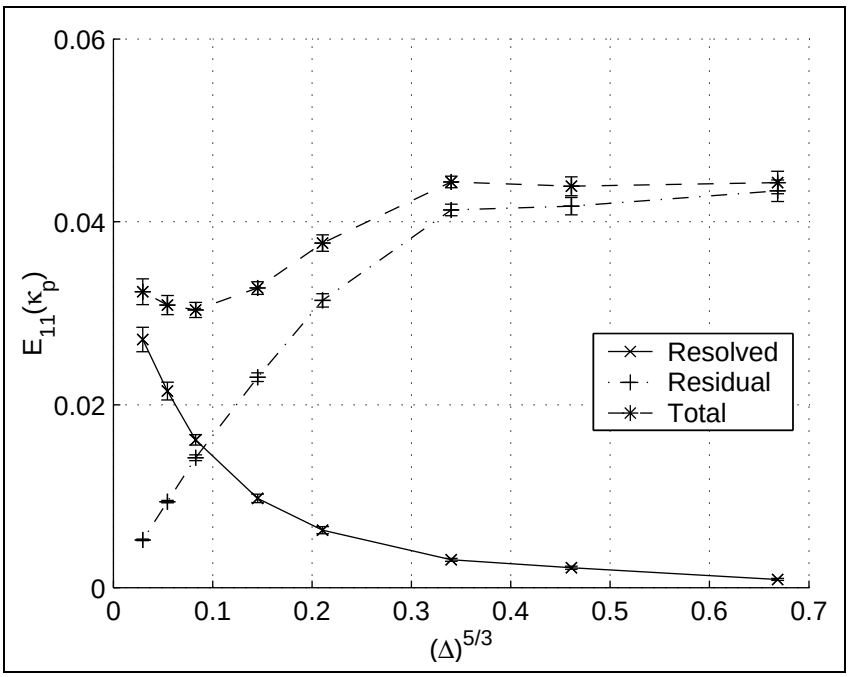

Figure 5.13: Convergence behaviour of the 1d velocity spectrum at $\kappa = \kappa_p = 4$ against $\Delta^{5/3}$.

bers to be similar when non-dimensionalized appropriately. Since we expect the 1d velocity spectrum to vary as $\kappa_p^{-5/3}\mathcal{P}^{2/3}$ in the inertial sub-range, the above was used to non-dimensionalize the 1d velocity spectrum. Using κ_p we can define a length scale, $\Delta_p = \pi/\kappa_p$ which can be used to non-dimensionalize Δ. The convergence characteristics of the non-dimensional 1d velocity spectrum at $\kappa_p = 4, 6, 10, 18$, and 24 were plotted on the same axes in Fig. 5.15. Clearly, all these curves collapse.

5.10.3 One-dimensional velocity correlation convergence results

In this sub-section we discuss preliminary convergence results for the volume- and time-averaged 1d velocity correlation. Figure 5.16 shows a sample variation of the resolved 1d velocity correlation $R_{11}^W(r_1)$ along with the model for the residual 1d

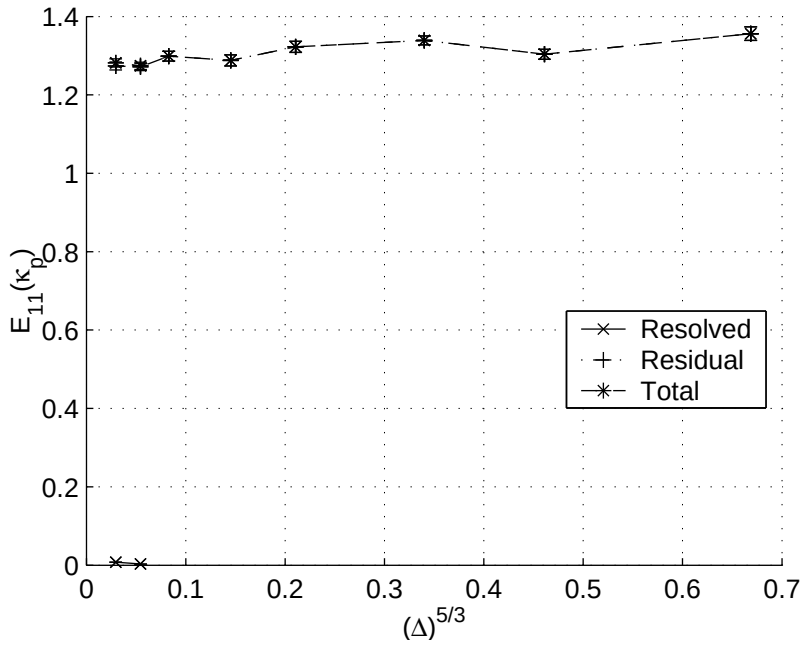

Figure 5.14: Convergence behaviour of the 1d velocity spectrum at $\kappa = \kappa_p = 32$ against $\Delta^{5/3}$.

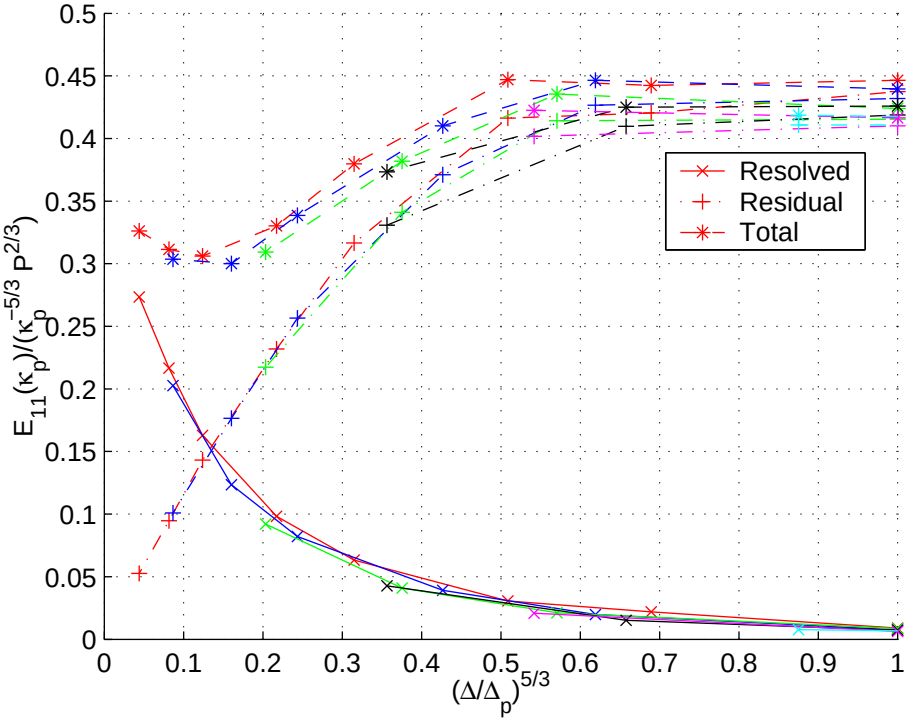

Figure 5.15: Convergence characteristics of the non-dimensional 1d velocity spectrum. Different colors represent different values for κ_p. $\kappa_p = 4 \rightarrow$ red, $\kappa_p = 6 \rightarrow$ blue, $\kappa_p = 10 \rightarrow$ green, $\kappa_p = 14 \rightarrow$ black, $\kappa_p = 18 \rightarrow$ magenta, $\kappa_p = 24 \rightarrow$ cyan

velocity correlation $R_{11}^{W}(r_1)$ given by Eq. (5.50)

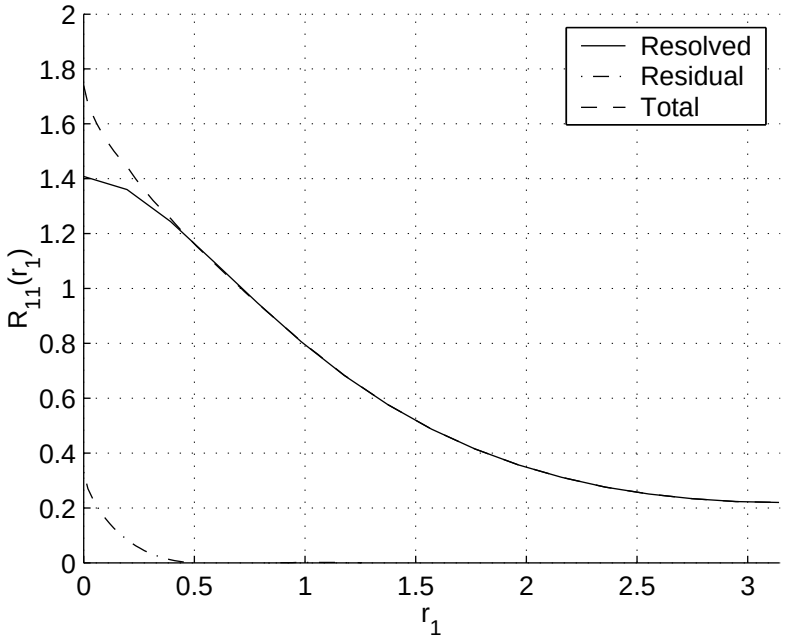

Figure 5.16: Volume- and time-averaged resolved 1d velocity correlation $R_{11}^{W}(\kappa_1)$ along with models for the residual 1d velocity correlation $R_{11}^{R}(r_1)$ and total 1d velocity correlation $R_{11}(r_1)$. Simulation carried out at $\Delta = \pi/\kappa_d = \pi/10$ using Smagorinsky model with $C_\nu = 0.094$ and $C_E = 0.7$.

In order to proceed with the convergence study for the 1d velocity correlation we have to determine the power of its leading order Δ variation. Using Eq. (5.51), our best guess for the leading order term is the same as that of residual KE k_R, namely $\Delta^{2/3}$. So we plotted all the convergence curves against $\Delta^{2/3}$.

Again we expect the convergence behaviour of 1d velocity correlation $R_{11}(r_1)$ to depend on the value $r_1 = \Delta_p$ (say) chosen for the study. We present the convergence behaviour results for two values: $r_1 = \Delta_p = 0.0$ and $r_1 = \Delta_p = 0.3927$ in Figs. 5.17 and 5.18, respectively.

Although Fig. 5.17 justifies a $\Delta^{2/3}$ leading-order variation at small values of Δ,

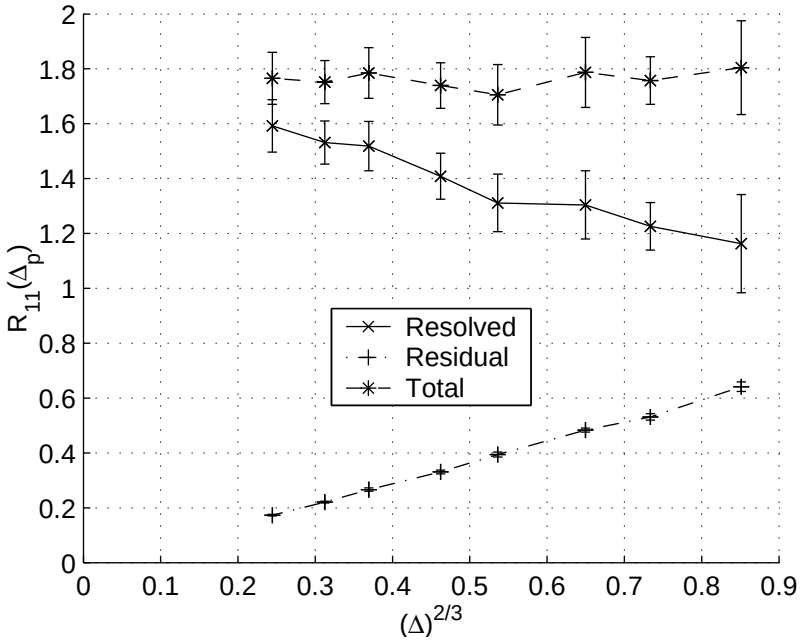

Figure 5.17: Convergence behaviour of the 1d velocity correlation at $r_1 = \Delta_p = 0.0$ plotted against $\Delta^{2/3}$.

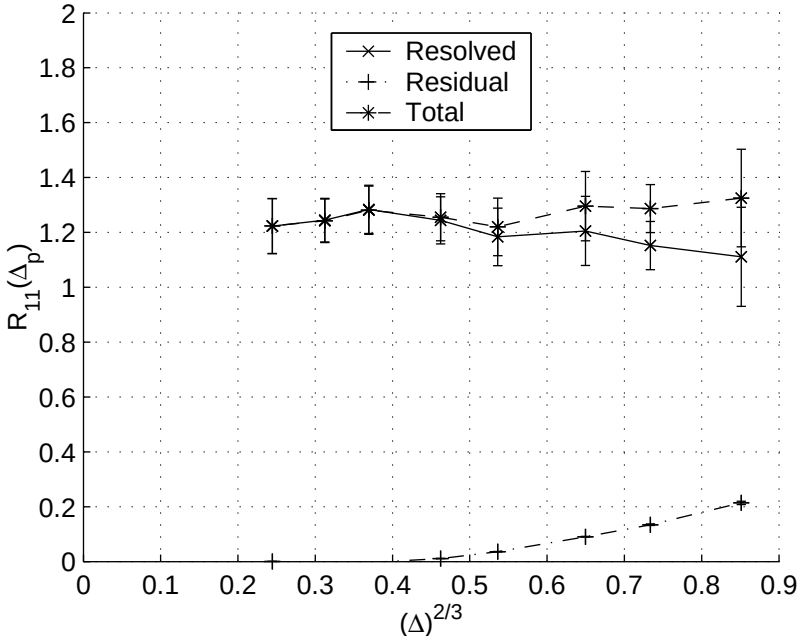

Figure 5.18: Convergence behaviour of the 1d velocity correlation at $r_1 = \Delta_p = 0.3927$ plotted against $\Delta^{2/3}$.

Fig. 5.18 seems to suggest a higher power than 2/3 for the leading order Δ term. The other important observation is that, in both figures, the total 1d velocity correlation is closer to the asymptote at $\Delta = 0$ than the resolved 1d velocity correlation.

We have here carried out only a preliminary convergence analysis for the 1d velocity spectrum and correlation. Further study is needed to determine the power of the leading order Δ term and compute the asymptote value at $\Delta = 0$. We also need to study the convergence using other values for the sub-grid model parameters and other sub-grid models as well.

Chapter 6

Temporally evolving mixing layer

Turbulent free shear flows are more complicated flows than forced, isotropic turbulence because they are statistically inhomogeneous in space and time. At the same time, their dynamics are not affected by the presence of solid boundaries, making them easier to study than wall-bounded flows. In this chapter, we apply the ideas developed for the new LES methodology to the temporally evolving mixing layer, which is a typical free shear flow.

As in the earlier chapter, we begin with a description of temporal mixing layers and their numerical simulation. It is tricky to obtain initial conditions for a *turbulent* mixing layer. We start with a laminar mixing layer and superimpose disturbances to hasten its transition to a turbulent flow. The velocity and pressure fields obtained at a specified time, after the flow becomes turbulent, are then used as initial conditions for the LES. These fields are restricted to the required LES grids by using appropriate Gaussian filters. Details on the disturbances and filter used are given. We also briefly comment on the lack of self-similarity observed in our simulations.

Next, the convergence properties of the Smagorinsky sub-grid model are studied by looking at the statistic of turbulent KE. We comment on the convergence of both the volume-averaged turbulent KE and the plane-averaged turbulent KE at various cross-stream locations and times. Improved model parameters which minimized the Δ variation of the volume-averaged turbulent KE at a specified time were calculated. We then comment on the dependence of these optimal model parameter values on the time at which the Δ variation was minimized. Analogous

convergence results are presented for the Model k_R equation sub-grid model.

An equally important statistic for the mixing layer is the Reynolds shear stress $\langle w_1 w_3 \rangle$. We studied the convergence properties of this Reynolds shear stress as well. Again, results are presented for both the Smagorinsky and Model k_R equation sub-grid models. The inability of the linear eddy-viscosity based sub-grid models to capture both the energy dissipation rate and the Re shear stress is noted.

6.1 Numerical simulation

Free shear layers are of great technological importance because they occur in many practical devices, especially those involving chemical reactions. The mixing layer that forms between two fluid streams moving with different velocities is an important model problem for the study of turbulence in free shear layers. The inflectional mean velocity profiles of mixing layers are subject to inviscid instabilities which trigger the transition to turbulence. A number of experimental [Winant & Browand (1974); Brown & Roshko (1974)] and computational [Rogers & Moser (1994); Metcalfe *et al.* (1987); Sandham & Reynolds (1991)] studies have been performed to understand the mechanisms responsible for the growth of three-dimensionality and the onset of turbulence. It is believed that a good understanding of turbulent mixing layers would aid in the understanding of other turbulent free shear layers occurring in engineering. In the recent past, LES of turbulent mixing layers [Vreman *et al.* (1996); Balaras *et al.* (2001)], with various sub-grid models, have also been carried out. Hence, the practical significance and the availability of a vast prior literature, makes the turbulent mixing layer a good model problem on which to test our ideas for a new LES methodology.

In this chapter we present results for the temporally evolving mixing layer

which occurs between two fluid streams moving with equal and opposite free-stream speeds, U_0. Figure 6.1 shows a schematic of the temporal mixing layer along with the coordinate system and numerical simulation domain used. In the

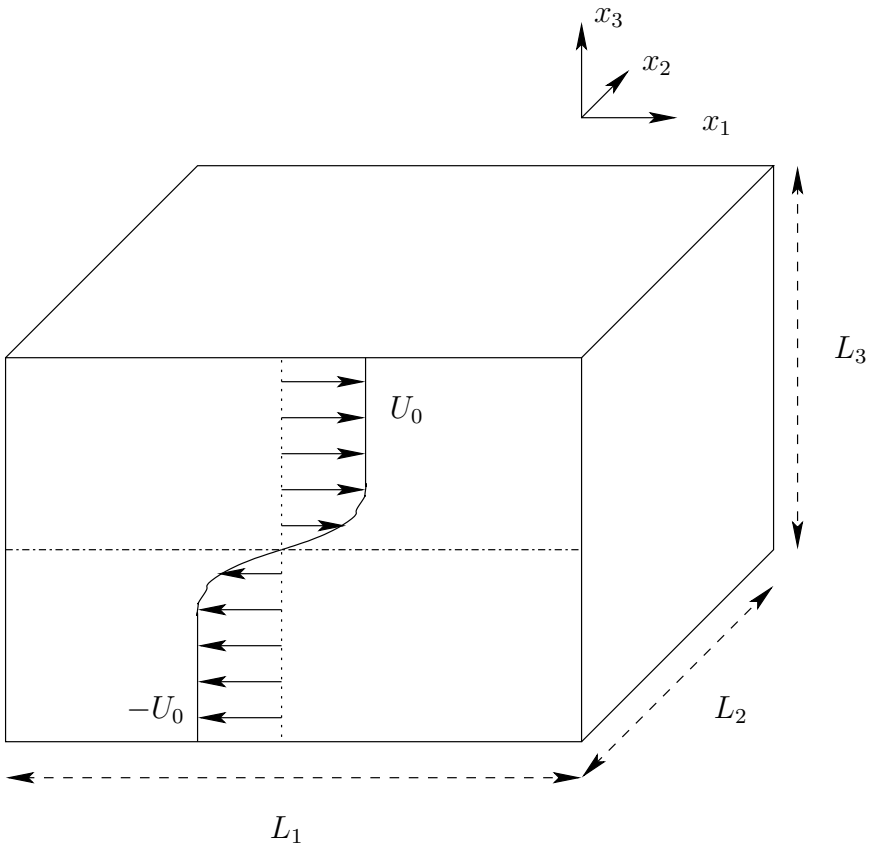

Figure 6.1: Schematic of the temporal mixing layer along with the coordinate system and numerical simulation domain used.

temporal mixing layer, the flow is statistically inhomogeneous *only* in the cross-stream direction, x_3. The statistics of the flow also evolve in time but they are believed to reach a statistically self-similar state. All available experimental data are on spatially evolving mixing layers which evolve to a self-similar state along the primary flow direction x_1 but are usually statistically stationary in time. However, it is harder to simulate spatially evolving mixing layers numerically because we

need to specify turbulent inflow boundary conditions and design non-reflecting outflow conditions. The temporal mixing layer avoids these problems because the flow evolves statistically in time while being statistically homogeneous in the x_1 direction. This allows us to apply simple periodic BCs in the x_1 direction. The temporal mixing layer may be thought of as an approximation to evolution of a single set of flow structures as they are convected downstream in the more common spatially evolving mixing layers.

The flow was simulated in a 3d cubic domain $[0, L_1] \times [0, L_2] \times [-\frac{L_3}{2}, \frac{L_3}{2}]$. We apply periodic BCs in the x_1 and x_2 directions. In the x_3 direction, we apply free-slip boundary conditions:

$$\begin{aligned}
\frac{\partial W_1}{\partial x_3} = \frac{\partial^3 W_1}{\partial x_3^3} = 0 \quad \text{at } x_3 = -\frac{L_3}{2}, \frac{L_3}{2} \\
\frac{\partial W_2}{\partial x_3} = \frac{\partial^3 W_2}{\partial x_3^3} = 0 \quad \text{at } x_3 = -\frac{L_3}{2}, \frac{L_3}{2} \\
W_3 = \frac{\partial^3 W_3}{\partial x_3^3} = 0 \quad \text{at } x_3 = -\frac{L_3}{2}, \frac{L_3}{2} \\
\frac{\partial \nu_r}{\partial x_3} = \frac{\partial^3 \nu_r}{\partial x_3^3} = 0 \quad \text{at } x_3 = -\frac{L_3}{2}, \frac{L_3}{2} \\
\frac{\partial k_R}{\partial x_3} = \frac{\partial^3 k_R}{\partial x_3^3} = 0 \quad \text{at } x_3 = -\frac{L_3}{2}, \frac{L_3}{2}
\end{aligned} \tag{6.1}$$

The BCs on the eddy viscosity ν_r and residual KE k_R were used only when required.

Uniform grid spacing was used in the periodic x_1 and x_2 directions. Since the largest flow gradients occur in the region between the two fluid streams, we used a stretched Cartesian grid in the x_3 direction. An algebraic mapping [Grosch & Orszag (1977); Boyd (1981)] was used to map the non-uniform grid in physical space x_i to the uniform grid in computational space ξ_i

$$\xi_3 = \frac{x_3}{|x_3| + \frac{L_3}{2}} \tag{6.2}$$

The above maps $x_3 : \left[-\frac{L_3}{2}, \frac{L_3}{2}\right] \rightarrow \xi_3 : [-\frac{1}{2}, \frac{1}{2}]$.

6.2 Initial Conditions

The LES of a turbulent temporal mixing layer requires the specification of a turbulent flow as initial conditions. In the case of forced, isotropic turbulence we started with a turbulent flow matching a given energy spectrum and evolved the flow until we reached a statistically stationary state. For the mixing layer, we performed a DNS starting from a laminar mixing layer velocity profile superimposed with eigenfunction perturbations to initiate turbulence. The flow obtained after the turbulence became fully developed was filtered and used as initial conditions for the various LES simulations. The filter width was chosen based on the resolution length scale to be used in the LES. Details on the above procedure used to generate initial conditions are discussed in this section.

6.2.1 Eigenfunction disturbances

The flow is started from a hyperbolic tangent mean velocity profile given by,

$$W_1 = U^0 \tanh\left(\frac{x_3}{0.5\delta_w^0}\right) \tag{6.3}$$

where

U^0 - Free-stream speed. U^0 is used as the reference velocity scale.

δ_w^0 - Half the initial vorticity thickness with vorticity thickness defined to be

$$\delta_w \equiv \frac{U^0}{(\partial W_3/\partial x_3)\big|_{\max}} \tag{6.4}$$

Half the initial vorticity thickness δ_W^0 is used as the reference length scale.

This hyperbolic tangent velocity profile has an inflection point making it susceptible to inviscid instabilities. Hence, to initiate turbulence, eigenfunction per-

turbations of the form

$$\tilde{w}_k\left(x_3;\alpha_1,\alpha_2\right)e^{i\alpha_1 x_1}e^{i\alpha_2 x_2} \tag{6.5}$$

are superimposed on the mean velocity profile. These eigenfunctions $\tilde{w}_k\left(x_3;\alpha_1,\alpha_2\right)$ corresponding to different stream-wise α_1 and span-wise α_2 wave numbers, can be obtained from linear stability analysis [Michalke (1964)]. They were normalized such that $\max\left(\tilde{w}_1\right)=1$.

The stream-wise wavelength of the most unstable eigenfunction from linear stability analysis is $\lambda_{x_1}=2.35\left(2\pi\delta_w^0\right)$. In our simulations, the most unstable eigenfunction and its sub-harmonics were superimposed on the mean velocity profile. From here on, these eigenfunctions are identified by their normalized wave numbers $\left(\frac{\alpha_1\lambda_{x_1}}{2\pi},\frac{\alpha_2\lambda_{x_1}}{2\pi}\right)$. Vreman provided us with the eigenfunction profiles to be used in our simulations. Here we do not describe the linear stability analysis used to compute these eigenfunctions, but physically motivate the choice of eigenfunctions used.

These eigenfunctions can be classified into 2d and 3d disturbances. The 2d eigenfunctions correspond to those with zero span-wise wavenumber, $\alpha_2=0$. The most unstable eigenfunction $(1,0)$ causes the shear layer to roll up into span-wise vortices called "rollers". The sub-harmonic 2d disturbances $(0.5,0)$ and $(0.25,0)$ induce two pairings of these roller vortices. Figure 6.2 illustrates the roll-up of the free shear layer subject to only these 2d disturbances, and the subsequent pairing of the roller vortices. At the end of each pairing, the number of roller vortices is reduced by half. Pairing is believed to be one of the fundamental mechanisms by which the mixing layer grows [Pierrehumbert & Widnall (1982); Moser & Rogers (1993)]. Since we wanted to simulate two pairings, the length of the computational domain was taken to be $L_1=L_2=L_3=4\lambda_{x_1}$.

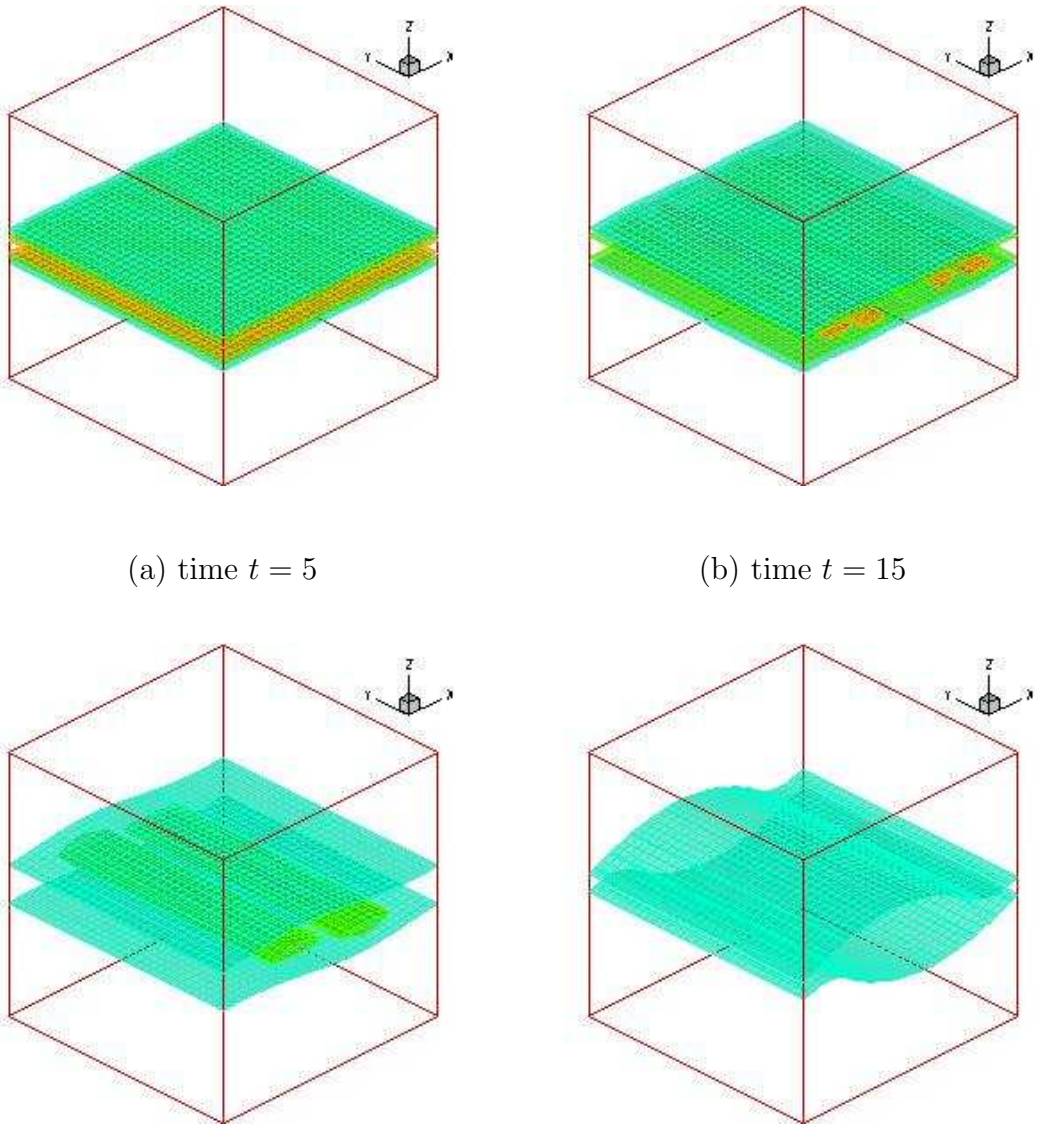

(a) time $t = 5$ (b) time $t = 15$

(c) time $t = 55$ (d) time $t = 90$

Figure 6.2: Roll-up of the free shear mixing layer subject to only 2d disturbances and the subsequent pairing of the roller vortices. Iso-surfaces of non-dimensional span-wise vorticity $\omega_2 \, (\delta_w^0 / U^0)$, are shown at 1.0 (blue-green), 1.8 (green), and 2.55 (orange). Results from LES using Smagorinsky model on a 32^3 grid are shown only for qualitative illustration of the flow physics.

In order to introduce three-dimensionality into the problem, we also used the 3d disturbances $(1, 1)$, $(1, -1)$, $(0.5, 0.5)$, $(0.5, -0.5)$, $(0.25, 0.25)$, and $(0.25, -0.25)$. So different span-wise locations evolve differently producing rib vortices which develop predominantly stream-wise vorticity. This onset of three-dimensionality is essential for the flow to become turbulent. Figure 6.3 shows the effect of adding 3d disturbances by looking at vorticity tubes at different times. It can be seen that at later times there is a strong stream-wise component of the vorticity and the flow becomes highly three-dimensional.

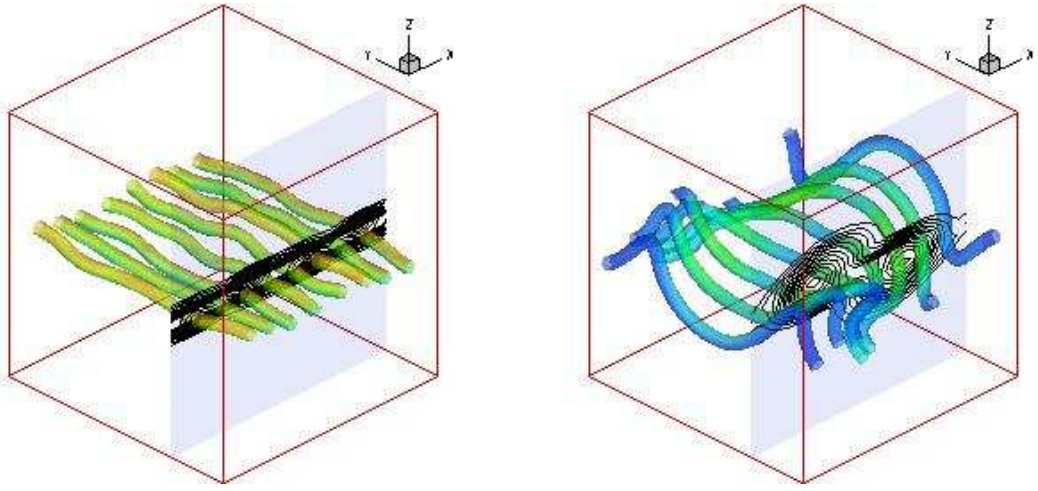

(a) time $t = 5$ (b) time $t = 90$

Figure 6.3: Effect of adding 3d eigenfunction disturbances. Vorticity tubes located in the plane between the two fluid streams are shown at different times. Also shown are the contours of vorticity magnitude in the x_1x_3 plane at $x_2/L_2 = 0.25$. Results from LES using Smagorinsky model on a 32^3 grid are shown only for qualitative illustration of the flow physics.

When adding these eigenfunction disturbances to the flow one needs to specify an amplitude $\tilde{a}_{j_1,j_2}$ and phase ϕ_{j_1,j_2} as well,

$$[\tilde{a}_{j_1,j_2}]\,\tilde{w}_k\left(x_3;\left[j_1\frac{2\pi}{\lambda_{x_1}}\right],\left[j_2\frac{2\pi}{\lambda_{x_1}}\right]\right)e^{i\left[j_1\frac{2\pi}{\lambda_{x_1}}\right]x_1}e^{i\left[j_2\frac{2\pi}{\lambda_{x_1}}\right]x_2}e^{i\left[\phi_{j_1,j_2}\right]} \tag{6.6}$$

Large amplitude disturbances [Vreman *et al.* (1996); Sandham & Reynolds (1991)] with randomly chosen phases, to break the symmetry in the initial conditions, were used.

We summarize below the values chosen for the different numerical parameters used to define the initial conditions and the DNS grid on which the flow was evolved.

$$\begin{aligned} U^0 &= 1.0 \\ \delta_w^0 &= 1.0 \\ \nu &= 0.02 \\ Re^0 = \frac{U^0\delta_w^0}{\nu} &= 50 \\ \lambda_{x_1} &= 2.35\,(2\pi) \\ L_1 = L_2 = L_3 &= 59 \approx 4\lambda_{x_1} \\ N_1 = N_2 = N_3 &= 192 \end{aligned} \tag{6.7}$$

It can be seen that the need to compare the statistics from LES with statistics from DNS has restricted us to small Re. The ideas used in isotropic turbulence to extrapolate the statistics from moderate to infinite Re were not investigated in the context of the mixing layer.

The amplitudes and phases used for the eigenfunction disturbances are summarized below,

$$\begin{aligned}
\tilde{a}_{1,0} = \tilde{a}_{0.5,0} = \tilde{a}_{0.25,0} &= 0.5 \\
\phi_{1,0} = \phi_{0.5,0} = \phi_{0.25,0} &= 0 \\
\tilde{a}_{1,1} = \tilde{a}_{1,-1} &= 0.15 \\
\phi_{1,1} = \phi_{1,-1} &= -0.3927 \\
\tilde{a}_{0.5,0.5} = \tilde{a}_{0.5,-0.5} &= 0.15 \\
\phi_{0.5,0.5} = \phi_{0.5,-0.5} &= -0.3927 \\
\tilde{a}_{0.25,0.25} = \tilde{a}_{0.25,-0.25} &= 0.15 \\
\phi_{0.25,0.25} = \phi_{0.25,-0.25} &= -0.1963
\end{aligned} \tag{6.8}$$

The flow conditions obtained at time $t = 30$ are filtered and used as initial conditions on the LES grid.

6.2.2 Discrete Gaussian filter

We need to develop filters to transfer the initial conditions generated on the grid used for DNS to the grid for LES. The DNS was carried out on a 192^3 uniform grid while a typical LES is carried out on a 32^3 grid. Any one-dimensional filter can be used to generate uniform, isotropic, three-dimensional filters. So in this section we compare various one-dimensional filters by studying their transfer functions. For the sake of simplicity, we first compare homogeneous, one-dimensional filters defined on a grid with uniform grid spacing. Based on these comparisons, the discrete Gaussian filter is identified as a good filter. We then present the extension of these filters to non-uniform grids and the treatment of boundaries.

In this section, the following notations and definitions are used. A discrete

function f is defined on a grid with uniform grid spacing Δ_g on the domain $[0, L]$. Let f_j denote the value of this function at location $j\Delta_g$. Also, we define the following quantities:

N_{DNS} - Number of grid points in the grid used for DNS.

Δ_{DNS} - Grid spacing in the grid used for DNS, $\Delta_{DNS} = L/N_{DNS}$.

N_{LES} - Number of grid points in the grid used for LES.

Δ_{LES} - Grid spacing in the grid used for LES, $\Delta_{LES} = L/N_{LES}$

Δ - Filter width of the filter used to transfer data from the DNS grid to LES grid.

The discrete filtering operation at grid point j is defined by the weighting functions b_l^j as follows,

$$\overline{f}_j \equiv \sum_{l=-P^j}^{Q^j} b_l^j f_{j+l} \tag{6.9}$$

where $\overline{f}$ denotes the filtered function which is represented on the LES grid. The weighting functions must necessarily satisfy,

$$\sum_{l=-P^j}^{Q^j} b_l^j = 1 \tag{6.10}$$

For simplicity, we restrict our discussion to homogeneous, symmetric filters:

$$\text{Homogeneous} \Rightarrow b_l^j \text{ is independent of grid point } j$$

$$\text{Symmetric} \Rightarrow \begin{cases} P_j & = Q_j \\ b_l^j & = b_{-l}^j \end{cases} \tag{6.11}$$

Using delta functions to describe the discrete filter, the transfer function $\hat{G}(\kappa)$ for a discrete, homogeneous, symmetric filter is found to be the real function

$$\hat{G}(\kappa) = b_0^j + \sum_{l=1} P^j b_l^j 2\cos(\kappa \Delta_{DNS} l) \tag{6.12}$$

The above expression for the transfer function allows us to compare the three discrete filters described below:

1. **Uniform, or Hat, filter:** The coefficients b_l^j are chosen to be uniform over the filter width Δ

$$b_l^j = \begin{cases} \frac{\Delta_{DNS}}{\Delta} & \text{when } |l\Delta_{DNS}| \leq \delta/2 \\ 0 & \text{when } |l\Delta_{DNS}| > \delta/2 \end{cases} \tag{6.13}$$

2. **Discrete Gaussian filter:** The coefficients b_l^j are chosen to vary as a Gaussian distribution,

$$b_l^j = \begin{cases} a' e^{-\frac{(l\Delta_{DNS})^2}{2\sigma^2}} & \text{when } |l\Delta_{DNS}| \leq 3\sigma \\ 0 & \text{when } |l\Delta_{DNS}| > 3\sigma \end{cases} \tag{6.14}$$

   where

   σ - Denotes the width of the Gaussian distribution relative to the given filter width Δ by setting the value of the transfer function $\hat{G}$ at $\kappa = \pi/\Delta$ to 0.5. For ease of calculation, the transfer function of the continuous Gaussian filter is used to determine the following relation between σ and Δ

$$\begin{aligned} \hat{G}(\kappa) &= e^{-\frac{\kappa^2\sigma^2}{2}} = 0.5 \quad \text{at } \kappa = \pi/\Delta \\ \Rightarrow \sigma &= \sqrt{\frac{2}{\pi}\ln 2} = 0.3748\Delta \end{aligned} \tag{6.15}$$

   a' - is a multiplicative constant chosen to satisfy condition 6.10.

3. **Vasilyev's discrete filter:** Vasilyev *et al.* (1998) have designed certain discrete filters with favorable properties for the transfer function. They realized these properties by imposing additional constraints on the moments of the filter, shape of the filter transfer function and the value of the filter transfer function at certain κ.

$|\hat{G}(\kappa)|^2$ signifies the fraction of the energy transfered from the DNS grid to LES grid at the given wavenumber κ. Hence, much insight can be obtained by looking at the variation of the transfer function $\hat{G}(\kappa)$ with κ. Figure 6.4 compares the transfer functions of the above three filters. For the sake of comparison, we chose

$$\begin{aligned} N_{DNS} &= 192 \\ N_{LES} &= 128 \\ L &= 1 \\ \Delta &= L/(N_{LES}/2) = 1/64 \end{aligned} \tag{6.16}$$

The number of stencil points required for the different filters is also indicated in the legend.

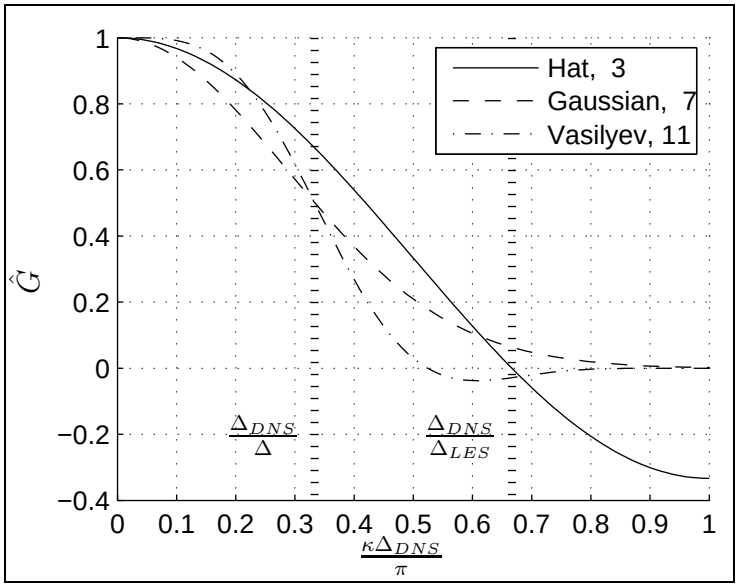

Figure 6.4: Comparison of the transfer functions of uniform, Gaussian and Vasilyev filters. The number of stencil points required for the various filters is also indicated in the legend. For comparison, we chose, $\Delta_{DNS} = 1/192$, $\Delta_{LES} = 1/128$, and $\Delta = 1/64$.

The filtered function $\overline{f}$ is represented on the LES grid with grid spacing Δ_{LES} and so any energy in wavenumbers greater than $\frac{\pi}{\Delta_{LES}}$ gets aliased back to the lower wavenumbers. It can be seen that the uniform filter does not damp out the motions in these high wavenumbers sufficiently well leading to aliasing of these high wavenumber motions to lower wavenumbers. The Vasilyev filter has good transfer function properties as the transfer function is close to one at the lower wavenumbers and drops to zero reasonably fast at the higher wavenumbers. However, this filter is not much better than the Gaussian filter depicted and the complexity involved in deriving the Vasilyev filter coefficients outweighed any benefits it might have. Further, the Gaussian filter requries many fewer stencil points for the same filter width. Hence, we decided to use the discrete Gaussian filter to transfer the data from the DNS grid to the requried LES grid. Figure 6.5 shows the transfer functions for the discrete Gaussian filter used on the various LES grids.

In order to extend the above described discrete Gaussian filter from uniform to non-uniform grids, we simply performed the above described filtering operation in the computational space which has uniform grid spacing [Vasilyev *et al.* (1998); Ghosal & Moin (1995)]. Please note that this results in a spatially varying filter width in physical space and the variation depends on the mapping used to transform from physical to computational space.

We account for boundaries simply by neglecting the weights b_l^j at points lying outside the domain. However, this results in non-symmetric filters near the boundaries. Symmetric filters alter the amplitude of the motions in a particular wavenumber without altering their phase while non-symmetric filters alter both the amplitude and phase. This is indicated by the fact that the transfer function of a non-symmetric filter has an imaginary, as well as a real, part. Figure 6.6 shows

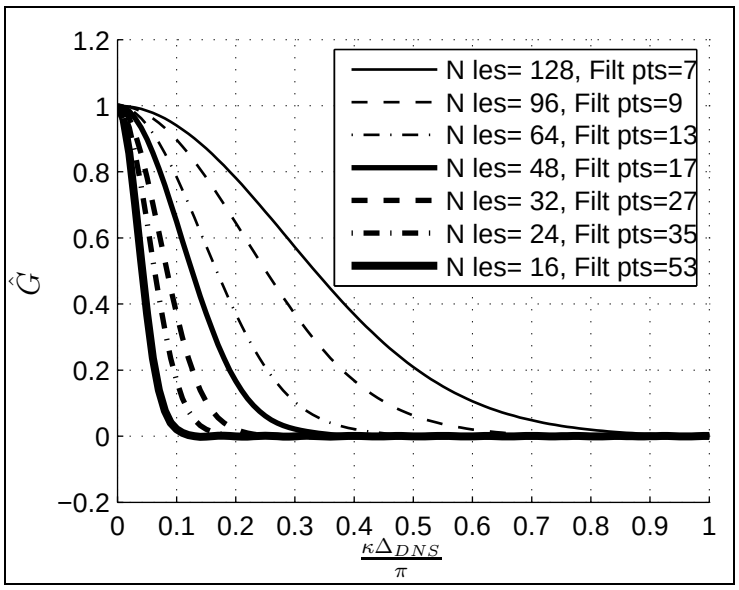

Figure 6.5: Comparison of transfer functions for the discrete Gaussian filter used on the various LES grids. The number of stencil points required for the various filters is also indicated in the legend. For comparison, we chose, $\Delta_{DNS} = 1/192$.

the effect of using non-symmetric filters at the boundaries by including the real and imaginary part of the transfer function of a non-symmetric filter.

As mentioned earlier, the above one-dimensional filter can be easily extended to three dimensions by simply applying the one-dimensional filter in successive coordinate direction.

Previous LES simulations [Gicquel *et al.* (2002); Vreman *et al.* (1997)] do not wait for the mixing layer to become turbulent before LES is used. LES is carried out directly from time $t = 0$ when the laminar mixing layer profile is superimposed with disturbances. It is expected that such LES simulations do not perform well because they require the LES to capture the transition to turbulence accurately. Again, LES is a methodology designed to work well for high Re flows, and may or may not work well in capturing the transition to turbulence. We avoided this

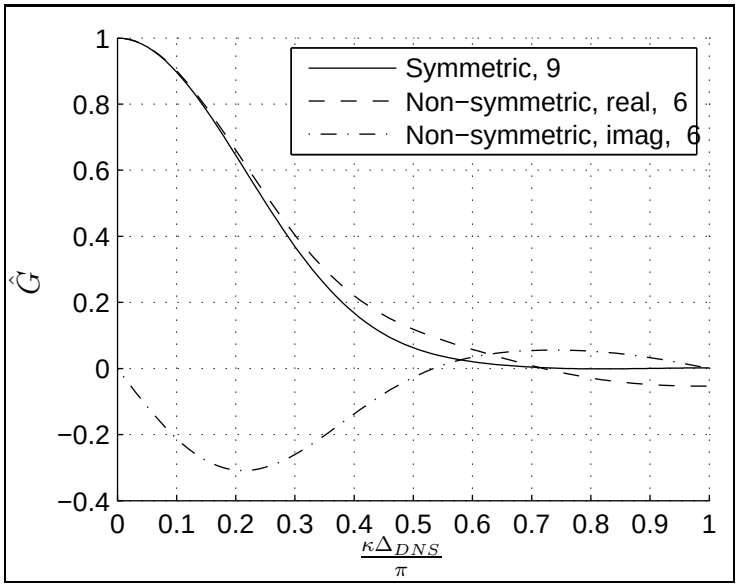

Figure 6.6: Effect of using non-symmetric filters at the boundaries. The transfer function has both a real and imaginary part, thereby altering the phase in the filtered motions. The number of stencil points used in the different filters is also indicated in the legend. For comparison, we chose, $\Delta_{DNS} = 1/192$, $\Delta_{LES} = 1/96$, and $\Delta = 1/48$.

problem by performing a DNS until time $t = 30$, thereby allowing the mixing layer to become turbulent before LES was carried out.

Another important concern here is that LES has been used to model a reasonably low Re mixing layer flow. The low Re restriction was placed by the computational requirements of the DNS with which the LES was compared. So LES may not perform well in predicting the statistics of the underlying turbulent flow.

6.3 Code Validation

The implementation of initial and boundary conditions was verified by comparing statistics obtained from our LES code with those from Gicquel *et al.* (2002). Sheikhi (2005) in Prof. Peyman Givi's research group provided us with statistics for comparison. Henceforth, this simulation is referred to as "Reza-LES". Reza-LES was carried out on a uniform 33^3 grid using the Smagorinsky sub-grid model. For the sake of fair comparison, we also performed the LES on a 32^3 uniform and non-uniform grid. The non-uniform grid refers to the grid with non-uniform grid spacing in the x_3 coordinate direction but uniform grid spacing in the x_1 and x_2 directions. The values of other numerical parameters, chosen to match those used in Reza-LES, are indicated below:

$$\begin{aligned} \Delta &= 2\frac{L_3}{N_3} = 3.6875 \\ C_\nu &= 0.094 \\ C_E &= 0.99446 \end{aligned} \tag{6.17}$$

The same initial conditions described in section 6.2.1 were used in all the LES simulations. Reza-LES was carried out from time $t = 0$, i.e., without using DNS

to capture the initial development of the turbulence. Hence, only for the purpose of validation, we also performed the LES starting at time $t = 0$. Further, the initial conditions at time $t = 0$ were filtered using a hat filter in order to be resolved on a 32^3 grid. The filter width used in all simulations was $\Delta = 3.6875$. Because of the slight differences in the implementation of filtering between our LES and Reza-LES, the initial conditions used may differ slightly.

Figures 6.7-6.10 plot the time evolution of the volume-integrated resolved KE, momentum thickness, volume-integrated SGS production, and volume-integrated physical dissipation. The definitions of these statistics are given below,

$$\text{Resolved KE} \equiv \left\langle \frac{1}{2} W_i W_i \right\rangle_{123} \times (L_1 L_2 L_3) \tag{6.18}$$

$$\text{Momentum thickness } \delta_m \equiv \frac{1}{4} \int_{-\frac{L_3}{2}}^{\frac{L_3}{2}} (1 - \langle W_1 \rangle_{12}) (1 + \langle W_1 \rangle_{12}) \, dx_3 \tag{6.19}$$

$$\text{SGS Production} \equiv \left\langle \tau_{ij}^r S_{ij}^W \right\rangle_{123} \times (L_1 L_2 L_3) \tag{6.20}$$

$$\text{Physical dissipation} \equiv \left\langle \nu S_{ij}^W S_{ij}^W \right\rangle_{123} \times (L_1 L_2 L_3) \tag{6.21}$$

where $\langle \bullet \rangle_{123}$ denotes volume-averaging and $\langle \bullet \rangle_{12}$ denotes plane-averaging over the $x_1 x_2$ plane. It can be seen that the statistics obtained from the different LES simulations are in good agreement. This further validates our LES code. The small differences in the implementation of the hat filter used in our LES and Reza-LES, are clearly evident in the initial time evolution of the SGS production shown in Fig. 6.9. This difference could also arise from differences in the numerical discretization and grids used.

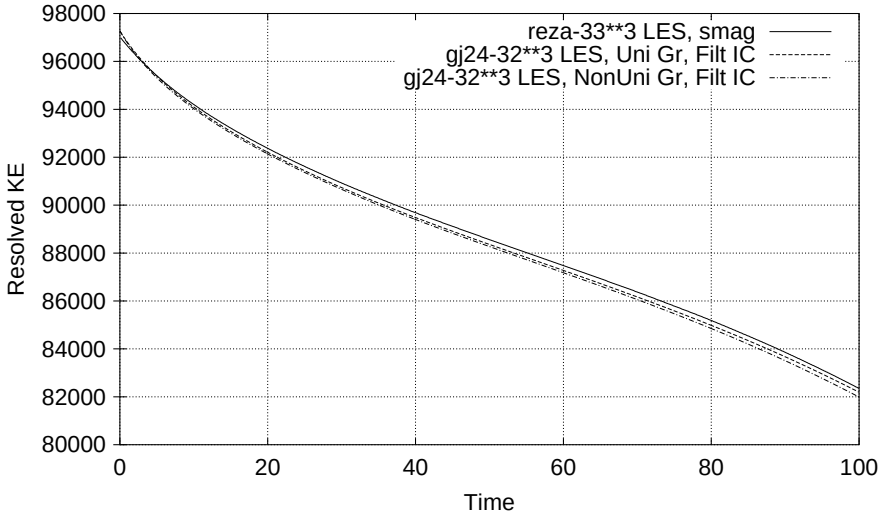

Figure 6.7: Comparison of the time evolution of volume-integrated resolved KE with that obtained from Reza. "gj24-LES" refers to statistics obtained from our LES simulation carried out on a uniform and a non-uniform 32^3 grid. "Reza" refers to the statistics obtained from Reza.

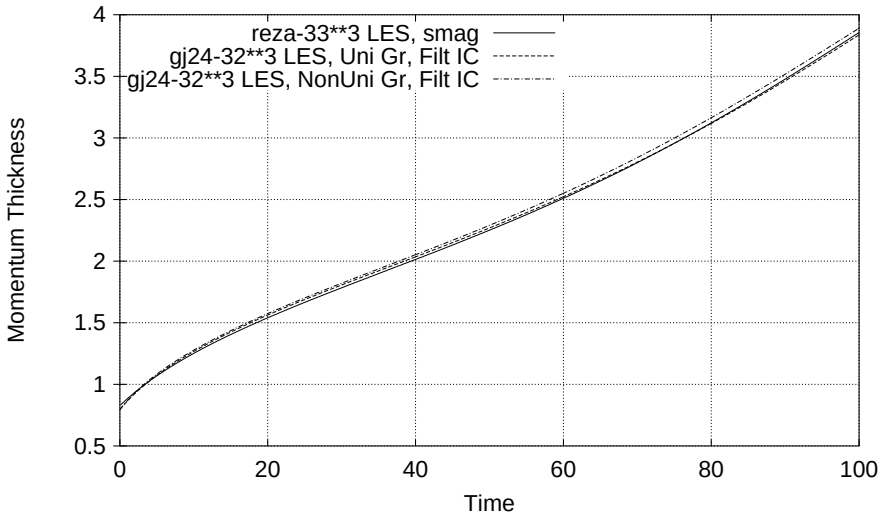

Figure 6.8: Comparison of the time evolution of momentum thickness with that obtained from Reza. "gj24-LES" refers to statistics obtained from our LES simulation carried out on a uniform and a non-uniform 32^3 grid. "Reza" refers to the statistics obtained from Reza.

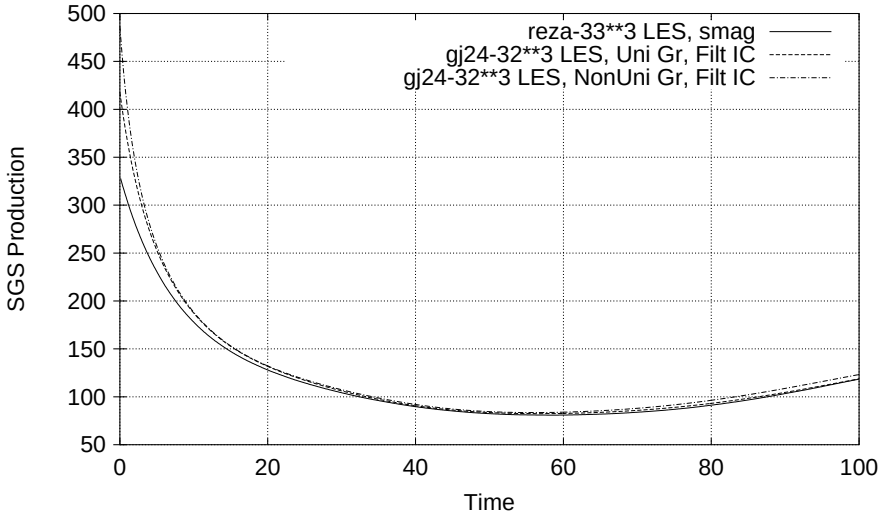

Figure 6.9: Comparison of the time evolution of volume-integrated SGS production with that obtained from Reza. "gj24-LES" refers to statistics obtained from our LES simulation carried out on a uniform and a non-uniform 32^3 grid. "Reza" refers to the statistics obtained from Reza.

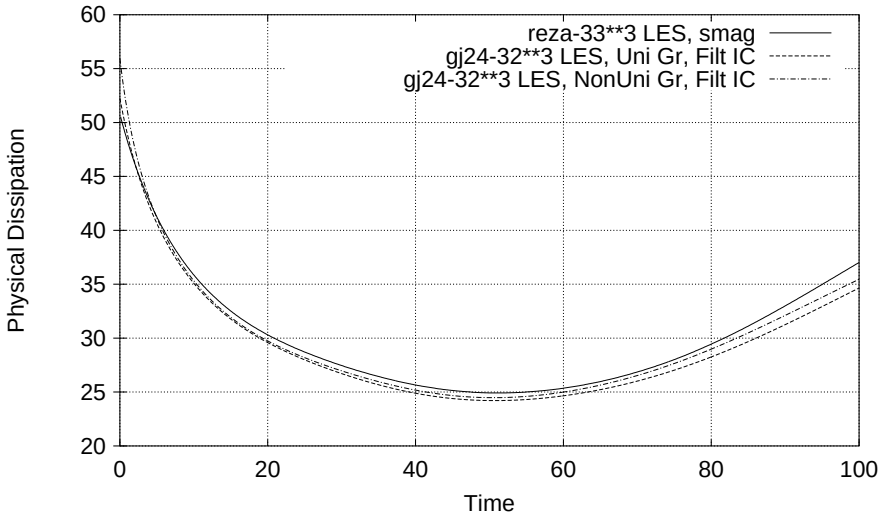

Figure 6.10: Comparison of the time evolution of volume-integrated physical dissipation with that obtained from Reza. "gj24-LES" refers to statistics obtained from our LES simulation carried out on a uniform and a non-uniform 32^3 grid. "Reza" refers to the statistics obtained from Reza.

6.4 Initial phase angle of eigenfunction disturbances

As mentioned in section 6.2.1, the eigenfunction disturbances superimposed on the mean velocity profile at time $t = 0$, require a phase angle ϕ_{j_1,j_2} to be specified. Different values for these phase angles result in different time evolutions of the mixing layer but the statistics of these different evolutions may not differ much. In order to estimate the sensitivity of the statistics to these phase angles, we performed a set of LES simulations with different randomly chosen initial phase angles. Rightfully, we should perform a set of DNS with different phase angles. But, because of the high computational cost of DNS, we instead performed a set of LES using a 32^3 non-uniform grid and the Smagorinsky sub-grid model. It is believed that this set of LES allows us to estimate the sensitivity of the statistics of the original turbulent flow to the initial phase angle. Again, only for the purpose of determining this sensitivity, the LES was started from time $t = 0$, with different phase angles for the eigenfunction disturbances. The values of other numerical parameters are given below:

$$\begin{aligned} \Delta &= 2\frac{L_3}{N_3} = 3.6875 \\ C_\nu &= 0.094 \\ C_E &= 0.99446 \end{aligned} \tag{6.22}$$

Figures 6.11-6.14 compare the time evolution of the volume-integrated resolved KE, momentum thickness, volume-integrated SGS production, and volume-integrated physical dissipation for simulations started from different initial phase angles. "Original phase" refers to the phase angles mentioned in Eq. (6.8) and "Random phase" refers to those generated randomly. Also shown in these figures is the time evolution of DNS carried out on 128^3 and 192^3 non-uniform grids. The

following comments can be made:

- Since the statistics obtained from LES carried out using different initial phase angles are very close, we can conclude that the measured statistics are not very sensitive to the initial phase angle.

- Since the statistics obtained from the DNS using 128^3 and 192^3 grids are close, we conclude that a 128^3 non-uniform grid is sufficient to numerically resolve all the flow features in the DNS.

- Since the time evolution of statistics obtained from the DNS and LES using Smagorinsky model are markedly different, we conclude that the Smagorinsky model does not perform well at initial times when the flow transitions to turbulence. This justifies our decision to evolve the flow using DNS until time $t = 30$ before carrying out the LES.

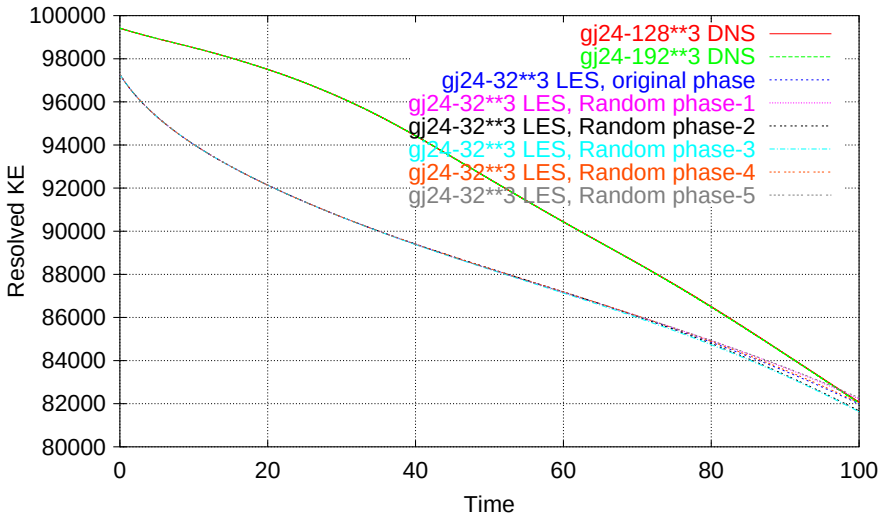

Figure 6.11: Sensitivity of the time evolution of volume-integrated resolved KE to initial phase angle. LES simulations carried out on non-uniform 32^3 grid with Smagorinsky sub-grid model. "Original phase" refers to the phase angles mentioned earlier and "Random phase" refers to those generated randomly.

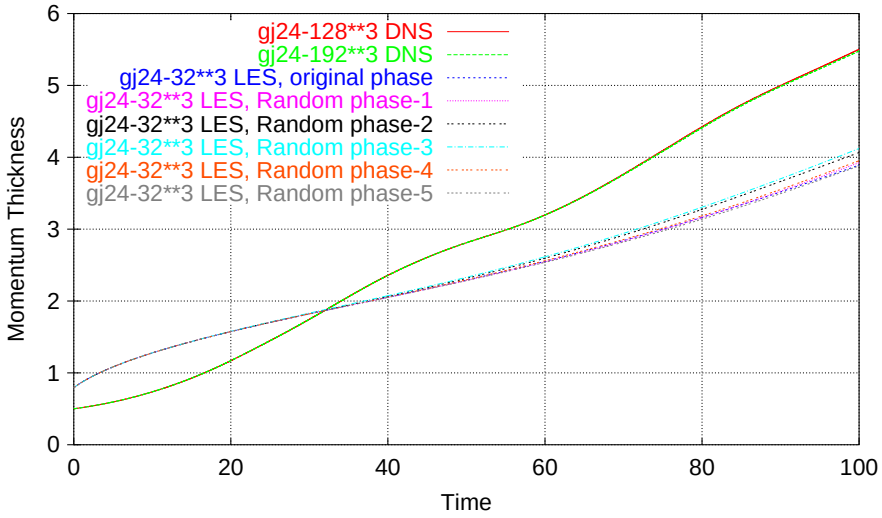

Figure 6.12: Sensitivity of the time evolution of momentum thickness to initial phase angle. LES simulations carried out on non-uniform 32^3 grid with Smagorinsky sub-grid model. "Original phase" refers to the phase angles mentioned earlier and "Random phase" refers to those generated randomly.

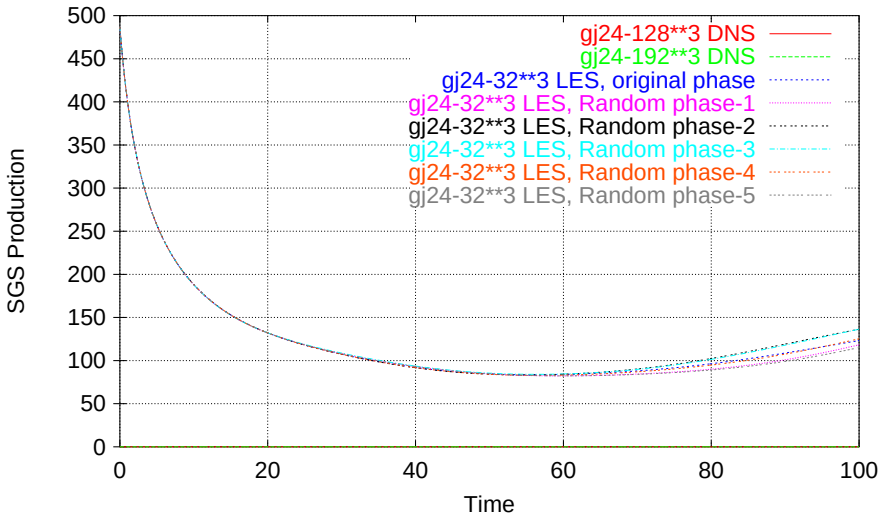

Figure 6.13: Sensitivity of the time evolution of volume-integrated SGS production to initial phase angle. LES simulations carried out on non-uniform 32^3 grid with Smagorinsky sub-grid model. "Original phase" refers to the phase angles mentioned earlier and "Random phase" refers to those generated randomly.

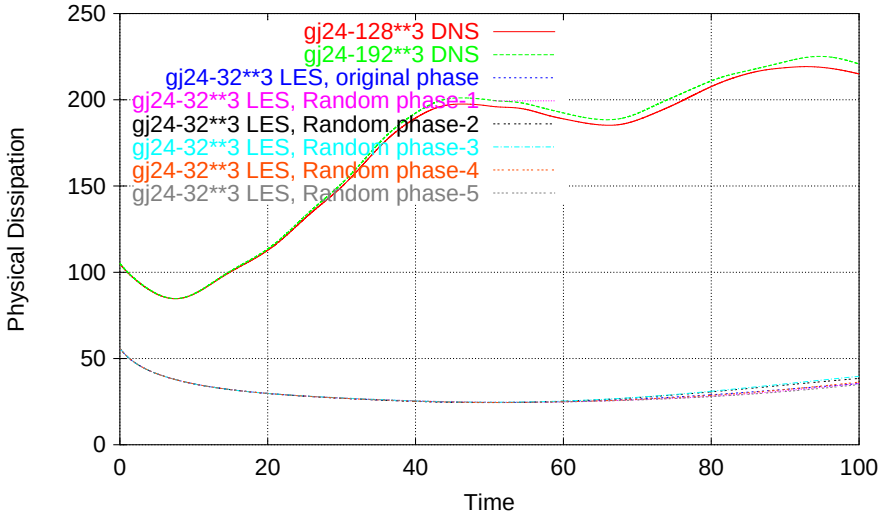

Figure 6.14: Sensitivity of the time evolution of volume-integrated physical dissipation to initial phase angle. LES simulations carried out on non-uniform 32^3 grid with Smagorinsky sub-grid model. "Original phase" refers to the phase angles mentioned earlier and "Random phase" refers to those generated randomly.

6.5 Lack of statistical self-similarity

It is expected that the profiles of the various statistics in the turbulent mixing layer become approximately self-similar after an initial evolution period. "Statistical self-similarity", in the case of the turbulent mixing layer, means that the cross-stream profiles of the various statistics collapse when normalized using the momentum thickness δ_m at that time and the free stream speed U^0.

Figure 6.15 shows the cross-stream profiles of the mean stream-wise velocity $\langle U_1 \rangle_{12}$ normalized by the momentum thickness δ_m and the free stream speed U^0 at various times. The data are obtained from the DNS carried out using the 128^3 non-uniform grid. It can be seen that the profiles of $\langle U_1 \rangle_{12}$ collapse, indicating that $\langle U_1 \rangle$ becomes self-similar.

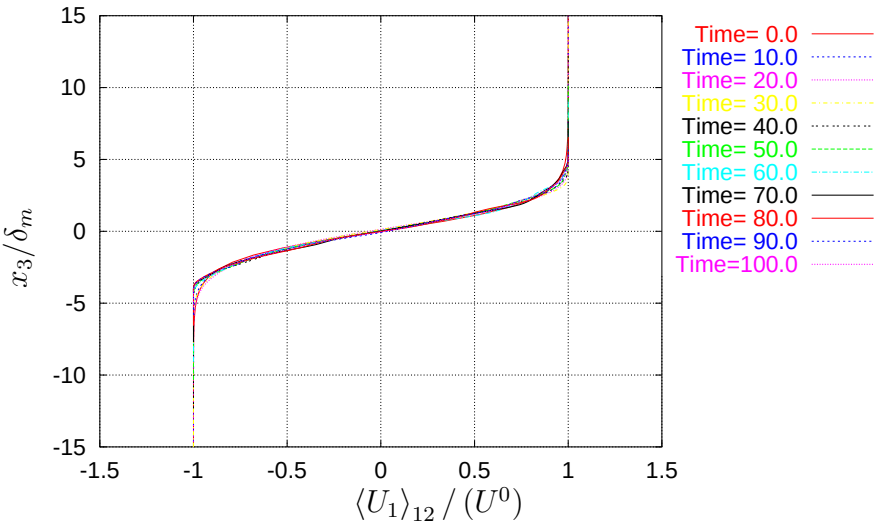

Figure 6.15: Cross-stream profiles of the plane-averaged streamwise velocity $\langle U_1 \rangle_{12}$, normalized by the momentum thickness δ_m and the free stream speed U^0, at various times. Data obtained from the DNS carried out using the 128^3 non-uniform grid.

However, the second-order velocity statistics did not collapse as well. We first

define the turbulent velocity fluctuations u_i as,

$$u_i \equiv U_i - \langle U_i \rangle_{12} \tag{6.23}$$

Figures 6.16 and 6.17 show the cross-stream variation of the normal Re stress $\langle u_1 u_1 \rangle_{12}$ and the cross Re stress $\langle u_1 u_3 \rangle_{12}$, normalized by the momentum thickness δ_m and the free stream speed U^0, at various times. From these figures, it appears that there is no time period in which these two statistics become self-similar. Since statistical self-similarity requires these statistics to become self-similar as well, we conclude that there is no time period in our simulations when the flow evolves in a self-similar manner.

The inability to observe a statistically self-similar flow evolution could be due to a number of reasons. One reason is that the statistics need to be averaged over a large number of flow structures while in our simulations we have four roller vortices at initial times which undergo pairings to form only one at later times. Hence, this small number of resolved flow structures, could account for the variation in the normalized profiles. Another reason could be that the flow has evolved for sufficient time that the mean velocity profiles become self-similar but the second-order velocity statistics require a longer time to become self-similar. However, the maximum time for which the simulation can be carried out is determined by the size of the computational box, $[0, L_1] \times [0, L_2] \times [-\frac{L_3}{2}, \frac{L_3}{2}]$. This is because the mixing layer thickness grows with time and the simulated flow evolution is physically meaningful only as long as the flow structures are small compared to the box size. The time evolution of the mixing layer thickness, Fig. 6.12, suggests that the size of the flow structures become comparable to the box size around time $t = 100$.

Since we could not establish a time period in which the flow becomes statis-

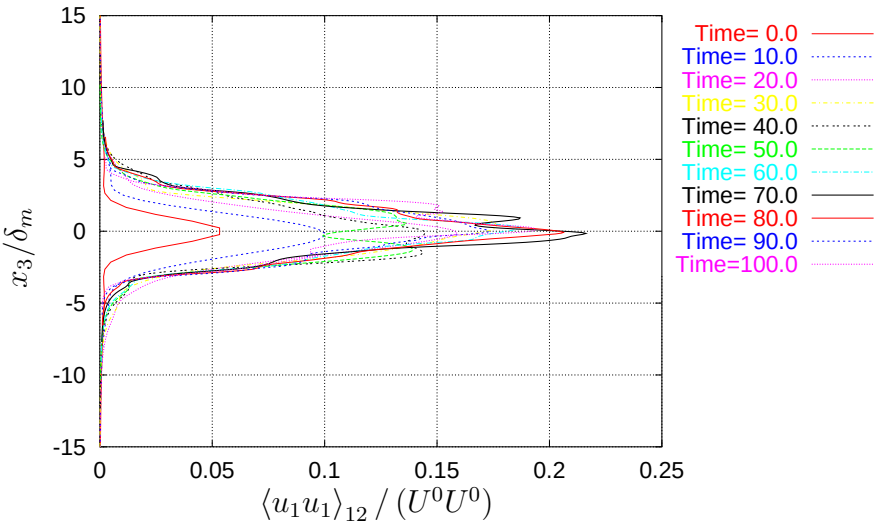

Figure 6.16: Cross-stream profiles of the plane-averaged normal Re stress, $\langle u_1 u_2 \rangle_{12} \equiv \langle (U_1 - \langle U_1 \rangle_{12}) (U_1 - \langle U_1 \rangle_{12}) \rangle_{12}$, normalized by the momentum thickness δ_m and the free stream speed U^0, at various times. Data obtained from the DNS carried out using the 128^3 non-uniform grid.

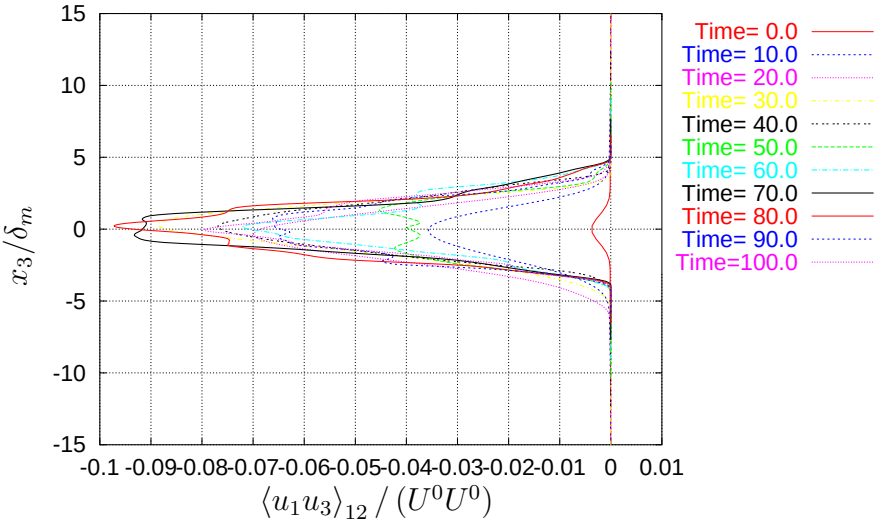

Figure 6.17: Cross-stream profiles of the plane-averaged cross Re stress, $\langle u_1 u_3 \rangle_{12} \equiv \langle (U_1 - \langle U_1 \rangle_{12}) (U_3 - \langle U_3 \rangle_{12}) \rangle_{12}$, normalized by the momentum thickness δ_m and the free stream speed U^0, at various times. Data obtained from the DNS carried out using the 128^3 non-uniform grid.

tically self-similar, we could not average the statistics over time as well. Hence, all statistical comparisons were made at specific times. Other researchers [Gicquel *et al.* (2002); Vreman *et al.* (1997)] have also resorted to making statistical comparisons at specific times without time-averaging.

6.6 Convergence characteristics of Smagorinsky sub-grid model

In this section we study the convergence with resolution length scale Δ of the various statistics obtained using the Smagorinsky sub-grid model. The turbulent mixing layer being modeled using LES was described in detail in sections 6.1 and 6.2. The flow obtained at time $t = 30$ was filtered using a discrete Gaussian filter and used as initial conditions for the LES. The filter width for the Gaussian filter was taken to be the resolution length scale used for the LES. The LES simulations described in this section were carried out using the Smagorinsky sub-grid model with model parameters,

$$\begin{aligned} C_\nu &= 0.094 \\ C_E &= 0.99446 \end{aligned} \tag{6.24}$$

A number of LES at different resolution length scales Δ were carried out to study the convergence with Δ. Table 6.1 summarizes the numerical parameters used in these simulations. Again, to provide a perspective on the times required to carry out these LES simulations, rough measurements of the wall-clock times are given in Table 6.2. Since a queuing system was not in place in the JIT cluster, other jobs may have been executed at the same time and in the same processes used for these LES.

Table 6.1: Summary of numerical parameters used in the LES of temporal mixing layer. These LES were carried out to study the convergence with Δ of the Smagorinsky model. Notation used: resolution length scale Δ, number of grid points in each direction N, and time step used in the LES Δt_{Smag}

Δ	N	Δt_{Smag}
7.375	16	0.1
4.917	24	0.05
3.688	32	0.05
2.548	48	0.025
1.844	64	0.02
1.229	96	0.01
0.922	128	0.008

Table 6.2: Rough measurements of the wall-clock times for the LES of temporal mixing layer from time $t = 30$ to $t = 100$. These LES were carried out to study the convergence with Δ of the Smagorinsky model. Notation used: resolution length scale Δ, number of grid points in each direction N, time step Δt, number of time-steps, N_{TS}, wall-clock time per time-step, $T_{\Delta t}$, wall-clock time, T_W, and number of processes, N_p.

Δ	N	Δt	N_{TS}	$T_{\Delta t}$ (secs)	T_W (secs)	T_W (days)	N_p
7.375	16	0.100	7000	0.275	192.7	0.002	1
4.917	24	0.050	1400	0.767	1073.5	0.012	4
3.688	32	0.050	1400	0.764	1069.6	0.012	4
2.548	48	0.025	2800	1.585	4439.2	0.051	4
1.844	64	0.020	3500	4.171	14600.2	0.169	4
1.229	96	0.010	7000	5.271	36899.3	0.427	4
0.922	128	0.008	8750	10.811	94597.3	1.095	4

6.6.1 Volume-averaged turbulent KE

The resolved turbulent fluctuations w_i, as the name suggests, are the turbulent fluctuations resolved in the LES and are defined as

$$w_i \equiv W_i - \langle W_i \rangle_{12} \tag{6.25}$$

The above equation is analogous to Eq. (6.23) used to define the turbulent fluctuations in the underlying turbulent velocity field. The volume-averaged resolved turbulent KE is simply,

$$\text{Resolved turbulent KE} \equiv \frac{1}{2} \langle w_i w_i \rangle_{123} \tag{6.26}$$

A model for the energy in the unresolved or residual velocity field u_i^R can be obtained by volume-averaging the modeled residual KE k_R.

$$\text{Residual turbulent KE} \equiv \frac{1}{2} \left\langle u_i^R u_i^R \right\rangle_{123} \stackrel{M}{=} \langle k_R \rangle_{123} \tag{6.27}$$

Hence, the volume-averaged total turbulent KE, which is a model for the turbulent KE in the underlying turbulent velocity field, is obtained by summing up the above two contributions:

$$\text{Total turbulent KE} \stackrel{M}{=} \frac{1}{2} \langle w_i w_i \rangle_{123} + \langle k_R \rangle_{123} \tag{6.28}$$

Figures 6.18 - 6.19 study the convergence of the resolved turbulent KE with Δ at four different times $t = 40$, 50, 60, and 70. Further, this is compared with the convergence of total turbulent KE. The value of the turbulent KE obtained from the DNS carried out on the 192^3 grid is also provided for reference. All quantities were non-dimensionalized using the free-stream velocity U^0 and half the initial vorticity thickness δ_w^0.

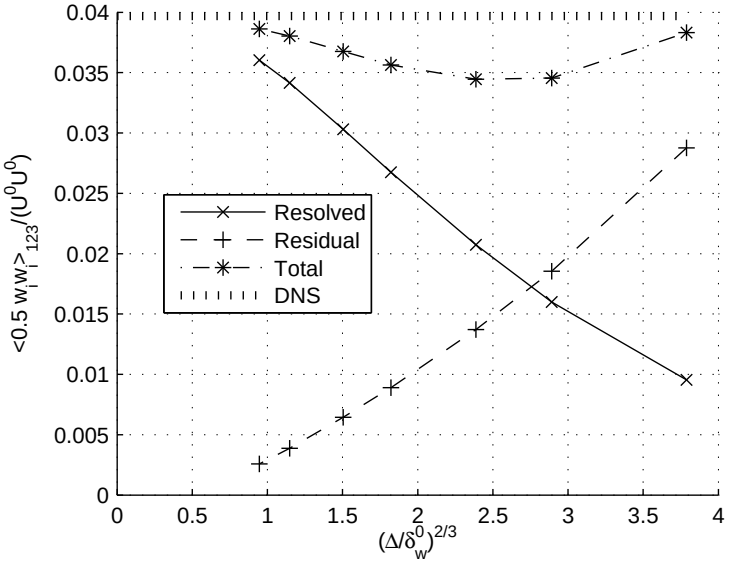

(a) time $t = 40$

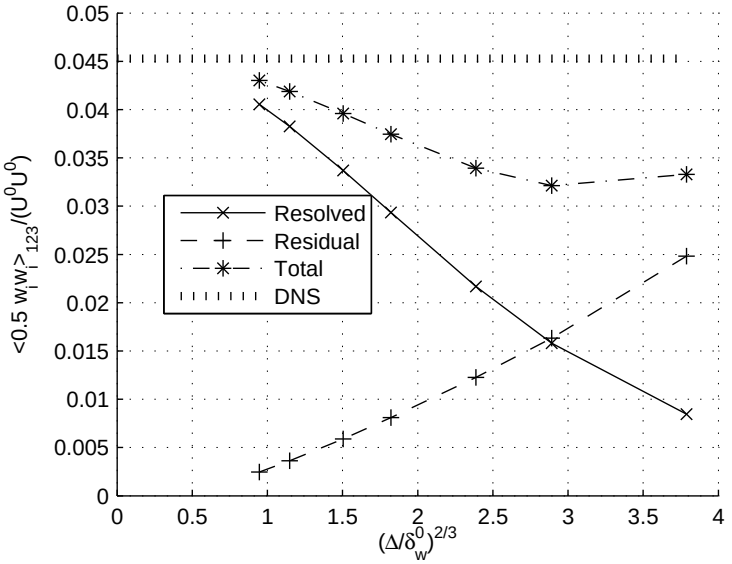

(b) time $t = 50$

Figure 6.18: Variation of volume-averaged turbulent KE $\left\langle \frac{1}{2} w_i w_i \right\rangle_{123}$ with resolution length scale Δ at times $t = 40$ and 50. LES carried out using Smagorinsky model with $C_\nu = 0.094$ and $C_E = 0.9946$.

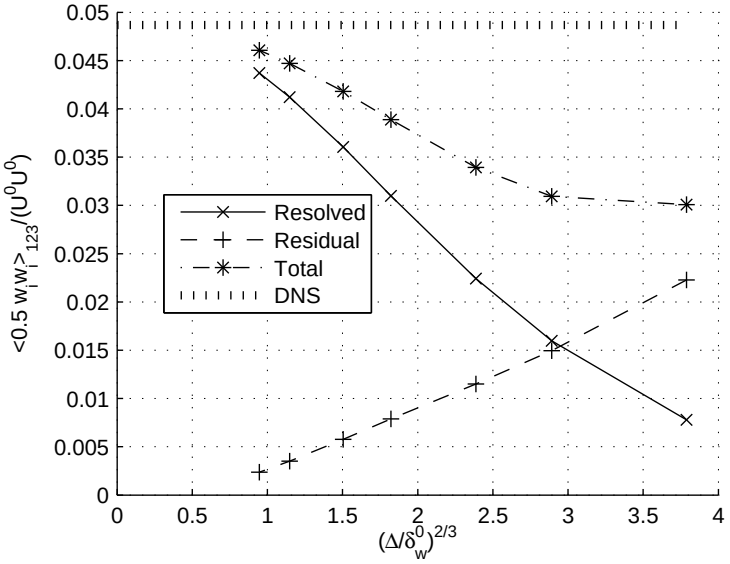

(a) time $t = 60$

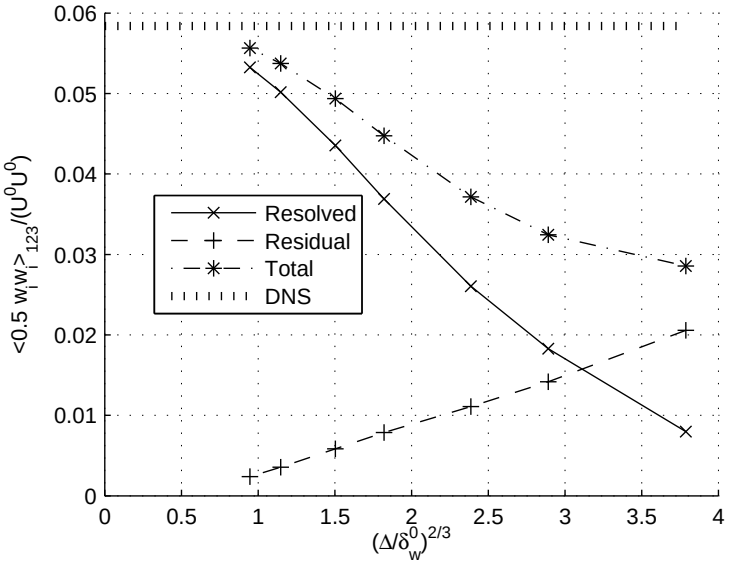

(b) time $t = 70$

Figure 6.19: Variation of volume-averaged turbulent KE $\left\langle \frac{1}{2} w_i w_i \right\rangle_{123}$ with resolution length scale Δ at times $t = 60$ and 70. LES carried out using Smagorinsky model with $C_\nu = 0.094$ and $C_E = 0.9946$.

For isotropic turbulence, the leading order Δ variation of the resolved KE was estimated to be $\Delta^{2/3}$ (see section 5.6.2). The above estimate is justified for the temporal mixing layer based on Kolmogorov's hypothesis. Most of the derivation for isotropic turbulence hinged on the model assumed for the residual energy spectrum in Eq. (5.22). According to Kolmogorov's hypothesis, the statistics of the turbulent motions in the inertial and dissipation ranges are *universal* i.e. independent of the actual flow. Since the resolution length scale Δ is assumed to be chosen in the inertial sub-range, assuming a similar model spectrum for the residual motions is a good assumption even for the mixing layer. This results in a $\Delta^{2/3}$ leading order variation for the turbulent KE in the temporal mixing layer as well.

It should be noted that in the current simulations, many of the above assumptions are violated. Most importantly, the temporal mixing layer being simulated is at a very low Re and hence there is probably no inertial sub-range. Further, for the LES carried out on the 16^3 grid (say), Δ is likely to be in the energy-containing range, while for the LES carried out on the 128^3 grid (say), Δ is likely to be in the dissipation range. Despite these violations, Figs. 6.18 - 6.19 indicate that $\Delta^{2/3}$ is a good leading order estimate for the turbulent KE variation.

The following comments can be made on Figs. 6.18-6.19 :

- The total turbulent KE is a much better estimate of the turbulent KE, at Δ values typically used in an LES, as compared with the resolved KE. This is evident from the fact that the total turbulent KE is closer to the turbulent KE obtained from DNS at all Δ. This was true for all the times shown in Figs. 6.18-6.19. Hence, including the model for the residual turbulent KE improves the LES estimate for the turbulent KE.

- The Δ variation of total turbulent KE was smaller than that of the resolved

turbulent KE at all times shown. This implies that even at a larger value of Δ we can obtain a reasonable estimate for the turbulent KE.

- The Δ variation of total turbulent KE increased at later times. This suggests that the Smagorinsky model was performing more poorly at later times.

6.6.2 Plane-averaged turbulent KE

We now look at the convergence of the turbulent KE averaged over the x_1x_2 plane at different cross-stream locations and times. This allows us to determine any changes in the Δ convergence of turbulent KE with cross-stream location. The definitions for the turbulent KE are the same as in the earlier section but averaged over the x_1x_2 planes instead of a volume-average.

$$\begin{aligned} \text{Resolved turbulent KE} &\equiv \frac{1}{2}\left\langle w_i w_i \right\rangle_{12} \\ \text{Residual turbulent KE} &\equiv \frac{1}{2}\left\langle u_i^R u_i^R \right\rangle_{12} \stackrel{M}{=} \left\langle k_R \right\rangle_{12} \\ \text{Total turbulent KE} &\stackrel{M}{=} \frac{1}{2}\left\langle w_i w_i \right\rangle_{12} + \left\langle k_R \right\rangle_{12} \end{aligned} \tag{6.29}$$

Figures 6.20 - 6.23 show the Δ convergence of the turbulent KE at seven different non-dimensional cross-stream locations $\xi_3 \equiv (x_3/\delta_m) = 0$, ± 0.5, ± 1, and ± 3 and two times $t = 40$ and 70. All the comments made for the volume-averaged turbulent KE in the earlier section also hold for the plane-averaged turbulent KE. Further,

- The Δ convergence of the plane-averaged turbulent KE at a given time is similar at different cross-stream locations ξ_3.

- The plane-averaged turbulent KE is symmetric about $\xi_3 = 0$ for the mixing layer. Any asymmetries observed are probably due to statistical error resulting from averaging over a finite plane.

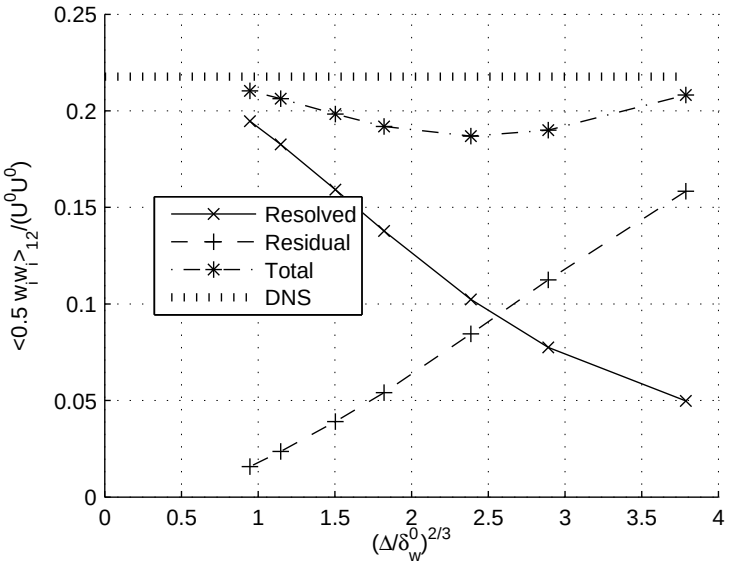

(a) $\xi_3 = 0$ and $t = 40$

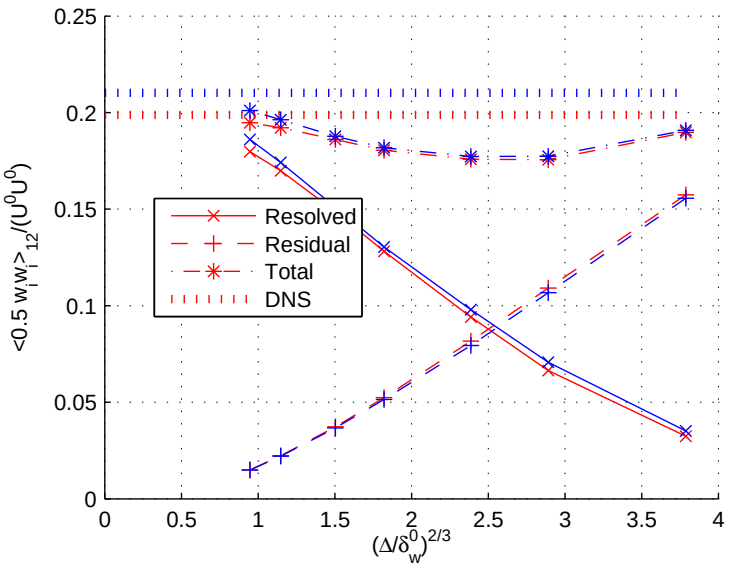

(b) $\xi_3 = +0.5$ (red), -0.5 (blue) and $t = 40$

Figure 6.20: Variation of plane-averaged turbulent KE $\left\langle \frac{1}{2} w_i w_i \right\rangle_{12}$ with resolution length scale Δ at non-dimensional cross-stream locations $\xi_3 \equiv (x_3/\delta_m) = 0$ and ± 0.5, and time $t = 40$. LES carried out using Smagorinsky model with $C_\nu = 0.094$ and $C_E = 0.9946$.

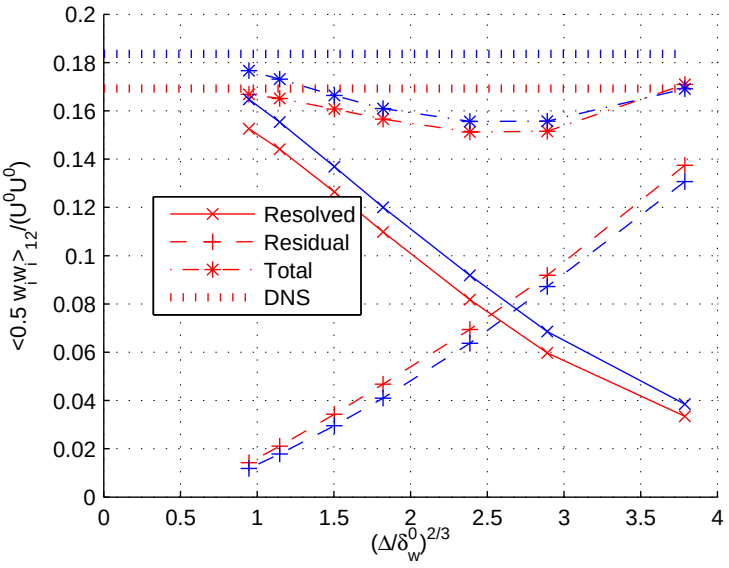

(a) $\xi_3 = +1$ (red), -1 (blue) and $t = 40$

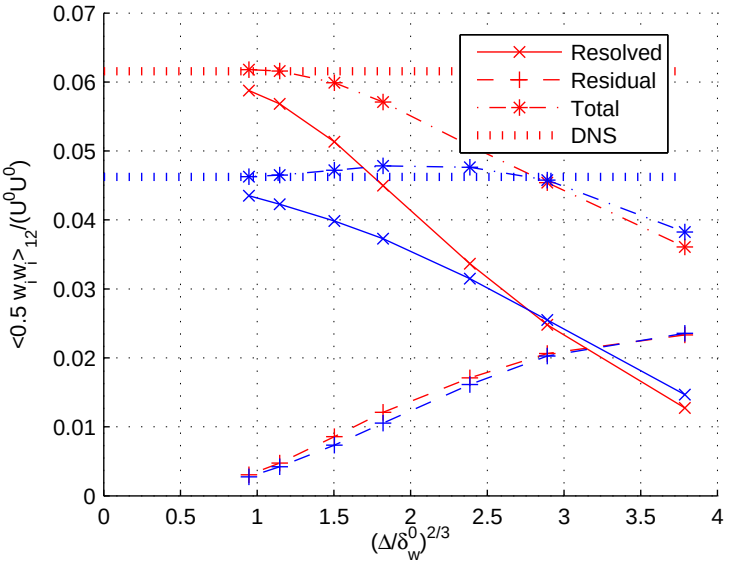

(b) $\xi_3 = +3$ (red), -3 (blue) and $t = 40$

Figure 6.21: Variation of plane-averaged turbulent KE $\left\langle \frac{1}{2} w_i w_i \right\rangle_{12}$ with resolution length scale Δ at non-dimensional cross-stream locations $\xi_3 \equiv (x_3/\delta_m) = \pm 1$ and ± 3, and time $t = 40$. LES carried out using Smagorinsky model with $C_\nu = 0.094$ and $C_E = 0.9946$.

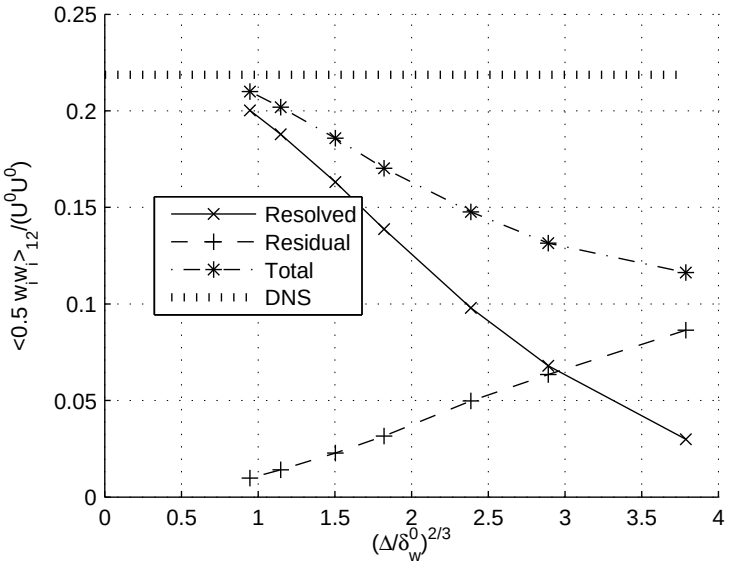

(a) $\xi_3 = 0$ and $t = 70$

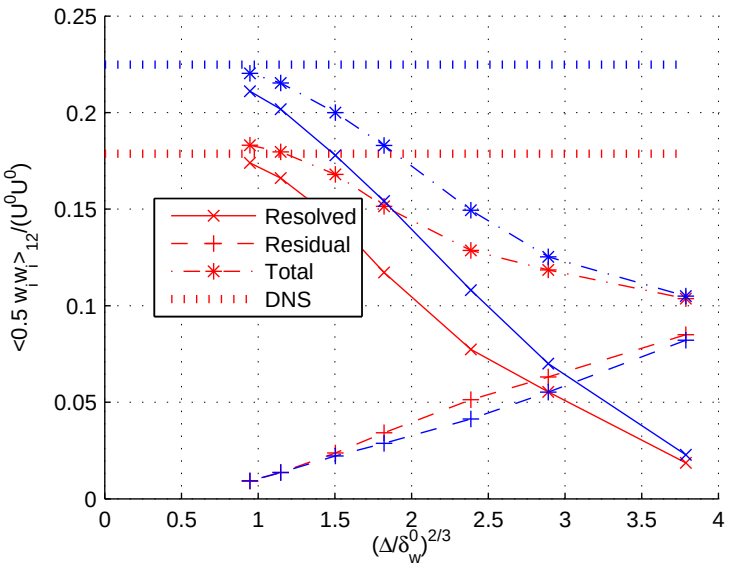

(b) $\xi_3 = +0.5$ (red), -0.5 (blue) and $t = 70$

Figure 6.22: Variation of plane-averaged turbulent KE $\left\langle \frac{1}{2} w_i w_i \right\rangle_{12}$ with resolution length scale Δ at non-dimensional cross-stream locations $\xi_3 \equiv (x_3/\delta_m) = 0$ and ± 0.5, and time $t = 70$. LES carried out using Smagorinsky model with $C_\nu = 0.094$ and $C_E = 0.9946$.

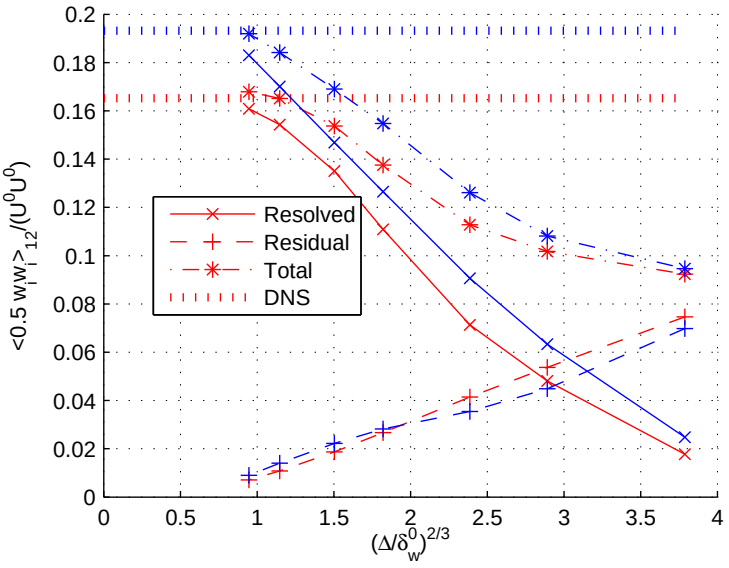

(a) $\xi_3 = +1$ (red), -1 (blue) and $t = 70$

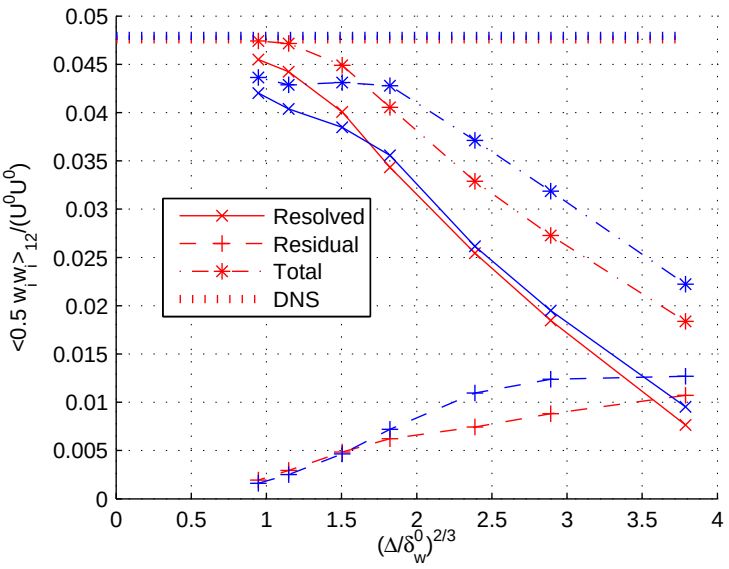

(b) $\xi_3 = +3$ (red), -3 (blue) and $t = 70$

Figure 6.23: Variation of plane-averaged turbulent KE $\left\langle \frac{1}{2} w_i w_i \right\rangle_{12}$ with resolution length scale Δ at non-dimensional cross-stream locations $\xi_3 \equiv (x_3/\delta_m) = \pm 1$ and ± 3, and time $t = 70$. LES carried out using Smagorinsky model with $C_\nu = 0.094$ and $C_E = 0.9946$.

6.6.3 Plane-averaged shear stress $\langle w_1 w_3 \rangle_{12}$

Another important second-order velocity statistic in the temporal mixing layer is the turbulent shear stress $\langle w_1 w_3 \rangle$. In this section we study the Δ convergence of the plane-averaged shear stress $\langle w_1 w_3 \rangle_{12}$. We first determine the leading order Δ variation for $\langle w_1 w_3 \rangle$. This then allows us to plot the Δ convergence plots against the right power of Δ. Lastly, we comment on the observed convergence behavior.

Based on Kolmogorov's hypothesis, the turbulent motions in the inertial and dissipation ranges are *statistically isotropic*, implying that the contribution of the residual or unresolved motions to $\langle u_1 u_3 \rangle$ is zero. However, Lumley (1967) provided a correction to the Kolmogorov's hypothesis by including the production of anisotropy due to shear.

These ideas are first developed in the context of isotropic turbulence and then extended to the temporal mixing layer. We first define the shear stress spectrum $E_{13}(\kappa)$ to be the average of the velocity-spectrum $\Phi_{13}(\boldsymbol{\kappa})$ over a spherical shell of radius κ.

$$E_{13}(\kappa) \equiv \iiint_{-\infty}^{\infty} \Phi_{13}(\boldsymbol{\kappa}) \delta\left(|\boldsymbol{\kappa}| - \kappa\right) \boldsymbol{d\kappa} \tag{6.30}$$

Lumley (1967) predicts the following inertial sub-range behavior for the shear-stress spectrum,

$$E_{13}(\kappa) = C_{13}^{S} \mathcal{S} \left\langle \epsilon \right\rangle^{1/3} \kappa^{-7/3} \tag{6.31}$$

where $\mathcal{S}$ is the characteristic strain rate producing the anisotropy. This $\kappa^{-7/3}$ behavior of the shear-stress spectrum should be contrasted with the $\kappa^{-5/3}$ behavior exhibited by the energy spectrum, indicating that the anisotropy dies off faster at high wave numbers. More details can be found in pages 246-249 of Pope (2000*c*). Using the above inertial sub-range form for the shear-stress spectrum in a model

for the residual shear-stress spectrum, we have,

$$E_{13}^{R}(\kappa) \stackrel{M}{=} \begin{cases} 0 & \text{for } \kappa < p_1\kappa_d \\ C_{13}^{S}\mathcal{S}\left\langle\epsilon\right\rangle^{\frac{1}{3}}\kappa^{-\frac{7}{3}} & \text{for } \kappa \geq p_1\kappa_d \end{cases} \tag{6.32}$$

This allows us to model the contribution to the shear stress $\langle u_1 u_3 \rangle$ from the residual motions u_i^R in a LES, as follows,

$$\begin{aligned} \left\langle u_1^R u_3^R \right\rangle &= \int_0^\infty E_{13}^R(\kappa) d\kappa \\ &= \int_{p_1\kappa_d}^\infty C_{13}^S \mathcal{S} \left\langle\epsilon\right\rangle^{\frac{1}{3}} \kappa^{-\frac{7}{3}} d\kappa \\ &= \frac{3}{4} C_{13}^S \mathcal{S} \left\langle\epsilon\right\rangle^{\frac{1}{3}} (p_1\kappa_d)^{-\frac{4}{3}} \\ &= \frac{3}{4} C_{13}^S \mathcal{S} \left\langle\epsilon\right\rangle^{\frac{1}{3}} (p_1\pi)^{-\frac{4}{3}} \Delta^{\frac{4}{3}} \end{aligned} \tag{6.33}$$

Hence, the leading order Δ term in the shear stress variation is $\Delta^{4/3}$, as opposed to the $\Delta^{2/3}$ variation expected in the turbulent KE.

The definitions for the resolved, residual and total contributions to the shear stress $\langle u_1 u_3 \rangle$ are summarized below:

$$\begin{aligned} \text{Resolved shear stress} &\equiv \left\langle w_1 w_3 \right\rangle_{12} \\ \text{Residual shear stress} &\equiv \left\langle u_1^R u_3^R \right\rangle_{12} \stackrel{M}{=} -\left\langle 2\nu_r S_{13}^W \right\rangle_{12} \\ \text{Total shear stress} &\stackrel{M}{=} \left\langle w_1 w_3 \right\rangle_{12} - \left\langle 2\nu_r S_{13}^W \right\rangle_{12} \end{aligned} \tag{6.34}$$

Figures 6.24 - 6.27 show the Δ convergence of the shear stress at seven different non-dimensional cross-stream locations $\xi_3 \equiv (x_3/\delta_m) = 0$, ± 0.5, ± 1, and ± 3 and two times $t = 40$ and 70.

Again, the inclusion of the model for the residual contributions improves the Δ convergence characteristics of the resolved shear stress. A striking observation is that the Δ variation of total shear stress (Figs. 6.24 - 6.27) is much larger than the Δ variation of total turbulent KE (Figs. 6.20 - 6.23). This is a problem

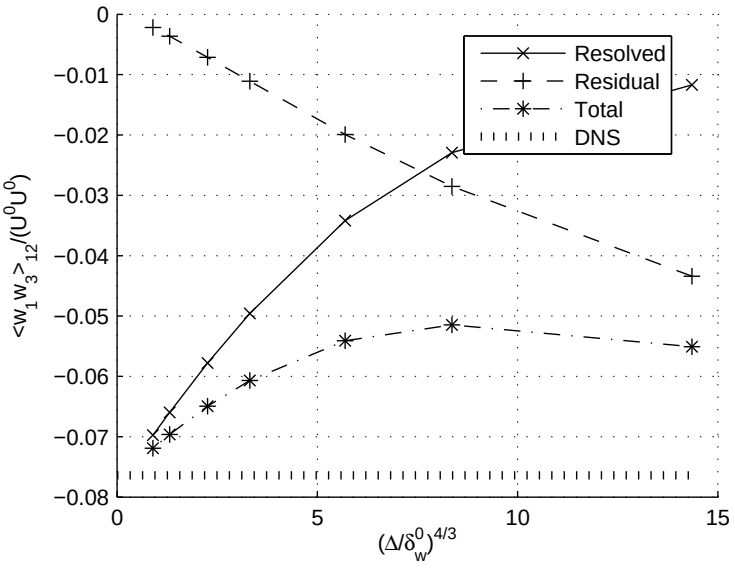

(a) $\xi_3 = 0$ and $t = 40$

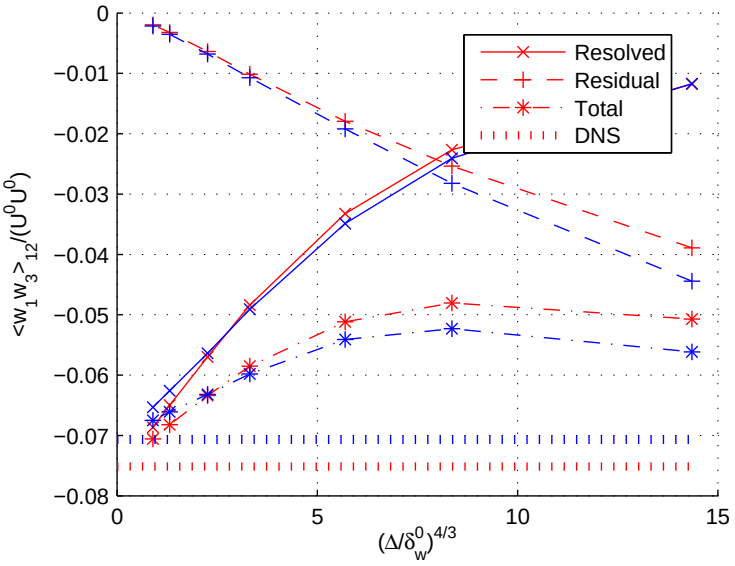

(b) $\xi_3 = +0.5$ (red), -0.5 (blue) and $t = 40$

Figure 6.24: Variation of plane-averaged turbulent shear stress $\langle w_1 w_3 \rangle_{12}$ with resolution length scale Δ at non-dimensional cross-stream locations $\xi_3 \equiv (x_3/\delta_m) = 0$ and ± 0.5, and time $t = 40$. LES carried out using Smagorinsky model with $C_\nu = 0.094$ and $C_E = 0.9946$.

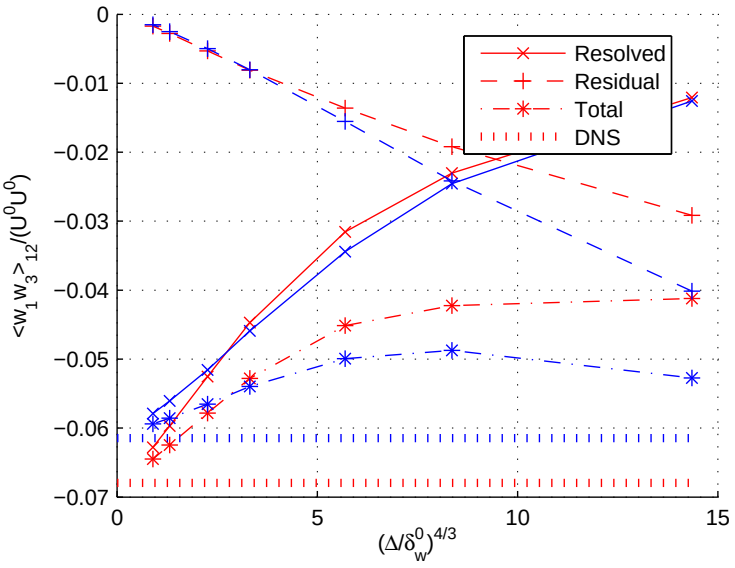

(a) $\xi_3 = +1$ (red), -1 (blue) and $t = 40$

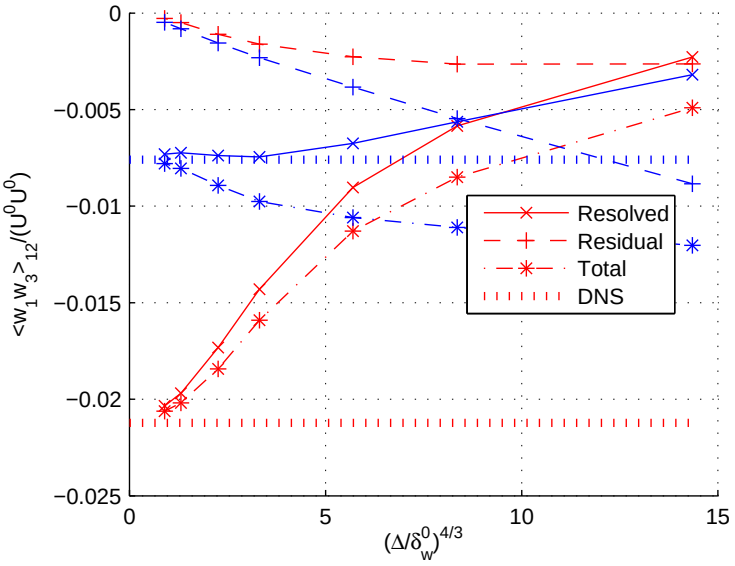

(b) $\xi_3 = +3$ (red), -3 (blue) and $t = 40$

Figure 6.25: Variation of plane-averaged shear stress $\langle w_1 w_3 \rangle_{12}$ with resolution length scale Δ at non-dimensional cross-stream locations $\xi_3 \equiv (x_3/\delta_m) = \pm 1$ and ± 3, and time $t = 40$. LES carried out using Smagorinsky model with $C_\nu = 0.094$ and $C_E = 0.9946$.

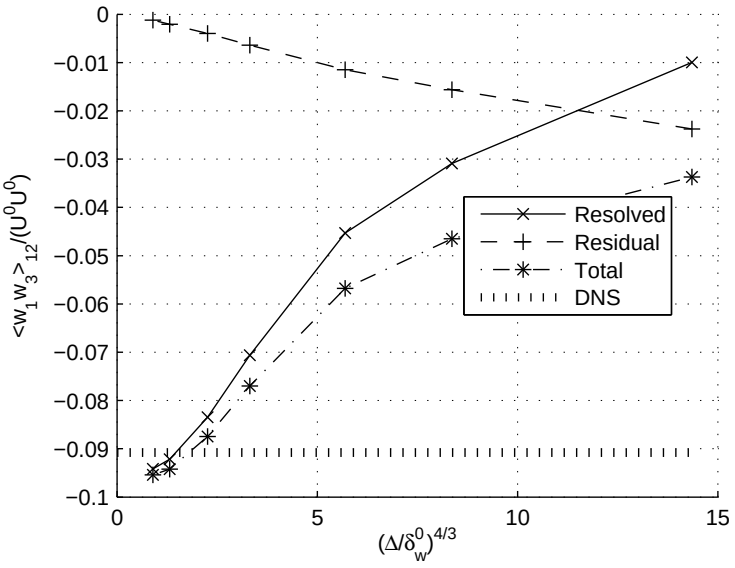

(a) $\xi_3 = 0$ and $t = 70$

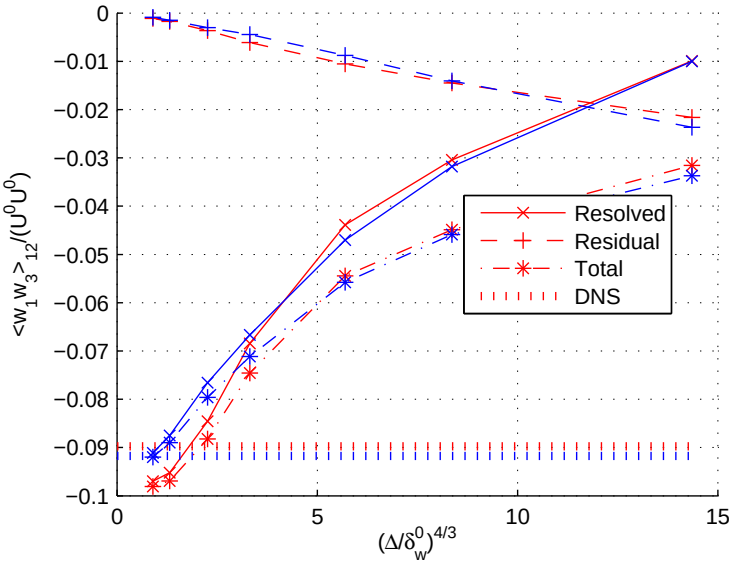

(b) $\xi_3 = +0.5$ (red), -0.5 (blue) and $t = 70$

Figure 6.26: Variation of plane-averaged turbulent shear stress $\langle w_1 w_3 \rangle_{12}$ with resolution length scale Δ at non-dimensional cross-stream locations $\xi_3 \equiv (x_3/\delta_m) = 0$ and ± 0.5, and time $t = 70$. LES carried out using Smagorinsky model with $C_\nu = 0.094$ and $C_E = 0.9946$.

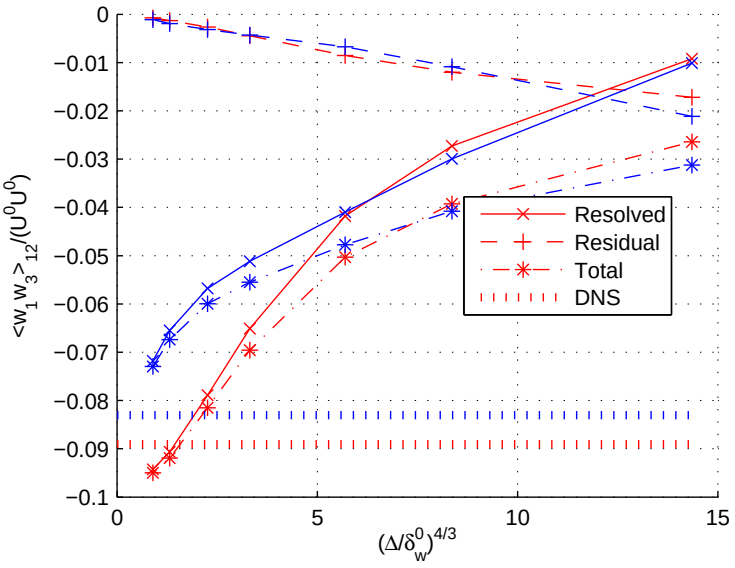

(a) $\xi_3 = +1$ (red), -1 (blue) and $t = 70$

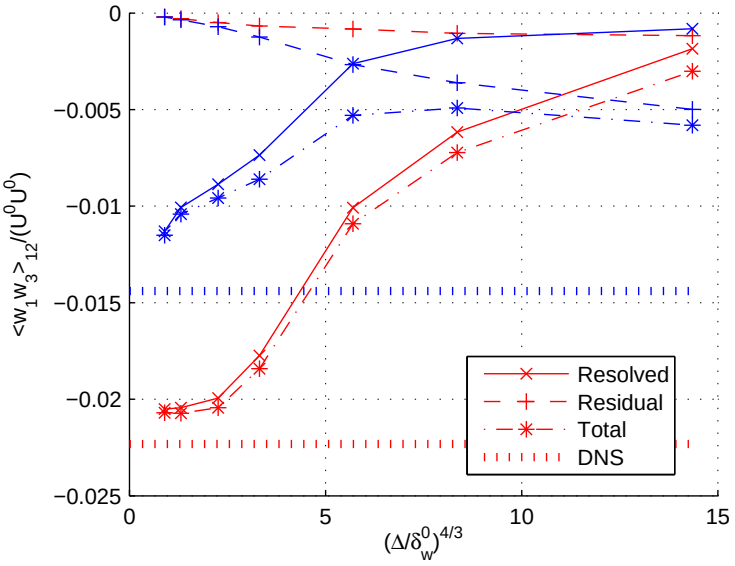

(b) $\xi_3 = +3$ (red), -3 (blue) and $t = 70$

Figure 6.27: Variation of plane-averaged shear stress $\langle w_1 w_3 \rangle_{12}$ with resolution length scale Δ at non-dimensional cross-stream locations $\xi_3 \equiv (x_3/\delta_m) = \pm 1$ and ± 3, and time $t = 70$. LES carried out using Smagorinsky model with $C_\nu = 0.094$ and $C_E = 0.9946$.

faced by all linear eddy-viscosity based sub-grid models because the model for the residual shear stress τ_{ij}^r is aligned with the resolved shear S_{ij}^W. This makes it hard to match both the residual shear stress $\left\langle u_i^R u_j^R \right\rangle$ and the dissipation of turbulent KE $\left\langle \nu_r S_{ij}^W S_{ij}^W \right\rangle$ in an LES. For unknown reasons, most LES simulations match the dissipation of turbulent KE resulting in smaller than desired values for the residual shear stress. The plane-averaged turbulent shear stress is also symmetric about $\xi_3 = 0$. However, the results at the edge of the mixing layer $\xi_3 = \pm 3$ appear asymmetric. This is because the statistical fluctuations are comparable to the value of the turbulent shear stress at this cross-stream location.

Note that this problem cannot be solved by changing the model parameters. In both the Smagorinsky and Model k_R equation model, there are three numerical parameters, Δ, C_ν, and C_E, which need to be specifed. However, these three parameters appear in the governing LES equations only as the groups $(C_\nu \Delta)$ and (C_E/Δ) reducing the effective number of model parameters to two. One of the parameters, $\frac{(C_\nu \Delta)^{3/4}}{(C_E/\Delta)^{1/4}} = \frac{C_\nu^{3/4}}{C_E^{1/4}} \Delta$, determines the length scales of the smallest resolved motions in the LES while the other, $(C_\nu \Delta)\,(C_E/\Delta) = (C_\nu C_E)$ relates the residual KE k_R to the resolved velocity field. Hence, there is no parameter in these sub-grid models which controls the residual shear stresses. The problem of small residual shear stresses might be solved by using a non-linear sub-grid model which includes a model parameter that controls the alignment between modelled residual shear stress τ_{ij}^r and the resolved shear S_{ij}^W.

A quantity closely related to the shear stress $< w_1 w_3 >$ is the non-dimensional growth rate of momentum thickness $(d\delta_m/dt)\,/(U^0)$. Figure 6.28 shows the strong dependence of the momentum thickness growth rate on the resolution length scale Δ. The time-averaged growth rate of momentum thickness is computed by aver-

aging over the time-period from $t = 50$ to 70.

$$r_{\delta_m} \equiv \frac{d\delta_m}{dt} \overset{C}{=} \frac{\delta_m|_{70} - \delta_m|_{50}}{70 - 50} \tag{6.35}$$

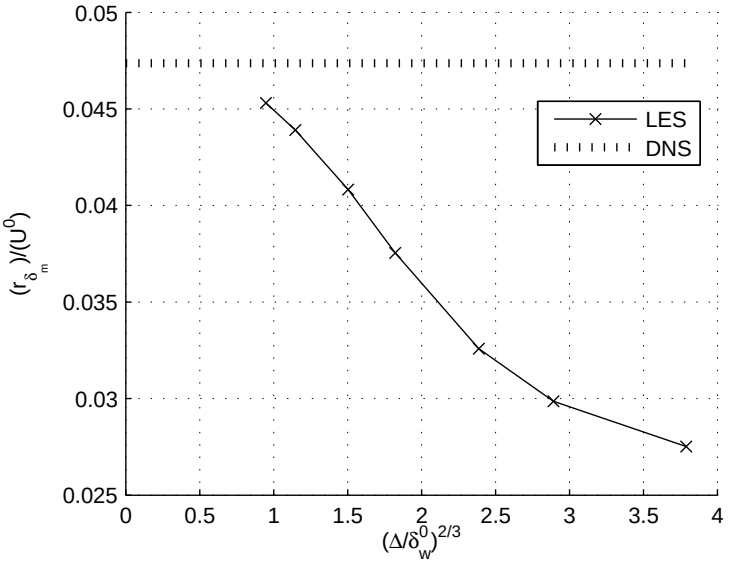

Figure 6.28: Strong dependence of the time-averaged momentum thickness growth rate r_{δ_m} on resolution length scale Δ. Growth rate was non-dimnesionalized using free-stream speed U^0. LES carried out using Smagorinsky model with $C_\nu = 0.094$ and $C_E = 0.9946$.

6.6.4 Choice of Model parameters, C_ν and C_E

In isotropic turbulence, improved model parameters were chosen to remove the leading order Δ term in the total KE variation. These ideas can be similarly extended to the mixing layer, where we determine the improved parameter values which minimize the Δ variation of the volume-averaged turbulent KE at a specifed time. Again, for the Smagorinsky model, if the model parameters are changed such

that,

$$\begin{aligned} C_\nu &\rightarrow a^{-1/2} C_\nu \\ C_E &\rightarrow a^{-3/2} C_E \end{aligned} \tag{6.36}$$

where a is some constant, then the LES velocity field W_i remains unaffected, but $k_R(\mathbf{x}, t)$ changes to,

$$k_R(\mathbf{x}, t) \rightarrow a k_R(\mathbf{x}, t) \tag{6.37}$$

This property was used to minimize the Δ variation of total turbulent KE without repeating the LES simulations. Figures 6.29-6.30 show the parameter values obtained by minimizing the Δ variation of the total turbulent KE at various times. Only the values on the 128^3, 96^3, 64^3, and 48^3 grids were taken into account during the optimization.

It can be seen that the improved parameter values strongly depend on the time at which the Δ variation was minimized. The improved values obtained for both C_ν and C_E decrease as time increases. This is not useful in practice because these model parameters are chosen before the LES simulation is carried out and held fixed through the LES. Hence, we conclude that, for the above low Re mixing layer LES, it is not possible to remove the Δ variation of the total turbulent KE *at all times*, by choosing a single set of values for C_ν and C_E.

In addition to the poor model for the residual shear stress, provided by the Smagorinsky model, the strong dependence of the LES statistics on Δ can also be due to the low Re of the flow being simulated. At low Re, there is either a small or no inertial sub-range, resulting in the resolution length scale Δ being located close to either the energy-containing or dissipation range or in the overlap between them. In high Re flows, for Δ chosen well within the inertial sub-range, we expect the LES statistics to be relatively insensitive to the actual value of Δ. For low

Re turbulent flows, a strong dependence of the LES statistics on the actual values of Δ/l_0 and Δ/η is not suprising where l_0 and η are the integral and Kolmogorov length scales, respectively. For the LES of the mixing layer, although Δ remains unaltered, the integral length scale l_0 grows with time, resulting in a decrease of Δ/l_0 with time. This could explain the strong dependence of the LES statistics on Δ.

6.7 Convergence characteristics of Model k_R equation model

In this section we present results for the convergence with resolution length scale Δ of the various statistics obtained using the Model k_R equation sub-grid model. The LES simulations described in this section were carried out using the following model parameters,

$$\begin{aligned} C_\nu &= 0.1041 \\ C_E &= 0.9514 \end{aligned} \tag{6.38}$$

A number of LES at different resolution length scales Δ were carried out to study the convergence with Δ. Table 6.3 summarizes the numerical parameters used in these simulations. Again, to provide a perspective on the times required to carry out these LES simulations, rough measurements of the wall-clock times are given in Table 6.4. Since a queuing system was not in place in the JIT cluster, other jobs may have been executed at the same time and in the same processes used for these LES.

Most of the trends and observations made for the Smagorinsky model in section 6.6 also hold for the Model k_R equation. So we simply present the results without much discussion.

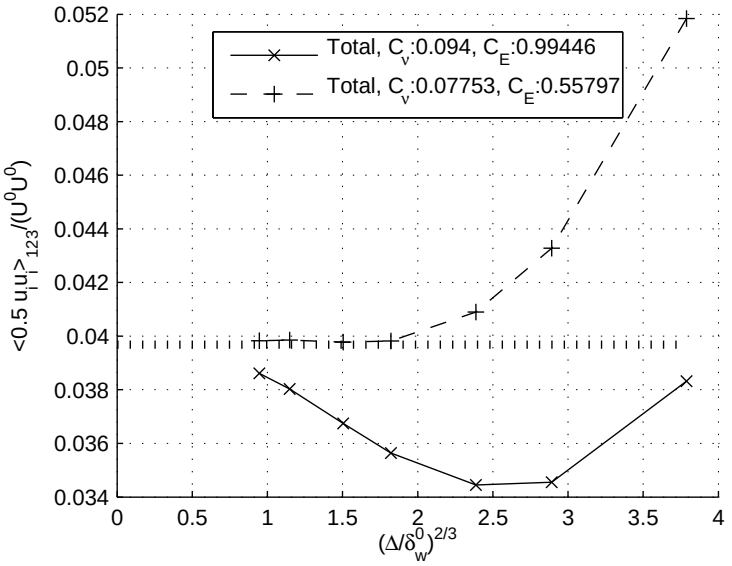

(a) time $t = 40$

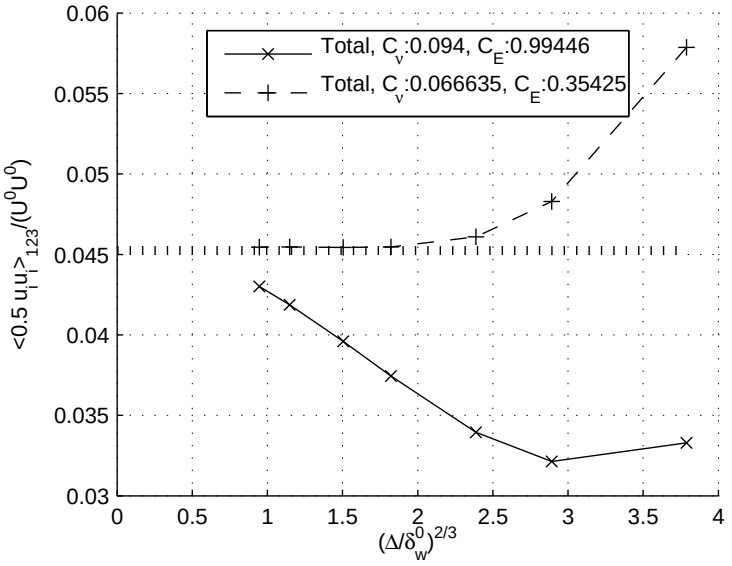

(b) time $t = 50$

Figure 6.29: Smagorinsky model parameter values obtained by minimizing the Δ variation of the total turbulent KE at times $t = 40$ and 50. Only the values on the 128^3, 96^3, 64^3, and 48^3 grids were taken into account during the minimization. Original LES carried out using Smagorinsky model with $C_\nu = 0.094$ and $C_E = 0.9946$.

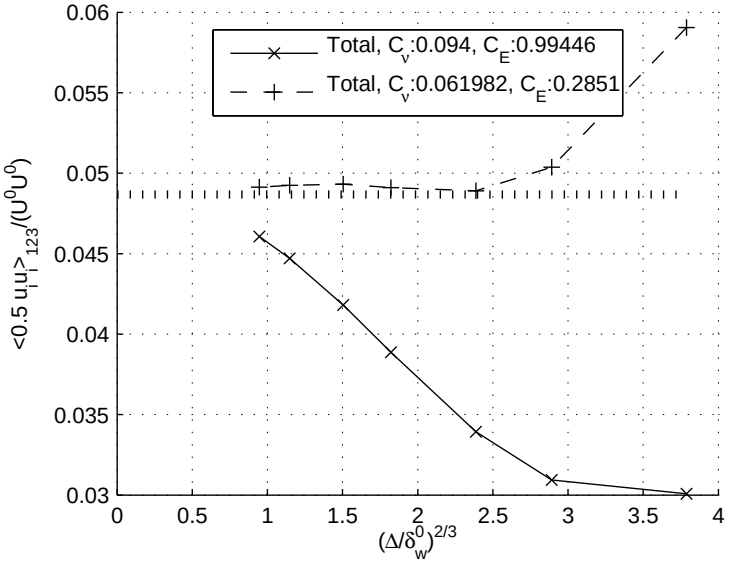

(a) time $t = 60$

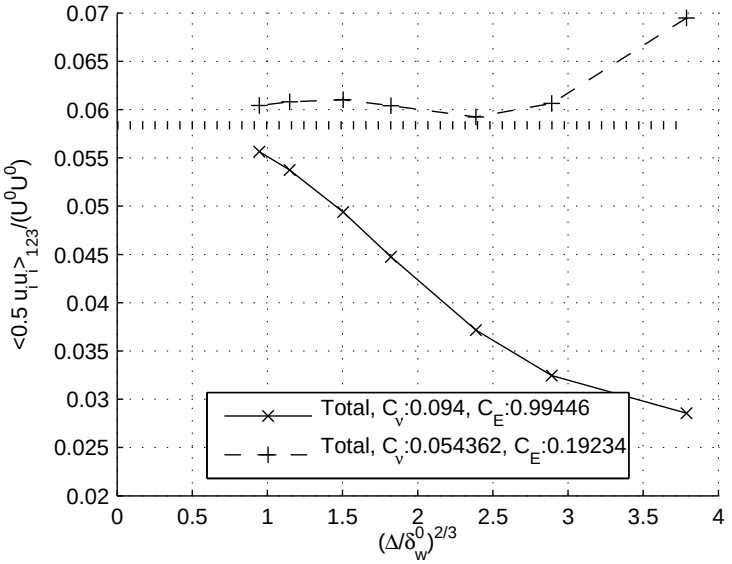

(b) time $t = 70$

Figure 6.30: Smagorinsky model parameter values obtained by minimizing the Δ variation of the total turbulent KE at times $t = 60$ and 70. Only the values on the 128^3, 96^3, 64^3, and 48^3 grids were taken into account during the minimization. Original LES carried out using Smagorinsky model with $C_\nu = 0.094$ and $C_E = 0.9946$.

Table 6.3: Summary of numerical parameters used in the LES of temporal mixing layer. These LES were carried out to study the convergence with Δ of the Model k_R equation model. Notation used: resolution length scale Δ, number of grid points in each direction N, and time step used in the LES Δt_{Modkr}

Δ	N	Δt_{Modkr}
7.375	16	0.1
4.917	24	0.05
3.688	32	0.05
2.548	48	0.025
1.844	64	0.02
1.229	96	0.01
0.922	128	0.008

Table 6.4: Rough measurements of the wall-clock times for the LES of temporal mixing layer from time $t = 30$ to $t = 100$. These LES were carried out to study the convergence with Δ of the Model k_R equation model. Notation used: resolution length scale Δ, number of grid points in each direction N, time step Δt, number of time-steps, N_{TS}, wall-clock time per time-step, $T_{\Delta t}$, wall-clock time, T_W, and number of processes, N_p.

Δ	N	Δt	N_{TS}	$T_{\Delta t}$ (secs)	T_W (secs)	T_W (days)	N_p
7.375	16	0.100	7000	0.293	192.7	0.002	1
4.917	24	0.050	1400	0.444	1073.5	0.007	1
3.688	32	0.050	1400	0.659	1069.6	0.011	4
2.548	48	0.025	2800	1.382	4439.2	0.045	4
1.844	64	0.020	3500	2.158	14600.2	0.087	4
1.229	96	0.010	7000	6.093	42649.2	0.494	4
0.922	128	0.008	8750	13.890	121536.0	1.407	4

Figures 6.31 - 6.32 present the convergence of the resolved turbulent KE with Δ at four different times $t = 40$, 50, 60, and 70. Further, this is compared with the convergence of total turbulent KE. The value of the turbulent KE obtained from the DNS carried out on the 192^3 grid is also provided for reference. All quantities were non-dimensionalized using the free-stream velocity U^0 and half the initial vorticity thickness δ_w^0. The total turbulent KE predicted using the Model k_R seems to have slightly better convergence characteristics than that from the Smagorinsky model (compare Figs. 6.31-6.32 and Figs. 6.18-6.19).

Figures 6.33 - 6.36 show the Δ convergence of the turbulent KE at seven different non-dimensional cross-stream locations $\xi_3 \equiv (x_3/\delta_m) = 0$, ± 0.5, ± 1, and ± 3 and two times $t = 40$ and 70.

Figures 6.37 - 6.40 show the Δ convergence of the shear stress at seven different non-dimensional cross-stream locations $\xi_3 \equiv (x_3/\delta_m) = 0$, ± 0.5, ± 1, and ± 3 and two times $t = 40$ and 70.

Figure 6.41 shows the strong dependence of the momentum thickness growth rate on the resolution length scale Δ. The time-averaged growth rate of momentum thickness is computed by averaging over the time-period from $t = 50$ to 70.

$$r_{\delta_m} \equiv \frac{d\delta_m}{dt} \stackrel{C}{=} \frac{\delta_m|_{70} - \delta_m|_{50}}{70 - 50} \tag{6.39}$$

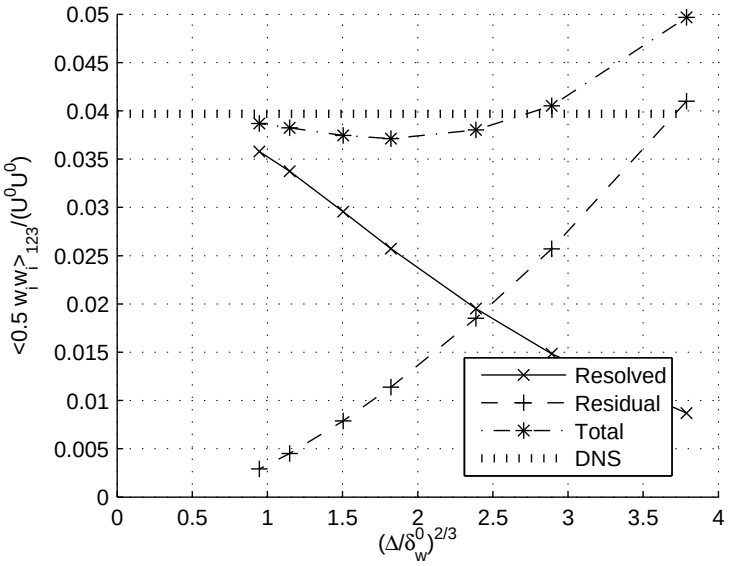

(a) time $t = 40$

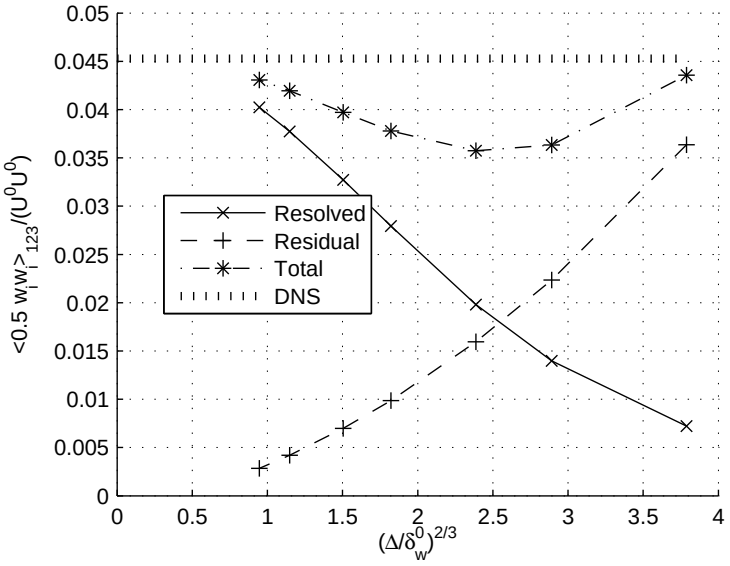

(b) time $t = 50$

Figure 6.31: Variation of volume-averaged turbulent KE $\left\langle \frac{1}{2} w_i w_i \right\rangle_{123}$ with resolution length scale Δ at times $t = 40$ and 50. LES carried out using Model k_R equation model with $C_\nu = 0.1041$ and $C_E = 0.9514$.

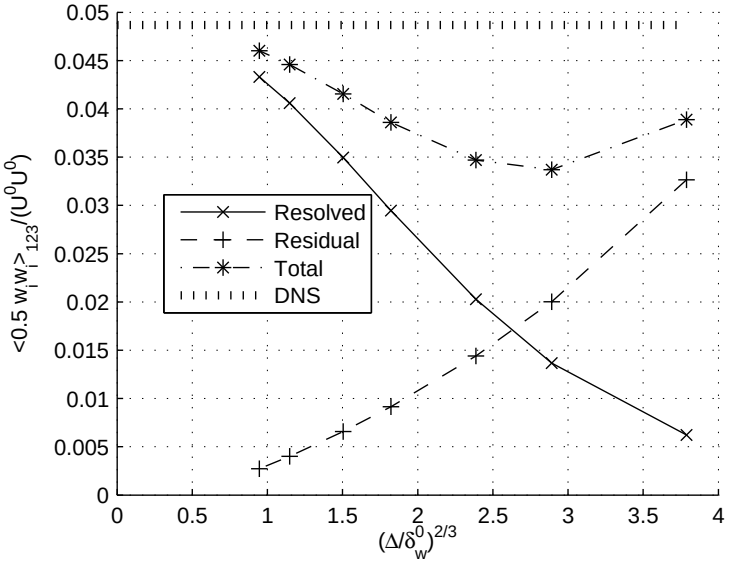

(a) time $t = 60$

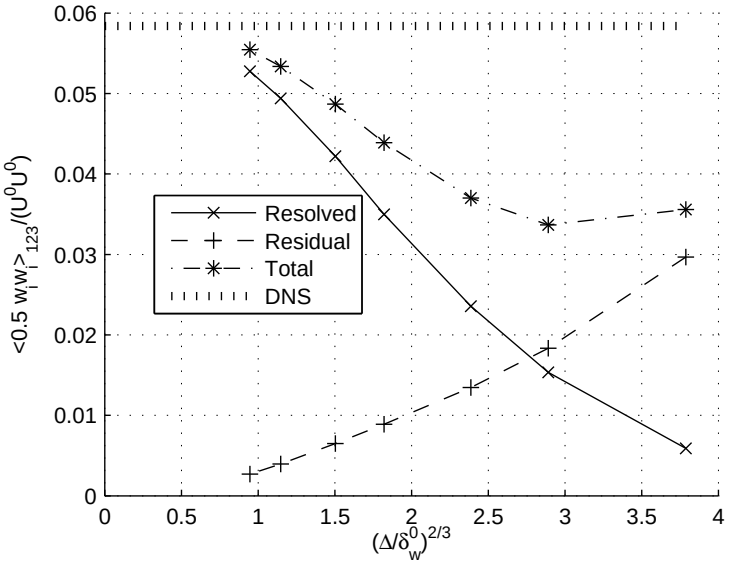

(b) time $t = 70$

Figure 6.32: Variation of volume-averaged turbulent KE $\left\langle \frac{1}{2} w_i w_i \right\rangle_{123}$ with resolution length scale Δ at times $t = 60$ and 70. LES carried out using Model k_R equation model with $C_\nu = 0.1041$ and $C_E = 0.9514$.

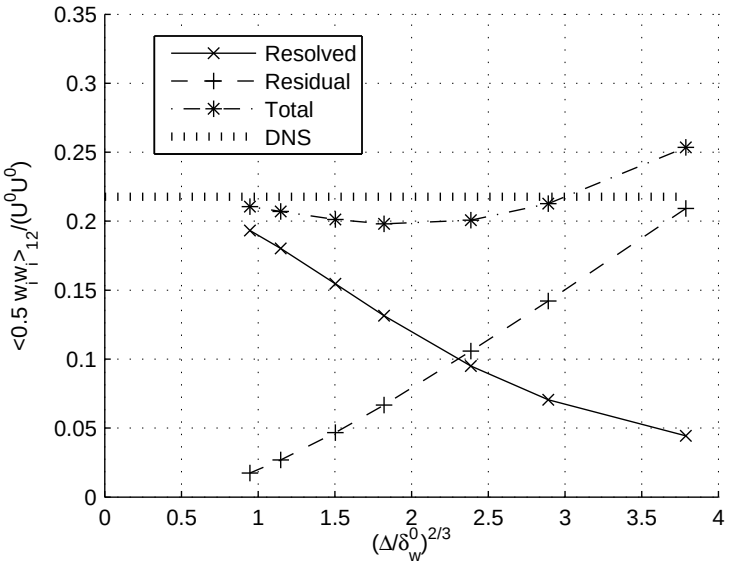

(a) $\xi_3 = 0$ and $t = 40$

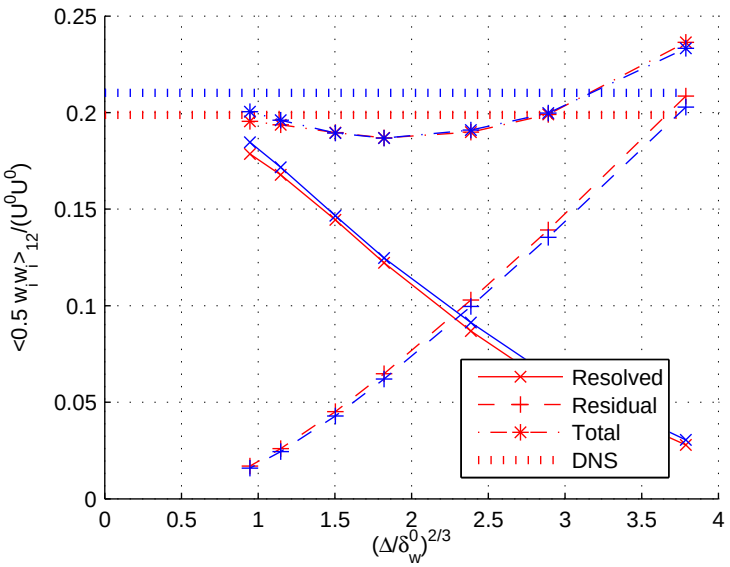

(b) $\xi_3 = +0.5$ (red), -0.5 (blue) and $t = 40$

Figure 6.33: Variation of plane-averaged turbulent KE $\left\langle \frac{1}{2} w_i w_i \right\rangle_{12}$ with resolution length scale Δ at non-dimensional cross-stream locations $\xi_3 \equiv (x_3/\delta_m) = 0$ and ± 0.5, and time $t = 40$. LES carried out using Model k_R equation model with $C_\nu = 0.1041$ and $C_E = 0.9514$.

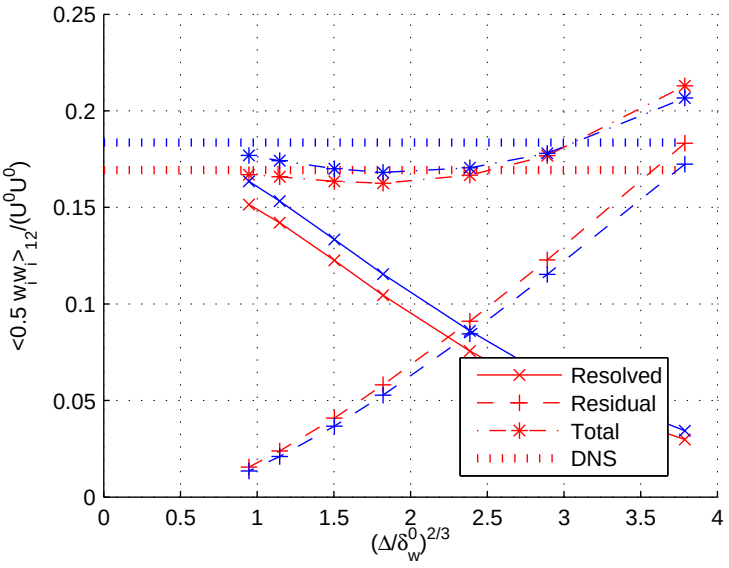

(a) $\xi_3 = +1$ (red), -1 (blue) and $t = 40$

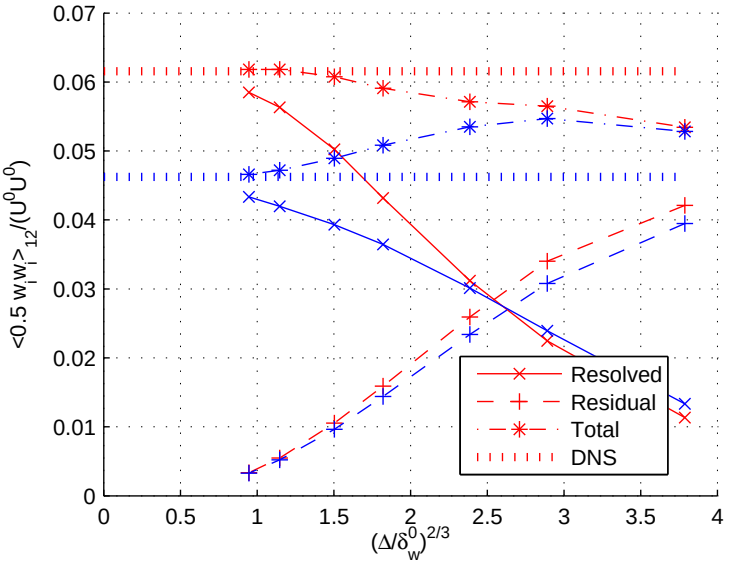

(b) $\xi_3 = +3$ (red), -3 (blue) and $t = 40$

Figure 6.34: Variation of plane-averaged turbulent KE $\left\langle \frac{1}{2} w_i w_i \right\rangle_{12}$ with resolution length scale Δ at non-dimensional cross-stream locations $\xi_3 \equiv (x_3/\delta_m) = \pm 1$ and ± 3, and time $t = 40$. LES carried out using Model k_R equation model with $C_\nu = 0.1041$ and $C_E = 0.9514$.

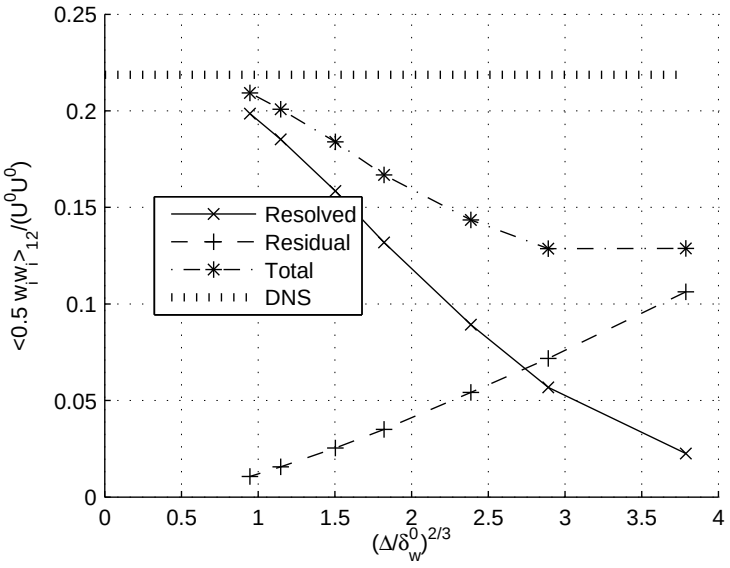

(a) $\xi_3 = 0$ and $t = 70$

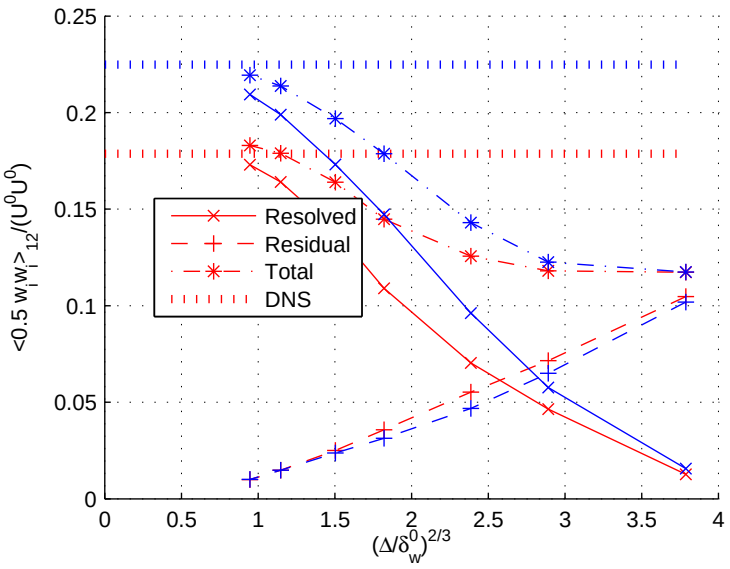

(b) $\xi_3 = +0.5$ (red), -0.5 (blue) and $t = 70$

Figure 6.35: Variation of plane-averaged turbulent KE $\left\langle \frac{1}{2} w_i w_i \right\rangle_{12}$ with resolution length scale Δ at non-dimensional cross-stream locations $\xi_3 \equiv (x_3/\delta_m) = 0$ and ± 0.5, and time $t = 70$. LES carried out using Model k_R equation model with $C_\nu = 0.1041$ and $C_E = 0.9514$.

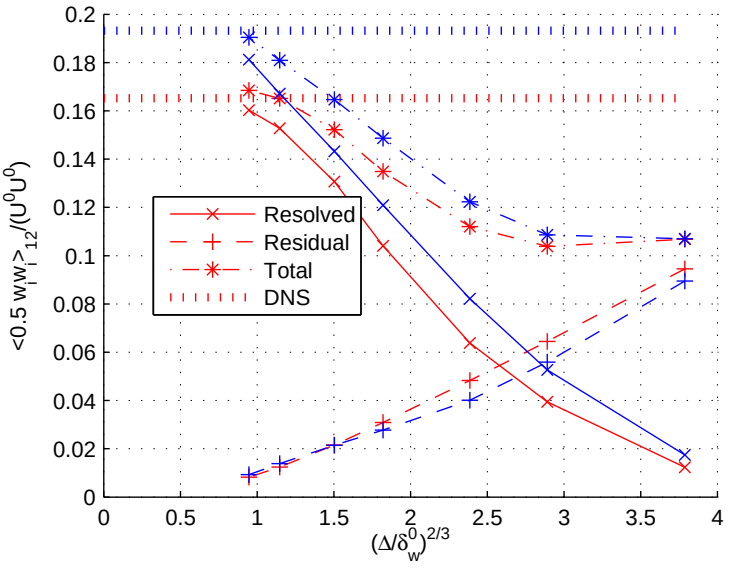

(a) $\xi_3 = +1$ (red), -1 (blue) and $t = 70$

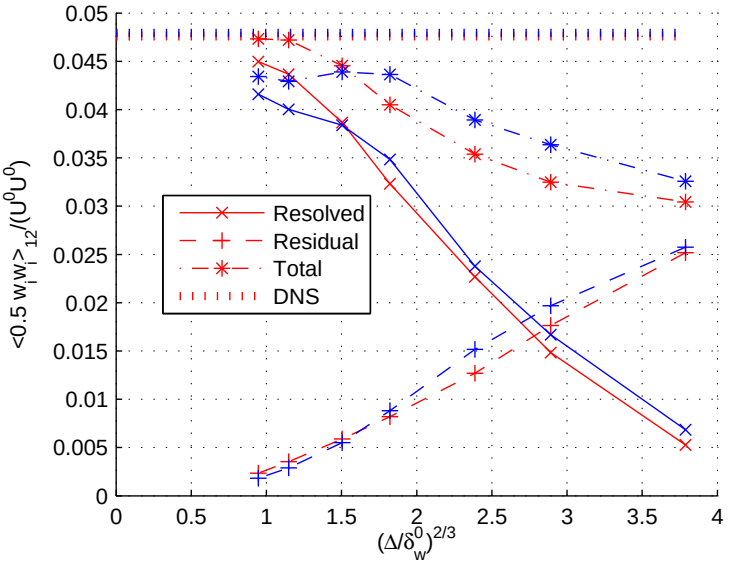

(b) $\xi_3 = +3$ (red), -3 (blue) and $t = 70$

Figure 6.36: Variation of plane-averaged turbulent KE $\left\langle \frac{1}{2} w_i w_i \right\rangle_{12}$ with resolution length scale Δ at non-dimensional cross-stream locations $\xi_3 \equiv (x_3/\delta_m) = \pm 1$ and ± 3, and time $t = 70$. LES carried out using Model k_R equation model with $C_\nu = 0.1041$ and $C_E = 0.9514$.

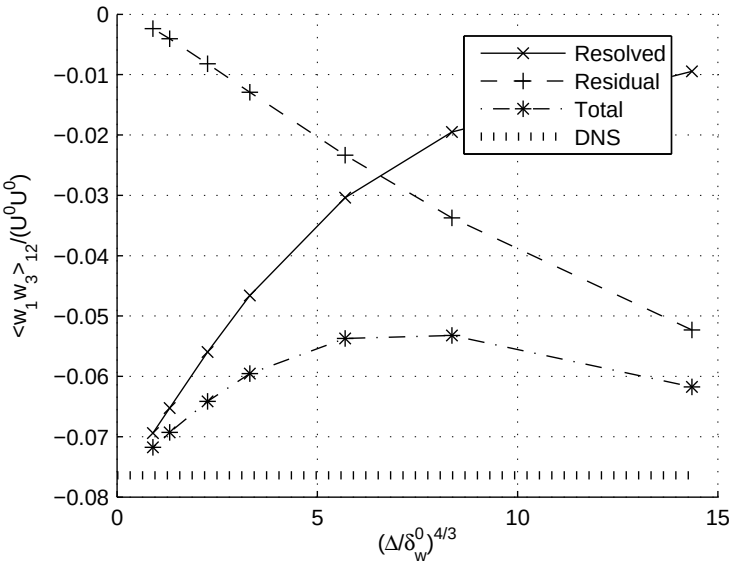

(a) $\xi_3 = 0$ and $t = 40$

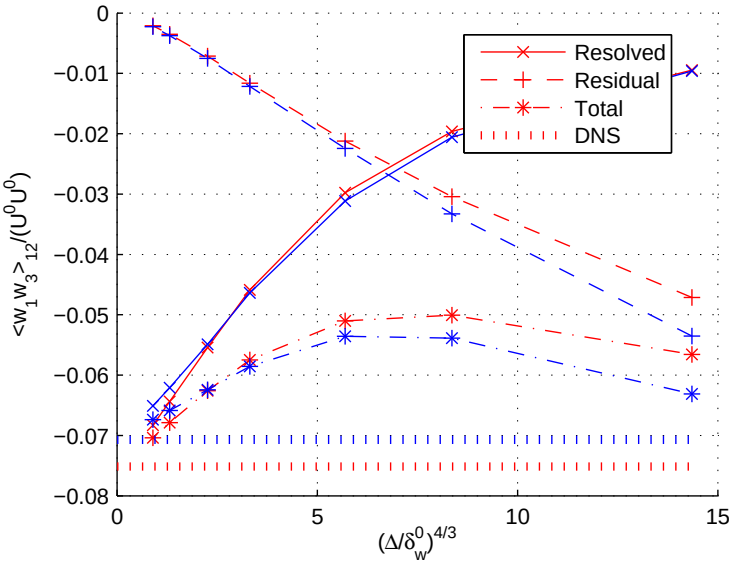

(b) $\xi_3 = +0.5$ (red), -0.5 (blue) and $t = 40$

Figure 6.37: Variation of plane-averaged turbulent shear stress $\langle w_1 w_3 \rangle_{12}$ with resolution length scale Δ at non-dimensional cross-stream locations $\xi_3 \equiv (x_3/\delta_m) = 0$ and ± 0.5, and time $t = 40$. LES carried out using Model k_R equation model with $C_\nu = 0.1041$ and $C_E = 0.9514$.

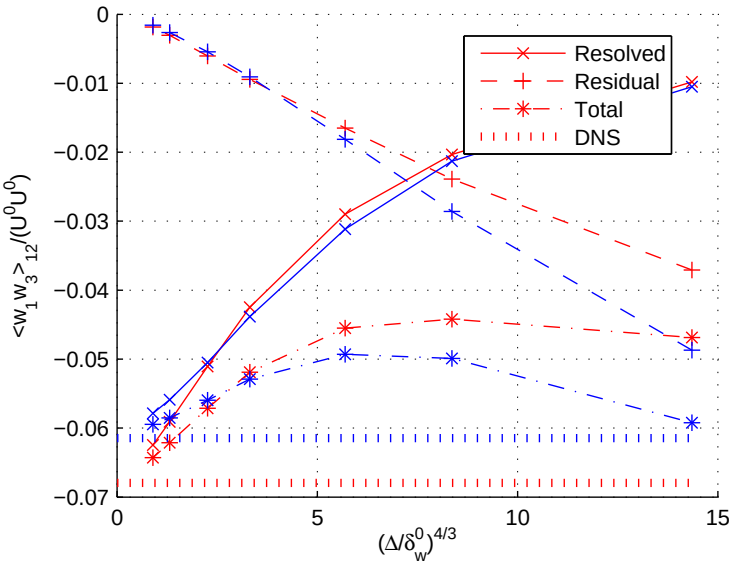

(a) $\xi_3 = +1$ (red), -1 (blue) and $t = 40$

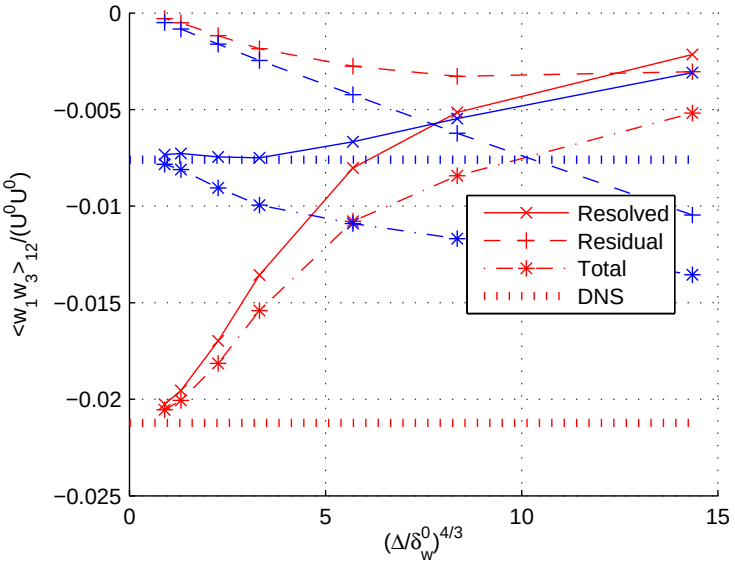

(b) $\xi_3 = +3$ (red), -3 (blue) and $t = 40$

Figure 6.38: Variation of plane-averaged shear stress $\langle w_1 w_3 \rangle_{12}$ with resolution length scale Δ at non-dimensional cross-stream locations $\xi_3 \equiv (x_3/\delta_m) = \pm 1$ and ± 3, and time $t = 40$. LES carried out using Model k_R equation model with $C_\nu = 0.1041$ and $C_E = 0.9514$.

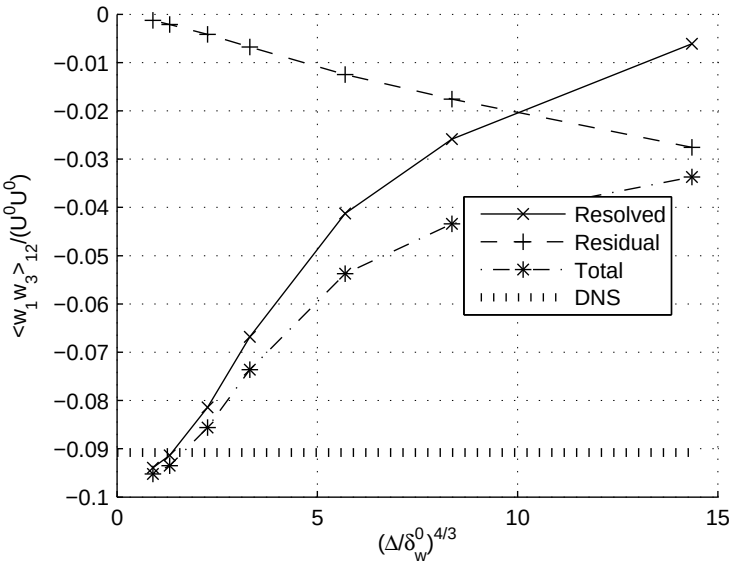

(a) $\xi_3 = 0$ and $t = 70$

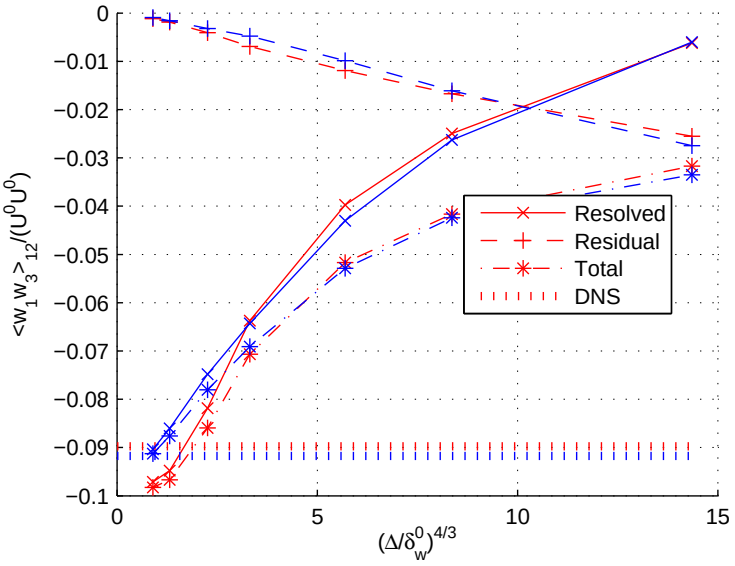

(b) $\xi_3 = +0.5$ (red), -0.5 (blue) and $t = 70$

Figure 6.39: Variation of plane-averaged turbulent shear stress $\langle w_1 w_3 \rangle_{12}$ with resolution length scale Δ at non-dimensional cross-stream locations $\xi_3 \equiv (x_3/\delta_m) = 0$ and ± 0.5, and time $t = 70$. LES carried out using Model k_R equation model with $C_\nu = 0.1041$ and $C_E = 0.9514$.

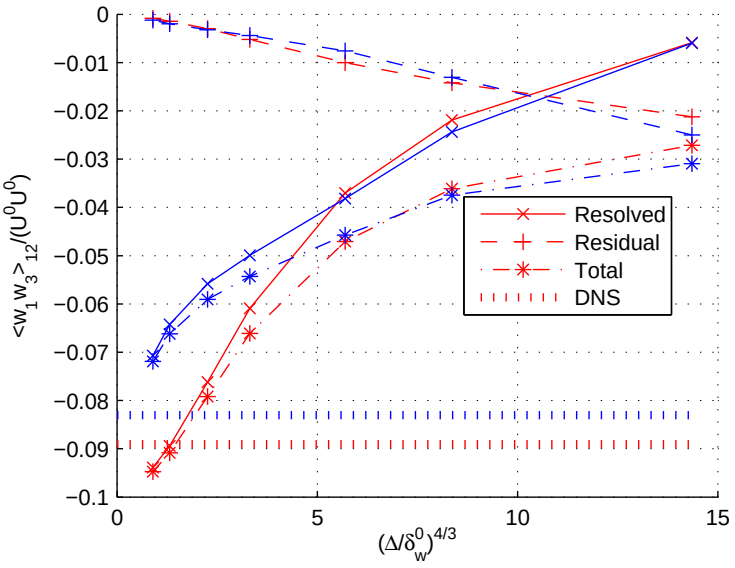

(a) $\xi_3 = +1$ (red), -1 (blue) and $t = 70$

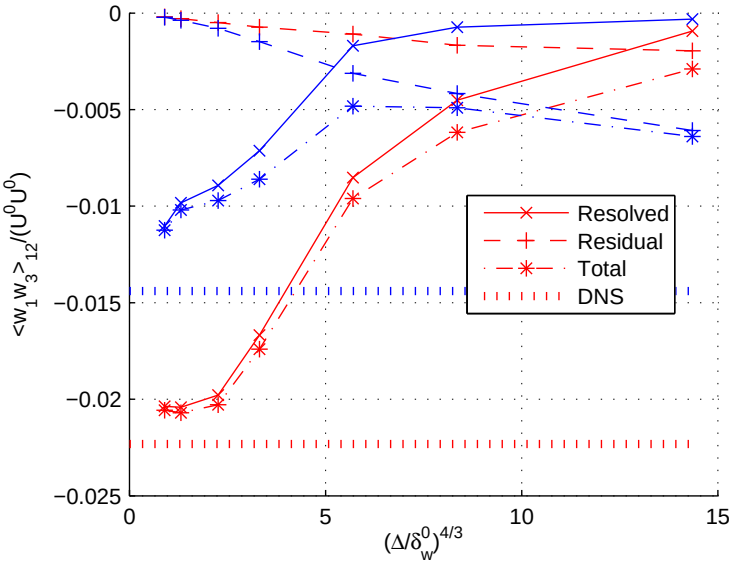

(b) $\xi_3 = +3$ (red), -3 (blue) and $t = 70$

Figure 6.40: Variation of plane-averaged shear stress $\langle w_1 w_3 \rangle_{12}$ with resolution length scale Δ at non-dimensional cross-stream locations $\xi_3 \equiv (x_3/\delta_m) = \pm 1$ and ± 3, and time $t = 70$. LES carried out using Model k_R equation model with $C_\nu = 0.1041$ and $C_E = 0.9514$.

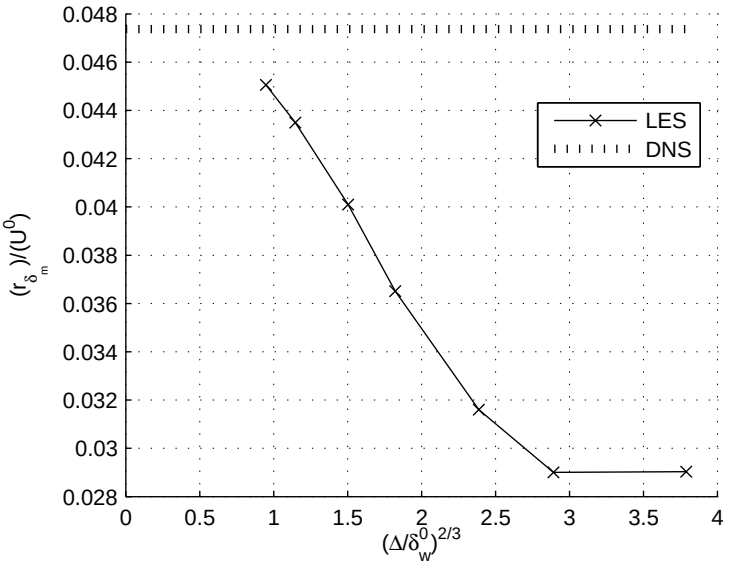

Figure 6.41: Strong dependence of the time-averaged momentum thickness growth rate r_{δ_m} on resolution length scale Δ. Growth rate was non-dimensionalized using free-stream speed U^0. LES carried out using Model k_R equation model with $C_\nu = 0.1041$ and $C_E = 0.9514$.

Chapter 7

Conclusions and future work

In this dissertation we have developed tools to make LES more easily applicable to practical engineering problems. We have addressed shortcomings in LES, both by developing an efficient numerical algorithm for LES of incompressible flows and by presenting a framework to deal with issues identified in the current LES methodology. We now summarize these contributions and provide directions for future research.

First, we provide details on the numerical algorithm. This includes the development of an iterative fractional step method, reduction in stencil size of the pressure Poisson equation and parallel implementation aspects. Next, the issues with the LES methodology, which make the effective use of LES to get meaningful results an art, are addressed. We obtain improved criteria for comparing sub-grid models by developing a clear notion of convergence of an LES approach with resolution length scale. The difficulty in assessing the accuracy of the statistics obtained from an LES is solved by modeling the statistics of the unresolved, or residual, motions. These models could be incorporated into an LES framework which automatically chooses the smallest length scale which needs to be resolved in LES to achieve a given error tolerance. We then combine the ideas of convergence of an LES approach and modeling statistics of residual motions to give a rationale for choice of better values for sub-grid model parameters. The performance of these ideas, as applied to isotropic turbulence and the temporal mixing layer, is also summarized here, along with directions for future work.

Many issues in the current LES methodology can be traced to the inadequate

representation of the unresolved or small scales. This problem was partly addressed by modeling the statistics of the residual motions. In the final section, we address these issues differently by presenting ideas for a new LES methodology which allows "statistical resolution" of eddies in all the length and time scales of the underlying turbulent flow. Certain mathematical tools required for this methodology are also briefly described in this section.

7.1 Numerical Algorithm

The governing equations for LES using linear eddy-viscosity based sub-grid models are similar in form to the incompressible NS equations. The fractional step method, which has proven to be an efficient time-stepping procedure for time-accurate incompressible flow calculations, was used for evolving the LES equations in time. Since these methods are known to become first-order time accurate in the presence of boundaries, we modified this method into an iterative fractional step method. Each iteration of this new method corresponds to the same sequence of steps performed in the normal fractional step method. A block-matrix-based procedure was used to analyze the discretized equations and prove that two iterations are sufficient to achieve the desired second-order temporal accuracy. The convective terms are discretized explicitly in time using the Adams-Bashforth scheme. Although this imposes a Courant-Friedrichs-Lewy (CFL) condition on the time-step based on stability considerations, such a condition is no more restrictive than that required for time-accurate evolution. The viscous terms and sub-grid stresses are treated implicitly using the Crank-Nicholson scheme which makes them unconditionally stable.

The flow was spatially discretized using a collocated grid scheme primarily for

ease of extension to curvilinear grids. Currently, we can use stretched Cartesian grids by mapping this grid onto a uniform computational grid. This allowed us to efficiently simulate flows with concentrated regions of flow gradients such as the temporally evolving mixing layer. An Energy-conserving discretization for the convective terms improved the robustness of the solver. The pressure Poisson equation in fractional step methods is determined completely by the discretization used for the divergence and pressure gradient operators. The use of fourth-order spatially accurate discretization for these operators results in a 7-point stencil in each coordinate direction for the pressure Poisson equation. We developed a clever way to reduce this stencil to 5 points in each coordinate direction, while still requiring the volume fluxes to satisfy a fourth-order spatially discretized continuity equation to machine precision.

All these algorithms were implemented in a parallel code designed to be executed in a cluster configuration. The code was written in Fortran 90 using MPI directives for communication between processes. A block data structure, which provided a natural way to store either the x_1x_2 planes or x_2x_3 planes of data in the same array, was used for the velocity and pressure fields. The code is currently capable of handling non-periodic boundary conditions only in the x_3 direction. The pressure Poisson equation was solved using Fourier transforms in the periodic x_1 and x_2 directions and linear system solves in the x_3 direction. Also, the use of implicit time discretizations for the viscous terms requires us to invert sparse linear systems with a large bandwidth. An iterative scheme using Alternating Direction Implicit (ADI) factorizations to reduce the bandwidth was developed. This scheme required us to invert linear systems only along lines in each coordinate direction. We further introduced a "broken lines" modification in the x_3 direction, for the

iterative ADI scheme to achieve near linear parallel speedup. This modification minimized the communication between processes.

We had mentioned earlier that the block data structure had poor performance because even while carrying out simple differencing operations we do not access contiguous memory locations. The proposed slab data structure needs to be implemented in this code to improve the code performance. To date, I have not found the need for non-periodic BCs in the x_1 and x_2 directions although they can be implemented easily. The use of a collocated grid layout also allows us to extend the code to general curvilinear grids which might be of use for simulating spatially-developing mixing layers and jets.

7.2 Issues with the LES methodology

In the conventional approach to *a posteriori* testing, which is widely used to compare LES sub-grid models, the statistics obtained from LES are compared with statistics obtained from filtered NS solutions. Such comparison could be misleading, as the goal of any LES is to obtain the statistics of the unfiltered NS equations. Our proposed approach to *a posteriori* testing corrects this problem by comparing the statistics from the LES field with those from unfiltered NS solutions.

This leads us to define convergence with resolution length scale Δ of an LES approach using a specified sub-grid model. This notion of convergence is independent of the filter width, and reinforces the sub-grid model comparison criterion mentioned earlier. Here, we are interested in the asymptote to which the LES statistics converge as $\Delta \to 0$, and how this asymptote compares with the statistics of the underlying turbulent flow we are trying to model using LES. If LES approaches using different sub-grid models converge to the same asymptote, how

rapidly they converge to this asymptote is an important measure of performance. The importance of studying the performance of a sub-grid model over a range of Δ, as opposed to a single Δ, when making sub-grid model comparisons is also brought out.

The assessment of accuracy of an LES solution is difficult because current LES methods carry little or no information about the unresolved eddies. Our solution to this problem is to model the statistic of the underlying turbulent motions as consisting of two parts: a resolved part obtained directly from the computed LES field, and a modeled part representing the contribution from the residual, or unresolved, motions. This allows us to estimate error in the LES solution by providing a measure for the contribution of unresolved motions to the statistic without comparing to DNS. Further, including this model for the contribution from residual motions, gives a better estimate for the relevant statistic of the underlying turbulent motions at much lower computational cost. We also describe two sub-grid models, existing in literature, which include such models for the residual KE.

Lastly, we present an alternative procedure to choose better values for sub-grid model parameters. The key idea in this procedure is to choose the model parameters such that the leading order Δ term in the estimate from LES for a desired statistic is removed. Note that this estimate includes both the resolved part and the model for the residual part. By removing this leading order term, we minimize the variation of this estimate with Δ. Hence, even when we perform the LES simulation using a non-zero value of Δ, the estimate obtained for the desired statistic is closer to its value at $\Delta = 0$.

The issues with the LES methodology and their proposed solutions were studied in two flows, forced, isotropic turbulence and the temporally evolving mixing

layer. We compared the convergence characteristics and performance of three eddy-viscosity based sub-grid models: Constant eddy viscosity, Smagorinsky, and Model k_R equation sub-grid models. The last two sub-grid models included models for the residual KE which is the KE in the unresolved or residual motions. These results are summarized in the sub-sections below.

7.2.1 Forced, isotropic turbulence

The simplest turbulent flow in which these issues can be addressed is forced, isotropic turbulence, as the statistics for this flow are independent of spatial location and time. Wray forcing is used to artificially force the small wave number Fourier modes. LES is a simulation methodology designed for high Re flows. So, all the simulations of isotropic turbulence were carried out in the limit of infinite Re by simply setting the physical viscosity to zero.

We first studied the convergence properties of the constant eddy viscosity model. The statistic whose convergence was studied was the resolved KE, which is computed as the volume- and time-average of the KE in the resolved, LES field. It was found that the resolved KE converges as $\Delta^{2/3}$ at sufficiently small values of Δ. Lilly's analysis using a spectral cutoff energy spectrum also predicts such a variation. The equivalence between carrying out an LES in the limit of infinite Re using the constant eddy viscosity model and a DNS at finite Re allows us to reinterpret the asymptote at $\Delta = 0$ as the value of the KE of the underlying turbulent flow in the limit of infinite Re. Such extrapolation techniques to determine the statistics of a high Re flow using the statistics computed from the DNS at a lower Re need to be more fully investigated and developed.

The resolved KE obtained from the LES using the Smagorinsky and Model k_R

equation sub-grid models converged as $\Delta^{2/3}$ as well. An interesting result was that all three LES approaches converged to the same asymptote at $\Delta = 0$, within the limits of statistical error. The model k_R equation performs the best because, for non-zero values of Δ at which an LES is usually performed, it estimates an resolved KE which is closer to the asymptote at $\Delta = 0$ than the other sub-grid models at the same Δ. The Smagorinsky model is a close second, while the performance of the Constant eddy-viscosity model is the worst.

We are ultimately interested in the KE of the underlying turbulent velocity field while the resolved KE represents only the KE in the resolved LES field. Hence, the residual KE, modeled in the Smagorinsky and Model k_R equation models, can be added to the resolved KE to obtain the total KE, our new estimate for the KE of the underlying turbulent flow. The total KE is closer to the asymptote at $\Delta = 0$ than the resolved KE at most values of Δ for both these sub-grid models. This suggests that the convergence property of any sub-grid model can be improved by including models for the contribution to the desired statistic from the residual motions.

Next we obtained improved values for the sub-grid model parameters, C_ν and C_E, by removing the leading order $\Delta^{2/3}$ term in the total KE. For the case of Smagorinsky model, there was a clever way to search for better model parameter values without repeating the LES simulations. However, one needs to repeat all the simulations for the model k_R equation sub-grid model.

Finally, we performed preliminary investigations of the convergence characteristics of the two-point, one-dimensional velocity correlation and its spectrum. We first developed a simple model for the contribution of the residual motions to the 1d velocity spectrum and correlation by modeling the energy spectrum function

of the residual velocity field and assuming local isotropy. We investigated the performance of this model in LES simulations using the Smagorinsky sub-grid model. The model suggested that at sufficiently small values of Δ the 1d velocity spectrum varies as $\Delta^{5/3}$, while the 1d velocity correlation varies as $\Delta^{2/3}$

The 1d velocity spectrum function at low wave numbers is well resolved by the LES while the residual 1d velocity spectrum contributes little to the total 1d velocity spectrum. But, at high wave numbers, the resolved 1d velocity spectrum has negligible contribution while the residual 1d velocity spectrum contributes most of the energy to the total 1d velocity spectrum. For this reason, the convergence of the 1d velocity spectrum function with resolution length scale Δ was studied at three different wave numbers:

1. A small wave number, $\kappa_1 = 1$, at which much of the energy had been resolved for all resolution length scales Δ used in the LES.

2. An intermediate wave number, $\kappa_1 = 4$, at which some of the LES simulations sufficiently resolved the energy, while other LES simulations at larger values of Δ do not.

3. A large wave number, $\kappa_1 = 32$ at which none of the LES simulations resolved the energy.

In all three cases, the total 1d velocity spectrum was closer to the asymptote at $\Delta = 0$ than the resolved 1d velocity spectrum. Further, the convergence behaviour at intermediate wave numbers collapsed when non-dimensionalized appropriately. Similar conclusions can be made from the convergence study of the 1d velocity correlation as well.

7.2.2 Temporal mixing layer

The temporally evolving mixing layer is a typical free shear flow which was used to study the performance of eddy-visocosity based sub-grid models in a more realistic flow. The temporal mixing layer is statistically non-stationary and inhomogeneous in the cross-stream direction. The Δ convergence properties of the Smagorinsky and Model k_R equation sub-grid models were similar in character. The Δ convergence of the volume-averaged total turbulent KE was improved by adding the model for the residual turbulent KE to the resolved turbulent KE. It was also observed that the Δ convergence of the volume-averaged total turbulent KE degraded with time. To study the variation of the Δ convergence with cross-stream location we looked at the plane-averaged turbulent KE at several cross-stream locations at a given time. The turbulent KE was averaged over the statistically homogeneous stream-wise and span-wise directions. It was observed that the Δ convergence was similar at the various cross-stream locations observed. Another dynamically important single-point, second-order velocity statistics is the turbulent shear stress. We also studied the Δ convergence of the plane-averaged turbulent shear stress at several cross-stream locations and times. It was observed that the eddy-viscosity models provided a poor model for the residual shear stress because the modeled residual shear stress is constrained to be aligned with the resolved strain rate in linear eddy-viscosity models. This poor performance of the model for the residual shear stress cannot be improved by adjusting the model parameters. Improved model parameters which minimized the Δ variation of the volume-averaged turbulent KE at a given time were instead calculated. The values obtained for both C_ν and C_E decreased as time increases. This is not useful in practice because these model parameters must be chosen before the LES simulation is carried out

and held fixed throughout the simulation. Hence, we conclude that, for the above low Re mixing layer LES, it is not possible to remove the Δ variation of the total turbulent KE *at all times*, by choosing a single set of values for C_ν and C_E. In addition to the poor model for the residual shear stress provided by the Smagorinsky model, the strong dependence of the LES statistics on Δ could also be due to the low Re of the flow being simulated.

7.2.3 Future Work

The long term objective of the work is to develop an LES framework which automatically determines the resolution length scale required to achieve a given error tolerance. Currently, we have developed models for a few statistics such as the residual KE. These allow us to estimate the error in the desired statistics given the resolution length scale. These ideas should be extended to solve the inverse problem in which we determine the resolution length scale given the error tolerance.

The LES simulations of the low Re temporal mixing layer identified the deficiency of the linear eddy-viscosity models in modeling the residual shear stress. An important improvement is to study the performance of non-linear eddy-viscosity sub-grid models for such free shear flows. These non-linear would include model parameters which control the alignment between the modeled residual shear stress and the resolved strain rate. The strong Δ dependence of the statistics from LES of the low Re mixing layer indicates that it is also important to develop low Re corrections to these sub-grid models when they are used for modeling low Re flows.

Currently, our ideas have been studied in simple turbulent flows without walls. An important extension would be to demonstrate these ideas in a simple wall-bounded flow, such as the flat plate turbulent boundary layer.

7.3 New LES methodology based on "statistical resolution of all scales"

In current approaches to LES, only the large scales are resolved while the effects of the small scales on the large scales are fully modeled. These sub-grid models are usually characterized by a single parameter such as the resolution length scale, Δ (as in the Smagorinsky Model) or sometimes by a resolution length Δ and a residual kinetic energy k_R. Such a representation of the small scales could be grossly inadequate to represent the complex phenomenon of turbulence. This issue becomes even more important in problems where the rate controlling processes are in the small scales, such as in turbulent combustion, or in situations where there are "no small" scales, such as near walls.

In order to address the above problem, we propose a new LES methodology in which the large scales are resolved while the small scales are "statistically" resolved. The idea was motivated by the following comment of Pope (2004): "Perhaps the holy grail of turbulence is the statistical resolution of all scales - a methodology in which representative samples of motions and processes on all scales are resolved and combined (without empiricism) in a way that remains computationally tractable at large Reynolds number". This proposed new LES methodology would be computationally more intensive than current LES methods but much cheaper than performing a DNS of the same high Re flow.

The rest of the section is organized as follows. In sub-section 7.3.1, I present a brief overview of the Variational Multiscale (VMS) method and its application to LES of turbulent flows. Decomposition of the flow into large and small scales is also discussed. In sub-section 7.3.2, we illustrate that most of the computa-

tional time in a DNS is spent in resolving the small scales and this motivates the computational advantage in the "statistical resolution" of the small scales. In sub-section 7.3.3, we outline the proposed LES methodology and clearly indicate the various assumptions made in the derivation of the model equations for the small scales. Finally, in sub-section 7.3.4, the polynomial chaos method, used for the stochastic evolution of the small scales, is described.

7.3.1 Variational Multiscale (VMS) method for LES

The Variational Multiscale method for LES was recently described by Hughes *et al.* (2000) as a method that utilizes *a priori* scale separation instead of spatial filtering as is commonly done in LES. Since then, a number of researchers have used this formulation in the LES of turbulent flows [Hughes *et al.* (2001*a*,*b*); Collis (2001); Gravemeier *et al.* (2004)] and even in turbulence control simulations [S.Ramakrishnan & Collis (2004)]. Collis (2002) points out that the primary advantages of this method over existing filter based methods are:

- The VMS framework provides a more solid mathematical foundation for turbulence modeling; and
- The extension to complex geometries is free from issues related to commutativity and homogeneity of filters.

In the current context, the VMS framework is used as it provides a clear description of the large and small scale velocity fields and the equations governing their evolution. This makes it easier to develop the ideas of statistical resolution of small scales in the later sub-sections. So the VMS formulation is briefly presented, focusing on the features motivating the statistical resolution of small scales. We

are interested in solving the incompressible NS equations,

$$\frac{\partial U_i}{\partial t} + \frac{\partial \left(U_i U_j\right)}{\partial x_j} = -\frac{\partial p}{\partial x_i} + \frac{\partial \left(2\nu S_{ij}\right)}{\partial x_j} \tag{7.1}$$

$$\frac{\partial U_i}{\partial x_i} = 0 \tag{7.2}$$

on a fixed spatial domain, $\mathcal{D}$, which is an open, connected and bounded subset of $\mathcal{R}^3$, with boundary, $\Gamma = \partial\mathcal{D}$. We search for a solution vector $\{U_i, p\}^T$ in an appropriate function space, $\mathcal{V}$. Details regarding the function space can be found in Temam (1984). Any particular function living in this space $\mathcal{V}$ can be represented by a linear combination of the basis functions of $\mathcal{V}$. The choice of the basis is not unique and some bases will be more convenient (in terms of computational efficiency or complexity of equations) than others. Let $\Pi_{(k)}$ represent a basis function in $\mathcal{V}$. Then, the velocity and the pressure can be represented as follows,

$$\begin{aligned} U_i(x_j, t) &= \sum_k v_{i,(k)}(t)\Pi_{(k)}(x_j) \\ p(x_j, t) &= \sum_k \phi_{,(k)}(t)\Pi_{(k)}(x_j) \end{aligned} \tag{7.3}$$

To simplify notation, we use boldface to denote the following vectors.

$$\begin{aligned} \mathbf{v_i}(t) &= \left\{v_{i,(1)}, v_{i,(2)}, \ldots\right\}^T \\ \phi(t) &= \left\{\phi_{,(1)}, \phi_{,(2)}, \ldots\right\}^T \end{aligned} \tag{7.4}$$

To construct the variational form of the NS equations we introduce a second function space, $\mathcal{W}$, composed of test functions $\{w_i, r\}^T$. The variational form of the equations is obtained by taking the inner product of test functions in $\mathcal{W}$ with Eqs. (7.1) and (7.2). More details can be found in a standard text on finite element methods (FEM).

In a multiscale (in particular, three scale) formulation, we begin with an *a priori* separation of scales where the solution and test function space are partitioned as,

$$\mathcal{V} = \overline{\mathcal{V}} \oplus \widehat{\mathcal{V}} \oplus \widetilde{\mathcal{V}} \tag{7.5}$$

$$\mathcal{W} = \overline{\mathcal{W}} \oplus \widehat{\mathcal{W}} \oplus \widetilde{\mathcal{W}} \tag{7.6}$$

where

$\overline{\mathcal{V}}$ - Large scale function space. It is the typical space in which the LES solutions are computed. This is a finite dimensional space. In the LES methodology proposed here, these scales of motion are "resolved".

$\widehat{\mathcal{V}}$ - Small scale function space. It is the space which needs to be added to $\overline{\mathcal{V}}$ in order to carry out a well resolved DNS. This is also a finite dimensional space. In the LES methodology proposed here, these scales of motion are "statistically resolved".

$\widetilde{\mathcal{V}}$ - Remaining scales of motion. It is unresolved even in a DNS. This is an infinite dimensional space. In the LES methodology proposed, these scales of motion continue to be "unresolved".

We also decompose the space of test functions $\mathcal{W}$ in similar lines. Such a partition leads to a natural decomposition of velocity and pressure onto large, small and unresolved scales through the use of projection onto the appropriate function spaces.

$$\begin{aligned} U_i(x_j,t) &= \overline{U}_i(x_j,t) + \widehat{U}_i(x_j,t) + \widetilde{U}_i(x_j,t) \\ p(x_j,t) &= \overline{p}(x_j,t) + \widehat{p}(x_j,t) + \widetilde{p}(x_j,t) \end{aligned} \tag{7.7}$$

So instead of filtering or averaging, scale separation is achieved through projection. The governing equations of motion for each scale are determined by the projection

of the NS equations onto the appropriate test function space. These equations are given below in a form where all the terms resulting from coupling between the different scales of motion are on the right hand side. Since it is assumed that the energy in the unresolved scales of motion is negligible we neglect all the terms involving $\widetilde{\bullet}$ and do not even give the equation governing the evolution of the unresolved scales.

- **Large Scale Equation**

$$\begin{aligned}\left(\overline{w}_i, \frac{\partial \overline{U}_i}{\partial t}\right) + \left(\overline{w}_i, \frac{\partial \left(\overline{U}_i \overline{U}_j\right)}{\partial x_j}\right) + \left(\overline{w}_i, \frac{\partial \overline{p}}{\partial x_i}\right) - \left(\overline{w}_i, \frac{\partial \left(2\nu \overline{S}_{ij}\right)}{\partial x_j}\right) \\ + \left(\overline{r}, \frac{\partial \overline{U}_i}{\partial x_i}\right) \\ = -\left(\overline{w}_i, \frac{\partial}{\partial x_j}\left(\overline{U}_i \widehat{U}_j + \widehat{U}_i \overline{U}_j\right)\right) - \left(\overline{w}_i, \frac{\partial \left(\widehat{U}_i \widehat{U}_j\right)}{\partial x_j}\right) \\ - \left(\overline{w}_i, \frac{\partial \widehat{U}_i}{\partial t}\right) - \left(\overline{w}_i, \frac{\partial \widehat{p}}{\partial x_i}\right) + \left(\overline{w}_i, \frac{\partial \left(2\nu \widehat{S}_{ij}\right)}{\partial x_j}\right) \\ - \left(\overline{r}, \frac{\partial \widehat{U}_i}{\partial x_i}\right)\end{aligned} \tag{7.8}$$

- **Small Scale Equation**

$$\begin{aligned}\left(\widehat{w}_i, \frac{\partial \widehat{U}_i}{\partial t}\right) + \left(\widehat{w}_i, \frac{\partial \left(\widehat{U}_i \widehat{U}_j\right)}{\partial x_j}\right) + \left(\widehat{w}_i, \frac{\partial \widehat{p}}{\partial x_i}\right) - \left(\widehat{w}_i, \frac{\partial \left(2\nu \widehat{S}_{ij}\right)}{\partial x_j}\right) \\ + \left(\widehat{r}, \frac{\partial \widehat{U}_i}{\partial x_i}\right) \\ = -\left(\widehat{w}_i, \frac{\partial}{\partial x_j}\left(\overline{U}_i \widehat{U}_j + \widehat{U}_i \overline{U}_j\right)\right) - \left(\widehat{w}_i, \frac{\partial \left(\overline{U}_i \overline{U}_j\right)}{\partial x_j}\right) \\ - \left(\widehat{w}_i, \frac{\partial \overline{U}_i}{\partial t}\right) - \left(\widehat{w}_i, \frac{\partial \overline{p}}{\partial x_i}\right) + \left(\widehat{w}_i, \frac{\partial \left(2\nu \overline{S}_{ij}\right)}{\partial x_j}\right) \\ - \left(\widehat{r}, \frac{\partial \overline{U}_i}{\partial x_i}\right)\end{aligned} \tag{7.9}$$

We make the following comments on the above equations:

1. The derivation of the above equations does *not* assume that the bases for $\overline{\mathcal{V}}$ and $\widehat{\mathcal{V}}$ are orthonormal. However, the use of an orthonormal basis causes terms such as

   (a) $\left(\overline{w}_i, \frac{\partial \widehat{U}_i}{\partial t}\right)$, $\left(\overline{w}_i, \frac{\partial \widehat{p}}{\partial x_i}\right)$, $\left(\overline{w}_i, \frac{\partial\left(2\nu \widehat{S}_{ij}\right)}{\partial x_j}\right)$, $\left(\overline{r}, \frac{\partial \widehat{U}_i}{\partial x_i}\right)$

   (b) $\left(\widehat{w}_i, \frac{\partial \overline{U}_i}{\partial t}\right)$, $\left(\widehat{w}_i, \frac{\partial \overline{p}}{\partial x_i}\right)$, $\left(\widehat{w}_i, \frac{\partial\left(2\nu \overline{S}_{ij}\right)}{\partial x_j}\right)$, $\left(\widehat{r}, \frac{\partial \overline{U}_i}{\partial x_i}\right)$

   to drop out. Hence, the use of an orthonormal basis reduces the complexity of the equations.

2. The use of basis functions with compact support for both $\overline{\mathcal{V}}$ and $\widehat{\mathcal{V}}$ largely simplifies the dependency between the coefficients of the different basis functions, $\overline{\mathbf{v}}_\mathbf{i}$, $\overline{\phi}$ and $\widehat{\mathbf{v}}_\mathbf{i}$, $\widehat{\phi}$. It will be seen later that for the purpose of statistical resolution of the small scales, this property is very useful in reducing the computational effort involved.

3. Thus, for our purposes the use of a hierarchical, orthogonal basis with compact support would be the most optimal. This naturally points to the use of wavelets or splines as a basis. However, it is only recently that research on using wavelets for flow simulations is gaining importance and to our knowledge, there are no VMS simulations of turbulent flow using wavelets. So, simply the implementation of VMS methods using wavelet or other hierarchical, orthogonal bases with compact support would in itself be an important contribution to the simulation of turbulent flows.

4. Although the use of an orthonormal basis reduces the complexity of the equations, the use of a basis with local support is more critical for reducing

the computational complexity of the proposed LES methodology and hence is the *only* assumption made for further derivation.

5. Equations (7.8) and (7.9) are the exact equations which need to be solved. If the omission or approximation of certain terms has little effect on the final solution, but leads to improved computational efficiency, then such a solution procedure should be investigated.

7.3.2 Need for statistical resolution of the small scales

For ease of presentation, we assume the hat functions shown in Fig. 7.1 (shown in 1d for simplicity) to be the bases for $\overline{\mathcal{V}}$ and $\widehat{\mathcal{V}}$. However, the comments made are general and should hold for any such basis with compact support. Please note

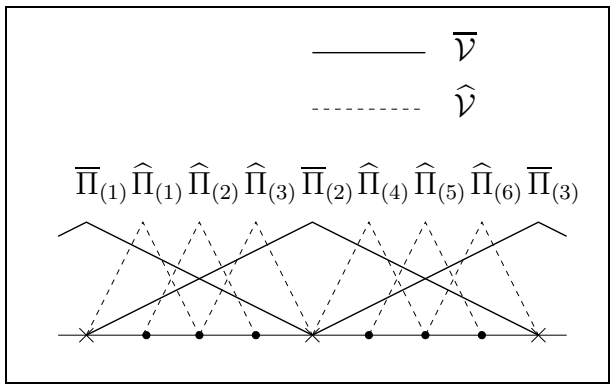

Figure 7.1: Example basis functions, $\overline{\Pi}_{(k)}$ for the large scale space, $\overline{\mathcal{V}}$ (solid line) and and $\widehat{\Pi}_{(k)}$ for the small scale space, $\widehat{\mathcal{V}}$ (dashed line).

that the basis functions:

- have compact support;
- are different from the standard FEM basis which goes to zero in the neighboring nodes. In this basis, the hat function centered on a cross goes to zero

only at the next cross.

- allow us to associate the large scale motions with $\overline{\mathcal{V}}$ and the small scale motions with $\widehat{\mathcal{V}}$; and
- can be extended to 3d in a trivial manner.

We now determine the computational time required to resolve the large and small scales. We define the following,

- $\overline{N} \equiv$ Number of basis functions in $\overline{\mathcal{V}}$ in each direction.
- $\widehat{N} \equiv$ Number of basis functions in $\widehat{\mathcal{V}}$ in each direction.
- $\widehat{N}_b \equiv \widehat{N}/\overline{N} =$ Number of small scale basis functions for each large scale basis function

The numbers of basis functions in 3d are simply the cubes of the above numbers. If we assume that computational work is directly proportional to the number of basis functions, then we note that the computational work involved in resolving the small scales is greater by a factor of $\left(\widehat{N}_b\right)^3$ than the computational work to resolve the large scales. For example, a typical DNS simulation of a turbulent flow could be performed on a 128^3 grid while the LES of the same flow could probably be simulated on a 32^3 grid. Since the resolved LES scales signify the large scales, by the above arguments, we are spending 27 times more computational work in resolving the small scales.

In DNS we *solve for all the coefficients of* the small scale basis functions $\overline{\mathbf{v}}_\mathbf{i}$, $\overline{\phi}$. Recognizing the fact that much of the computational effort is spend in resolving the small scales and hoping that the small scales can be easily and universally characterized, *current LES methodologies were developed in which all the small*

scales were modeled. Although, this methodology works well for a number of flows, there are a number of situations in which the sub-grid models used to characterize the effect of the small scales are inadequate.

The proposed LES methodology is a compromise between these two extremes and one in which a representative sample of the small scales are resolved. In fact, we solve stochastic equations for a representative sample of the small scales, and the large scale quantities which appear on the right hand side of Eq. (7.9) are modeled as stochastic input processes in time. The Spectral Stochastic Finite Element Method (also called generalized polynomial chaos) is used to evolve the small scale equations stochastically.

7.3.3 Model Stochastic Equations for the small scales

We now develop model stochastic equations for the small scales using hat functions as example basis functions for both the large and small scales. For simplicity of explanation, we look at a two-dimensional problem. It is again relatively straight forward to extend these ideas to the general three-dimensional problem using any basis functions with compact support. In Fig. 7.2 the nodes at which the large scale and small scale basis functions are centered are shown. The sub-domain, $\mathcal{D}_k$ is defined to be the intersection of the support of the large scale basis functions centered at nodes 1, 2, 3 and 4.

In order to evolve the small scales contained in sub-domain, $\mathcal{D}_k$, we need the coefficients of *only* the large scale basis functions centered at nodes 1, 2, 3 and 4 and the boundary conditions applied to the sub-domain, $\mathcal{D}_k$. It should be noted here that the use of bases with compact support greatly reduces the number of coefficients of the large scale basis functions on which the small scales in the sub-

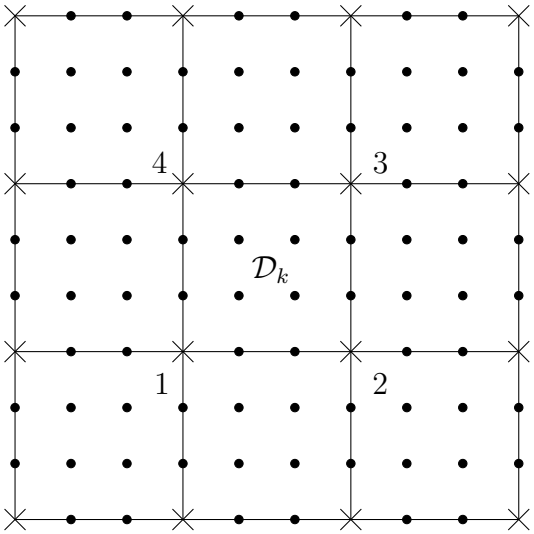

Figure 7.2: Sample nodes at which the large scale (denoted by crosses) and small scale (denoted by dots) basis functions are centered. Also shown is the partition of the complete domain, $\mathcal{D}$ into sub-domains, $\mathcal{D}_k$ based on the support of the large scale basis functions.

domain, $\mathcal{D}_k$ depends.

We first look at the issue of boundary conditions on the sub-domain, $\mathcal{D}_k$. The original problem without the scale separation has boundary conditions imposed on the boundary, $\partial\mathcal{D}$ of the entire domain, $\mathcal{D}$. After the scale separation, the boundary conditions for the large ($\overline{U}_i$, $\overline{p}$) and small scales($\widehat{U}_i$, $\widehat{p}$) are still applied on the boundary, $\partial\mathcal{D}$. (It should be mentioned here that all VMS methods make some assumptions in splitting the boundary conditions applied on the original problem among the different scales of motion.) Since we do not have any boundary conditions on the sub-domain, $\mathcal{D}_k$, these need to be modeled. For example, if we are simulating homogeneous isotropic turbulence, a natural boundary condition to apply is the periodic boundary condition on the boundary of sub-domain, $\mathcal{D}_k$. By applying the boundary conditions on the boundaries of the sub-domains, $\mathcal{D}_1$, $\mathcal{D}_2$, $\mathcal{D}_3$, ... we have successfully decoupled the evolution of the small scales in the different sub-domains. (This statement is not quite true, as the small scale solutions in the different sub-domains are still indirectly coupled thorough the large scale solution.)

Next comes the problem of determining on which sub-domains $\mathcal{D}_k$ we need to solve for the small scales. Please note that in order to evolve the large scales in the entire domain, $\mathcal{D}_k$, we need to evolve the small scales in *all* the sub-domains, $\mathcal{D}_1$, $\mathcal{D}_2$, $\mathcal{D}_3$, ... However, solving the small scales in all the sub-domains is computationally as intensive as carrying out a DNS. The only difference is that here the evolution of the small scales in each sub-domains is decoupled from the others because of the boundary conditions applied on the sub-domain boundary. Although this makes the solution procedure more easily parallelized, it does not reduce the computational cost as compared to DNS.

However, we can reduce the computational cost by adopting a statistical approach. Note that the only difference between the solution of the small scales in the different sub-domains, $\mathcal{D}_1$ and $\mathcal{D}_2$ (say), is the value of the coefficients of the large scale basis functions which are forcing the small scales. We choose a representative region $\mathcal{D}_k$ (say) and model the coefficients of the large scale basis functions using a stochastic process in time. The small scale field in $\mathcal{D}_k$ now becomes a stochastic process in space and time. Finally, we assume this small scale field in $\mathcal{D}_k$ to be statistically representative of the small scales in all the sub-domains. We have achieved a great reduction in computational cost by solving for a stochastic small scale field in *only* a representative region $\mathcal{D}_k$ instead of solving for the small scale field in the entire domain $\mathcal{D}$. The stochastic small scale field is represented using the generalized polynomial chaos method. More details on this method are given in subsection 7.3.4.

The information for modeling the required coefficients of the large scale basis comes from the large scale equations (LES equations) which are simultaneously solved. The hope is that the essential dynamics of the time evolution of the required subset of coefficients of the large scale basis ($\overline{\mathbf{v}}_\mathbf{i}$, $\overline{\phi}$) can be closely approximated using 2 or 3 independent random variables with an assumed distribution. For example, representations such as the Karhunen-Loeve expansion allow us to approximate a random process in time using its autocorrelation. This information can be extracted from solving the large scale equations, and the representation could be improved as the simulation progresses. Finally, the stochastic representation of the small scale field can be used to model the effect of the small scales on the evolution of the large scales.

7.3.4 Polynomial Chaos representation of small scales

The Generalized Polynomial chaos / Spectral Stochastic Finite Element Method (SSFEM) is an approach pioneered by Ghanem & Spanos (1991) in the context of FEM for solids, and was used to formulate algorithms to accurately reflect the propagation of uncertainty in stochastic inputs. The uncertainty in physical problems could be associated with the boundary or initial conditions, constitutive laws, transport coefficients, source and interaction terms, geometric irregularities, etc ... In the current LES methodology it is used to model the evolution of the small scales subject to different large scale forcing.

The essential concept in SSFEM is to regard uncertainty as generating a dimension and the solution as being dependent on this dimension. A convergent expansion along the new dimension is then sought in terms of polynomial chaos expansions [Ghanem & Spanos (1991); Ghanem (1999)] and the coefficients in this representation are determined through a Galerkin approach. SSFEM generally results in efficient uncertainty propagation schemes. It has been used in various applications including structural mechanics problems [Ghanem & Spanos (1991)], flow in random porous media [Ghanem (1998); Ghanem & Dham (1998)], flow with uncertainties in boundary conditions [Xiu & Karniadakis (2003); Narayanan & Zabaras (2005)] and mixing in micro-channels [Maitre *et al.* (2001)]. In our proposed LES methodology, SSFEM is used to stochastically evolve the small scales subject to a large scale forcing. To our knowledge, this would also be the first application of SSFEM using a stochastic input process in time.

Let $\widehat{\mathbf{vr_i}}$, $\widehat{\phi\mathbf{r}}$, denote the subset of the coefficients of the small scale basis functions, $\widehat{\mathbf{v}}_\mathbf{i}$, $\widehat{\phi}$, which are considered to be a statistically representative sample of the small scales. In Fig. 7.2 this would refer to the coefficients of all the small

scale basis functions in the representative sub-domain, $\mathcal{D}_k$. Let $\overline{\mathbf{vr_i}}$, $\overline{\phi\mathbf{r}}$ denote the subset of the coefficients of the large scale basis functions, $\overline{\mathbf{v}}_\mathbf{i}$, $\overline{\phi}$ which would appear on the right hand side of Eq. (7.9). In Fig. 7.2 this would refer to the coefficients of the large scale basis functions centered at the nodes 1, 2, 3 and 4. It is these large scale quantities, $\overline{\mathbf{vr_i}}$, $\overline{\phi\mathbf{r}}$ which are modeled as a stochastic input for the evolution of the small scales in the representative sub-domain, $\mathcal{D}_k$. They are modeled as a stochastic random process in time using S independent random variables, $\xi \equiv \left\{\xi^{\{1\}}, \xi^{\{2\}}, \ldots, \xi^{\{S\}}\right\}^T$. For example:

$$\overline{vr}_{i,(1)}(t) \stackrel{M}{=} \overline{vr}^{\{0\}}_{i,(1)}(t) + \sum_{s=1}^{S} \overline{vr}^{\{s\}}_{i,(1)}(t) \times \xi^{\{s\}} \tag{7.10}$$

where $\overline{vr}^{\{s\}}_{i,(1)}(t)$ are deterministic functions of time, t, obtained by some means from the statistics of $\overline{vr}_{i,(1)}(t)$ extracted from the large scale equations being simultaneously solved. It is hoped that the number of independent random variables, S, used to represent $\overline{\mathbf{vr_i}}$, $\overline{\phi\mathbf{r}}$ would be small, maybe of the order of 2 to 3.

The dependence of the small scale solution on the stochastic large scale coefficients, $\overline{\mathbf{vr_i}}$, $\overline{\phi\mathbf{r}}$, is expressed by expanding the small scale velocity and pressure field as

$$\begin{aligned} \widehat{ur}_i(x_j,t) &\stackrel{M}{=} \widehat{ur}_i^{[0]}(x_j,t) + \sum_{p=1}^{P} \widehat{ur}_i^{[p]}(x_j,t) \times \psi^{[p]}(\xi) \\ \Rightarrow \widehat{vr}_{i,(k)}(t) &\stackrel{M}{=} \widehat{vr}^{[0]}_{i,(k)}(t) + \sum_{p=1}^{P} \widehat{vr}^{[p]}_{i,(k)}(t) \times \psi^{[p]}(\xi) \end{aligned} \tag{7.11}$$

$$\begin{aligned} \widehat{pr}(x_j,t) &\stackrel{M}{=} \widehat{pr}^{[0]}(x_j,t) + \sum_{p=1}^{P} \widehat{pr}^{[p]}(x_j,t) \times \psi^{[p]}(\xi) \\ \Rightarrow \widehat{\phi r}_{,(k)}(t) &\stackrel{M}{=} \widehat{\phi r}^{[0]}_{,(k)}(t) + \sum_{p=1}^{P} \widehat{\phi r}^{[p]}_{,(k)}(t) \times \psi^{[p]}(\xi) \end{aligned} \tag{7.12}$$

where

- $\psi^{[p]}(\xi)$ denotes the polynomial chaos functions in the random variables, ξ.

- $\widehat{ur}_i^{[p]}(x_j,t)$, $\widehat{pr}^{[p]}(x_j,t)$ denote the *unknown deterministic* small scale fields which arise in the polynomial chaos expansion. Solving for $\widehat{ur}_i^{[p]}(x_j,t)$, $\widehat{pr}^{[p]}(x_j,t)$ is equivalent to solving for the coefficients of the small scale basis functions, $\widehat{\mathbf{vr}}_\mathbf{i}^{[p]}(t)$, $\widehat{\phi\mathbf{r}}^{[p]}(t)$, used to represent these fields. So the two forms of Eqs. (7.11) and (7.12) are equivalent.

- P is the order of the polynomial chaos expansion

The polynomial chaos functions are usually chosen to be optimal for representing the stochastic fields arising from specified input random variables and to be orthonormal functions with respect to a weighting function based on the probability density function of the random variables. For example: Weiner-Hermite polynomial expansions are used to solve stochastic differential equations with Gaussian inputs. These polynomials are orthogonal with respect to the weighting function, $W(\xi) = e^{-\frac{\xi^T\xi}{2}}$. More details on polynomial chaos expansions can be found in the literature [Xiu & Karniadakis (2003); Ghanem (1999); Maitre *et al.* (2001)]. Much of the early work on polynomial chaos functions was restricted to the use of stochastic Gaussian inputs and Werner-Hermite chaos expansions. Later, Xiu & Karniadakis (2003) generalized this method to stochastic inputs with other probability distributions (such as uniform, Beta, Gamma distributions) using orthogonal polynomial functions from the Askey scheme as trial bases to represent the random space. This generalization gives much greater flexibility in the representation of stochastic random inputs and has already been used to simulate flows with random boundary conditions [Xiu & Karniadakis (2003); Narayanan & Zabaras (2005)]. Also, Narayanan & Zabaras (2005) have derived FEM formulations for solving these stochastic differential equations. The work on polynomial chaos expansions is still in its infancy and much research is required to develop better

expansions.

The governing equations for the evolution of the small scale fields, $\widehat{ur}_i^{[p]}(x_j,t)$, $\widehat{pr}^{[p]}(x_j,t)$ (or, equivalently, $\widehat{\mathbf{vr}}_{\mathbf{i}}^{[p]}(t)$, $\widehat{\phi\mathbf{r}}^{[p]}(t)$) can be obtained by substituting the polynomial chaos expansions for the small scale velocity and pressure fields, Eqs. (7.11) and (7.12), along with the stochastic representation of the large scale velocity fields, Eq. (7.10), into the small scale evolution equation (7.9), multiplying the result by $\psi^{[p]}(\xi)$ and then computing the expected value of the resulting equation. The orthogonality of the polynomial chaos functions helps reduce the complexity of the resulting equations. For details, refer to the cited literature [Maitre *et al.* (2001); Xiu & Karniadakis (2003); Ghanem (1999)].

The above procedure results in a system of P coupled equations for the small scale fields, $\widehat{ur}_i^{[p]}$, $\widehat{pr}^{[p]}$. Although the resulting equations are more complicated than the original small scale evolution equation (7.9), it has been demonstrated [Maitre *et al.* (2001); Xiu & Karniadakis (2003)] that the computational cost involved in solving these equations is comparable to solving P original small scale evolution equations.

Hence, the computational advantage of the proposed LES methodology as compared with a DNS, is obtained from the fact that we expect the order of the expansion, P to be *much smaller* than the number of sub-domains in the whole domain, $\mathcal{D}$. The increase in computational cost of the proposed LES methodology as compared with existing LES methodologies would be the cost for statistically resolving the small scales, which is of the order of $P\left(\widehat{N}_b\right)^3$, where $\left(\widehat{N}_b\right)^3$ was defined to be the number of small scale basis functions in the representative sub-domain, $\mathcal{D}_k$. This small additional cost is justified on the basis of

1. The provision of better sub-grid models for the large scale equations;

2. The provision of statistical information for both the large and small scale fields which gives us a better estimate of the statistics of the underlying turbulent flow; and

3. The potential to use statistics of the small scales to estimate errors in the LES simulations and to modify the *a priori* scale separation to achieve a given error tolerance level.

We believe concepts such as the statistical resolution of small scales and the solution of different scales on different sized domains could be an integral part of future LES methodologies. We have presented one way of implementing these concepts. The choice of Variational Multiscale (VMS) methods to formulate the LES equations is justified on the basis on the strong mathematical foundation they provide. Further, the use of wavelets and other hierarchical basis functions in these methods would result in powerful tools for turbulence research. The use of the polynomial chaos method for statistical representation of the small scales is motivated by its success in representing uncertainty in a wide variety of problems and its recent generalization to non-Gaussian random variables.

BIBLIOGRAPHY

Balaras, E., Piomelli, U. & Wallace, J. M. 2001 Self-similar states in turbulent mixing layers. *Journal of Fluid Mechanics* **446**, 1–24.

Bardina, J., Ferziger, J. H. & C., R. W. 1983 Improved turbulence models based on les of homogeneous incompressible turbulent flows. *Tech. Rep.* TF-19. Mechanical Engineering Department, Stanford University.

Boyd, J. P. 1981 The optimization of convergence for Chebyshev polynomial methods in an unbounded domain. *Journal of Computational Physics* **45**, 43–79.

Brachet, M. E., Meiron, D. I., Orszag, S. A., Nickel, B., Morf, R. H. & Frisch, U. 1983 Small-scale structure of the taylor-green vortex. *Journal of Fluid Mechanics* **130**, 411–452.

Brown, G. L. & Roshko, A. 1974 On density effects and large structures in turbulent mixing layers. *Journal of Fluid Mechanics* **64**, 775–816.

Choi, D. & Merkle, C. L. 1985 Application of Time-Iterative schemes to incompressible flow. *AIAA Journal* **23**, 1518–1524.

Chorin, A. J. 1967 A numerical method for solving incompressible viscous flow problems. *Journal of Computational Physics* **2**, 12–26.

Chorin, A. J. 1968 Numerical solution of the Navier-Stokes equations. *Mathematics of Computation* **22**, 745–762.

Clark, R. A., Ferziger, J. H. & Reynolds, W. C. 1979 Evaluation of sub-grid-scale models using an accurately simulated turbulent flow. *Journal of Fluid Mechanics* **91**, 1–16.

Collis, S. S. 2001 Monitoring unresolved scales in multiscale turbulence modeling. *Physics of Fluids* **13** (6), 1800–1806.

Collis, S. S. 2002 Multiscale methods for turbulence simulation and control. In *VKI Lecture Series - Multiscale Methods* (ed. H. Deconinck), , vol. 06, pp. 29–40.

Comte-Bellot, G. & Corrsin, S. 1971 Simple eulerian time correlations of full- and narrow-band velocity signals in grid-generated isotropic turbulence. *Journal of Fluid Mechanics* **48**, 273–337.

Deardorff, J. W. 1974 Three-dimensional numerical study of the height and mean structure of a heated planetary boundary layer. *Boundary-layer meteorology* **7**, 81–106.

Deardorff, J. W. 1980 Stratocumulus-capped mixed layers derived from a three-dimensional model. *Boundary-layer meteorology* **18**, 495–527.

Dukowicz, J. K. & Dvinsky, A. S. 1992 Approximate Factorization as a High Order Splitting for the Implicit Incompressible Flow Equations. *Journal of Computational Physics* **102**, 336–347.

Eswaran, V. & Pope, S. B. 1988 An examination of forcing in direct numerical simulations of turbulence. *Computers and Fluids* **16**, 257–178.

Flynn, M. 1972 Some computer organizations and their effectiveness. *IEEE Transactions on Computing* (C-21), 948–960.

Germano, M. 1992 Turbulence: the filtering approach. *Journal of Fluid Mechanics* **238**, 325–336.

Germano, M., Piomelli, U., Moin, P. & Cabot, W. H. 1991 A dynamic subgrid-scale eddy viscosity model. *Physics of Fluids A* **3**, 1760–1765.

Geurts, B. 2004 *Elements of Direct and Large-Eddy Simulation*. R. T. Edwards.

Ghanem, R. G. 1998 Probabilistic characterization of transport in heterogenous porous media. *Computer methods in applied mechanics and engineering* **158**, 199.

Ghanem, R. G. 1999 Ingredients for a general purpose stochastic finite elements implementation. *Computer methods in applied mechanics and engineering* **168**, 19–34.

Ghanem, R. G. & Dham, S. 1998 Stochastic finite element analysis for multiphase flow in heterogenous porous media. *Transport in Porous Media* **32**, 239.

Ghanem, R. G. & Spanos, P. 1991 *Stochastic Finite Elements: A Spectral Approach*. Springer.

Ghosal, S., Lund, T. S., Moin, P. & Akselvoll, K. 1995 A dynamic localization model for large-eddy simulation of turbulent flows. *Journal of Fluid Mechanics* **286**, 229–255.

Ghosal, S. & Moin, P. 1995 The basic equations for the large eddy simulation of turbulent flows in complex geometries. *Journal of Computational Physics* **118**, 24–37.

Gicquel, L. Y. M., Givi, P., Jaberi, F. A. & Pope, S. B. 2002 Velocity filtered density function for large eddy simulation of turbulent flows. *Physics of Fluids* **14** (3), 1196–1212.

Golub, G. H. & Loan, C. F. V. 1996 *Matrix Computations*, 3rd edn., pp. 508–517. The Johns Hopkins University Press.

Gravemeier, V., A.Wall, W. & Ramm, E. 2004 A three-level finite element method for the instationary incompressible navier-stokes equations. *Computer Methods in Applied Mechanics and engineering* **193** (15-16), 1323–1366.

Gresho, P. M. 1991 Incompressible Fluid Dynamics: Some fundamental formulations issues. *Annual Review of Fluid Mechanics* **23**, 413–53.

Grosch, C. E. & Orszag, S. A. 1977 Numerical solution of problems in unbounded regions: Coordinate transforms. *Journal of Computational Physics* **25**, 273–296.

Harlow, F. H. & Welch, J. E. 1965 Numerical calculation of time-dependent viscous incompressible flow with free surface. *Physics of Fluids* **8** (12), 2182–2189.

Hughes, T. J., Mazzei, L. & Jansen, K. E. 2000 Large eddy simulation and the variational multiscale method. *Computing and Visualization in Science* **3**, 47–59.

Hughes, T. J., Mazzei, L., Oberai, A. A. & Wray, A. A. 2001*a* The multiscale formulation of large eddy simulation: Decay of homogenous isotropic turbulence. *Physics of Fluids* **13** (2), 505–512.

Hughes, T. J., Oberai, A. A. & Mazzei, L. 2001*b* Large eddy simulation of turbulent channel flows by the variational multiscale method. *Physics of Fluids* **13** (6), 1784–1799.

Issa, R. I., Gossman, A. D. & Watkins, A. P. 1986 The computation of compressible and incompressible recirculating flows by an non-iterative implicit scheme. *Journal of Computational Physics* **62**, 66–82.

Karniadakis, G. E. 1991 High-Order Splitting Methods for the Incompressible Navier-Stokes Equations. *Journal of Computational Physics* **97**, 414–443.

Kim, J. & Moin, P. 1985 Application of a Fractional-Step Method to Incompressible Navier-Stokes Equations. *Journal of Computational Physics* **59**, 308–323.

Kolmogorov, A. N. 1991 The local structure of turbulence in incompressible viscous fluid for very large reynolds numbers. *Proceedings of the Royal Society. London. Series A.* **434**, 9–13.

Kurganov, A. & Tadmor, E. 2000 New high-resolution central schemes for nonlinear conservation laws and convection-diffusion equations. *Journal of Computational Physics* **160**, 241–282.

Kwak, D., Chang, J. L. C., Shanks, S. P. & Chakravarthy, S. K. 1986 A three-dimensional incompressible Navier-Stokes solver using primitive variables. *AIAA Journal* pp. 390–396.

Kwak, D., Kris, C., Dacles-Mariani, J., Rogers, S. & Yoon, S. 1998 Incompressible Navier-stokes Computations in Aerospace Applications and Beyond. In *Frontiers of Computational Fluid Dynmics 1998* (ed. D. A. Caughey & M. M. Hafez). World Scientific.

Lamorgese, A. G., Caughey, D. A. & Pope, S. B. 2005 Direct numerical simulation of homogeneous turbulence with hyperviscosity. *Physics of Fluids* **17** (015106).

Langford, J. A. & Moser, R. D. 1999 Optimal les formulations for isotropic turbulence. *Journal of Fluid Mechanics* **398**, 321–346.

Langtangen, H. P., Mardal, K.-A. & Winther, R. 2002 Numerical Methods for incompressible viscous flow. *Advances in Water Resources* **25**, 1125–1146.

Lesieur, M. & Metais, O. 1996 New trends in large-eddy simulations of turbulence. *Annual Review of Fluid Mechanics* **28**, 45–82.

Lilly, D. K. 1967 The representation of small-scale turbulence in numerical simulation experiments. In *Proceedings of IBM Scientific Computing Symposium on Environmental Sciences* (ed. H. H. Goldstine), pp. 195–210.

Liu, S., Meneveau, C. & Katz, J. 1994 On the properties of similarity subgrid-scale models as deduced from measurements in a turbulent jet. *Journal of Fluid Mechanics* **275**, 83–119.

Lumley, J. L. 1967 Similarity and the turbulent energy spectrum. *The Physics of Fluids* **10** (4), 855–858.

Mahesh, K., Constantinescu, G. & Moin, P. 2004 A numerical method for large-eddy simulation in complex geometries. *Journal of Computational Physics* **197**, 215–240.

Maitre, O. P. L., Knio, O. M., Najm, H. N. & Ghanem, R. G. 2001 A Stochastic Projection Method for Fluid Flow - basic formulation. *Journal of Computational Physics* **173**, 481–511.

Mason, P. J. 1989 Large-eddy simulation of the convective atmospheric boundary layer. *Journal of the Atmospheric Sciences* **46**, 1492–1516.

McMillan, O. J. & Ferziger, J. H. 1979 Direct testing of sub-grid scale models. *AIAA Journal* **17**, 1340–1346.

Metcalfe, R. W., Orszag, S. A., Brachet, M. E., Menon, S. & Riley, J. J. 1987 Secondary instability of a temporally growing mixing layer. *Journal of Fluid Mechanics* **184**, 207–243.

Michalke, A. 1964 On the inviscid instability of the hyperbolic-tangent profile. *Journal of Fluid Mechanics* **19**, 543–556.

Moin, P. & Mahesh, K. 1998 Direct numerical simulation: A tool in turbulence research. *Annual Review of Fluid Mechanics* **30**, 539–578.

Morinishi, Y., Lund, T. S., Vasilyev, O. V. & Moin, P. 1998 Fully conservative higher order finite difference schemes for incompressible flow. *Journal of Computational Physics* **143**, 90–124.

Moser, R. D. & Rogers, M. M. 1993 The three-dimensional evolution of a plane mixing layer: pairing and transition to turbulence. *Journal of Fluid Mechanics* **247**, 275–320.

Mydlarski, L. & Warhaft, Z. 1996 On the onset of high-reynolds-number grid-generated wind tunnel turbulence. *Journal of Fluid Mechanics* **320**, 331–368.

Narayanan, V. A. B. & Zabaras, N. 2005 Variational multiscale stabilized FEM formulations for transport equations: stochastic advection-diffusion and

incompressible stochastic Navier-Stokes equations. *Journal of Computational Physics* **202**, 94–133.

Orszag, S. A., Israeli, M. & Deville, M. O. 1986 Boundary Conditions for Incompressible Flows. *Journal of Scientific Computing* **1** (1), 75–110.

Orszag, S. A. & Patterson, G. S. 1972 Numerical simulation of three-dimensional homogeneous isotropic turbulence. *Physical Review Letters* **28**, 76–79.

Overholt, M. R. & Pope, S. B. 1998 A deterministic forcing scheme for direct numerical simulations of turbulence. *Computers and Fluids* **27** (1), 11–28.

Papoulis, A. 1991 *Probability, random variables, and stochastic processes*, 3rd edn. McGraw Hill.

Patankar, S. V. 1975 Numerical prediction of three-dimensional flows. In *Studies in Convection: Theory, Measurement and Applications* (ed. B. E. Launder), , vol. 1, pp. 1–78. Academic.

Patankar, S. V. 1980 *Numerical Heat Transfer and Fluid Flow*. Hemisphere.

Perot, J. B. 1993 An analysis of the fractional step method. *Journal of Computational Physics* **108**, 51–58.

Pierce, C. D. 2001 Progress-variable approach for large eddy simulation of turbulent combustion. PhD thesis, Stanford University.

Pierrehumbert, R. T. & Widnall, S. E. 1982 The two- and three-dimensional instabilities of a spatially periodic shear layer. *Journal of Fluid Mechanics* **114**, 59–82.

Pope, S. B. 1999 A perspective on turbulence modeling. In *Modeling Complex Turbulent Flows* (ed. M. D. Salas), pp. 53–67. Kluwer Academic Publishers.

Pope, S. B. 2000*a* *Turbulent Flows*, chap. Direct Numerical Simulation, pp. 344–357. Cambridge University Press.

Pope, S. B. 2000*b* *Turbulent Flows*, p. 87. Cambridge University Press.

Pope, S. B. 2000*c* *Turbulent Flows*. Cambridge University Press.

Pope, S. B. 2000*d* *Turbulent Flows*, chap. Large-eddy Simulation, pp. 558–640. Cambridge University Press.

Pope, S. B. 2000*e* *Turbulent Flows*, pp. 76–79. Cambridge University Press.

Pope, S. B. 2000*f* *Turbulent Flows*, chap. The scales of turbulent motion, pp. 182–263. Cambridge University Press.

Pope, S. B. 2004 Ten questions concerning the large-eddy simulation of turbulent flows. *New Journal of physics* **6** (35).

Press, W. H., Teukolsky, S. A., Vellering, W. T. & Flannery, B. P. 1992 *Numerical Recipes in C*, 2nd edn., pp. 504–531. Cambridge University Press.

Rhie, C. M. & Chow, W. L. 1983 Numerical study of turbulent flow past an airfoil with trailing edge separation. *AIAA Journal* **21**, 1525–1532.

Richardson, L. F. 1922 *Weather Prediction by Numerical Process*. Cambridge University Press.

Rogallo, R. S. 1981 Numerical experiments in homogeneous turbulence. *Tech. Rep.* TM-81315. NASA.

Rogallo, R. S. & Moin, P. 1984 Numerical simulation of turbulent flows. *Annual Review of Fluid Mechanics* **16**, 99–137.

Rogers, M. M. & Moser, R. D. 1994 Direct simulation of a self-similar turbulent mixing layer. *Physics of Fluids* **6** (2), 903–923.

Saddoughi, S. G. & Veeravalli, S. V. 1994 Local isotropy in turbulent boundary layers at high reynolds number. *Journal of Fluid Mechanics* **268**, 333–372.

Sagaut, P. 2002 *Large eddy simulation for incompressible flows: an introduction*. Springer.

Sandham, N. D. & Reynolds, W. C. 1991 Three-dimensional simulation of large eddies in the compressible mixing layer. *Journal of Fluid Mechanics* **224**, 133–158.

Schmidt, H. & Schumann, U. 1989 Coherent structure of the convective boundary layer derived from large-eddy simulations. *Journal of Fluid Mechanics* **200**, 511–562.

Sheikhi, R. M. H. 2005 Private communication.

Shen, X. & Warhaft, Z. 2000 The anisotropy of the small scale structure in high reynolds number turbulent shear flow. *Physics of Fluids* **12**, 2976–2989.

Shih, T. I.-P. & Caughey, D. A. 1994 *Foundations of Computational Fluid Dynamics*, draft edn., pp. 110–114.

Smagorinsky, J. 1963 General circulation experiments with the primitive equations. *Mon. Weather Rev.* **91**, 99–164.

Spector, D. 2000 *Building Unix Clusters*. O'Reilly.

S.Ramakrishnan & Collis, S. 2004 Turbulence control simulation using the variational multiscale method. *AIAA Journal* **42** (4), 745–753.

van der Steen, A. J. & Dongarra, J. J. 2004 Overview of Recent Supercomputers. www.top500.org/ORSC/2004/, website.

Steger, J. L. & Kutler, P. 1976 Implicit finite-difference procedures for the computation of vortex wakes. In *AIAA Paper, 76-385*.

Sterling, T., Salmon, J., Becker, D. & Savaresse, D. 1999 *How to Build a Beowulf*. The MIT Press.

Tannehill, J. C., Anderson, D. A. & Pletcher, R. H. 1997*a* *Computational Fluid Mechanics and Heat Transfer*, 2nd edn., pp. 649–677. Taylor Francis.

Tannehill, J. C., Anderson, D. A. & Pletcher, R. H. 1997*b* *Computational Fluid Mechanics and Heat Transfer*, 2nd edn., pp. 338–341. Taylor Francis.

Temam, R. 1984 *Navier-Stokes equations - Theory and Numerical Analysis*, 3rd edn. North-Holland.

Thomas, P. D. & Lombard, C. K. 1978 The Geometric Conservation Law - a Link between Finite-Difference and Finite-Volume Methods of Flow Computation on Moving Grids. In *AIAA Paper, 78-1208*.

Vasilyev, O. V. 2000 High Order Finite Difference Schemes on Non-uniform Meshes with Good Conservation Properties. *Journal of Computational Physics* **157**, 746–761.

Vasilyev, O. V., Lund, T. S. & Moin, P. 1998 A general class of commutative filters for les in complex geometries. *Journal of Computational Physics* **146**, 82–104.

Vinokur, M. 1974 Conservation Equations of Gas-Dynamics in Curvilinear Coordinate Systems. *Journal of Computational Physics* **14**, 105–125.

Viviand, H. 1974 Conservative forms of Gas Dynamic Equations. *La Rech. Aerosp.* (1974-1), 65–68.

Vreman, B., Geurts, B. & Kuerten, H. 1994 Realizability conditions for the turbulent stress tensor in large-eddy simulation. *Journal of Fluid Mechanics* **278**, 351–362.

Vreman, B., Geurts, B. & Kuerten, H. 1996 Comparison of numerical schemes in large-eddy simulation of the temporal mixing layer. *International journal for numerical methods in fluids* **22**, 297–311.

Vreman, B., Geurts, B. & Kuerten, H. 1997 Large-eddy simulation of the turbulent mixing layer. *Journal of Fluid Mechanics* **339**, 357–390.

Wasistho, B. & Moser, R. D. 2005 Simulation strategy of turbulent internal flow in solid rocket motor. *Journal of Propulsion and Power* **21** (2), 251–263.

Wilcox, D. C. 1998 *Turbulence Modeling for CFD*, 2nd edn. DCW Industries, Inc.

Winant, C. D. & Browand, F. K. 1974 Vortex pairing: the mechanism of turbulent mixing-layer growthat moderate reynolds number. *Journal of Fluid Mechanics* **63**, 237–255.

Xiu, D. & Karniadakis, G. E. 2003 Modeling uncertainty in flow simulations via generalized polynomial chaos. *Journal of Computational Physics* **187**, 137–167.

Yanenko, N. N. 1971 *The method of fractional steps. The solution of problems of mathematical physics in several variables*. Springer-Verlag.

Yeung, P. K. & Brasseur, J. G. 1991 The response of isotropic turbulence to isotropic and anisotropic forcing at the large scales. *Physics of Fluids A* **3**, 884–897.

Yeung, P. K. & Pope, S. B. 1989 Lagrangian statistics from direct numerical simulations of isotropic turbulence. *Journal of Fluid Mechanics* **207**, 531–586.

Zang, Y., Street, R. L. & Koseff, J. R. 1993 A dynamic mixed subgrid-scale model and its application to turbulent recirculating flows. *Physics of Fluids A* **5**, 3186–3196.

Zang, Y., Street, R. L. & Koseff, J. R. 1994 A Non-staggered Grid Fractional Step Method for Time-Dependent Incompressible Navier-Stokes Equations in Curvilinear Coordinates. *Journal of Computational Physics* **114**, 18–33.